The Voronoi liquid : a new model to probe the glass transition

Céline Ruscher

Direction de la Recherche
Université de Strasbourg

UNIVERSITÉ DE STRASBOURG

ÉCOLE DOCTORALE PHYSIQUE ET CHIMIE-PHYSIQUE

INSTITUT CHARLES SADRON

THÈSE présentée par :

Céline RUSCHER

soutenue le : **05 octobre 2017**

pour obtenir le grade de : **Docteur de l'université de Strasbourg**

Discipline/ Spécialité : **Physique**

The Voronoi Liquid: a new model to probe the glass transition

THÈSE dirigée par :

Pr. FARAGO Jean Professeur des Universités, Université de Strasbourg

RAPPORTEURS :

Dr. COSLOVICH Daniele Maître de Conférences, HDR, Université de Montpellier

Dr. ROYALL Christopher Patrick Reader, Bristol University, Bristol

---

AUTRES MEMBRES DU JURY :

Dr. JANSSEN Liesbeth Assistant Professor, Eindhoven University of Technology

Dr. HEBRAUD Pascal Directeur de recherche, IPCMS, Strasbourg

Pr. BASCHNAGEL Jörg Professeur des Universités, Université de Strasbourg

A mon père qui aurait aimé lire ces pages.

Acknowledgements

Ce manuscrit clôture mon cycle universitaire à Strasbourg ainsi que trois ans d'un long et passionnant travail de recherche. Cette thèse a été, sans nul doute, une prise de risque, mais aujourd'hui je constate avec plaisir que tout ce travail a permis de faire émerger un tout nouveau système qui, je l'espère, aura l'attention qu'il mérite. Malgré la solitude qui va de paire avec la nouveauté, j'ai eu l'opportunité d'avoir un grand nombre d'échanges enrichissants avec des personnes de tous horizons et je voudrais les en remercier.

En premier lieu, je tiens à exprimer ma gratitude aux deux personnes qui ont grandement contribuer à façonner la jeune scientifique que je suis devenue. D'abord Jean Farago, mon directeur de thèse, qui a eu la patience de m'encadrer tout au long de cette thèse (et même bien avant !). Ta présence et ton aide tout au long de ce travail m'ont été plus que précieuses. Mais je voudrais surtout te dire merci pour ton exigence (même parfois *too much*). En me demandant constamment de repousser mes limites, d'aller toujours plus en profondeur, j'ai progressé bien plus que je n'aurais pu l'imaginer.
Ensuite, je voudrais remercier tout particulièrement Jörg Baschnagel pour la confiance qu'il m'a témoigné en soutenant de façon toujours enthousiaste mes projets de la licence au doctorat. Son aide précieuse ainsi que ses conseils avisés m'ont permis de vivre des expériences enrichissantes et d'avancer dans mon travail de la meilleure façon qui soit.

Je tiens aussi à remercier Paddy Royall et Daniele Coslovich pour l'intérêt qu'ils ont témoigné envers mon travail au cours des différentes conférences dans lesquelles nous nous sommes croisés. De plus, je leur suis très reconnaissante d'avoir bien accepté d'être les rapporteurs de cette thèse et d'avoir pris le temps de lire et commenter mon travail. Je remercie aussi les examinateurs de mon jury, Liesbeth Janssen et Pascal Hébraud, pour leurs remarques constructives.

Un grand merci à Olivier Benzerara pour son aide avec les simulations numériques et bien plus ! Ton amitié a été précieuse pour moi durant ces dernières années et je te suis très reconnaissante de m'avoir soutenue même dans les moments les plus difficiles. Je te remercie aussi pour ta formation express au premier secours numérique et j'ai une pensée pour nos indispensables acolytes : remus, kalliope, romulus, est33, data5 et surtout data8 que j'ai si souvent maltraité.

Merci à tous mes collègues de l'équipe de simulations et théories ainsi qu'à toutes les personnes de l'Institut Charles Sadron avec qui j'ai eu le plaisir de discuter de science ou de tout autre chose pendant ces 3 ans.

Je voudrais remercier aussi l'IRTG SoMaS pour m'avoir permis de participer à un grand nombre de conférences. Je suis très reconnaissante envers Jana Husse et Birgitta Zovko pour leur aide au cours de ces trois dernières années.

J'ai eu le privilège de partager mes joies et mes galères avec des personnes qui vont me manquer. D'abord mon co-bureau, Julien Fierling alias Julian Fielding, avec qui j'ai passé deux super années. Merci pour ton amitié, ton soutien et pour tous nos fou-rires. On se rappellera toujours de la chapelle, du parc et des PhD movies. Ce bureau n'aurait jamais été le même sans la boule à Thierry, le rouleau de Sopalin, Bob, Ben & Nuts et Fabrice le lion.
Ensuite Vivien Walter, mon acolyte de TP et un super ami ! Je te remercie pour le Faisan qui couine, la pause café du matin, ton aide diverse et variée, nos blagues plus que douteuses, nos discussions sur le futur, merci d'être toujours là pour me pousser à croire en mes rêves. Grâce à toi, j'ai aussi pu rencontrer Céline, ton épouse, qui est une personne merveilleuse. Je la remercie pour ses super recettes. Aligot forever ! Nos soirées de vieux couples à tester différents jeux me manqueront.
Merci aussi à Othmene, Viktoria, Morgane et tous ceux que j'oublie !

Merci à Amandine, Michael, Sarah et Falko pour toutes ces belles découvertes culinaires lors de nos soirées restaurants. Je remercie aussi Juliette, Constance et Emma Farago pour leur accueil chaleureux chez elles, ainsi que leur délicieuses recettes. Le *jujutella* me manquera !

Je voudrais exprimer ma gratitude envers toutes les personnes qui m'ont aidé à traverser les épreuves personnelles qui se sont accumulées ces trois dernières années.
Birgitta, je ne saurais jamais comment te remercier pour le temps que tu as passé à me réconforter. Si j'ai poursuivi cette thèse jusqu'au bout c'est très certainement grâce à ton soutien. Je suis plus qu'heureuse de t'avoir comme amie et d'avoir partagé tous ces moments avec toi. Merci aussi à Iva, Kaja et Bozo pour tous les moments de joie au restaurant ou en ballade à Freiburg.
Maria, ma soeur marocaine, tu as toujours cru en moi, tu as toujours su m'aider à aller de l'avant. Si j'en suis là aujourd'hui, c'est aussi grâce à toi. Je te remercie pour tous ces moments partagés ces dernières années, nos soirées raclettes à refaire le monde, nos expériences de recherches à l'IPHC, les cours et puis récemment les visites à Saint-Louis et Bâle.
Merci aussi à Juliette et Pauline pour leur amitié indéfectible.

En dernier lieu, je voudrais remercier ma famille. D'abord mes parents qui m'ont donné le goût du travail et qui m'ont toujours poussé à donner le meilleur de moi-même. Je suis très reconnaissante envers mon père pour avoir partagé avec moi son goût de la science. Je sais qu'il aurait été fier de voir l'aboutissement de ce travail. Je remercie aussi ma

mère pour son soutien au cours de toutes ces années et pour m'avoir toujours encouragé à aller au bout des mes rêves.
Finalement, je remercie mon mari, Pierre, qui a eu la patience de me supporter tout au long de cette thèse. Tu sais toujours trouver les mots pour m'encourager ou me réconforter et je me réjouis déjà des belles aventures qui nous attendent !

Contents

Résumé

Lorsqu'un liquide est refroidi, il se peut que ce dernier évite la cristallisation. Il entre alors dans un état métastable par rapport au cristal, qu'on appelle régime surfondu. Ce régime se caractérise par un accroissement important du temps de relaxation et de la viscosité du système étudié. Lorsqu'on poursuit le refroidissement, il existe une température, appelée température de transition vitreuse, en deçà de laquelle, aux échelles de temps accessibles à l'expérimentation, le liquide se retrouve dans un état hors équilibre et forme un verre. La température de transition vitreuse est définie expérimentalement lorsque la viscosité atteint 10^{13}Poise ou que le temps de relaxation est de l'ordre de $100 - 1000$s. Bien que le ralentissement de la dynamique semble indiquer la présence d'une transition, la nature thermodynamique de celle-ci n'a jamais été clairement identifiée [8].

Le temps de relaxation dans le liquide surfondu est lié à des réarrangements structuraux impliquant un nombre fini de particules [8, 14]. L'augmentation du temps de relaxation suggère donc qu'un nombre croissant de particules est impliqué dans des réorganisations. Ces dernières ne sont pas des évènements isolés les uns des autres mais au contraire résultent de processus coopératifs. Ces observations suggèrent l'existence d'une longueur de corrélation croissante au voisinage de la transition vitreuse, réminiscente du scénario ordinaire des phénomènes critiques. Cependant la difficulté principale réside dans l'application de la méthodologie classique des transitions de phases. Quel est le paramètre d'ordre pertinent ? Quelle fonction de corrélation utiliser ? De nombreux travaux se sont attelés à la recherche de cette longueur en étudiant les fonctions de corrélations mettant en jeu les fluctuations de densité. Cependant aucune longueur pertinente n'a pu être extraite [8]. À ce jour, trouver cette longueur de corrélation reste donc un défi ainsi qu'une quête de première importance pour clarifier la nature de la transition vitreuse. En partant du constat que les réarrangements structuraux jouent un rôle clé, il est intéressant d'étudier le voisinage des particules composant le liquide et de voir comment ce dernier change avec la température. Un outil intensivement utilisé en physique des liquides pour obtenir des informations à la fois sur le voisinage d'une particule et sur sa topologie sont les tessellations de Voronoï. Ces dernières correspondent à un découpage mathématique de l'espace en cellules qui sont construites à partir des points de l'espace les plus proches

d'une particule donnée que de n'importe quelle autre particule appartenant à ce même espace.

Nous avons récemment proposé, non pas de se servir des tessellations de Voronoï comme un simple outil, mais pour la première fois d'utiliser leurs propriétés géométriques afin de définir le champ de force d'un nouveau type de liquide dit *liquide de Voronoï* [26, 27]. Ce dernier se distingue de la majorité des liquides étudiés dans le cadre de la transition vitreuse car d'une part ses interactions ne sont pas de paires mais intrinsèquement à plusieurs corps. D'autre part, la nature des interactions impliquent que le liquide de Voronoï est constamment sous tension dans le sens où deux particules voisines s'attirent en permanence. Une première étude théorique et numérique menée sur la forme monodisperse du liquide de Voronoï a permis de constater que ce système présente des similitudes avec les fluides usuels tels que ceux de Lennard-Jones, mais a également sa propre phénoménologie : des propriétés de scaling anormales des fonctions thermodynamiques, un scaling particulier de l'atténuation des ondes sonores dans le régime mésocopique [27], ainsi qu'une importante mobilité dans la phase cristalline. Dans sa forme monodisperse, le système est néanmoins incapable d'éviter la cristallisation. L'objet de cette thèse est d'étudier une extension de ce modèle en introduisant de la polydispersité de façon à empêcher la cristallisation et de permettre ainsi de sonder le régime surfondu. La question fondamentale à laquelle nous cherchons à répondre est la suivante : de quelle façon les interactions à plusieurs corps modifient-elles le scénario habituel de la transition vitreuse ? Afin d'essayer d'apporter une réponse à cette question, nous avons étudié un mélange binaire du liquide de Voronoï par le biais de la théorie et des simulations numériques.

Considérations théoriques

L'introduction de la polydispersité a été possible grâce à l'utilisation des tessellations de Voronoï-Laguerre qui permettent d'associer à des particules ponctuelles j un rayon intrinsèque R_j. Dans le cas des tessellations de Voronoï classiques, la cellule d'une particule j est construite à partir de l'intersection des plans médiateurs entre la particule j et ses plus proches voisins i. Les tessellations de Voronoï-Laguerre, quant à elles, prennent en compte la présence des rayons intrinsèques R_j et R_i associés à chaque type de particules. De ce fait, les plans délimitants les bords de la cellule ne sont plus forcément médians.

L'énergie potentielle du liquide de Voronoï polydisperse est définie de la façon suivante :

$$E_P = \frac{\gamma}{2} \sum_j \int_{v_j} d^3r [r^2 - R_j^2 + R^2]$$

ou $\boldsymbol{r}$ est un vecteur partant de la particule et parcourant toute la cellule j. R correspond au rayon moyen des particules et γ est une constante arbitraire. Le champ de forces dérive de l'énergie potentielle de telle sorte que $\boldsymbol{f}_j = -\boldsymbol{\nabla}_j E_P$, avec

$$\boldsymbol{f}_j = \gamma \boldsymbol{\tau}_j = \gamma \boldsymbol{M}_j \boldsymbol{G}_j$$

La force s'exerçant sur la particule j est donc directement proportionnelle au vecteur allant de la position de la particule vers le barycentre de la cellule j comme illustré sur la Figure 1.

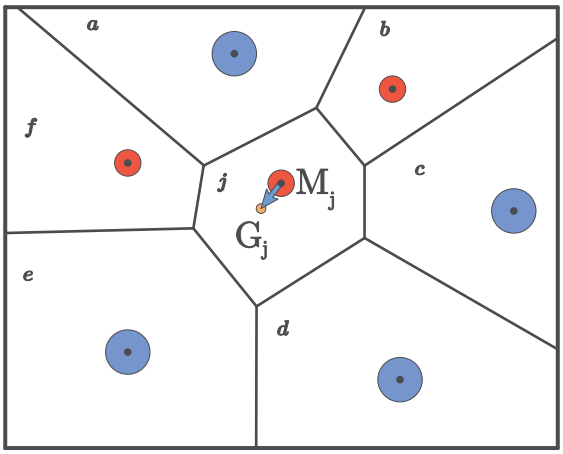

FIGURE 1: Représentation 2d d'une tessellation de Voronoï-Laguerre pour un mélange bidisperse.

Comme mentionné précédemment, notre étude s'est limité à la caractérisation d'un mélange binaire $(A : B)$ avec $R_A > R_B$. Le mélange de référence étudié est équimolaire, $N_A = N_B = 500$ particules. Nous avons travaillé à densité constante de telle sorte que $v = V/N = 1$. Les simulations ont été réalisée avec une version modifiée de LAMMPS [46] qui permet l'interfaçage avec la librairie Voro++ [35].

Au cours de ce travail, nous avons remarqué que la bidispersité est gouvernée par un seul paramètre $\eta = \sqrt{R_A^2 - R_B^2}/v^{1/3}$. En effet, lorsque $R_A = R_B$, $\eta = 0$ et on retrouve la limite monodisperse du liquide de Voronoï [26]. Nous avons montré que l'aptitude du liquide de Voronoï bidisperse à éviter la cristallisation est directement lié à la valeur de η. Ainsi des expériences de refroidissement ont montré que lorsque $\eta \geq 0.25$, la disparité de taille entre les deux types de rayons est suffisamment importante pour empêcher la cristallisation. Nous avons choisi de travailler avec $\eta = 0.375$ pour être certain, d'une part, d'être dans le régime où la cristallisation est évitée. D'autre part cette valeur de η est suffisamment faible pour considérer que le système se trouve dans une limite de

faible polydispersité. Pour $\eta = 0.375$, nous avons estimé que la température de transition vitreuse $T_G \approx 0.66$.

Thermodynamique

Nous avons débuté l'analyse du liquide de Voronoï bidisperse en s'intéressant aux propriétés thermodynamiques. Nous avons formulé analytiquement l'expression des potentiels d'excès tels que l'énergie libre ou l'entropie. Comme attendu, ces potentiels thermodynamiques se sont révélés être peu sensibles au voisinage de la transition vitreuse, nous nous sommes donc par la suite intéressés à leurs dérivés premières qui sont connues pour manifester des changements notables aux alentours de T_G. Nous avons eu un intérêt tout particulier pour la chaleur spécifique à volume constant C_v^e qui présente un accroissement relativement fort au voisinage de la transition vitreuse comparativement à d'autres systèmes vitreux. En effet, nous avons comparé l'évolution de la chaleur spécifique du liquide de Voronoï avec celles calculées pour 3 liquides de Lennard-Jones (LJ) :

1. Le mélange binaire de Kob-Andersen (KA) [28, 29].
2. Le modèle de Wahnström (WAHN) [30].
3. Un mélange binaire (AMLJ-0.80) pour lequel les interactions sont additives et le ratio $\sigma_{BB}/\sigma_{AA} = 0.80$ [21].

Sur la Figure 2, on remarque très clairement l'augmentation de C_v^e/N, lorsque T diminue est plus importante pour le liquide de Voronoï. Pour expliquer ce comportement, nous nous sommes intéressés aux paysages d'énergie potentielle (PEL) et nous avons calculé l'énergie moyenne $\langle e_{IS} \rangle$ des structures inhérentes IS (ou minima) pour le liquide de Voronoï et les 3 systèmes LJ (voir Figure 3). Nous avons ainsi pu montrer que la forte décroissance de $\langle e_{IS} \rangle$ pour le liquide de Voronoï est responsable de l'accroissement important de C_v^e/N au voisinage de la transition vitreuse.

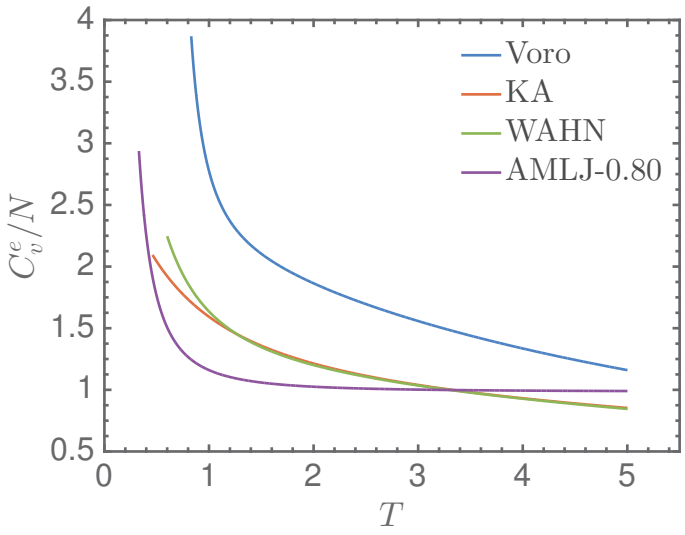

FIGURE 2: Evolution de la chaleur spécifique d'excès à volume constant par particule C_v^e/N en fonction de la température pour le liquide de Voronoï bidisperse ainsi que pour 3 liquides de Lennard-Jones.

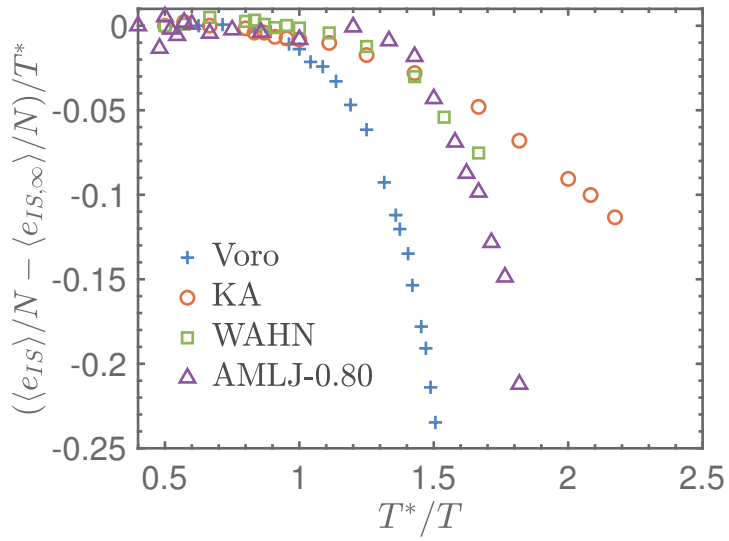

FIGURE 3: Comparaison de l'évolution, en fonction de la température adimensionnée T/T^*, de l'énergie moyenne des IS relativement à un état de référence pris à haute température pour le liquide de Voronoï et les 3 liquides LJ.

Observables microscopiques structurales

Nous avons ensuite étudié les observables microscopiques du liquide de Voronoï bidisperse et nous nous sommes dans un premier temps intéressé aux observables structurales. Nous

avons calculé les fonctions de paires partielles $g_{ab}(r)$ ainsi que les facteurs de structures statiques partiels $S_{ab}(k)$. Comme tous les systèmes vitreux, ces grandeurs structurales sont peu sensibles au refroidissement (voir Figure 4) [8, 29, 73].

Ensuite, pour le liquide de Voronoï bidipserse, dans la limite de faible bidispersité, la position des extrema des fonctions de paires partielles et des facteurs de structures partiels peuvent être exprimés de manière analytique, et ce quelque soit la nature de la composition. Ainsi, nous avons pu montrer que pour la fonction de paire, la position des extrema r^*_{AB}, associée à l'interaction entre grandes et petites particules, est donnée par :

$$r^*_{AB} = \frac{1}{2}(r^*_{AA} + r^*_{BB})$$

Cette dernière relation implique que les positions des extrema de $g_{AB}(r)$ sont toujours localisés au milieu de ceux de $g_{AA}(r)$ et $g_{BB}(r)$ comme montré sur la Figure 5.

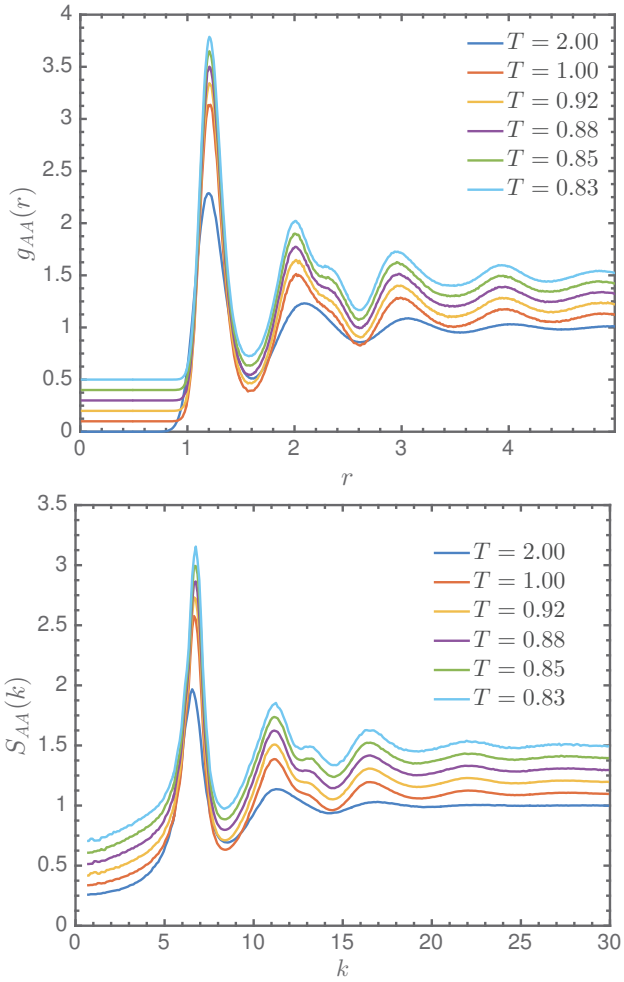

FIGURE 4: Haut : Evolution avec la température de la fonction de corrélation de paire partielle $g_{AA}(r)$. Bas : Evolution avec la température du facteur de structure statique partiel $S_{AA}(k)$.

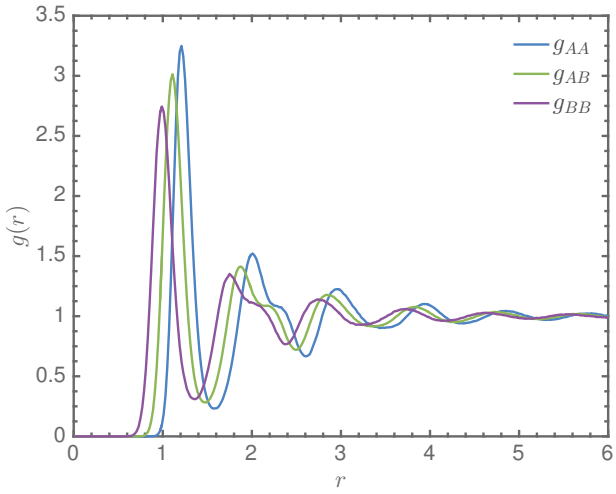

FIGURE 5: Positions relatives des différentes fonctions de corrélations de paires à $T = 0.85$.

Observables microscopiques dynamiques

Dans un second temps, nous nous sommes intéressés aux observables microscopiques dynamiques qui sont connues pour être très sensibles au voisinage de la transition vitreuse. Nous avons calculé le déplacement carré moyen (MSD) le facteur de structure dynamique cohérent $F(k,t)$, ainsi que sa partie incohérente $F_s(k,t)$. Nous avons pu observer le scenario typique de relaxation en deux étapes [8, 69]. La connaissance de $F_s(k,t)$ et du MSD nous a permis d'extraire respectivement le temps de relaxation structurale τ_α et le coefficient de diffusion D. La représentation de ces grandeurs à la Figure 6 montre qu'à haute température, le liquide de Voronoï bidisperse présente un caractère Arrhénien et que lorsque la température est abaissée, en deçà d'une température T^*, dite température de *crossover*, τ_α et D manifestent un comportement super-Arrhénien. Ces observations sont valables quelque soit la composition $(A:B)$.

Fragilité

Cette deviation du comportement Arrhénien est observée pour un grand nombre de matériaux surfondus et l'explication de son origine est toujours manquante. Pour tenter de comparer différents systèmes vitreux entre-eux, Angell a proposé de représenter graphiquement l'évolution des quantités de transport : viscosité, coefficient de diffusion, temps de relaxation en fonction de T_G/T [2]. Cette renormalisation de la température permet de comparer différents liquides surfondus en fonction d'un seul paramètre, la fragilité, qui quantifie le degré de déviation de la loi Arrhénienne. Afin de déterminer la fragilité

du liquide de Voronoï, et à l'instar de ce qui a été proposé par Coslovich et Pastore [21], nous avons utilisé un fit permettant de passer de façon continue du régime Arrhénien au régime super-Arrhénien. Nous avons pu montrer que des changements dans la composition du mélange influencent la fragilité. Ainsi, plus le nombre de grandes particules A est augmentée, moins la déviation du régime Arrhénien est marquée (voir Figure 6).

Nous avons ensuite comparé nos résultats avec ceux des 3 mélanges LJ. Cette comparaison est loin d'être triviale car les unités du liquide de Voronoï diffèrent des unités Lennard-Jones. Il a donc été essentiel de déterminer des échelles de longueur, de temps et d'énergie afin de pouvoir adimensionner nos observables. Une première possibilité consiste à representer un graphe d'Angell où la quantité de transport est, elle aussi, adimensionnée. Pour se faire nous avons adimensionné τ_α et D respectivement par le temps de relaxation τ_∞ et le coefficient de diffusion D_∞ que nous avons extrait à l'amorce du régime Arrhénien. Cette représentation permet de comparer l'évolution des grandeurs de transports entre deux points de référence, l'un pris à haute température et l'autre à basse température. En effet, comme mentionné précédemment, la température dans un graphe d'Angell est adimensionnée par T_G. Pour les systèmes étudiés, T_G est largement inférieure à la température la plus basse accessible numériquement. Nous avons donc utilisé une temperature de référence T_r jouant le rôle d'une T_G numérique, définie de telle sorte que $\tau_\alpha(T_r) = 4 \cdot 10^4$. De façon similaire, pour le coefficient de diffusion, nous avons défini T_r^D telle que$D(T_r^D) = 10^5$. Les résultas présentés sur la Figure 7 montrent que "l'ordre" dans le graphe d'Angell n'est pas respecté pour le liquide de Voronoï bidisperse. Ainsi lorsque $T \to T_r$ le liquide est relativement fragile lorsqu'on sonde l'environnement microscopique, c'est à dire τ_α. En revanche, lorsque la limite hydrodynamique est considérée, i.e lorsqu'on regarde D, cette fragilité est beaucoup moins prononcée.

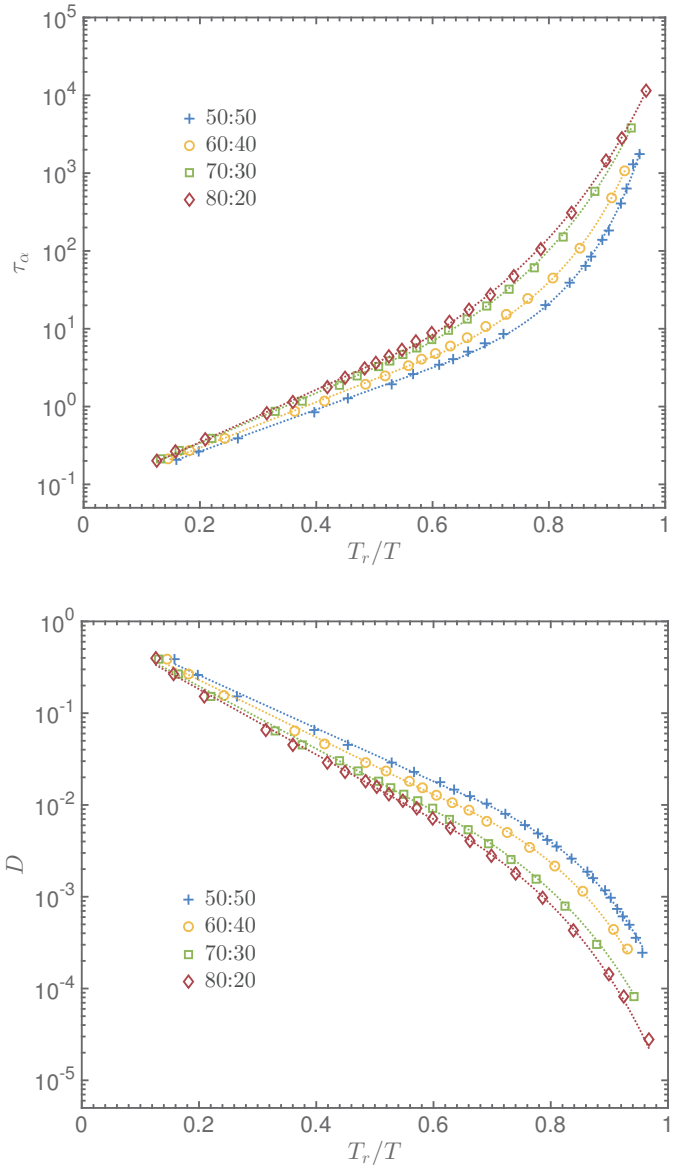

FIGURE 6: Evolution du temps de relaxation τ_α(haut) et du coefficient de diffusion D (bas) en fonction de la température et pour différentes compositions du mélange binaire. T_r est définie telle que $\tau_\alpha(T_r) = 4 \cdot 10^4$.

Adimensionnement et évolution du temps de relaxation en fonction de la température

Ce comportement particulier du liquide de Voronoï, nous a amené à nous questionner sur la pertinence des graphes d'Angell. Nous avons donc reconsidéré le problème dans son ensemble et cherché des échelles microscopiques de longueur, de temps et d'énergie afin de comparer de façon pertinente le liquide de Voronoï bidisperse avec les systèmes LJ. Comme échelle de longueur microscopique nous avons choisi la longueur associée au

volume par particule $v^{1/3}$. Comme échelle de temps microscopique nous avons choisi la fréquence d'Einstein Ω_0 qui est le temps physique accessible le plus court qui peut être calculé. Pour l'échelle d'énergie microscopique, le choix s'est avéré être plus complexe et nous avons proposé trois candidats possibles :

1. Le travail microscopique E_μ exercé sur une particule lors de son déplacement sur l'échelle de longueur caractéristique $v^{1/3}$: $E_\mu = \sqrt{\langle F^2(0)\rangle}$
2. Les fluctuations de l'énergie potentielle $\sqrt{\langle \delta E_P^2 \rangle}$. Dans l'ensemble canonique, ces dernières sont directement reliées à la chaleur spécifique à volume constant C_v^e par la relation $\sqrt{\langle \delta E_P^2 \rangle} = T\sqrt{k_B C_v^e}$.
3. Le module de cisaillement G_∞ calculé au temps $t = 0$. Son utilisation a déjà était proposée dans le cadre du *Shoving Model* développé par Dyre [84, 86, 88]. Dans ce cas, l'énergie caractéristique est donnée par $E(T) = vG_\infty(T)$.

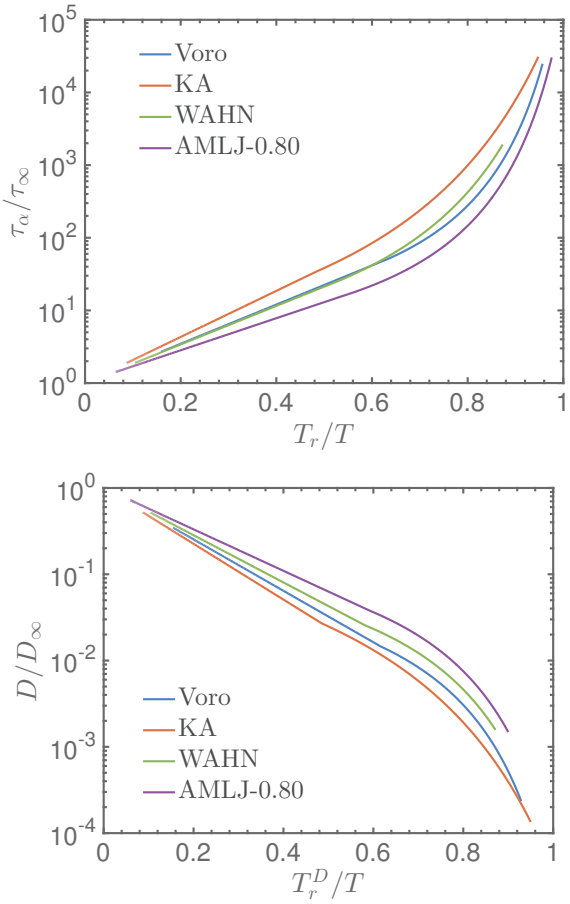

FIGURE 7: Comparaison de l'évolution de τ_α/τ_∞ (haut) et de D/D_∞ (bas) en fonction de la température adimensionée T_r/T. τ_∞ et D_∞ sont des constantes extraites du fit Arrhénien à haute température. T_r et T_r^D sont des températures de référence arbitrairement choisies comme les températures pour lesquelles $\tau_\alpha = 4 \cdot 10^4$ et $D(T_r^D) = 10^5$.

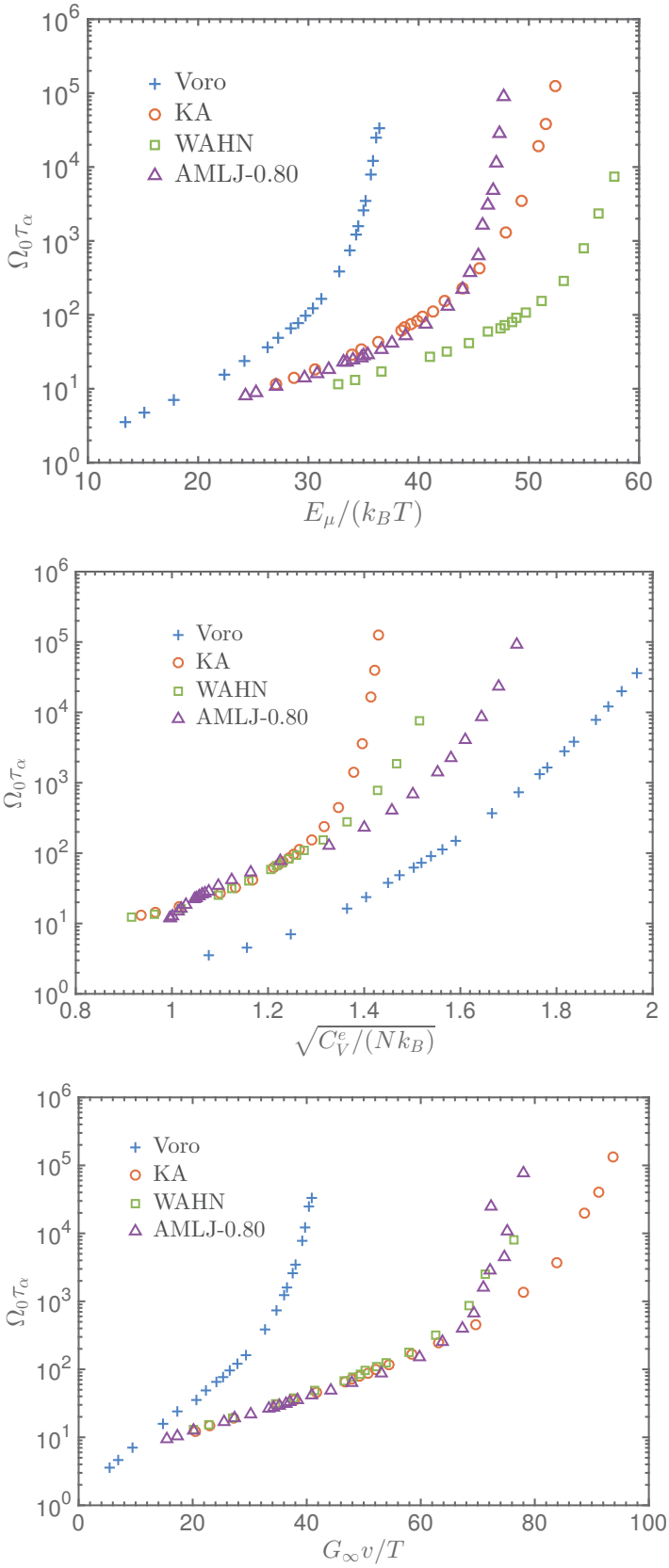

FIGURE 8: Evolution du temps de relaxation τ_α adimensionné par la fréquence d'Einstein Ω_0 en fonction de l'inverse de la température adimensionnée par le travail microscopique E_μ (haut), les fluctuations de l'énergie potentielle (milieu) et le module de cisaillement G_∞ calculé à $t = 0$ (bas).

Sur la Figure 8 est représentée l'évolution de $\Omega_0\tau_\alpha$ en fonction de l'inverse de la température adimensionnée par chacune des trois propositions précédentes pour l'échelle d'énergie microscopique. De façon très générale, on remarque que quelque soit la représentation choisie, le liquide de Voronoï se distingue des liquides de Lennard-Jones. Cette distinction est directement liée aux différences qui existent entre le potentiel de LJ qui est de coeur dur et le potentiel du liquide de Voronoï qui est lui de coeur mou. À l'exception de l'adimensionnement par E_μ, ces représentations mettent en avant les similitudes entre les différents modèles appartenant à la famille des potentiels LJ.

Relaxations collectives et individuelles du temps de relaxation

Nous nous sommes également intéressés à l'évolution des relaxations individuelles et collectives à différentes échelles (voir Figure 9).

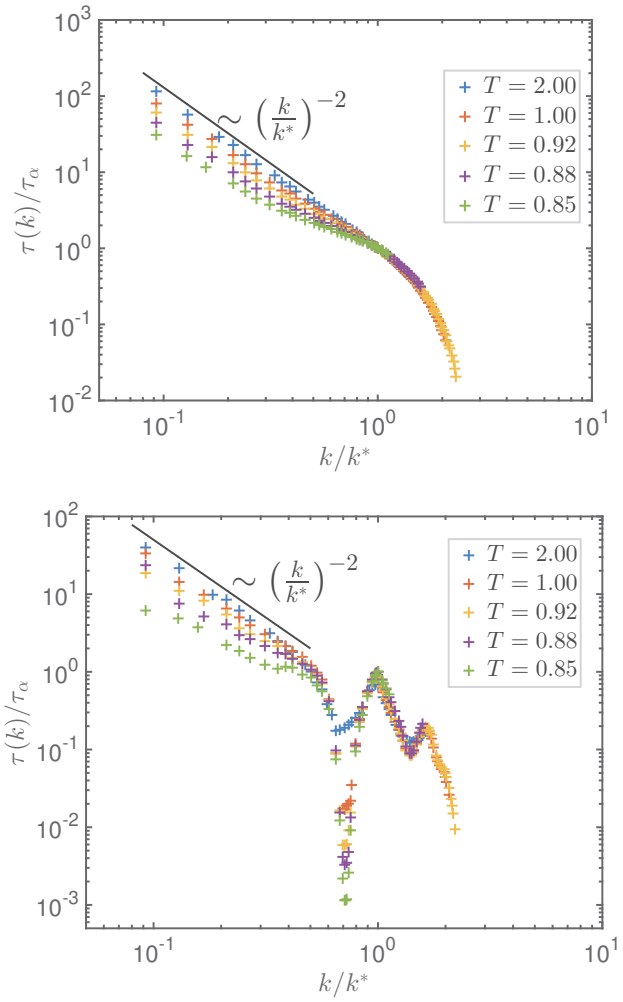

FIGURE 9: Evolution pour différentes températures de la relaxation individuelle (haut) et de la relaxation collective (bas) pour différentes valeurs du vecteur d'onde k adimensionné par sa valeur k^* prise au premier pic de $S(k)$.

La présence d'une courbe maitresse pour $k > k^*$ suggère que, à grands vecteurs d'ondes, relaxations individuelles et collectives sont pilotées par τ_α et k^*. Pour $k < k^*$, dans chacun des deux cas, un départ de la courbe maitresse ainsi qu'une transition vers un régime en loi de puissance sont observés. On note également une décroissance importante du temps de relaxation collectif dans le régime mésoscopique pour $k \sim 4.90$. Ceci signifie qu'à l'échelle de longueur $\sim 2\pi/4.90$, le temps de relaxation collectif est découplé du temps de relaxation structural, suggérant très certainement la présence d'un état de transition qui n'a pas été identifié pour le moment.

Analyse avec la théorie du couplage de mode (MCT)

Nous avons également testé les prédictions de la théorie de couplage de mode (MCT) dans sa version idéale [97, 98]. Nous avons ainsi vérifié que le principe de superposition temps-température (TTSP) était valide pour les températures les plus basses accessibles dans notre système. De la même façon nous avons testé le principe de factorisation qui s'est avéré valide pour tous vecteurs d'onde $q \gtrsim 6.00$. En effet, la violation du principe de factorisation est liée à la présence, dans le régime mésoscopique et pour le facteur de structure cohérent, d'oscillations amorties très importantes dans le régime β. Ceci est visible dans la Figure 10 (haut) où on observe très clairement les oscillations pour le plus petit q. Cette phénoménologie n'étant pas prise en compte dans une description MCT idéale, il n'est donc pas surprenant d'observer une violation des prédictions de la MCT dans ce régime de vecteurs d'ondes.

Nous avons ensuite poursuivi l'analyse MCT en déterminant l'exposant b à partir d'un fit de von Schweidler :

$$\phi_q(t) = f_q^c - \tilde{h}_q(t/t'_\sigma)^b + \tilde{h}_q\tilde{B}_q(t/t'_\sigma)^{2b}$$

Afin de vérifier la valeur obtenue pour b ainsi que la qualité du fit à q^*, nous avons fixé les paramètres t'_σ, f_q^c et b puis nous avons essayé le fit de von Schweidler pour le facteur de structure cohérent calculé pour différents vecteurs d'ondes (voir Figure 10). Pour $q \gtrsim 6.00$, nous avons remarqué, d'une part, que le fit de von Schzeilder contraint ne permet pas de décrire correctement le régime mésoscopique que ce soit pour le facteur de structure cohérent ou pour l'incohérent. D'autre part, en ne contraignant pas le fit de von Schweidler, nous avons remarqué que l'exposant b augmente lorsque q diminue. Cette apparente violation des prédictions de la MCT dans le régime mésoscopique tend à suggérer la présence de phénomènes physiques sous-jacents non pris en compte par la MCT.

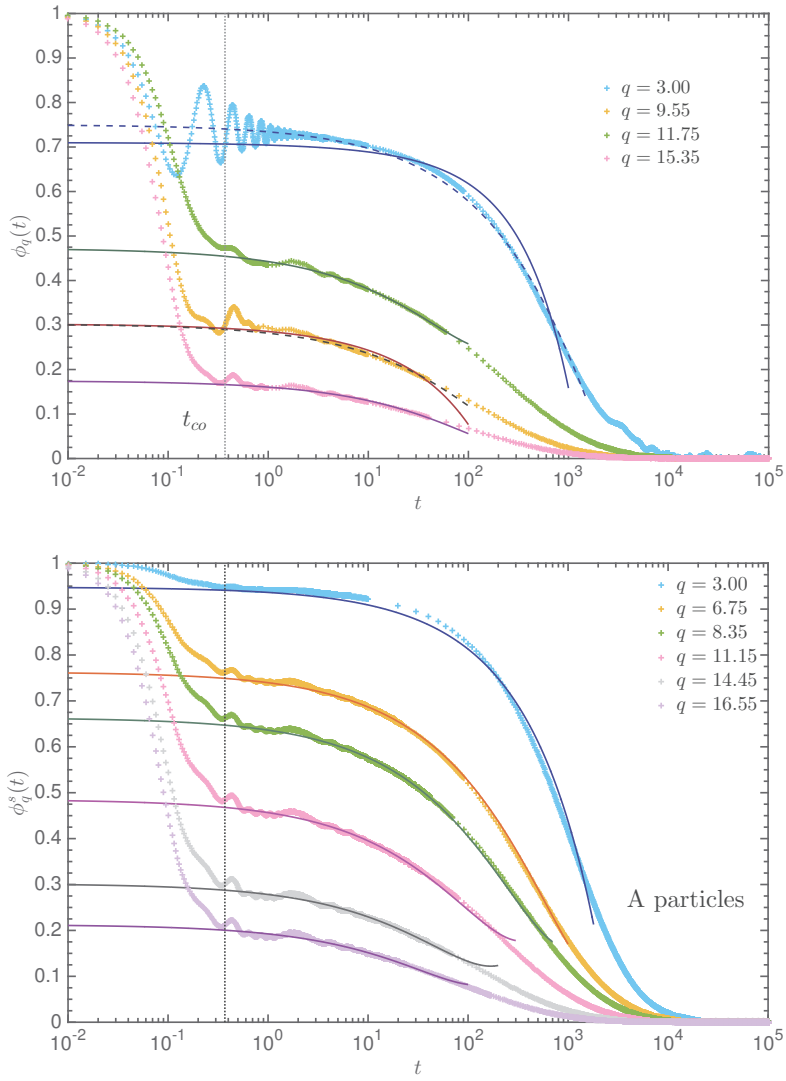

FIGURE 10: Test pour le facteur de structure cohérent (haut) et pour le facteur de structure intermédiaire (bas) du fit de von Schweidler avec contraintes pour différents vecteurs d'onde q.

Toutefois, afin de déterminer la température de couplage de mode T_c, nous avons fait l'hypothèse que la MCT pouvait s'appliquer à notre système et nous avons ainsi pu trouver que $T_c = 0.7989$.

Etude du paysage d'énergie potentielle

Afin de comprendre plus en profondeur la phénoménologie de la transition vitreuse, nous avons étudié le paysage d'énergie potentielle (PEL) dans lequel coexistent deux types de

points stationnaires : les minima appelés également structures inhérentes et les points selles.

Analyse des structures inhérentes

Dans un premier temps, nous avons analysé les structures inhérentes (IS). Pour se faire, à l'instar de Stillinger et Weber [105], nous avons minimisé l'énergie potentielle E_P de configurations thermalisées en utilisant l'algorithme FIRE [107]. La minimisation de E_P permet un découpage clair du PEL sous forme de bassins contenant chacun une IS.

En représentant l'énergie moyenne des IS, $\langle e_{IS} \rangle$, en fonction de l'inverse de la température $1/T$, on a remarqué (voir Figure 11) qu'il existait une relation linéaire entre ces deux grandeurs à basse température :

$$\langle e_{IS} \rangle = E_{max} - \frac{\sigma^2}{k_B T}$$

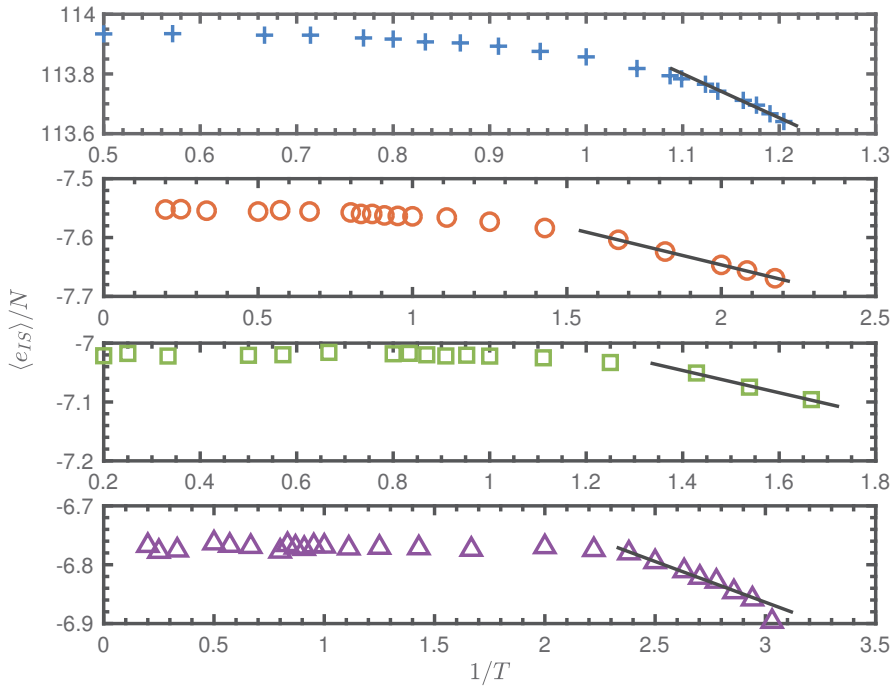

FIGURE 11: Evolution de l'énergie moyenne des IS $\langle e_{IS} \rangle / N$ en fonction de l'inverse de la température $1/T$ pour le liquide de Voronoï (+), le mélange KA (○) , le modèle de Wahnström (□) et AMLJ-0.80 (△).

Cette relation linéaire provient du fait que la distribution des IS, $\Omega(e_{IS})$, dans notre système a été identifiée comme étant Gaussienne. On s'est intéressé ensuite à la valeur

prise par σ^2 dans l'équation précédente. De manière intéressante, on a remarqué que cette valeur est dix fois plus grande pour le liquide de Voronoï bidisperse que pour les liquides LJ.

Nous avons également voulu tester la validité de l'approximation harmonique. Nous avons remarqué que cette dernière semble valide à très basses températures. A plus haute température, mais toujours en dessous de la température de crossover T^*, nous avons noté la présence d'anharmonicité relativement importantes qui ne peuvent pas être envisagées simplement comme une faible perturbation du régime harmonique.

Test de la théorie de Adam-Gibbs

En faisant l'hypothèse que l'approximation harmonique est valide, nous avons calculé l'entropie configurationnelle comme étant la différence entre l'entropie du liquide et l'entropie du solide désordonné, $S_c = S_{liq} - S_{sol}$.

Nous avons ensuite montré qu'à basse température, $\tau_\alpha \approx \exp(B/(TS_c))$ (voir Figure 12). La théorie de Adam-Gibbs semble ainsi être vérifiée pour le liquide de Voronoï bidisperse.

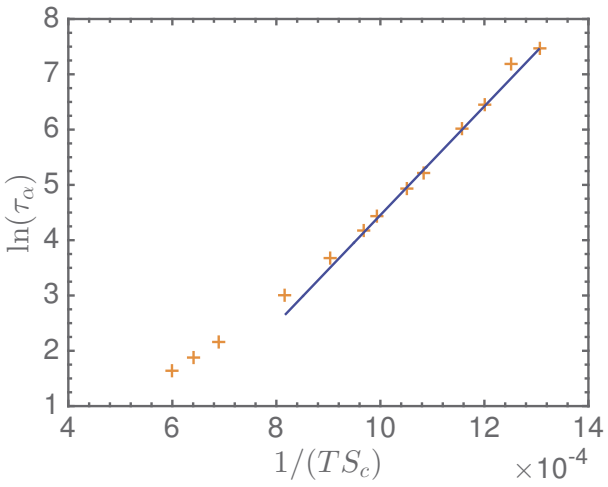

FIGURE 12: Evolution du temps de relaxation en fonction de $1/(TS_c)$.

Analyse des points selles

Nous avons eu un intérêt tout particulier pour l'analyse des points-selles qui sont des points stationnaires caractérisés par un nombre K de directions négatives. Nous avons calculé les points selles de deux façons différentes à partir d'une configuration thermalisée. La première façon consiste à minimiser la fonction $W = \boldsymbol{\nabla} E_P^2$ tandis que la seconde méthode, nommée *Eigenvector Following* (EV), consiste en une maximisation de E_P le

long des K directions montantes et une minimisation le long des $3N - K$ directions descendantes. Alors que la première méthode converge vers des quasi-point-selles (QS), pour lesquelles $W \approx 10^{-2}$, la seconde méthode permet de trouver de vrais points-selles $W \approx 0$.

Dans un premier temps, nous nous sommes intéressés à l'évolution de la densité de direction négative $k = K/(3N)$ en fonction de la densité énergétique des points-selles $u = U/N$. Nous avons ainsi observé que $k(u)$ est une fonction croissante monotone. Au cours de cette analyse nous avons observé que la méthode EV ne nous permettait pas d'avoir accès aux faibles densités de k.

Nous avons aussi évalué les barrières entre points-selles de deux façons différentes en considérant des analyses uniquement sur les QS.
La première consiste à évaluer $\Delta U_b \approx du/dk$ qui correspond à la barrière énergétique entre un point-selle ayant K directions négatives et un autre point-selle ayant $K + 1$ directions négatives. Nous avons remarqué que la barrière énergétique entre deux points selles adjacents augmente de façon significative lorsque la température diminue (voir Figure 13 haut).
La seconde méthode permet d'évaluer l'écart énergétique $u - e_{IS}$ entre un point-selle ayant K directions négatives et la structure inhérente la plus proche. Nous avons comparé nos résultats avec ceux de différents systèmes LJ et nous avons ainsi pu remarquer que tous les résultats se trouvaient sur une courbe maitresse (voir Figure 13 bas). Ceci suggère qu'il existe une phénoménologie commune entre tous ces systèmes.

Nous avons ensuite utilisé l'analyse des QS pour déterminer la température de couplage de mode T_c. Nous avons trouvé que $T_c \approx 0.804$, ce qui est très proche de la valeur déterminée par la vraie analyse de couplage de mode. Nous avons noté que contrairement aux systèmes LJ, l'estimation de T_c faite sur des petits systèmes de $N = 125$ particules, donnait de moins bons résultats en surestimant la valeur de T_c.

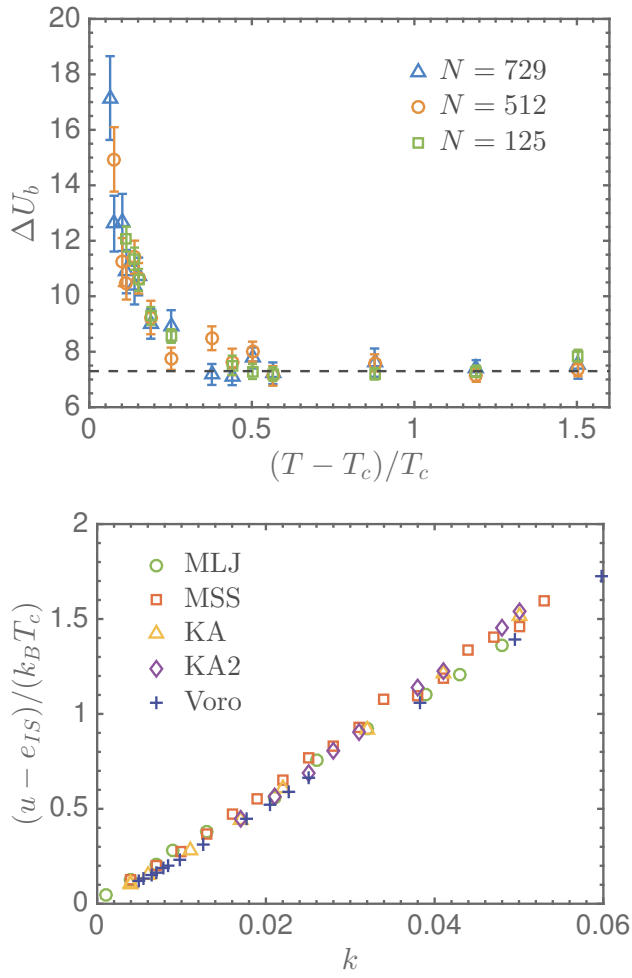

FIGURE 13: Haut : évolution de la hauteur de barrière énergétique entre deux points-selles adjacents en fonction de la température. Bas : évolution de l'écart énergétique entre un point-selle ayant K directions négatives et l'IS sous-jacent en fonction de la densité de directions négatives $k = K/(3N)$.

Analyse des structures localement favorables (LFS)

Identification des LFS

Dans une dernière partie, nous nous sommes intéressés aux structures localement favorables (LFS) qui minimisent localement l'énergie potentielle. Différentes techniques permettent de déterminer ces structures [21, 22, 143], nous avons retenu la méthode proposée par Coslovich et Pastore [21]. Cette dernière se base sur une analyse des cellules (polyèdres) de Voronoï, les polyèdres qui apparaissent le plus souvent sont ceux permettant de remonter à la structure la plus favorable. Ainsi nous avons montré que le liquide de Voronoï bidisperse a tendance à favoriser des arrangements d'icosaèdres.

Cette tendance est d'autant plus prononcée que la température est basse (voir Figure 14).

Cette tendance à former des icosaèdres n'est pas spécifique au liquide de Voronoï. Elle est par exemple partagée avec le modèle de Wahnström ou AMLJ-0.80, comme on peut le voir sur la figure 15. Il semble donc que le liquide de Voronoï partage des spécificités avec WAHN ou AMLJ-0.80, ce qui permet d'observer ces similitudes structurales.

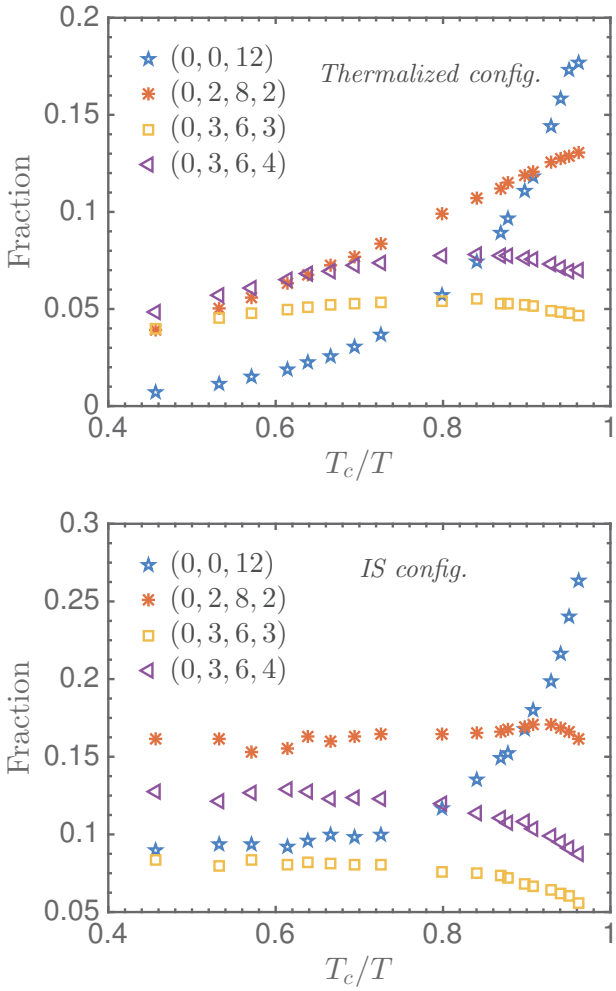

FIGURE 14: Représentation de la fraction des principales LFS en fonction de T_c/T où $T_c = 0.7989$ est la température de couplage de modes. Les fractions ont été calculées pour des configurations thermalisées (haut) et également pour des configurations correspondant à des IS (bas).

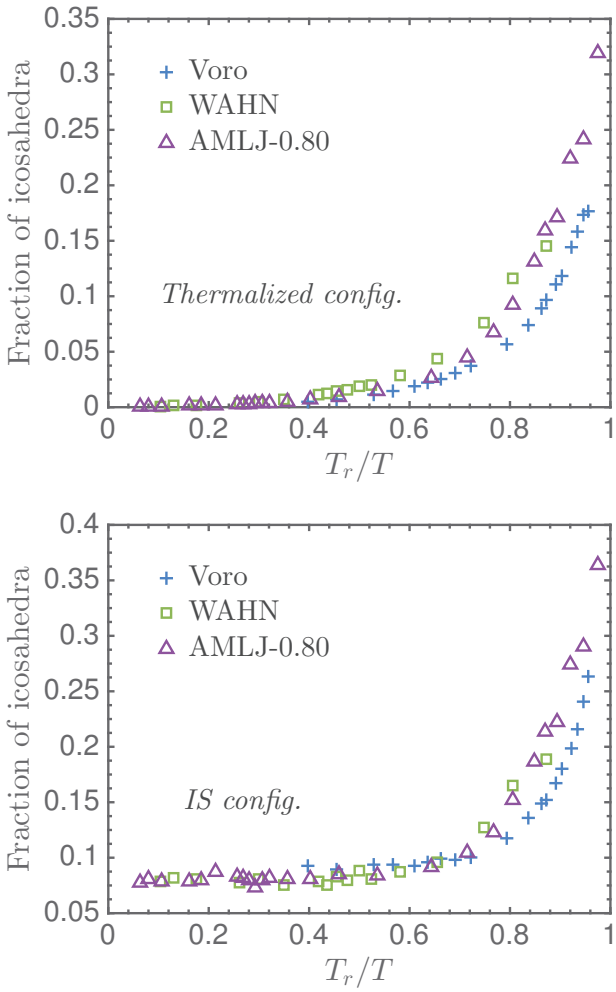

FIGURE 15: Evolution de la fraction d'icosaèdres en fonction de T_r/T pour le liquide de Voronoï bidisperse et deux liquides LJ. Les fractions ont été calculées pour des configurations thermalisées (haut) et également pour des configurations correspondant à des IS (bas).

Présence de domaines

Nous nous sommes ensuite intéressés à l'extension spatial de ces icosaèdres, et pour cela nous avons cherché si ces derniers formaient des clusters. Nous avons noté que lorsque la température était abaissée, le système avait tendance à former de grand clusters pouvant contenir plus de 100 icosaèdres (voir Figure 16).

Ces clusters ont un impact direct sur la dynamique. En effet, nous avons calculé les temps de relaxation des particules au centre des icosaèdres et nous avons remarqué que ces temps de relaxation sont bien plus importants que ceux des particules n'appartenant pas du tout à des icosaèdres.

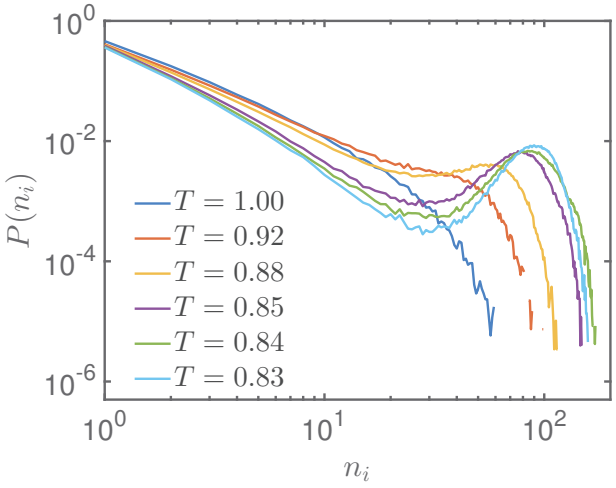

FIGURE 16: Evolution de la probabilité $P(n_i)$ de trouver un cluster composé de n_i icosaèdres.

Cristallisation

A très basse température, nous avons observé que le système formait un pseudo-cristal. L'énergie potentielle transite vers une valeur de plus basse énergie, comme montrée sur la Figure 17 et cette transition s'accompagne par un accroissement très brutal du nombre d'icosaèdres. De plus, nous avons noté que les LFS associés aux grandes particules A changeaient radicalement par rapport à la phase liquide. Ces nouveaux LFS suggèrent la présence d'une phase de Frank-Kasper que nous n'avons pas encore identifiée pour le moment.

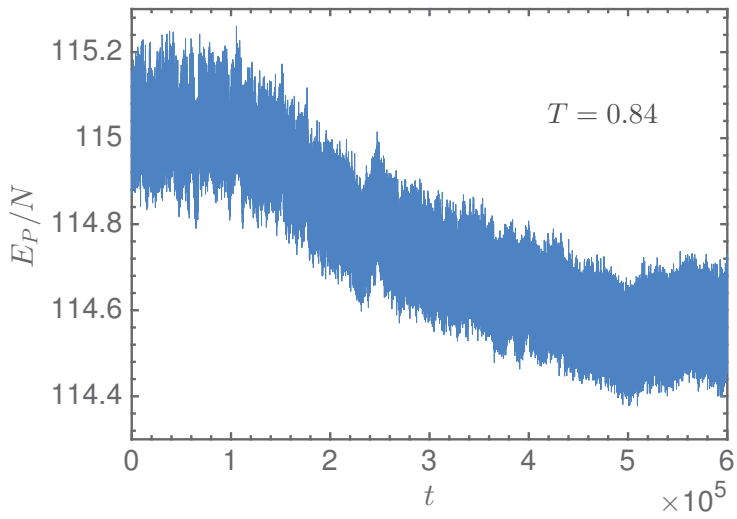

FIGURE 17: Evolution de l'énergie potentielle au cours du temps à $T = 0.84$.

Introduction

When a liquid is cooled down, crystallization can be avoided and the liquid enters into the metastable supercooled regime. This regime is characterized by an important slowing down of the dynamics. Upon cooling, a temperature is reached below which, on experimental time-scales, the system falls out of equilibrium and forms a glass. This temperature, named glass transition temperature, is defined arbitrarily as the temperature for which the viscosity reaches 10^{13}Poise or for which the relaxation time is of the order of 10-1000s [8–10]. Although the slowing down of the dynamics points toward the existence of a transition, the thermodynamic nature of this latter has never been clearly identified and is still today subjected to debates [11].

Understanding the microscopic origin of dynamical arrest is still one of the fundamental problems of condensed matter physics. The increase of the relaxation is a common trend to all glass formers, however it changes from a material to another one. For some materials, such as SiO_2, the relaxation time can be described by an Arrhenian law, whereas some other species like organic glasses, exhibits a super-Arrhenius relaxation [2, 9, 12]. These observations lead to the famous Angell's classification of strong/fragile glass formers [2, 13]. The deviation from the Arrhenian behavior is associated with the presence of free energy barriers which increase with temperature. But nowadays, the origin of these free energy barrier is still not well understood.

It is well-accepted that the relaxation time in supercooled liquids is related to structural rearrangements implying only a finite number of particles and that the increase of the relaxation time results from an increasing number of particles that move in a cooperative way to reorganize. In the 60's, Adam and Gibbs defined the concept of cooperative rearranging region (CRR), and proposed a theory where the free energy barrier is considered to be directly proportional to the number of particles involved in these regions [14]. Moreover, upon cooling, the size of the CRR are assumed to grow. All these observations point toward the existence of an increasing correlation length which would be reminiscent of classical critical phenomena. Nevertheless, the main issue comes from difficulties to apply that classical methodology of critical phenomena. What is a reliable

order parameter ? Which correlation function have to be used ? Numerous work have tried to identify this growing correlation length [15–17] but no proper definition of this correlation length have been proposed. Moreover other studies point toward a dynamical correlation length instead of a structural one [15, 18–20].

Considering that structural rearrangements play a key role in the phenomenology of glass transition, numerous studies have focused on characterizing the local neighborhood of particles [21, 22] and investigated how this environment evolves upon cooling. The existence of local preferred structures minimizing the local energy has been found [21, 23–25]. It was also shown that upon cooling, this local favored structures form domains where the dynamics is significantly slower than in the surrounding liquid [21, 22, 25]. When looking for such structures, a tool intensively used in physics to obtain information on the neighborhood of particles, are Voronoi tessellations that tile space into cells where one cell is built from point of space closer from a given particle than from the other ones.

We recently proposed to consider Voronoi tessellations, not only as a tool, but for the first time, we use their intrinsic geometrical properties to define the force field of a new liquid called *The Voronoi Liquid* [26]. As the interactions in this liquid are not pairwise but intrinsically manybody and put the system always under tension (in a way neighboring particles are constantly attracting each other) the Voronoi liquid is different from most of the liquids used nowadays to investigate glass transition. A first theoretical and numerical study of the monodisperse form of the Voronoi liquid revealed that this system shares similarities with usual liquids, as for instance Lennard-Jones liquids. However the Voronoi liquid has also its own phenomenology as for instance: a characteristic scaling of thermodynamical functions, a specific scaling of the sound attenuation in the mesoscopic regime and an relative mobility within the crystalline phase [26, 27]. In its monodisperse form, the Voronoi liquid crystallizes.

The aim of this thesis is to study an extension of the monodisperse Voronoi liquid, where polydispersity has been introduced to prevent crystallization. Therefore with the *polydisperse Voronoi liquid*, we want to probe the neighborhood of glass transition by trying to answer the following question: *How do these exotic interactions disrupt the classical scenario of the glass transition ?* The idea is that this strongly uncommon interactions, which preserve the thermodynamic stability of the liquid, would modify the classical scenario of glass transition in a significative way. In this way this new model would act as a probe of glass transition.

In order to answer this question, throughout this work, we will investigate theoretically and numerically (with molecular dynamic simulations) the properties of a binary mixture of the Voronoi liquid. To quantify the differences between the bidisperse Voronoi liquid

and the usual glass formers, we compare our model with Lennard-Jones binary mixtures which have been intensively studied last decades [28–30].

This work is organized as follow: in Chapter 1 we define the bidisperse Voronoi liquid and we recall some results obtained for the monodisperse system. Then in Chapter 2 we investigate the thermodynamics properties of the bidisperse Voronoi liquids. In Chapter 3 and Chapter 4 we focus on microscopic observables and we describe first the structural properties of the liquid and then we investigate its dynamical behavior. Chapter 5 is devoted to the study of the potential energy landscape. Finally in Chapter 6 we present preliminaries investigations on the locally favored structures.

Chapter 1

A brand new class of liquids

Contents

1.1 Geometrical properties of Voronoi tessellations

1.1.1 Classical Voronoi tessellations

We consider N point particles contained into a cubic box of volume $V = L^d$ where L is the length of the box and d is the dimension of the space. In this work we will focus on dimension $d = 2$ and $d = 3$. Voronoi tessellations are a mathematical way of partitioning the space into Voronoi cells. Given the set of points $\varphi = \{x_1, \cdots, x_j, \cdots, x_N\}$ where $x_j \in \mathbb{R}^d$, to each $x_j \in \varphi$ there is an associated Voronoi cell $C(x_j, \varphi)$ defined by

$$C(x_j, \varphi) = \{y \in \mathbb{R}^d \ : \ ||y - x_j|| \leq ||y - x_i|| \ \ \forall x_i \in \varphi\} \tag{1.1}$$

Each cell is obtained from the intersection of half-spaces and it results that Voronoi cells are convex d-polytopes (polygons in 2d and polyhedra in 3d). Note that the strict equality in equation 1.1 defines the equation of the limiting hyperplane between two cells.

In other words equation 1.1 means that the d-polytope associated to the j^{th} particle is defined from the point of space which are closer from the particle j than from any other particles. In figure 1.1 is represented an example of 2-d Voronoi tessellation.

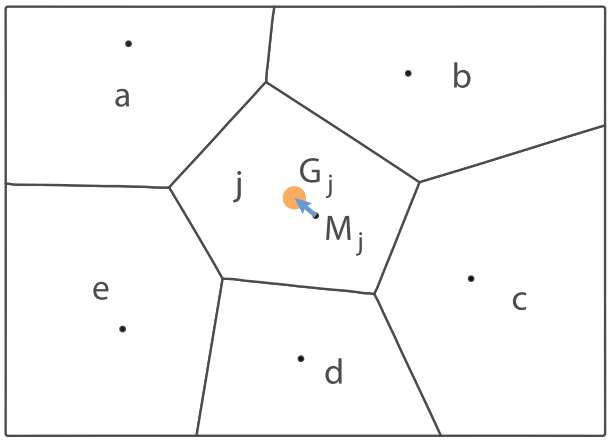

FIGURE 1.1: Representation of 2-dimensional Voronoi tessellation. The polygon associated to the particle j is built from the nearest neighbors of j. Each segment composing the polygon corresponds to the median plane between j and one of its nearest neighbors. The intersection of these median planes defines the polygon.

We can define scalar and vectorial observables related to the tessellations. We consider the j^{th} polytope and we denote its volume v_j. As the total volume is conserved we can write $V = \sum_j v_j$. Then the particle j is located at M_j and we denote G_j the centroid of the j^{th} polytope. The origin O of the coordinate system is arbitrarily defined, therefore the position of particle j is given by $\boldsymbol{r}_j = \boldsymbol{OM}_j$.

We define now a vectorial observable named the geometrical polarization, denoted $\boldsymbol{\tau}_j$, and given by :

$$\boldsymbol{\tau}_j = v_j \boldsymbol{M_j G_j} \tag{1.2}$$

This quantity is similar to the electric dipole moment where charge q is multiplied by the vector starting from the barycenter of negative charges and going to the barycenter of positive charges. In our case, v_j would play the role of the charge, the centroid G_j would correspond to the barycenter of the positive charge uniformly distributed in the polygon and M_j would be the local negative point charge.

An important property related to the geometrical polarization is that the total polarization is conserved for any given configuration of particles :

$$\sum_j \boldsymbol{\tau}_j = \mathbf{0} \tag{1.3}$$

Later, the conservation of the total geometrical polarization will be of huge interest when we will define the interaction among particles. Especially we will see that the force exerts on particle j is directly proportional to $\boldsymbol{\tau}_j$. This force field derives from a potential energy. A demonstration of equation 1.3 based only on geometrical argument is not obvious and more details can be found in [31].

With classical Voronoi tessellations all the particles are identical regarding the partitioning of the space [32]. However when disparities are introduced between particles we could be interested to find them back in the tessellation. A way to process is to deal with weighted Voronoi diagrams which enable to take into account disparities in the strength of influence among particles. In these tessellations cells are defined in term of a distance function which are different from the usual Euclidian distance. For most of weighted Voronoi diagrams resulting cells have curved edges but it exists one particular tessellation which captures the idea of influence without dealing with nonlinear edges: the Voronoi-Laguerre tessellations. Additionally we will see that this extension of the classical Voronoi tessellation enables also the conservation of the geometrical polarization as seen in equation 1.3.

1.1.2 Voronoi-Laguerre tessellations

As for the classical Voronoi tessellations, N point particles ($1 \leq j \leq N$) are contained into a cubic box of volume $V = L^d$ with L the length of the box and d the dimension of the space. For weighted point particles we associated to each of them an intrinsic length that we call radius for convenience and denote R_j. This intrinsic length plays a role in the construction of the polytopes as in this case the plane between two nearest neighbors is not necessarily median. For building the Laguerre tessellations we define first the distance between particle j located at M_J and a point M by the power of M with respect to the hypersphere of center M_J and radius R_j as

$$\mathrm{pow}(M, (M_j, R_j)) = M_j M^2 - R_j^2 \tag{1.4}$$

This relation is illustrated in figure 1.2. We immediately see that depending on the position of M the power could be :

- $\mathrm{pow}(M, (M_j, R_j)) < 0$, M is inside the hypersphere

- $\text{pow}(M,(M_j,R_j))=0$, M is on the hypersphere
- $\text{pow}(M,(M_j,R_j))>0$, M is outside the hypersphere and in this case, if H is the intersection between the hypersphere and its tangent hyperplane we have $\text{pow}(M,(M_j,R_j))=HM_j{}^2$

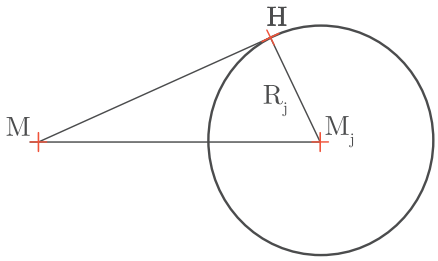

FIGURE 1.2: Geometric representation of the power of M with respect to the circle of center M_J and radius R_j.

Given the set $\varphi=\{(r_j,R_j)\}$, where r_j is the location of the point particle and R_j its intrinsic length. To each couple (r_j,R_j) there is an associated Voronoi-Laguerre cell $C((r_j,R)j),\varphi)$ defined by :

$$C((x_j,R_j),\varphi)=\{y\in\mathbb{R}^d \quad : \quad ||y-r_j||^2-R_j^2\leq||y-r_i||^2-R_i^2 \quad \forall(r_i,R_i)\in\varphi\} \tag{1.5}$$

One can show that Voronoi-Laguerre tessellations is a mathematical partitioning of the space into convex polytopes where the polytope associated to particle j is built from the point of space which are closer to the particle j (in term of power distance) than to any other particles.

Points $y\in\mathbb{R}^d$ satisfying the strict equality in equation 1.5 form the plane $P(\boldsymbol{r}_i,\boldsymbol{r}_j)$ between two point-particles i and j. Therefore the plane is given by the following equation :

$$P(\boldsymbol{r}_i,\boldsymbol{r}_j)=\{y\in\mathbb{R}^d:\langle\boldsymbol{y},2(\boldsymbol{r}_i-\boldsymbol{r}_j)\rangle=||\boldsymbol{r}_i||^2-||\boldsymbol{r}_j||^2-R_i^2+R_j^2\} \tag{1.6}$$

The distance from the plane $P(\boldsymbol{r}_i,\boldsymbol{r}_j)$ to the particle located in $\boldsymbol{r}_i$ is

$$\begin{aligned} d_{r_i,P} &= \frac{\langle\boldsymbol{r}_i,2(\boldsymbol{r}_i-\boldsymbol{r}_j)\rangle-(||\boldsymbol{r}_i||^2-||\boldsymbol{r}_j||^2-R_i^2+R_j^2)}{2||\boldsymbol{r}_i-\boldsymbol{r}_j||} \\ &= \frac{r_{ji}^2+R_i^2-R_j^2}{2r_{ji}} \\ &= \frac{r_{ji}}{2}+\frac{R_i^2-R_j^2}{2r_{ji}} \end{aligned} \tag{1.7}$$

where $\boldsymbol{r}_{ji} = \boldsymbol{r}_i - \boldsymbol{r}_j$ and $r_{ji} = ||\boldsymbol{r}_{ji}||$. From equation 1.7 we observe that for Voronoi-Laguerre tessellation the plane is no more located at $r_{ji}/2$ but its position depends on the intrinsic length associated to each point particle. In the case where all these intrinsic lengths are equal we find back the result expected for classical Voronoi tessellation that is $d_{r_i,P} = r_{ji}/2$. In Figure 1.3 is represented different possibilities for the plane position regarding the placement of two particles with different intrinsic lengths. The distance is kept fixed between the two particles and the size of the large particle is increased.

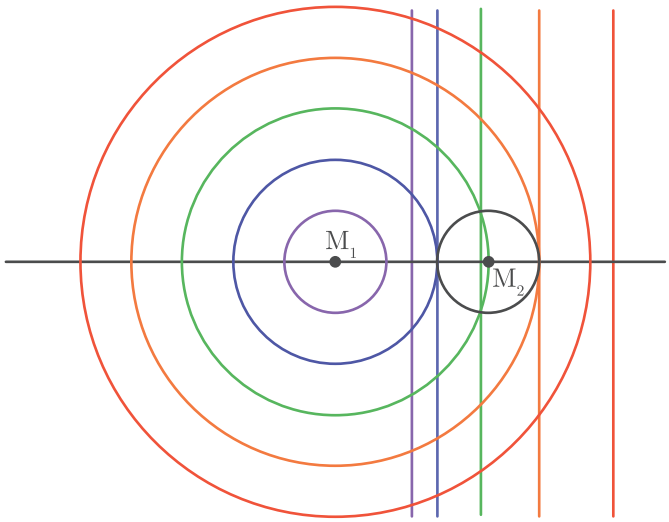

FIGURE 1.3: Localization of the hyperplane between a small particle (black circle) and a large particle whose size is increased (coloured).

We notice that as the biggest particle grows, the position of the plane is more and more shifted to the right. At a certain size of the big particle, the plane is not located between the two particles. It happens when the small particle is included in the largest one. It immediately raises the question of the possibility that a particle is not contained into its Voronoi cell. In Figure 1.4 is represented an example of Voronoi-Laguerre tessellation for particles with various intrinsic length. It is important to mention that :

- A Laguerre cell can be empty. In Figure 1.4 the particle C_3 has no cell at all.
- It may not contain its point-particle. It is for instance the case of the cell $V(C_2)$ associated to particle C_2.
- It may contain other point-particles even those whose cell is empty. C_3 and C_2 are contained into the Voronoi cell of C_1.

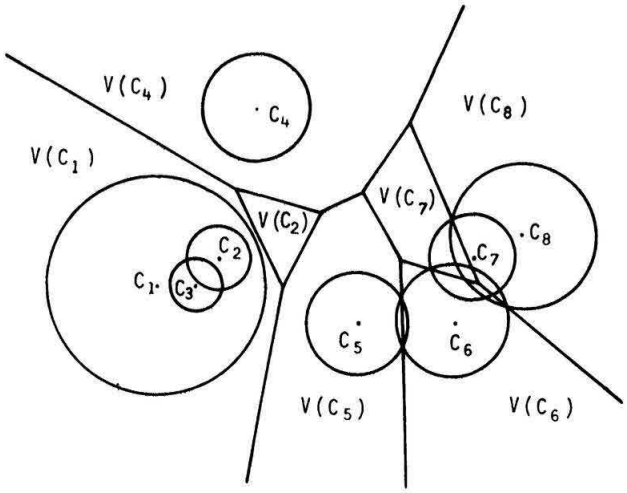

FIGURE 1.4: Geometric representation of Voronoi-Laguerre tessellation. Figure is taken from [1].

In Figure 1.5 is represented an exemple of a two dimensional Voronoi-Laguerre tessellation where to each point particle is associated a Voronoi cell. Similarly to the classical tessellation, the total volume is conserved $V = \sum_j v_j$, the centroid of the j^{th} cell is located in G_j and the particle j of radius R_j is in M_j. The position of the particle j is given by $\boldsymbol{r}_j = \boldsymbol{OM}_j$.

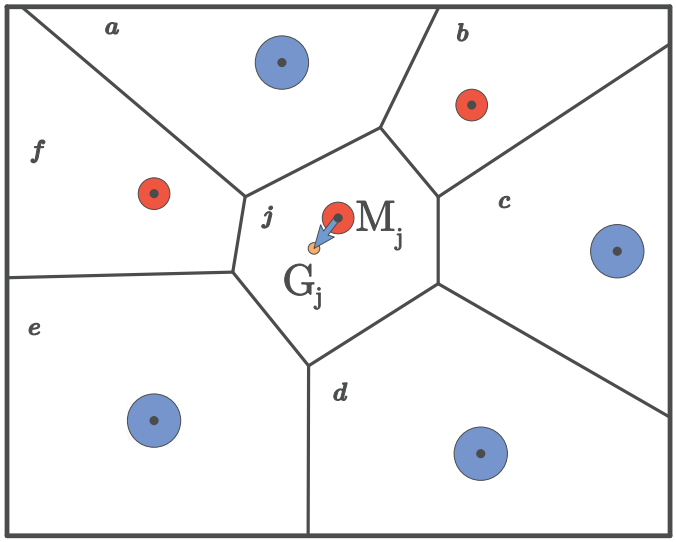

FIGURE 1.5: Representation of 2-dimensional Voronoi-Laguerre tessellation.

As in equation 1.2 the geometrical polarisation is given by $\boldsymbol{\tau}_j = v_i \boldsymbol{M_j G_j}$.

We have presented some geometrical characteristics of the Voronoi tessellation and of one of its possible extension the Voronoi-Laguerre tessellation. Whereas the first one is

used to deal with systems where particles play identical role the second tessellation is more suited to work with polydisperse systems. In both cases we have observed that the geometrical polarization is conserved. In what follows we will give a mechanical role to this vectorial quantity. As a matter of fact the force exerted on each particle will be directly proportional to the geometrical polarization. In next section we will first focus on the potential energy as its derivation will naturally lead to an expression of the force field. Then a link with the geometrical polarization will be provided.

1.2 Energy and force field : general expressions

For the moment we have considered the tessellations from a geometrical point of view. Numerous recent studies [31, 33] have used them as a tool to recover information from the local neighborhood of particles in liquids. In what follows we propose to use the geometrical properties of Voronoi tessellation to define a brand-new class of liquids.

It has been shown for granular materials that an analogous Hamiltonian can be defined to describe the microstate of jammed matter in term of volume function. This volume function is equivalent to the Voronoi volume associated to each particle [34]. Starting from this observation we propose a new Hamiltonian to describe a system of N identical particles.

If we consider a function f which depends only on $r = ||\boldsymbol{r}||$ where $\boldsymbol{r}$ is the vector starting from the particle i to a running point spanning the Voronoi cell as represented on figure 1.6, we can define the potential energy:

$$E_P = \frac{\gamma}{2} \sum_{i=1}^{N} \int_{v_i} d^d \boldsymbol{r} f(r) \tag{1.8}$$

where v_i is the volume of the voronoi cell associated to particle i and γ is an arbitrary constant.

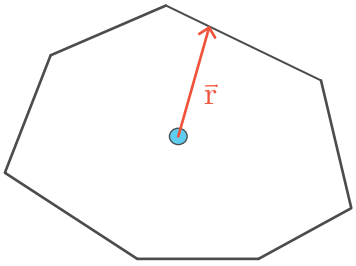

FIGURE 1.6: Representation of the vector $\boldsymbol{r}$ in 2 dimensions.

We can extend the formulation of the Hamiltonian for taking into account the disparity between particles. To do so, we work in the framework of the Voronoi-Laguerre tessellation where the distance function is not Euclidian. We consider the function $r^2 - R_i^2$:

$$E_P = \frac{\gamma}{2} \sum_{i=1}^{N} \int_{v_i} d^d\boldsymbol{r}(r^2 - R_i^2) \tag{1.9}$$

From equations 1.8 and 1.9 we see that the energy is the sum over a local term which is not a pairwise function. These new Hamiltonians are describing a system where interactions among particles are intrinsically many-body. We need to know the information on the positions of particle i and of all its nearest neighbors in order to define the Voronoi cell of particle i and its volume v_i over which the integration is performed.

For both equations 1.8 and 1.9 we can show that $-\boldsymbol{\nabla}_j E_p = \boldsymbol{F}_j$ where $\boldsymbol{F}_j$ is the force acting on particle j. We find that for the monodisperse system the force is given by :

$$\boldsymbol{F}_j = \frac{\gamma}{2} \int_{v_j} d^d\boldsymbol{r} \boldsymbol{\nabla} f(r) \tag{1.10}$$

Note that passing from equation 1.8 to equation 1.10 is not trivial. For the polydisperse case we find:

$$\boldsymbol{F}_j = \frac{\gamma}{2} \int_{v_j} d^d\boldsymbol{r} \boldsymbol{\nabla}(r^2 - R_j^2) \tag{1.11}$$

We have presented general equations for the potential energy and for the forces for a system with identical particles and also for a system where size disparities could be introduced. In what follows we give a specific form of the general function f defined in the monodisperse case. It enables on the one hand to deal with a quite simple expression of the potential energy and on the other hand to make a link between the geometrical polarization and the forces.

1.3 The monodisperse Voronoi liquid

In this section we focus our attention on a system, named the monodisperse Voronoi liquid, where the N point particles playing an identical role are contained into a box of volume $V = L^d$ at density $v = V/N$. By choosing the function $f(r) = r^2$ in equation 1.8, the Hamiltonian becomes

$$E_p = \frac{\gamma}{2} \sum_{i=1}^{N} \int_{v_i} d^d\boldsymbol{r} r^2 \tag{1.12}$$

where γ has the dimension of the energy divided by the length L^{d+2}. The potential energy E_p is a sum of local, positive and non pairwise elements that can be seen as the moments of inertia of the polytopes with respect to the particles. Moreover the potential is ultrasoft, there is no excluded volume. Consequently superposing two particles has a finite cost in energy.

As the force derives from the potential energy, following 1.10 we can write $\boldsymbol{F}_j = \gamma \int_{v_j} d^d\boldsymbol{r}\boldsymbol{r}$. In this case the force is proportional to geometrical polarization as $v_j = \int d^d r 1$ and $\boldsymbol{M}_j\boldsymbol{G}_j = \int d^d r \boldsymbol{r} / \int d^d r 1$. Consequently the expression for the force is given by :

$$\boldsymbol{F}_j = \gamma \boldsymbol{\tau}_j = \gamma \int_{v_j} d^d\boldsymbol{r}\boldsymbol{r} \tag{1.13}$$

The interactions among particles are thus local, invariant by translation or rotation and non pairwise. They are also directly related to the inherent geometrical properties of the Voronoi tessellations.

The monodisperse Voronoi liquid has been described in details in [26], in what follows we sum up its main properties. For sake of generality most of theoretical expressions are given for any dimension d. However all results coming from molecular dynamic simulations are performed in 3 dimensions with a modified version of LAMMPS that takes into account elements from the library Voro++ [35]. The system is composed of $N = 8000$ point particles contained into a cubic box of length $L = 20$ such as $v = 1$. The constant γ is arbitrarily chosen equal to 1000. Due to the dimensionality of γ, $\gamma v^{\frac{d+2}{d}}$ has the dimension of an energy and this ensures that the characteristic energy of interaction as $E_v = 0.001\gamma v^{\frac{d+2}{d}}$.

1.3.1 Scaling relation for the potential energy and thermodynamics

The potential energy obeys a scaling relation as shown in equation 1.14. This scaling is similar to the one derived for liquids with inverse power law potential [36, 37] at the difference that the power is positive for the monodisperse Voronoi liquid.

$$E_p(\lambda\boldsymbol{r}_1 \cdots, \lambda\boldsymbol{r}_N) = \lambda^{d+2} E_p(\boldsymbol{r}_1 \cdots, \boldsymbol{r}_N) \tag{1.14}$$

This scaling relation has two direct consequences. The first one is that we can express easily the variation of the partition function in the case of a small dilatation and consequently find the pressure P which is given by

$$P = \frac{N k_B T}{V} - \frac{d+2}{d}\frac{\langle E_p \rangle}{V} \tag{1.15}$$

A second consequence is that the partition function relative to the potential energy Z_{pot} inherits the scaling properties. As a result all the thermodynamic observables can be expressed in term of a scaling function ϕ which depends on only one parameter the scaling variable x given by

$$x = \frac{k_B T}{\gamma} v^{-\frac{d+2}{d}} \tag{1.16}$$

We have the following expression for the excess free energy and the excess chemical potential :

$$F_e(N,V,T) = N k_B T \phi(x) = N v^{\frac{d+2}{d}} \gamma x \phi(x) \tag{1.17}$$

$$\mu_e(N,V,T) = \left.\frac{\partial F_e}{\partial N}\right|_{T,V} = k_B T \left(\phi(x) + \frac{d+2}{d} x\phi'(x)\right) \tag{1.18}$$

For a system in 3D, these two thermodynamic functions are represented in Figure 1.7.

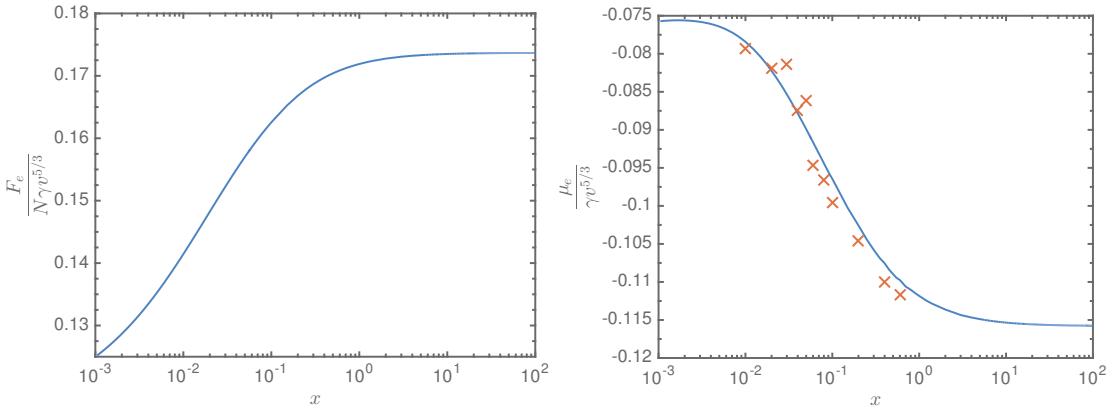

FIGURE 1.7: Left: Evolution of the scaled excess free energy per particle $F_e/(N\gamma v^{5/3})$ as a function of the scaling variable x. Right: Evolution of the scaled excess chemical potential as a function of x (blue line). The red crosses represent the value of $x\ln(g(0))$ for several values of x.

These scaling relations make the investigation of the space of state variable easier as when thermodynamic observables are known as a function of one of the state variable, the scaling variable x enables to express the result as a function of the other state variables.

For this system a unique relation between the excess chemical potential μ_e and the pair correlation function $g(r)$ which measures the probability that two particles are separated by distance r. In the limit where $r \to 0$ it has been found that :

$$\mu_e = k_B T \ln(g(0)) = \gamma v^{\frac{5}{3}} x \ln(g(0)) \tag{1.19}$$

This relation, illustrated in Figure 1.7 (Right), is a direct consequence of the ultrasoft character of the potential energy since the superposition of two particles has a finite cost in energy. More precisely the energy of a system with $N+1$ particles is the same as the one for a system with N particles in the specific case where $\boldsymbol{r}_{N+1} \to \boldsymbol{r}_N$.

$$\lim_{\boldsymbol{r}_{N+1}\to\boldsymbol{r}_N} E_p(\boldsymbol{r}_1, \cdots, \boldsymbol{r}_{N+1}) = E_p(\boldsymbol{r}_1, \cdots, \boldsymbol{r}_N) \tag{1.20}$$

This property is only valid for this system and cannot be found for a system with pairwise interactions. However, equation 1.19 is reminiscent of the zero separation theorem derived for cavities in hard spheres [38].

The thermodynamics of the monodisperse Voronoi liquid has been described. An unexpected link between the excess chemical potential and a microscopic observable, the pair correlation function, has been found. In what follows results on microscopic observables such as the structure factor or the mean square displacement are provided.

1.3.2 Microscopic observables: similarities with usual simple liquids

We look now at structural quantities such as the pair correlation function $g(r)$ or the static structure factor $S(k)$ to see to what extent the monodisperse Voronoi liquid is similar usual simple liquids. We recall first the definitions of these two quantities. The pair correlation function measures the probability that two distinct particles are separated by a distance r:

$$g(\boldsymbol{r}) = \frac{V}{N^2} \sum_{i,j/i\neq j} \langle \delta(\boldsymbol{r} - \boldsymbol{r}_{ij}) \rangle \quad \text{with} \quad \boldsymbol{r}_{ij} = \boldsymbol{r}_j - \boldsymbol{r}_i \tag{1.21}$$

Assuming the invariance by translation, the isotropy implies that the pair correlation depends only on $r = |\boldsymbol{r}|$. Liquids are characterized by a pair correlation function structured at short range which results from a local order. Contrary to crystals the order is not preserved at larger distance and consequently $g(r) \to 1$. Structure factor and pair correlation complement one another. In the reciprocal space the static structure factor measures the fluctuations of density:

$$S(k) = N^{-1} \langle \rho(-\boldsymbol{k}) \rho(\boldsymbol{k}) \rangle \quad \text{with} \quad \rho(\boldsymbol{k}) = \sum_{j=1}^{N} \exp(-i\boldsymbol{k} \cdot \boldsymbol{r}_j) \tag{1.22}$$

With $\boldsymbol{k}$ the wavevector defined as $\boldsymbol{k} = \frac{2\pi}{L}(n_x, n_y, n_z)$. One of the main advantages of the structure factor is that it is experimentally accessible from X-Ray or neutron

experiments [39, 40] and it is linked to the pair correlation function by the relation :

$$S(\boldsymbol{k}) = 1 + \frac{N}{V}\int d\boldsymbol{r} g(\boldsymbol{r}) \exp(-i\boldsymbol{k}\cdot\boldsymbol{r}) \tag{1.23}$$

Once again assuming isotropy in the system we can express the static structure factor as a function of $k = |\boldsymbol{k}|$:

$$S(\boldsymbol{k}) = 1 + 4\pi\frac{N}{V}\int_0^\infty dr\, r^2 g(r)\frac{\sin(kr)}{kr} \tag{1.24}$$

Denoting σ the diameter of particles, for $k \gg 2\pi/\sigma$ the structure factor probes distances lower than the interparticle distance for which the pair correlation is close to zero and consequently $S(k) \to 1$ when $k \to \infty$. On the opposite, looking at very small values of the wavector, $k \ll 2\pi/\sigma$, means probing the hydrodynamic limit. It can been shown that the value of $S(k)$ when $k \to 0$ is related to the compressibility χ_T [40]:

$$S(k \to 0) = \frac{N}{V} k_B T \chi_T \tag{1.25}$$

The small values of $S(k)$ when $k \to 0$ generally observed for simple liquids are representative of the difficulties encountered for compressing the liquid. When $k \sim \sigma$ the structure factor brings information on the local environment of particles.

In Figure 1.8 is represented for several temperatures the pair correlation function (left) and the static structure factor (right). The first peak of the pair correlation function informs on the location of the nearest neighbors. In this case they are located at $r \sim 1.1$. When temperature is decreased the pair correlation gets more and more structured but remains decorrelated at long distances. The different peaks represent the successive shells of neighbors. The distance between two of these shells is ~ 0.9. The period of oscillations in the pair correlation function can be found in the position of the first peak of the static structure factor. This later is located at $k_{max} \sim 7$ which in real space gives a distance $2\pi/7.0 \sim 0.9$. For $k \to 0$ the static structure factor has very small values, meaning that in this range of temperature the monodisperse Voronoi liquid is difficult to compress as it is often the case for usual simple liquids. Looking at the distance σ_r below which $g(r) \sim 0$ we observe that σ_r is decreasing when the temperature increases. This behavior results from the ultrasoft nature of interactions and is also observed in soft-core model such as Gaussian Core Model (GCM) [41].

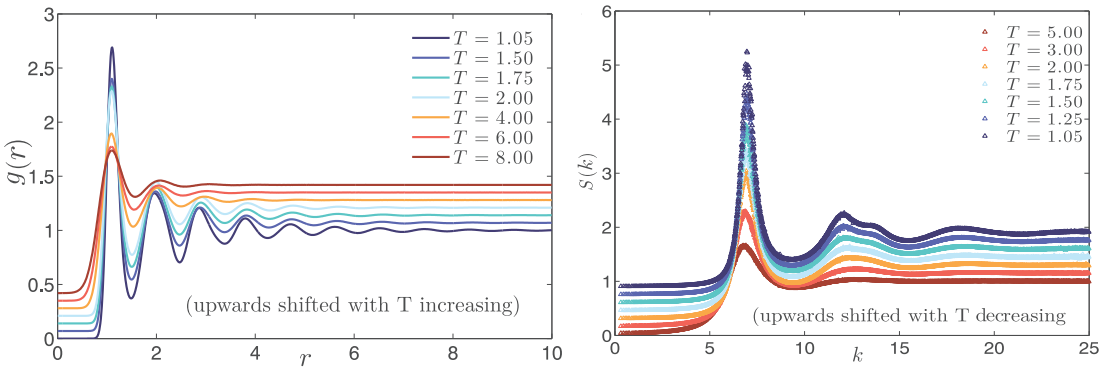

FIGURE 1.8: For different temperatures are represented the pair correlation function $g(r)$ (left) and the structure factor $S(k)$ (right).

Regarding all the observations on structural quantities the monodisperse Voronoi liquid behaves like usual simple liquids.

We now investigate the dynamical properties of this system by looking for instance at the mean square displacement which measures the correlation between the position of a tagged particle at time $t = 0$ and its position at time t. The mean square displacement (MSD) is given by

$$\delta r^2(t) = \langle [\boldsymbol{r}_i(t) - \boldsymbol{r}_i(0)]^2 \rangle \tag{1.26}$$

At short time scale, the mean free path of the tagged particle can be seen as a ballistic motion an consequently $\delta r^2(t) \propto t^2$. At larger time scale, the movement of the tagged particle appears as erratic and it can be described by a diffusive process. Consequently $\delta r^2(t) = 6Dt$ in 3 dimensions and therefore we can extract from long-time limit the diffusion coefficient D. In Figure 1.9 (left) is represented the scaled MSD for different temperatures.

We observed that at high temperature the ballistic regime is immediately followed by the diffusive regime and we can describe the MSD with the Enskog theory. Assuming that successive collisions are decorrelated one from each other leading to a Markovian process. Thus the velocity autocorrelation is given by an exponential law $\langle v(t)v(0) \rangle = (3k_BT/m)\exp(\Gamma t)$ where $\Gamma = T/D$ and consequently the MSD which is also given by the integral of the velocity autocorrelation becomes:

$$\delta r^2(t) = 6D[\exp(-\Gamma t) - 1 + \Gamma t]/\Gamma \tag{1.27}$$

In Figure 1.9 (left) the good collapse between points (circle in the graph) evaluated with equation 1.27 and the mean square displacement directly calculated with equation 1.26

(straight line in graph) suggests that at high enough temperature the Enskog description seems to apply to our system. However when looking at the asymptotic behavior of the diffusion coefficient a difference arises with the Enskog prediction which gives $D \sim \sqrt{(T)}$. In the case of the monodisperse Voronoi liquid we find $D \sim T^{5/2}$ (see insert in Figure 1.9 (right)). To understand this difference we use a kinetic description of the diffusion coefficient that is $D \sim v_T \ell_{mfp}$ where v_T is the thermal velocity and ℓ_{mfp} the mean free path. We know that $v_T \sim \sqrt{T}$ and $\ell_{mfp} = V/(N\sigma_c) \sim v/R^2$ with $\sigma_c = \pi R^2$ the collision cross section and R the effective radius of particles. As a result $D \sim v\sqrt{(T)}/R^2$. Due to the soft core character of particles an expansion of effective radius in the high temperature limit gives $R \sim 1/T$ and thus as a result $D \sim T^{5/2}$.

When the temperature is lowered the emergence of an intermediate regime in the MSD, characterized by the presence of a plateau whose length increases as temperature decreases, suggests that the tagged particle is trapped into its cage of nearest neighbor. The cage picture proposed by Eyring implies that the trapped particle has to overcome an energy barrier E_A in order to escape the first shell of neighbors. The dynamic is thus activated and the diffusion coefficient can be expressed as the Arrhenian relation $D \propto \exp(-E_A/k_BT)$. This assumption can be verified when looking at the evolution of diffusion coefficient with temperature. In Figure 1.9 (right) is represented the logarithm of the scaled diffusion coefficient $\ln(D\gamma^{-1/2}v^{-7/6})$ vs. $1/x$. We observe the presence of an Arrhenian behavior for large value of $1/x$ (which means small values of T according to relation 1.16) and an estimation of the energy barrier gives $E_A \sim 4.95$.

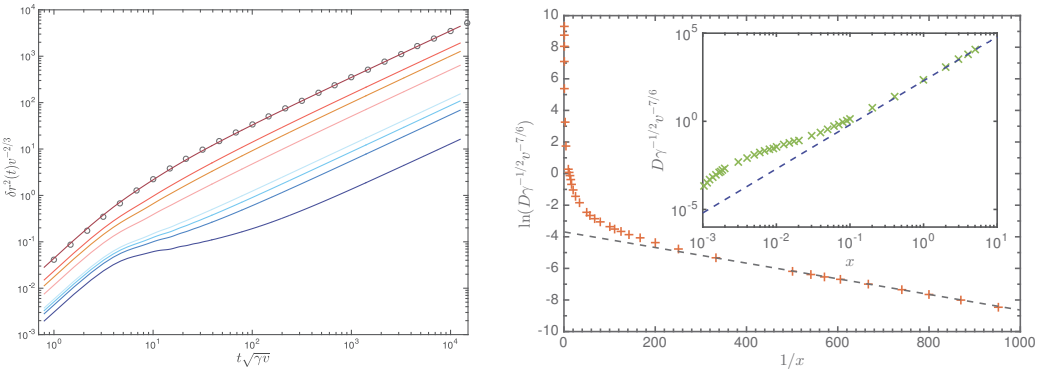

FIGURE 1.9: (Left) Evolution of scaled mean square displacement for different temperature. From bottom to top : $T = 1.05, 1.50, 1.75, 2.00, 4.00, 6.00, 8.00, 15.00$. The circles corresponds to the Enskog theory for the highest temperature. (Right) Logarithm of the scaled diffusion coefficient as a function of $1/x$. The dashed line corresponds to an Arrhenian fit. Insert: Scaled diffusion coefficient as a function of the scaling variable x.The dashed line underlines the asymptotic behavior where $D \sim T^{5/2}$.

The MSD of the monodisperse Voronoi liquid reminds the one of usual simple liquids. At low temperature, the diffusion coefficient informs on the presence of an Arrhenian regime

where particles have to wait a certain time before being able to overcome the energy barrier and escape the nearest neighbor shell. At enough high temperature the MSD is well described by the Enskog theory which assumes that the velocity autocorrelation obeys a Markov process. Only the diffusion coefficient D behaves differently from what expected from Enskog theory but this difference is easily explained by the fact that we work with an ultrasoft potential instead of the hard spheres model.

As we mentioned before the mean square displacement describes different regimes regarding the time scale or the length scale observed. In the study of liquids it is the case for numerous time-dependent and we can defined these regimes by comparing length and time to respectively mean free path ℓ_{mfp} and collision time τ_c. Generally observables are defined in the space of wavelength k and frequency ω. Therefore by analyzing the value of products $k\ell_{mfp}$ and $\omega\tau_c$ we identify three types of regimes as illustrated in Figure 1.10.

1. The hydrodynamic regime when $k\ell_{mfp} \ll 1$ and $\omega\tau_c \ll 1$. The behavior of the liquid can be described by the equations of hydrodynamics.
2. The kinetic regime when $k\ell_{mfp} \approx 1$ and $\omega\tau_c \approx 1$. The distances probe at this scale are the ones of the molecular structure and the dynamic should be described by microscopic equations of motion.
3. The ballistic regime when $k\ell_{mfp} \gg 1$ and $\omega\tau_c \gg 1$. In this regime distances and time are so small that the particles move as if they were alone in the medium. There are no correlation among them.

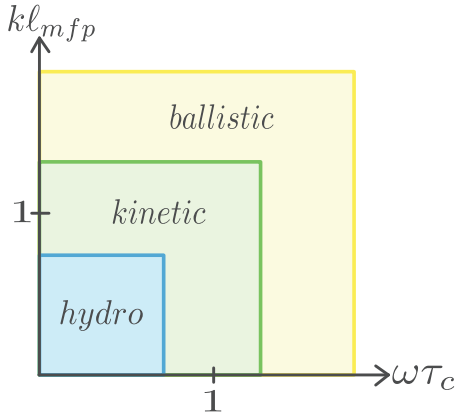

FIGURE 1.10: Schema of wavelength as a function of frequency shows three types of regimes observed in liquids. Wavelength and frequency have been rescaled respectively by the mean free path ℓ_{mfp} and the collision time τ_c.

In what follow our attention is restricted to the hydrodynamic regime which is characterized by slow variations of local properties on microscopic time and length scales.

1.3.3 Anomalous sound attenuation

When investigating the MSD, we notice that a relation exists between a microscopic quantity, the velocity autocorrelation, and a transport coefficient, the diffusion coefficient. This is one of the most famous example of Green-Kubo relations which in the context of linear response theory make the link between transport coefficient and integral of time correlation functions.

Time correlations play a central role in the description of liquids and it is therefore interesting to consider a general theoretical framework to express time correlation functions for different wavelengths and frequencies.

In what follow we investigate the hydrodynamic limit of the intermediate scattering function $F(k,t)$ which is defined as the time correlation of the fluctuation of the density δn.

$$F(k,t) = \frac{1}{N}\langle \delta n(-\boldsymbol{k},0)\delta n(\boldsymbol{k},t)\rangle \tag{1.28}$$

In the hydrodynamic limit this time correlation function is given by:

$$\frac{F(k,t)}{F(k,0)} = \frac{c_V}{c_P}\left[\varepsilon \exp(-D_T k^2 t) + \exp(-k^2\Gamma t)[\cos(v_s k t) + bk\sin(v_s k t)]\right] \tag{1.29}$$

where $c_P = C_P/N$ and $c_V = C_V/N$ are the heat capacity at respectively constant pressure and constant volume, ε is related to both of heat capacities by the following relationship:

$$\varepsilon = \frac{c_P}{c_V} - 1 \tag{1.30}$$

The thermal diffusivity D_T implied in the first exponential in equation 1.29 is related to the thermal conductivity via :

$$D_T = \frac{\kappa}{\rho c_P} \tag{1.31}$$

In the second exponential appears the sound attenuation Γ which is linked to the thermal diffusivity and longitudinal viscosity η_L :

$$\Gamma = \frac{D_T\varepsilon}{2} + \frac{\eta_L}{2\rho} \qquad \text{with} \quad \eta_L = \frac{4}{3}\eta + \xi \tag{1.32}$$

where η is the shear viscosity and ξ is the bulk viscosity. Finally the parameter b in equation 1.29 is given by :

$$b = \frac{3\Gamma - \eta_L/\rho}{(\varepsilon + 1)v_s} \tag{1.33}$$

In equation 1.29 we observe that relaxation of density fluctuation is made through :

1. diffusion of energy as it is suggested by the presence of the thermal diffusivity D_T
2. propagation of acoustic waves which are damped by the combined effect of viscosity and thermal conduction (see equation 1.32)

Assuming that we can neglect the thermal contributions, we can rewrite 1.29 as :

$$\frac{F(k,t)}{F(k,0)} \simeq \exp(-k^2\Gamma t)[\cos(v_s k t) + \frac{\Gamma}{v_s} k \sin(v_s k t)] \tag{1.34}$$

where $\Gamma = \eta_L/(2\rho)$. Consequently we define the spectrum of density fluctuations:

$$\frac{S(k,\omega)}{S(0)} \approx \frac{1}{2\pi}\left[\frac{\Gamma k^2}{(\omega + v_s k)^2 + (\Gamma k^2)^2} + \frac{\Gamma k^2}{(\omega - v_s k)^2 + (\Gamma k^2)^2}\right] \tag{1.35}$$

In the hydrodynamic limit, Γ is expected to be constant, i.e it will not depend on the wave vector k. To test the validity of this hypothesis for the Voronoi liquid, we try to express $S(k,\omega)/S(k)$ as a scaling function. For the purpose of the scaling we define $\delta\omega = \omega - \omega_{max} = \omega - v_s k$.

$$\begin{aligned}\frac{S(k,\omega)}{S(k)} &= \frac{1}{2\pi}\frac{\Gamma k^2}{(\omega - vsk)^2 + (\Gamma k^2)^2} \\ &= \frac{1}{2\pi}\frac{\Gamma k^2}{(\delta\omega)^2 + (\Gamma k^2)^2} \\ &= \frac{1}{2\pi}\frac{1}{k^2}\frac{\Gamma}{(\delta\omega/k^2)^2 + \Gamma^2}\end{aligned} \tag{1.36}$$

Thus for Γ constant, $k^2 S(k,\omega)/S(k)$ will be a function of $\delta\omega/k^2$. Results of this approach are presented in the inset of Figure 1.11 where $k^2 S(k,\omega)/S(k)$ is plotted as a function of $\delta\omega/k^2$ for different values of k. We observe that for the Voronoi liquid, the data do not collapse on the same curve, which would have been the case if Γ were constant.

We assume that Γ is k dependent and linear in k such as $\Gamma(k) = \Gamma_0/k$ where Γ_0 is a constant. Once again we search for a scaling of $S(k,\omega)/S(k)$.

$$\begin{aligned}\frac{S(k,\omega)}{S(k)} &= \frac{1}{2\pi}\frac{\Gamma k^2}{(\omega - vsk)^2 + (\Gamma k^2)^2} \\ &= \frac{1}{2\pi}\frac{\Gamma_0 k}{(\omega - vsk)^2 + \Gamma_0^2 k^2} \\ &= \frac{1}{2\pi}\frac{1}{k}\frac{\Gamma}{(\omega/k - vs)^2 + \Gamma^2}\end{aligned} \tag{1.37}$$

Thus in this case $kS(k,\omega)/S(k)$ is simply a function of ω/k and it is represented for different k in Figure 1.11. We notice the good collapse of the different curves meaning that for the Voronoi liquid Γ is apparently linear in k.

We gave evidences that the sound attenuation Γ^{-1} scales as k and not as k^2 as expected. The explanation of this behavior is rather complicated and a detailed analysis can be found in [27].

In what follow descriptions of the metastable zone and of the crystalline phase, which appears below $T = 1.05$, are provided.

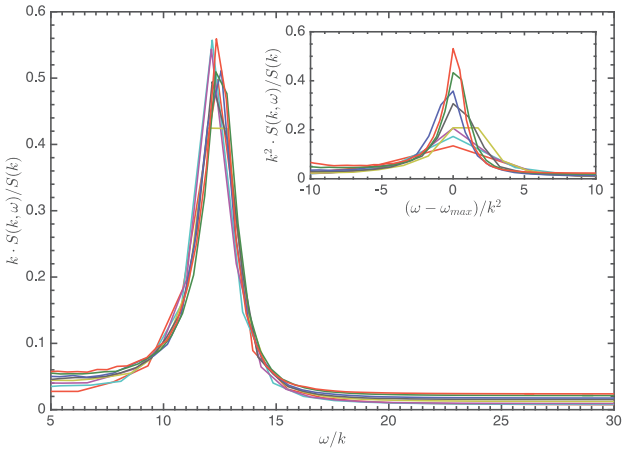

FIGURE 1.11: Test of scaling $kS(k,\omega)/S(k)$ as a function of ω/k for $T/E_V = 1.50$, $N = 65536$ particles and $k \in [0.3, 1.0]$. The same data are represented for the scaling $k^2 S(k,\omega)/S(k)$ vs. $[\omega - \omega_{max}]/k^2$

1.3.4 Metastability and crystalline phase

The presence of a liquid/crystal transition is revealed by a discontinuity in the first derivatives of the thermodynamic potentials. Consequently to probe its existence the system has been progressively cooled down than heated up at two different cooling rates denoted as fast and slow and having for values $k_f = dT/dt = 2.5 \cdot 10^{-4}$ and

$k_s = dT/dt = 2.5 \cdot 10^{-5}$. Then the potential energy per particle has been calculated as a function of temperature as represented in Figure 1.12. In both cases (fast in grey and slow in orange) jumps in the value of E_p/N informs on the presence of a first order transition and marks boundaries of the metastable regime. In the same figure are represented mean values of the potential energy per particle evaluated on isotherms. The black and blue crosses represent $\langle E_P \rangle / N$ for systems of respectively $N = 8000$ and $N = 8192$ particles. The choice of $N = 8192$ is motivated by the fact that this number allows a matching between the box size and the b.c.c crystal which is the crystalline structure of the monodisperse Voronoi liquid.

It is interesting to notice that the slower the process the larger the hysteresis and the greater the value of E_P/N. However the slow process (in orange in the graph) seems to be well equilibrated as the data points from isotherms collapse on the curve. This result is surprising because one could imagine that by leaving more time to relax, the system would have pass from the liquid to the solid phase at higher temperature. An explanation for this phenomenon is still lacking.

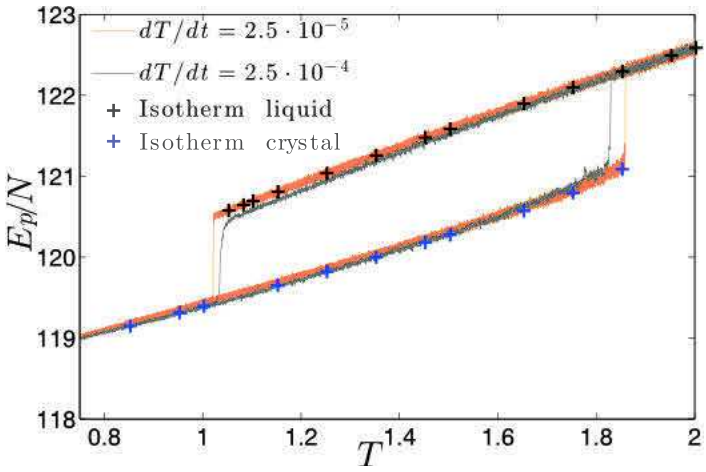

FIGURE 1.12: Representation of the potential energy per particule in the metastability zone for temperatures $1.05 \leq T \leq 1.85$. Grey and orange curves correspond to cooling and heating process at rates respectively $dT/dt = 2.5 \cdot 10^{-4}$ and $dT/dt = 2.5 \cdot 10^{-5}$. The black and blue crosses are mean values of E_P/N evaluated on several isotherms with respectively $N = 8000$ and $N = 8192$.

Metastability affects both structural and dynamical quantities. In what follows we briefly compare results obtained for isotherms in the liquid phase (black crosses) with isotherms in the crystalline phase (blue crosses). We first look at the pair correlation function which is represented for three different temperatures in Figure 1.13. While in the liquid phase (in blue) the pair correlation function is slightly more structured upon cooling, in the crystalline phase (dashed red lines) it get is already well structured at $T = 1.85$ and when T is lowered, peaks are getting sharper and long-range correlation are increasing.

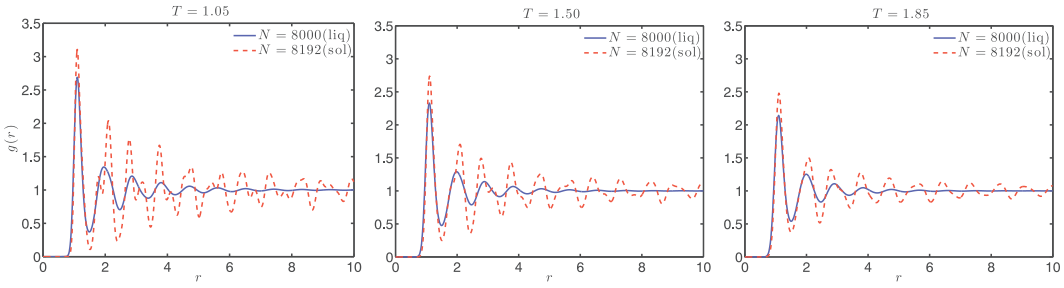

FIGURE 1.13: Representation of the pair correlation function for three temperatures taken in the metastable zone. The straight blue lines correspond to isotherms in the liquid phase with $N = 8000$ particles whereas the dashed red lines are data from isotherms in the crystalline phase for $N = 8192$ particles.

The MSD is also sensitive to metastability as it is observed in Figure 1.14. When looking at data taken from isotherms in the crystalline phase, the ballistic regime is followed by a regime, characterized by a plateau, where particles vibrates around their equilibrium position. Moreover we notice that the size of the plateau increases upon cooling until reaching a temperature where no diffusion takes place during the time observed.

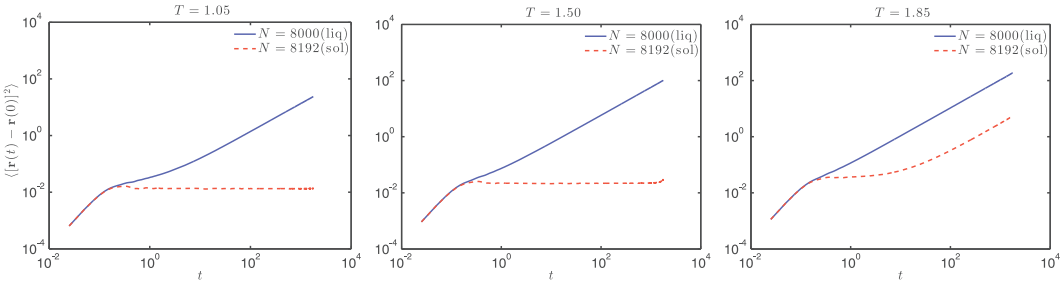

FIGURE 1.14: Representation of the MSD for three temperatures taken in the metastable zone. The straight blue lines correspond to isotherms in the liquid phase with $N = 8000$ particles whereas the dashed red lines are data from isotherms in the crystalline phase for $N = 8192$ particles.

When investigating the mobility within the crystalline phase in the metastable region we notice that particles jumps from site to site leaving the whole structure unchanged. The jumping process is Arrhenian and particles need to overcome an activation energy E_A in order to move.

Cooling then heating the system at different rates enabled to reveal a metastable zone in a range of temperature $1.05 \leq T \leq 1.85$. The precise value of the melting temperature has been found by thermodynamic integration and is equal to $T_m \sim 1.65$.
Whereas many monodispere Lennard-Jones liquids crystallize into face centered cubic (FCC) crystals [42, 43], the crystalline phase of the monodisperse Voronoi liquid is a body centered cubic (BCC) lattice. This can be explained by the fact that the sphere

minimizes the local potential energy $e_p^{(i)} = (\gamma/2)\int_{v_i} d^3r^2$. The Voronoi cell associated to the FCC lattice is the rhombic dodecahedron (12 faces) whereas the Voronoi cell associated to the BCC lattice is the truncated octahedron (14 faces). By comparing these two structures (see Figure 1.15) we see that the truncated octahedron has more faces than de rhombic dodecahedron and consequently is closer to a spherical structure. The energy is therefore minimized by the truncated octahedron structure.

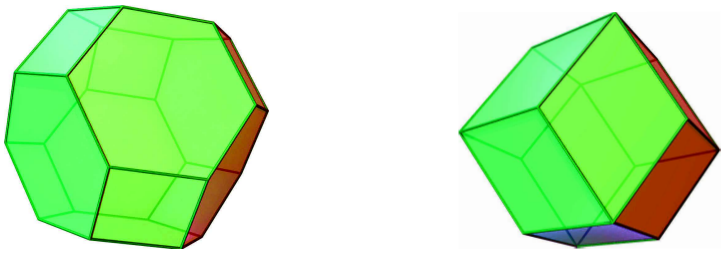

FIGURE 1.15: Left: Truncated octahedron corresponding to the BCC Voronoi cell. Right: Rhombic dodecahedron corresponding to the FCC Voronoi cell.

To sum up, the monodisperse Voronoi liquid is a system of point particles whose interactions directly expressed via the inherent geometrical properties of classical Voronoi tessellation are intrinsically manybody. This system presents a scaling of the potential energy whom partition function inherits. As a result all the thermodynamic observables in the system can be expressed as a function of a scaling variable. The ultrasoft character of the potential energy enables to derive an unusual relation between the excess chemical potential and the pair correlation function thus providing a link between microscopic structural quantities and macroscopic observables. On the structural point of view, the Voronoi liquid shares similarities with soft-core potential liquids such as GCM. The dynamics of the system is also similar to what has been observed for simple liquids. However in the range of temperature $1.05 \leq T \leq 2.00$ the relaxation of the correlation of density fluctuation in the hydrodynamic limits shows that the sound attenuation does not scale as k^{-2} but as k^{-1}. In the same range of temperature, metastability is observed and depending on the initial configuration the system is either liquid or crystal. At enough high temperature the crystalline phase is relatively mobile and it is interesting to notice that jumps of particles occur also below the melting point $T_m \sim 1.65$ Finally below $T = 1.05$ the Voronoi liquids crystallizes into a BCC crystal.

The monodisperse Voronoi liquid is thus a model with exotic features that could reveal some interesting information when probing glass transition. Therefore in order to avoid crystallization, we propose an extension of this model by using Voronoi-Laguerre tessellations where size disparities are introduced among particles. Firstly a general description of the polydisperse Voronoi liquid is proposed in next section, then we introduce the selected model, a binary mixture, whose study is the aim of this work.

1.4 The polydisperse Voronoi liquid

We define now an extension of the monodisperse Voronoi liquid, named the polydisperse Voronoi liquid, where size disparity among particles is introduced. As mentioned before to take into account the polydispersity in the system, Voronoi-Laguerre tessellations are required. Assuming a box of length L such as $V = L^d$ we consider N point particles to which is associated an intrinsic length R_i that we call radius for convenience. Following equation 1.9, the potential energy is

$$E_P = \frac{\gamma}{2} \sum_{i=1}^{N} \int_{v_i} d^d\boldsymbol{r}(r^2 - R_i^2 + R^2) \tag{1.38}$$

where R^2 is the square of the mean radius and is given by $R^2 = N^{-1} \sum_{i=1}^{N} R_i^2$. Adding the square value of the mean radius ensures to recover the monodisperse Voronoi liquid when all the radii are equal. It is interesting to notice that the potential energy can be decomposed into the sum of two terms $E_P = E_P^{(m)} + E_P^{(a)}$ where $E_P^{(m)}$ is defined as:

$$E_P^{(m)} = \frac{\gamma}{2} \sum_{i=1}^{N} \int_{v_i} d^d\boldsymbol{r} r^2 \tag{1.39}$$

and the second term can be written as

$$E_P^{(a)} = \frac{\gamma}{2} \sum_{i=1}^{N} \int_{v_i} d^d\boldsymbol{r}(R^2 - R_i^2) = \frac{\gamma}{2} \sum_{i=1}^{N} v_i(R^2 - R_i^2) \tag{1.40}$$

Equation 1.11 gives the expression of the force exerted on particle j which is defined as:

$$\boldsymbol{F}_j = \gamma \boldsymbol{\tau}_j = \gamma \int_{v_j} d^d\boldsymbol{r}\boldsymbol{r} \tag{1.41}$$

1.4.1 The bidisperse Voronoi liquid

The polydispersity could be described either by discrete values or by a continuous distribution of the radii sizes. In what follows and all through this work we deal with a binary mixture meaning that intrinsic lengths R_A and R_B are associated to respectively N_A and N_B particles. We chose arbitrarily that $R_A > R_B$. The choice of the size ratio $x = R_B/R_A$ and the fraction of A and B particles (respectively N_A/N and N_B/N) are of great importance regarding the ability of the system to be a reasonably good glass former. It has been shown for hard spheres that for a sufficiently marked size disparity, typically a size ratio $x \lesssim 0.6$, an increase of the percentage of small particles leads to a speed up of the dynamic. On the contrary when the size disparity is not so pronounced $x \gtrsim 0.8$, increasing the fraction of small particles leads to a slowing down of the dynamic

[44]. As this last effect is the key feature of glass transition we decide to follow what has been found for hard spheres and consequently the size ratio is fixed at $x = 0.83$ and the fractions of small and large particles are taken equal, $N_A/N = N_B/N = 0.5$.

We notice that polydispersity is governed by only one parameter denoted η and given by:

$$\eta = \frac{\sqrt{R_A^2 - R_B^2}}{v^{1/3}} \tag{1.42}$$

If $R_A = R_B$, $\eta = 0$ we find back the monodisperse case. A too large value of η, typically, $\eta \gtrsim 0.6$, would lead to cases where a fraction of particles could be outside their own cells or worse could have empty cells (zero volume). To avoid these unphysical possibilities we work with intermediate values of η which should ensure to avoid crystallization and systems where particles do not generate their own cells. Definition of size ratio x and equation 1.42 enable to define values of R_A and R_B:

$$R_A = \frac{\eta v^{1/3}}{\sqrt{1 - x^2}} \qquad \text{and} \qquad R_B = xR_A \tag{1.43}$$

To test which numerical values of η are appropriate to define properly the system in the range of temperature of interest, i.e $T \leq 2.00$, we perform cooling processes for different values of η, $0.20 \leq \eta \leq 0.70$. More details about the molecular dynamic simulation will be given in next subsection but for the cooling processes, we worked with $N = 1000$ particles at $v = V/N = 1$. We start from equilibrate configurations at $T_{start} = 2.00$ and we progressively decrease the temperature until we reach the final temperature $T_{stop} = 0.1$. The cooling rate is $dT/dt = 8 \cdot 10^{-5}$. We measure the value of the energy per particle E_P/N as a function of temperature T for $0.1 \leq T \leq 2.00$.

Results are presented in Figure 1.16 where we observe that for :

- $\eta = 0.20$ a marked discontinuity in the curve of $Ep/N(T)$ is present. A first order transition occurs, the system crystallizes for $T \sim 0.95$
- $\eta \in [0.25; 0.60]$ no discontinuities are present in the curve of Ep/N meaning that first order transition is prevented. In this range of η, systems falls out of equilibrium for $T < T_G$ where T_G is the glass transition temperature.
- When the value of η is increased, the value of the total energy per particle E_P/N decreases. We notice however that for $\eta \in [0.20; 0.30]$ the values of E_P/N are closed from the one measured for the monodisperse system as observed in Figure 1.12 meaning that the polydispersity can be seen as a small perturbation of the monodisperse system.

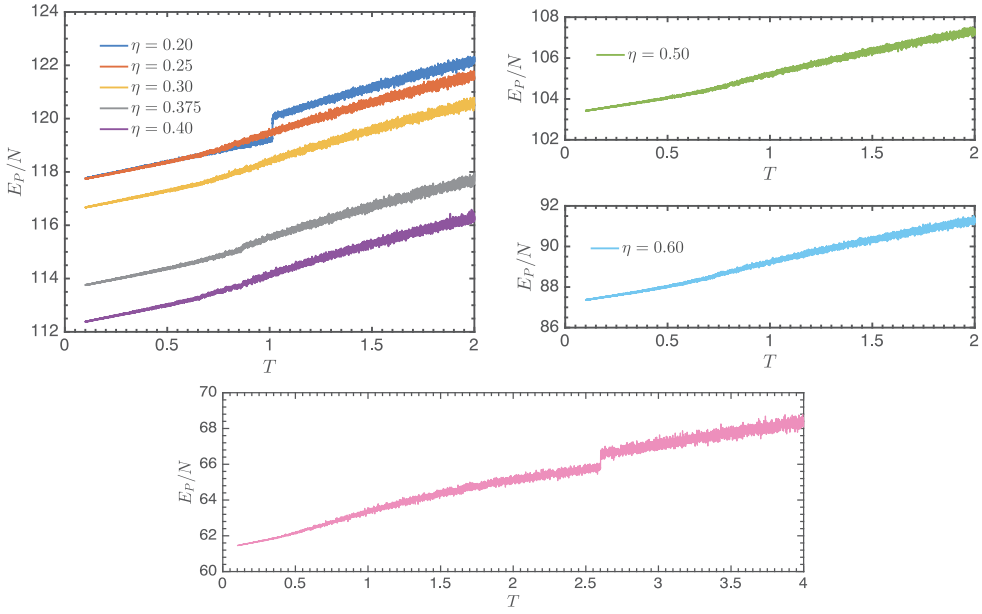

FIGURE 1.16: Upper part left and right : Cooling processes between $T = 2.00$ and $T = 0.1$ for different values of $\eta \in [0.20, 0.60]$. For clarity high values of η are presented on separated graphs (Right). Lower part : Cooling processes between $T = 4.00$ and $T = 0.1$ for $\eta = 0.70$.

- For $\eta = 0.70$ the cooling process has been done between $T_{start} = 4.00$ and $T_{stop} = 0.1$ as it appears that crystallization occurs for $T \sim 2.60$. Thus it exists a limiting value of η upper which systems crystallizes again. This can be explain by the fact that when η is increased, the intrinsic lengths of particles A and B are also increased. By keeping the density constant the probability of having small particles sharing Voronoi cell of large particles is also increased as it confirms by the representation in Figure 1.17 (Top) of the partial pair correlation function $g_{AB}(r)$ which measures the distance between particles A and B. In the inset the partial pair correlation is represented for a system at $\eta = 0.70$ in the liquid phase at $T = 4.00$. We notice that there is a nonzero probability for finding particle in close "contact" as it appears that $g_{AB}(r) \to 0.45$ when $r \to 0$. Even in the crystalline phase, at $T = 2.00$, the pair correlation tends to a nonzero value when $r \to 0$. On the contrary at the same temperature, for systems with $\eta \leq 0.60$ which are in the liquid phase, we observe that particles A and B are well separated.

  To go a step further, for $\eta = 0.70$, we have computed the distribution of volumes of the Voronoi cells v_B and v_A of respectively small and large particles. Results are shown in Figure 1.17 (Bottom). We notice that the distribution associated to large particle is a gaussian well-centered around its mean value $\langle v_A \rangle \sim 1.91$ whereas the distribution associated to small particles shows a huge probability for having small volumes. In the inset we see that the distribution is well described by a power law $P(v) \sim v^{-0.6}$ when $v \to 0$. Therefore a substantial fraction of

small particles have a volume $v_B \sim 0$. The absence of cells for these particles leads to a zero contribution in term of potential energy and forces. Consequently these particles are "ghost" and the system behaves as there were only one type of particles and we recover the monodisperse Voronoi liquid.

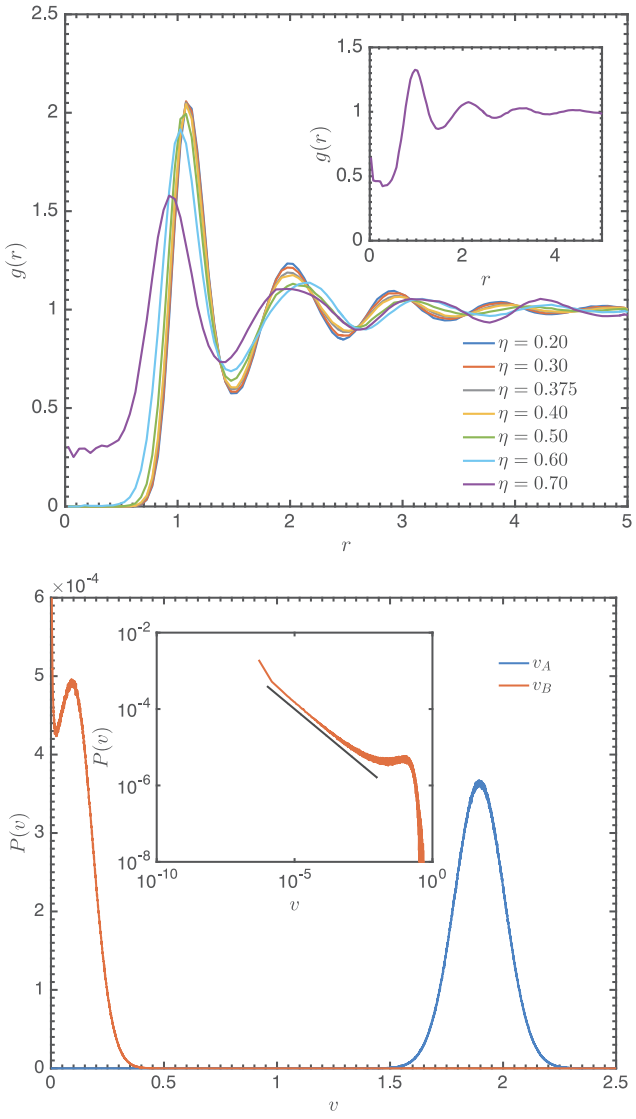

FIGURE 1.17: Top: Pair correlation function for different values of η at $T = 2.00$. Inset: Pair correlation function for $\eta = 0.70$ and $T = 4.00$. Bottom: For $\eta = 0.70$, distribution of the volume of the Voronoi cell. Inset Distribution of volumes v_B for very small values of v. The power law behavior is emphasized by the black straight line.

All these observations on η are valid in a certain range of temperatures. Obviously for enough high temperature even systems with low values of η would encounter the same type of observations as those done for $\eta = 0.70$. As a matter of fact, when kinetic energy is no more negligible compared to potential energy, situations with particles close one

from each other ($g_{AB}(r) \neq 0$ when $r \to 0$) or particles with no associated Voronoi cell ($v \sim 0$) would become more frequent.

Regarding the previous results, we chose $\boldsymbol{\eta = 0.375}$ as when looking at the potential energy of the cooling process, it remains on the first hand sufficiently far from the one of the monodisperse liquids for expecting that crystallization would be avoided even at slower cooling rate. On the other hand E_P/N is sufficiently close from the one of the monodisperse to see the polydispersity as a weak perturbation. This point of view is reinforced by the fact the partial pair correlation function $g_{AB}(r)$ is not strongly varying when η goes from 0.20 to 0.375. The position of first peak, as well as the global shape remains unchanged. However as the bidisperse Voronoi liquid does not seem to crystallize for $\eta = 0.375$, huge differences with the monodisperse model are expected for dynamical observables.

Now that the value of η is chosen we deduce the values of intrinsic lengths according to equation 1.43. Thus $R_A = 0.6729$ and $R_B = 0.5585$. We have now defined a set of parameters that should enable us to access the supercooled regime and the neighborhood of the glass transition. In what follows we will mostly work at constant density, $v = V/N = 1$, and we will test the sensitivity of different observables, generally used to described supercooled liquids, upon cooling. To do so, by means of molecular dynamic simulations we generated trajectories of N particles contained into a cubic box of length L.

1.4.2 Molecular dynamics (MD) simulations

In molecular dynamic simulations, the motion of particles is described by the Verlet algorithm [45]. The position $\boldsymbol{r}_j(t + \Delta t)$ of particle j at time $t + \Delta t$ is given by :

$$\boldsymbol{r}_j(t + \Delta t) = 2\boldsymbol{r}_j(t) - \boldsymbol{r}_j(t - \Delta t) + \frac{\boldsymbol{F}_j}{m}\Delta t^2 + O(\Delta t^4) \tag{1.44}$$

where $\boldsymbol{F}_j$ is the force exerted on particle j and it corresponds to the one defined in equation 1.41. It requires the knowledge of geometrical polarization $\boldsymbol{\tau}$ (see equation 1.2) meaning that we need to have access to the centroid and the volume of each Voronoi cell. To this purpose we use a modified version of LAMMPS [46] interfacing with the Voro++ library [35]. This library enables to perform efficiently Voronoi tessellation on 3D systems and so far to get access to plenty of geometrical elements relative to Voronoi tessellation.

The dynamic is correctly describe by the Verlet algorithm if the term Δt^4 is small enough to be considered as negligible. The choice of the timestep Δt in MD is therefore not

so trivial. It has to be chosen by taking into account that a too large timestep could imply difficulties for well-equilibrated the system whereas a timestep too small would lead to an important increase of calculation time. A way to determine the limit upper which Δt would be too big to describe accurately the dynamic, is to search for the characteristic time of the system τ_c by nondimensionalizing equation 1.44. By assuming the the characteristic length in the system is $v^{1/d}$ we can define $\boldsymbol{r}^* = \boldsymbol{r}/v^{1/d}$. We need now to nondimensionalize the force. To this purpose we consider equation 1.41:

$$\boldsymbol{F}_j = \gamma \int_{v_j} d^d\boldsymbol{r}\boldsymbol{r} \quad \overset{r=v^{1/d}r^*}{=} \quad \gamma v^{\frac{d+1}{d}} \int_{v_j^*} d^d\boldsymbol{r}^*\boldsymbol{r}^* = \gamma v^{\frac{d+1}{d}} \boldsymbol{F}_j^* \tag{1.45}$$

Now we can rewrite equation 1.44 by dividing each term by $v^{1/d}$:

$$\boldsymbol{r}_j^*(t+\Delta t) = 2\boldsymbol{r}_j^*(t) - \boldsymbol{r}_j^*(t-\Delta t) + \gamma v \frac{\boldsymbol{F}_j^*}{m}\Delta t^2 + O(\Delta t^4) \tag{1.46}$$

As the last term in equation 1.46, $\gamma v \boldsymbol{F}_j^*/m\Delta t^2$ should have no dimension, we conclude that the characteristic time is given by :

$$\tau_c = \sqrt{\frac{m}{\gamma v}} \tag{1.47}$$

As the definition of the force field is the same for monodisperse and polydisperse systems (see equation 1.13 and 1.41), the characteristic time remains the same for both models. We arbitrarily chose to work with $\gamma = 1000$, $m = 1$ whatever the type of the particle and at $v = 1$. In this case it implies that $\tau_c = \sqrt{1/1000} \approx 0.03$.

The term of order 4 in equation 1.44 can be neglected if $\Delta t/\tau_c \ll 1$. For all MD simulations done in this work we chose the timestep $\Delta t = 0.001$. Thus the ratio $\Delta t/\tau_c \approx 0.03$ is small enough to say that terms of order 4 are negligible and that the Verlet algorithm may describe accurately the dynamic of particles.

In Chapter 4 we will see that the reliable characteristic time Ω_0^{-1} is associated to the Einstein frequency and is represented in Figure 4.15. As $\Omega_0^{-1} \approx 0.05$, we see that the choice of our timestep is well-adapted as $\Delta t/\Omega_0^{-1} \approx 0.02$

Up to now we have defined a characteristic length $v^{1/d}$, a characteristic time τ_c, for completing the description we need to provide a characteristic potential energy for the

polydisperse Voronoi liquid. Starting for instance from equation 1.38 we can nondimensionalize the potential energy:

$$\begin{aligned} E_P &= \frac{\gamma}{2}\sum_{j=1}^{N}\int_{v_j} d^d\boldsymbol{r}(r^2 - R_j^2 + R^2) \\ &= \frac{\gamma}{2}v^{\frac{d+2}{d}}\sum_{j=1}^{N}\int_{v_j^*} d^d\boldsymbol{r}^*\left((r^*)^2 - (R_j^*)^2 + (R^*)^2\right) \\ &= \frac{\gamma}{2}v^{\frac{d+2}{d}}E_P^* \end{aligned} \tag{1.48}$$

We notice that $\gamma v^{\frac{d+2}{d}}$ has the dimension of an energy. Furthermore we recall that we consider the polydispersity as a perturbation of the monodisperse system that's why as for as the monodisperse Voronoi liquid, assuming that $\gamma = 1000$, the characteristic potential energy E_v is defined as

$$E_v = 0.001\gamma v^{\frac{d+2}{d}} \tag{1.49}$$

where the factor 10^{-3} was chosen to work with temperatures of the order of the unit.

To sum up we propose to study a reference binary mixture such as:

- The total number of particles is $N = 1000$ and $N_A = N_B = 500$
- The density is kept constant meaning $v = V/N = 1$
- The system is designed in such a way that crystallization should be avoided : $\eta = 0.37 \Rightarrow R_A = 0.6729$ and $R_B = 0.5585$
- Most of the work is done in the NVT ensemble and a wide range of temperatures is investigated via MD simulations with Nosé-Hoover thermostat.

We defined the bidisperse Voronoi liquid. In Figure 1.16 we have seen that the system seems to be able to avoid crystallization at least for a cooling rate of $dT/dt = 8\cdot 10^{-5}$. In Chapter 2, we will test slower cooling rates to check the ability of the bidisperse Voronoi liquid to avoid nucleation. Then, we will investigate its thermodynamic properties.

Chapter 2

Thermodynamic properties

Contents

When a material is cooled down, under certain conditions, it may avoid crystallization and enters into a metastable state named the supercooled regime. If one keeps on cooling, a temperature is reached below which the liquid falls out of equilibrium and becomes an amorphous solid [11]. This temperature at which this occurs, the ergodicity breaking, is defined as the glass transition temperature T_G. It is important to stress that this temperature does not correspond to a universal critical temperature of a thermodynamic phase transition. Actually T_G depends on the cooling rate and on the preparation protocol [11]. The glass transition temperature, defined as the temperature for which relaxation times are in the range of $100 - 1000$s, reflects the time limitation of experiments. Indeed below T_G the system needs a very long period of time to relax and therefore the material appears as solid on timescale accessible experimentally. However if one would have an infinite time, one could observe the flow of the material.

For a given material, its ability to form a glass depends on the probability to avoid the onset of crystallization upon cooling, i.e to avoid nucleation [47]. Whatever the technique used to manufacture the glassy material, the underlying principle is to quench sufficiently rapidly the material from its liquid state to be sure that crystallization is avoided [48–51]. However it was reported that the cooling protocol directly influences the physical properties of the resulting amorphous material [49, 50].

The influence of the cooling rate is directly visible on thermodynamics accessible from experiments, whereas the signature of the ergodicity breaking is visible on derivative of thermodynamics observables, such as the heat capacity [48, 49, 52, 53]. Thermodynamic observables are thus of huge importance to probe the neighborhood of glass transition and to get more physical insight about what happens when the material is cooled towards T_G.

In Chapter 1, we have seen that depending on the value of η (defined in equation 1.42) the system is able to avoid crystallization. This latter is indeed avoided for $\eta \in [0.25, 0.60]$. Therefore the choice of $\eta = 0.375$ has appeared reasonable to study the supercooled regime of the bidisperse Voronoi liquid. On the one hand as one should not be concerned by crystallization. On the other hand $\eta = 0.375$ should be enough small to enable to work in the limit of weak bidispersity meaning that the polydispersity might be seen as a perturbation of the monodisperse case that would thereby remain a state of reference.

In this chapter we will first check the ability of the bidisperse Voronoi liquid to avoid crystallization by performing cooling processes at very slow cooling rates. This will also gives us a rough estimation of T_G. In a second time, we will focus on the study of the thermodynamics of the system. Excess quantities with respect to the ideal gas state will be computed in a range of temperature starting from $T = 2.00$ and going to the smallest equilibrated temperature $T = 0.83$. A special interest will be given to the pressure as we will see that it is strongly negative revealing the fact that the bidisperse Voronoi liquid is always under tension. However we will see that the nature of the interactions keeps the system stable preventing cavitation phenomenon to occur.

2.1 Cooling processes

In order to test the ability of the bidisperse Voronoi liquid to avoid crystallization, we perform cooling processes at different cooling rates $k = dT/dt$. For $\eta = 0.375$ the cooling process has been done at the rate $k = 10^{-4}$ and the crystallization is prevented. Therefore the cooling rates are progressively decreased to see whether nucleation is avoided. As a matter of fact, by leaving more time to the system to relax upon cooling it might be able to rearrange and find a crystalline order.

Before giving more details on the cooling procedure, it is important here to highlight the fact that our cooling processes are performed in the NVT ensemble, whereas most of simulations focusing on cooling processes have been done in the NpT ensemble to reproduce the same protocols as in experiments performed at constant pressure. [54–57]. Most of time glass transition is experimentally tracked by dilatometry which follows

the variation of specific volume as temperature is decreased, or by differential scanning calorimetry (DSC) which measures the difference of the amount of heat between the sample analyzed and a sample of reference. This method enables to determine the enthalpy and thereafter the heat capacity at constant pressure [58, 59].

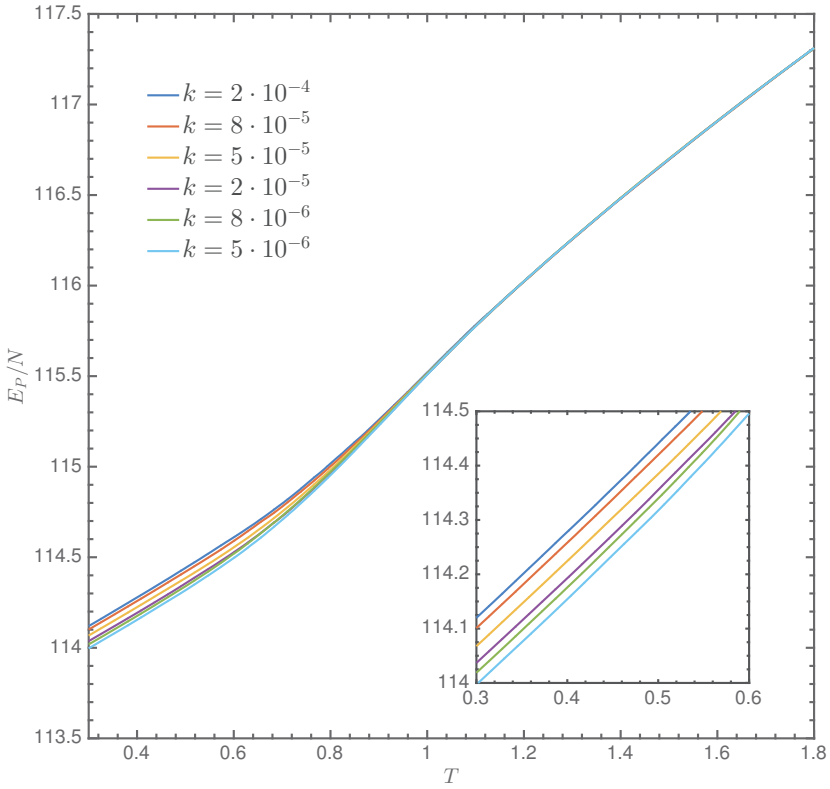

FIGURE 2.1: Evolution of the potential energy per particle E_P/N with temperature T for several cooling rates $k \in [5 \cdot 10^{-6}, 2 \cdot 10^{-4}]$. The inset corresponds to a zoom on the glass part.

In our case, we monitor the evolution of the internal energy and more precisely we focus on the evolution with temperature of the potential energy per particle E_P/N for different cooling rates $k = dT/dt \in \{5 \cdot 10^{-6}; 2 \cdot 10^{-4}\}$. The choice of the slowest cooling rate comes from "experimental" time limitation as it requires approximately one month of simulation on 16 cores (Intel(R) Xeon(R) CPU E5-2680 v4, 2.40GHz) to obtain the MD trajectory. Going to slower cooling rates would be too time consuming regarding the purpose of the simulation.

In Figure 2.1 are represented the different results for E_P/N vs. T where we have performed moving averages on E_P/N in order to suppress fluctuations.

- The main observation is the absence of discontinuity in the different curves of E_P/N vs. T meaning that crystallization is avoided even for the slower cooling rate.
- We also remark the superimposition on the same curve of all the liquid branches. This can be explained by the fact that the cooling rates investigated are slow enough to represent the liquid equilibrium. This superimposition has also been observed for the enthalpy as noticed by Vollmayr *et .al* who investigated the effect of cooling on the properties of the Kob-Andersen mixture [55].
- Below a given temperature, the glass transition temperature T_G, a change in a slope occurs and this change is related to the fact that below T_G the system falls out of equilibrium and becomes a glass. The inset of Figure 2.1 shows that the slower the cooling rate, the lower the potential energy in the glassy branch. An explanation can be found by considering the free energy landscape of the system. When it is rapidly quenched, system has no time to relax and thus to explore the free energy landscape. It can only visit shallow minima. However when more time is given to relax, the system is able to rearrange and to explore lower minima of the free energy landscape.

As mentioned above, if one searches numerically for a precise value of T_G, one should consider working in the NpT ensemble. However in our case performing NpT simulations was not possible at this stage of the work as the expression of the pressure tensor, which relies on the knowledge of the stress tensor, is rather complicated as we are going to see in the last section of this chapter.

Nevertheless in the rest of this work, we will consider thermalized configurations obtained from NVT simulations therefore having an idea about the localization of T_G, even roughly, is helpful to have, in a first phase, one temperature of reference with which one can rationalize our observations. Of course as observed, T_G depends on the cooling rate, and we need to investigate its evolution as function of the cooling rate k. To this purpose we can first notice that when $T \to T_G$ we can fit linearly both liquid and glassy branches. The intersection of the two lines gives the value of T_G. This method is illustrated in Figure 2.2 where the glass transition temperature is estimated for the slowest cooling rate.
In Table 2.1 are recorded the values of T_G for the other cooling rates where we notice that T_G decreases when the cooling rate becomes slower. Vollmayr *et .al* also observed that the glass transition temperature of the Kob-Andersen mixture decreases while decreasing the cooling rate. However they observe that below a certain value of k, the decrease is much more slower [55]. We notice the same as in the range of cooling rates investigated, the decrease is relatively weak as the value of T_G changes only by 3% when the cooling

rate is lowered by a factor 10. This means that in the range of cooling rates accessible, the glass transition temperature is weakly sensitive to the speed of the cooling processes.

Thermalized equilibrated configurations would correspond to a $k = 0$ cooling rate. Therefore it makes sense to select the value of T_G obtained with the lowest value of k and thus for the remaining work we will consider that $T_G \sim 0.66$.

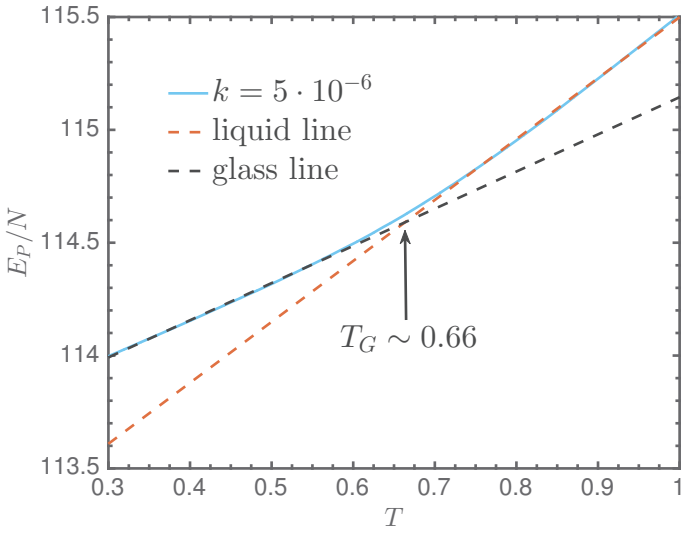

FIGURE 2.2: Illustration of the method used for finding T_G.

Cooling rate $k = dT/dt$	$2 \cdot 10^{-4}$	$8 \cdot 10^{-5}$	$5 \cdot 10^{-5}$	$2 \cdot 10^{-5}$	$8 \cdot 10^{-6}$	$5 \cdot 10^{-6}$
T_G	0.6983	0.6950	0.6866	0.6845	0.6716	0.6633

TABLE 2.1: Estimation of the glass transition temperature T_G for several cooling rates.

We have confirmed that the bidisperse Voronoi liquid is able to avoid crystallization and is consequently a good model to probe the behavior of observables near the neighborhood of glass transition. We estimated the value of the glass transition temperature to be $T_G \sim 0.66$ for the range of cooling rates accessible numerically.

In what follow we investigate the principal thermodynamic observables of the bidisperse Voronoi liquid to see how they behave upon cooling.

2.2 Thermodynamic observables

2.2.1 General expressions

For the monodisperse Voronoi liquid the scaling relation for the partition function has enabled us to express easily all the thermodynamic observables. Such a scaling relation does not exist for the bidisperse Voronoi liquid making thus more complicated to describe the system for the whole space of state variables. Before computing the thermodynamic observables, we define them and we focus on their excess part with respect to the ideal gas.

For the bidisperse Voronoi liquid it is possible to write the free energy $F_e(V, T, N, N1, R_A^2 - R_B^2)$ as the function of only 3 dimensionless intensive parameters:

$$F_e(V, T, N, N1, R_A^2 - R_B^2) = F_e(x, \eta, \alpha_A) = N v^{5/3} \gamma x \phi(x, \eta, \alpha_A) \tag{2.1}$$

where the ϕ is non-dimensional function of variables x, η and α_A defined as follow:

$$x = \frac{T}{\gamma v^{5/3}} \qquad \eta = \frac{\sqrt{R_A^2 - R_B^2}}{v^{1/3}} = \frac{\tilde{\eta}}{v^{1/3}} \qquad \alpha_A = \frac{N_A}{N} \tag{2.2}$$

Consequently by taking the first two derivatives of the excess free energy F_e it is possible to have access to the excess part of the usual thermodynamic observables.

1. **Excess entropy** S_e

   The excess entropy corresponds to the first derivative of the excess free energy with respect to temperature.

$$\begin{aligned} S_e(x, \eta, \alpha_A) &= -\frac{\partial F_e(x, \eta, \alpha_A)}{\partial T}\bigg|_{N,\eta,\alpha_A} = -\frac{\partial F_e(x, \eta, \alpha_A)}{\partial x}\frac{\partial x}{\partial T}\bigg|_{\eta,\alpha_A} \\ &= -N\left[\phi(x, \eta, \alpha_A) - x\,\frac{\partial \phi(x, \eta, \alpha_A)}{\partial x}\bigg|_{\eta,\alpha_A}\right] \end{aligned} \tag{2.3}$$

2. **Excess internal energy** U_e

   Excess internal energy is directly accessible from simulations as it is directly related to the average of the potential energy. On the other hand, to compute U_e from F_e we use the Helmholtz formula :

$$\begin{aligned} U_e(x, \eta, \alpha_A) = \langle E_P(x, \eta, \alpha_A)\rangle &= F_e(x, \eta, \alpha_A) - T\frac{\partial F_e(x, \eta, \alpha_A)}{\partial T} \\ &= -NTx\,\frac{\partial \phi(x, \eta, \alpha_A)}{\partial x}\bigg|_{\eta,\alpha_A} \end{aligned} \tag{2.4}$$

This last equation is interesting as it provides a direct link between the first derivative with respect to x of the unknown function ϕ and the numerical data $\langle E_P \rangle$. Therefore one should be able to determine from the integration of $\langle E_P \rangle$, the x dependence of ϕ.

3. **Excess pressure** P_e

The excess pressure is the first derivative of the free energy with respect to the volume:

$$P_e = -\frac{\partial F_e}{\partial V} = -\frac{\partial F_e}{\partial x}\frac{\partial x}{\partial V} - \frac{\partial F_e}{\partial \eta}\frac{\partial \eta}{\partial V} \tag{2.5}$$

$$= -\frac{5}{3}\frac{U_e}{N} + \frac{T}{3}\eta\frac{\partial \phi}{\partial \eta} \tag{2.6}$$

The second term of the R.H.S of equation 2.6 describing the excess pressure can be rewritten as function of $\tilde{\eta}$ defined in equation 2.2:

$$\eta\frac{\partial \phi}{\partial \eta} = \eta\frac{\partial \phi}{\partial \tilde{\eta}}\frac{\partial \tilde{\eta}}{\partial \eta} = \tilde{\eta}\frac{\partial \phi}{\partial \tilde{\eta}} \tag{2.7}$$

The function ϕ is given by $\phi = -\frac{1}{N}\ln\left(\frac{Z_{pot}}{V^N}\right)$ where Z_{pot} is the part of the partition function relative to the potential energy and is defined by:

$$Z_{pot}(T, \tilde{\eta}, \alpha_A) = \int d^{3N}\boldsymbol{r} \exp\left(\frac{-E_P(\boldsymbol{r}; \tilde{\eta})}{k_B T}\right) \tag{2.8}$$

Here, and more generally all through this work, $k_B = 1$.

Thus the derivative of ϕ versus $\tilde{\eta}$ is related to the average value of the derivative of potential energy versus $\tilde{\eta}$ assuming that the positions of particles are kept constant.

$$\frac{\partial \phi}{\partial \tilde{\eta}} = \frac{1}{NT}\frac{1}{Z_{pot}}\int d^{3N}\boldsymbol{r}\frac{\partial E_P(\boldsymbol{r}; \tilde{\eta})}{\partial \tilde{\eta}} \exp\left(\frac{-E_P(\boldsymbol{r}; \tilde{\eta})}{k_B T}\right) = \frac{1}{NT}\left\langle \frac{\partial E_P}{\partial \tilde{\eta}}\bigg|_{\boldsymbol{r}} \right\rangle \tag{2.9}$$

It can be shown that, when the positions of particles are kept constant, the derivative of the potential energy with respect to $\tilde{\eta}$ is expressed as:

$$\frac{\partial E_P}{\partial \tilde{\eta}}\bigg|_{\boldsymbol{r}} = \frac{2E_P^{(a)}}{\tilde{\eta}} = \gamma\tilde{\eta}\left(V_B\alpha_A - V_A\alpha_B\right) \tag{2.10}$$

Therefore equation 2.10 provides a rather simple expression for $E_P^{(a)}$:

$$E_P^{(a)} = \frac{\gamma}{2}\tilde{\eta}^2\left(V_B\alpha_A - V_A\alpha_B\right) \tag{2.11}$$

Finally using equation 2.10 in equation 2.9 and inserting the final result in equation 2.6 allows to express the excess pressure P_e, as a function of the average values of

the two components of the potential energy:

$$P_e v = -\frac{5}{3}\frac{\langle E_P^{(m)}\rangle}{N} - \frac{\langle E_P^{(a)}\rangle}{N} \tag{2.12}$$

4. **Excess chemical potential relative to A particles** $\mu_{e,A}$

   Finally the excess chemical potential is obtained as follow:

$$\begin{aligned}
\mu_{e,A}(x,\eta,\alpha_A) &= \frac{\partial F_e}{\partial N_A}\Big|_{T,V,N_2} \\
&= \frac{\partial F_e}{\partial x}\frac{\partial x}{\partial N_A}\Big|_{T,V,N_2} + \frac{\partial F_e}{\partial \eta}\frac{\partial \eta}{\partial N_A}\Big|_{T,V,N_2} + \frac{\partial F_e}{\partial \alpha_A}\frac{\partial \alpha_A}{\partial N_A}\Big|_{T,V,N_2} \\
&= \frac{5}{3}Tx\frac{\partial \phi}{\partial x} + \frac{\eta}{3}T\frac{\partial \phi}{\partial \eta} + T\phi + \alpha_B T\frac{\partial \phi}{\partial \alpha_A} \\
&= P_e v + T\phi + \alpha_B T\frac{\partial \phi}{\partial \alpha_A} \\
&= \mu_{e,B} + T\frac{\partial \phi}{\partial \alpha_A}
\end{aligned} \tag{2.13}$$

As for the monodisperse Voronoi liquid, a "zero-separation" theorem exists for the bidisperse system. For instance we can obtain a configuration of $N_A - 1$ particles of type A by superimposing two particles A on top of each other. On top of this possibility, two other situations must be take into considerations: i) superimposing two particles of type B and ii) superimposing particle of type A with a particle of type B.

(i) In the case where the two superimposed particles are of the same type:

$$\mu_{e,\alpha} = k_B T \ln(g_{aa}(r=0)) \quad \text{where } a \in \{A,B\} \tag{2.14}$$

$g_{\alpha\alpha}(r)$ is the partial pair correlation function evaluated on particles of the same type defined in Chapter 3 via equation 3.1.

(ii) When particles A and B are on top of each other, the smaller particle acts as a ghost particle and has an empty cell as the Voronoi-Laguerre tessellation is entirely determined by the larger particle. We recall that $R_A > R_B$ leading to a configuration with $N_B - 1$ particles and as a result:

$$\mu_{e,B} = k_B T \ln(g_{AB}(r=0)) \tag{2.15}$$

The two previous relationships are interesting while working at high temperature. In our case as we limit our attention to low temperatures they are of little use the repulsion between particles prevents from being in contact, i.e having cases where $g_{ab}(r=0) \neq 0$.

We derived analytical expression for the main excess thermodynamical observables. Their computation will be done in what follow but prior to that we verify that the mixing is homogeneous, i.e there is no phase separation between the small and the large particles.

2.2.2 Strong mixing

As we are working with a binary mixture the question of the demixing naturally arises. We wonder if there is a possibility that upon cooling the two components of the mixture separate to form two distinct phases at it is illustrated in the left picture of Figure 2.3. In this case, apart from the interface (grey dashed line) each phases are identical to a monodisperse configurations. Indeed particles are of the same type and Voronoi-Laguerre tessellation are equivalent to classical Voronoi tessellation where radii are equal. The energetic contribution of the interface is $\propto L^2$ and is thus negligible in the thermodynamics limit where bulk contributions are predominant.

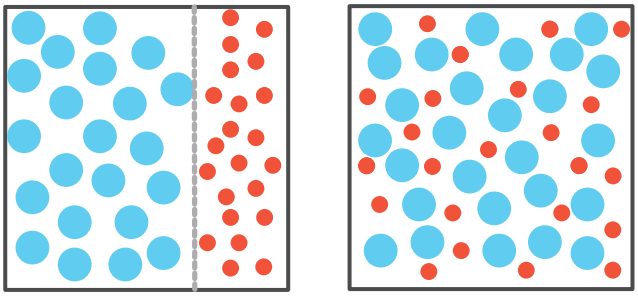

FIGURE 2.3: Left: Representation of the demixing case. The dashed grey line represents the interface between the two phases of the mixture. Right: Perfect mixing of the bidisperse Voronoi liquid.

To test whether the mixing mixture, represented in Figure 2.3 (Right), is more stable than the demixing system we evaluate the variation of excess free energy $\Delta F_e^{mix} = F_e^{mixed} - F_e^{unmixed}$ where $F_e^{unmixed}$ is F_e when $\eta = 0$ and thus corresponds to the excess free energy of the monodisperse system. Equations 2.9 and 2.10 play a central role as the polydispersity contribution is carried by the term $E_P^{(a)}$ in the potential energy. Therefore we can write:

$$\Delta F_e^{mix} = NT \int_0^\eta d\eta' \frac{\partial \phi}{\partial \eta'} = -\gamma v^{1/3} \int_0^\eta d\eta' \eta' \langle V_A \alpha_B - V_B \alpha_A \rangle = -\gamma v^{1/3} \int_0^\eta d\eta' \eta' (\langle v_A \rangle - v) \tag{2.16}$$

As the average volume of large particle is larger than the average volume per particle, i.e $\langle v_A \rangle > v$ the integral in equation 2.16 is always positive leading to $\Delta F_e^{mix} < 0$ and

as a result the mixing state is always more stable than the state where two phases may coexist. We conclude that demixing is always avoided in the bidisperse Voronoi liquid.

2.2.3 Computing thermodynamical observables

Theoretical expression of the thermodynamic observable have been derived above and in this section we compute the different excess quantities to how they behave upon cooling and see how the neighborhood of glass transition may affect them.

2.2.3.1 Excess free energy

We start logically by computing the excess free energy as it allows the determination of all the other observables. We restrict our attention to the temperature interval $T \in [0.83; 2.00]$ and we perform a thermodynamic integration.

The thermodynamics of the monodisperse Voronoi liquid has been studied previously during my master thesis and we thus consider it as the state of reference for thermodynamic integration.

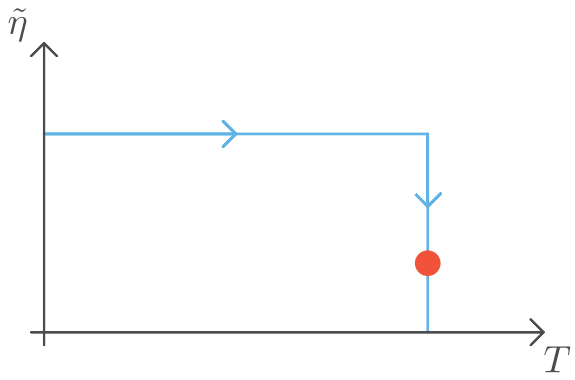

FIGURE 2.4: Schematic $\tilde{\eta}$-T diagram illustrating the path (blue line) chosen to reach the state represented by the red point.

We start from the reference point $(T = 2.00, \tilde{\eta} = 0.00)$ and we integrate, with respect to $\tilde{\eta}$, the excess free energy along the $T = 2.00$ isotherm (or equivalently $x = 0.002$) until reaching the values of $\tilde{\eta} = 0.375v^{1/3}$. To this purpose we use the thermodynamic identity:

$$F_e(x, \eta, \alpha_A) = F_e(x, \eta = 0.0) + \int_{\tilde{\eta}=0.0}^{\tilde{\eta}=0.375v^{1/3}} \frac{\partial F_e(x, \tilde{\eta}, \alpha_A)}{\partial \tilde{\eta}} d\tilde{\eta} \tag{2.17}$$

$$= F_e(x, \eta = 0.0) + \int_{\tilde{\eta}=0.0}^{\tilde{\eta}=0.375v^{1/3}} \frac{2\langle E_P^{(a)} \rangle}{\tilde{\eta}} d\tilde{\eta} \tag{2.18}$$

Once $F_e(T = 2.00, \tilde{\eta} = 0.375v^{1/3})$ is determined we can perform an integration along the "iso-$\tilde{\eta}$" path $v = 1$ from $T_0 = 2.00$ to any temperature T. To this aim we use the Helmholtz formula $U_e = -T^2\partial(F_e/T)/\partial T$ which links the excess free energy F_e to the excess internal energy U_e as $U_e = \langle E_P \rangle$ is directly accessible numerically. Therefore the excess free energy is given by the following thermodynamic relation:

$$F_e(T, \tilde{\eta}, \alpha_A) = \frac{T}{T_0}\left[F_e(T_0, \tilde{\eta} = 0.0) + \int_{\tilde{\eta}=0.0}^{\tilde{\eta}=0.375v^{1/3}} \frac{2\langle E_P^{(a)} \rangle}{\tilde{\eta}} d\tilde{\eta}\right] - T\int_{T_0}^{T} dT' \frac{U_e(T')}{T'^2} \tag{2.19}$$

The last equation shows that the computation of the excess free energy requires the knowledge of both integrals on $\tilde{\eta}$ and T. These integrals can be found numerically as the functions to integrate are directly related to the potential energy and consequently are directly accessible from MD simulations. Different fitting processes were used to describe the functions to integrate:

- The function $E_P^{(a)}/\tilde{\eta}$ is well described by a cubic polynomial expression as observed in Figure 2.5 (Upper graph) where we see that the fit represented by a straight line is in good agreement with the data points. The integration of the polynomial expression is easily performed numerically.
- Regarding U_e/T^2 we notice that $U_e(T) = \langle E_P \rangle$ can be fitted by a rational expression $U_e(T) = \dfrac{aT^2 + bT + c}{T^2 + dT + e}$ as observed in Figure 2.5 (Lower graph) where we observe that $U_e(T)/N$ is given by a solid line that corresponds to the fit and it goes well through all the data points $\langle E_P \rangle/N$. As consequence U_e/T^2 is given by the formula $\dfrac{U_e(T)}{T^2} = \dfrac{aT^2 + bT + c}{T^4 + dT^3 + eT^2}$. The integration of this rational function has been done numerically.

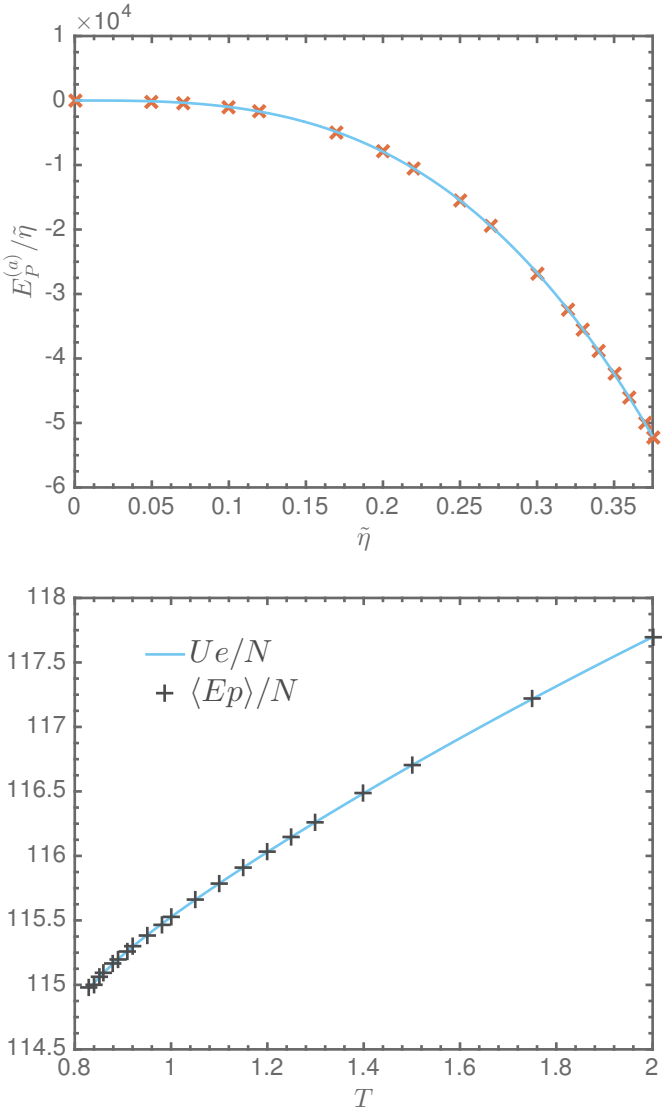

FIGURE 2.5: Upper graph: Representation of $E_p^{(a)}/\tilde{\eta}$ as a function of $\tilde{\eta}$. The red crosses are the data points coming from simulations whereas the blue solid line corresponds to a cubic polynomial fit. Lower graph: Representation of the average potential energy per particle $\langle E_P \rangle/N$ as a function of temperature (black crosses). The solid blue line represents U_e/N vs T which has been found by fitting $\langle E_P \rangle/N$ with a rational expression.

Finally we can compute 2.19 numerically and the result is presented in Figure 2.6 where we observe that F_e is increasing with temperature.

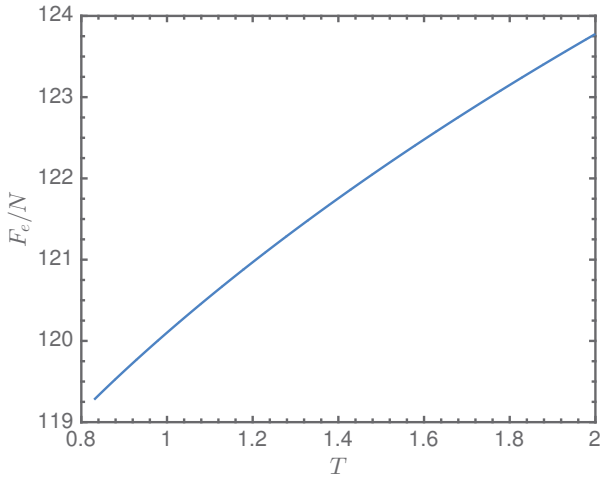

FIGURE 2.6: Excess free energy as a function of temperature T.

2.2.3.2 Excess entropy

We have determined the excess internal energy and the excess free energy, we can thus compute easily the excess entropy by considering the following thermodynamic relationship:

$$S_e(T) = \frac{U_e(T) - F_e(T)}{T} \tag{2.20}$$

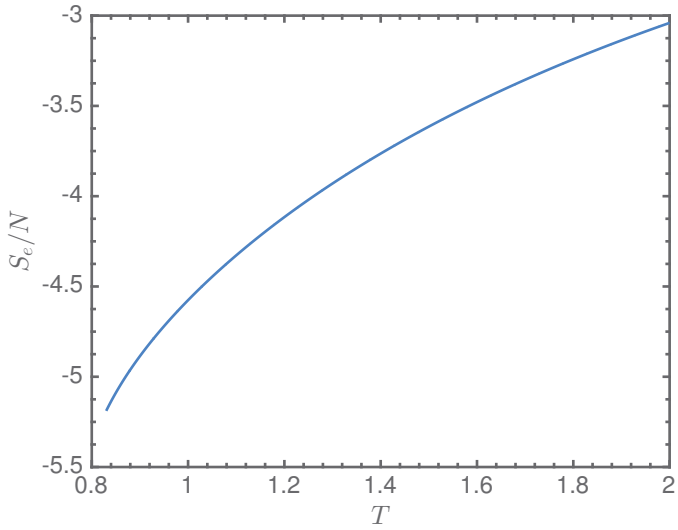

FIGURE 2.7: Excess entropy as a function of temperature T.

Result is presented in Figure 2.7 where we observe that:

- the entropy is negative. This is related to the fact that F_e is monotonously increasing as $F_e = -\partial S_e/\partial T$.
- the entropy increases with temperature. This observation allows the conclusion that c_V^e/T (where c_V^e is the excess heat capacity at constant volume) is positive.

The computation of the heat capacity at constant volume allows to test the reliability of $S_e(T)$ and as a consequence of the whole fitting procedure. $c_V^e = C_V^e/N$ can be determined from three different routes. Firstly we use the usual expression which links c_V^e to U_e via the equation:

$$c_V^e = \frac{1}{N}\frac{\partial U_e}{\partial T} \tag{2.21}$$

An alternative expression valid in the NVT ensemble enables to make a link between c_V^e and the fluctuations of the potential energy E_P:

$$c_V^e = \frac{\langle E_P^2\rangle - \langle E_P\rangle^2}{N k_B T^2} \tag{2.22}$$

Finally we can also take the first derivative of the entropy versus the temperature to determine c_V^e

$$c_V^e = \frac{T}{N}\frac{\partial S_e}{\partial T} \tag{2.23}$$

Assuming the fitting procedure describe above is valid, the three different equations should give the same results for the excess heat capacity at constant volume and it is indeed what is observed in Figure 2.8.

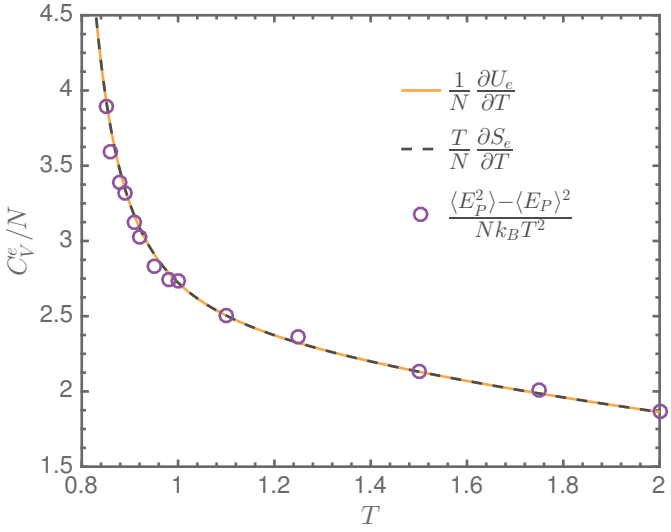

FIGURE 2.8: Excess heat capacity as a function of temperature T.

The heat capacity is increasing while the temperature is decreasing and we notice that the phenomenon starts to be more marked for temperature below $T \leq 1.10$. This increase of heat capacity at constant volume upon cooling is a typical feature of systems close to glass transition [57]. Explanation can be found by considering what happens in the potential energy landscape (whose framework will be described in details in Chapter 5). Indeed it is possible to rewrite the potential energy as the energy of the minima (inherent structure), to which is added a contribution which corresponds to the vibration around minima, $E_P = e_{IS} + e_{vib}$ [60]. The square of fluctuations of E_p, that we denote $\langle \Delta E_P^2 \rangle$ is expressed as:

$$\langle \Delta E_P^2 \rangle = \langle \Delta e_{IS}^2 \rangle + \langle \Delta e_{vib}^2 \rangle + \langle \Delta e_{IS} \Delta e_{vib} \rangle \tag{2.24}$$

If we assume that the cross-term is negligible, the heat capacity c_V^e is now given by:

$$c_v^e = c_v^{IS} + c_v^{vib} \tag{2.25}$$

When the temperature is decreased, $c_v^{vib} \to 3k_B/2$ which is the harmonic limit determined by Dulong and Petit [60]. It has been shown that when the temperature is decreased below a certain temperature that we denote T^*, a rapid decrease of $\langle e_{IS} \rangle$ is observed [61, 62]. This strong variation leads to an increase of contribution of $d\langle e_{IS} \rangle / dT$ to the c_v^{IS} and thus to c_v^e as c_v^{vib} remains approximately constant.

We will see in Chapter 4, that the temperature T^* corresponds actually to a dynamical crossover between Arrhenian and super-Arrhenian regime.

2.2.3.3 Excess pressure

The excess pressure defined in equation 2.12, is the easiest thermodynamic observable to compute as it requires only the knowledge of the two components of the potential energy which are represented in Figure 2.9. We notice that regarding the absolute values of the two components, $E_P^{(m)}$ is 10 times greater than $E_P^{(a)}$, the part relative to polydispersity. This observation is in agreement with the fact that we work in a regime of weak polydispersity. We can now focus on the excess pressure described by equation 2.12 and by quickly analyzing the order of magnitude of the different terms we find

— $5/(3v)\langle E_P^{(m)}/N \rangle \sim 5/3 \cdot 125 \sim 210$

— $(1/v)\langle E_P^{(a)}/N \rangle \sim -10$

As a result $P_e \sim -200$. The excess pressure is thus strongly negative for $T \in [0.83; 2.00]$ and this implies that the total pressure P is also negative as the kinetic term T/v is of the order of 1 and cannot counterbalance P_e in the range of temperature of interest.

Having a negative pressure means that the bidisperse Voronoi liquid (it is also the case for the monodisperse system) is always under tension. Usual liquids can experience negative pressure in a certain range of volume and in this case they are in a metastable state [63]. However when pressure is too negative, cavitation phenomenon occurs and positive pressure is recovered. Therefore the system is at thermodynamic equilibrium and a coexistence between liquid and gas phases is observed.

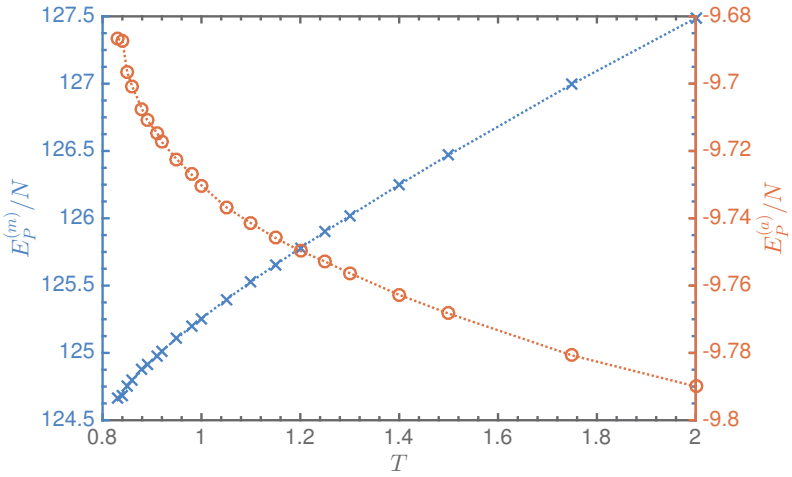

FIGURE 2.9: Representation of the two components of the total bidisperse potential energy: in blue the monodisperse part and in orange the component relative to polydispersity.

Nevertheless in the case of the Voronoi liquid, negative pressure cannot drive a cavitation instability as the nature of forces ensures the stability of the liquid, even if pressure is strongly negative. The cavitation process cannot occur due to the *nearest neighbor long-range interactions*. This formulation might sound weird at first sight especially because we mention in Chapter 1 that interactions are short-range. It is indeed the case as the definition of the forces requires only the knowledge of the first shell of neighbors. However, to better understand what happens we can do the thought experiment of generating a imaginary bubble in the bidisperse Voronoi liquid as it is depicted in Figure 2.10.

We focus on a tagged particle labelled M_j close to a fictive cavity. Most of its nearest neighbors (with a black contour in the graph) are located on the same side of the cavity as the tagged particle. Only one nearest neighbor M_k is at the opposite side of the cavity leading to a larger distance between M_j and M_k than the average distance between M_j and the other nearest neighbors. Despite this larger distance, the particle M_k is essential to build the Voronoi cell (in green in the graph). The Voronoi cell is therefore enlarged in the direction of M_k, the centroid G is located inside the fictive cavity and as a result

the force exerted on M_j tends to push the particle inside the cavity decreasing therefore its volume. Same scenarii apply on all particles close to the cavity, making this latter unstable.

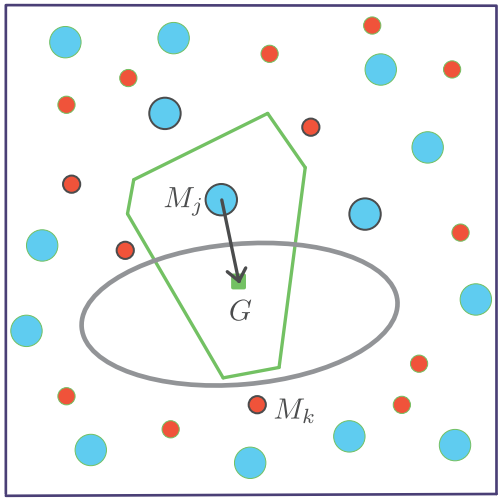

FIGURE 2.10: Schematic representation of what would happen for the bidisperse Voronoi liquid in case of cavitation.

This sketch shows thus that the force field prevents from the formation of cavitation in the Voronoi liquid and that is why the liquid can have a strong negative pressure while remaining stable.

In the next section we will compute the excess pressure first by using equation 2.12, and then by mean of the Virial theorem which links pressure to the stress tensor when wavevector $k = 0$. This latter requires the use of pair forces. We will see that we can define pseudo pair forces for the bidisperse Voronoi liquid that enable to compute correctly the stress tensor in the case of periodic boundary conditions.

2.3 A stable fluid under tension

As just mentioned there are two routes to determine the excess pressure, the first one is to use equation 2.12:

$$P_e v = -\frac{5}{3}\frac{\langle E_P^{(m)} \rangle}{N} - \frac{\langle E_P^{(a)} \rangle}{N} \tag{2.26}$$

The second route is to use the Virial theorem [40]:

$$P_e v = \frac{1}{N}\langle \sigma_{zz}^e(k=0) \rangle \tag{2.27}$$

where we have chosen on purpose to limit our attention to the excess part of the Virial relationship. σ^e_{zz} corresponds to the last diagonal components of the microscopic stress tensor and the e superscript is here to mention that we focus on the potential contribution to the stress tensor.

However in the case of system with periodic boundary conditions (P.B.C), the definition of the stress tensor could be problematic.

(i) The Clausius expression for the Virial $\sigma^e_{zz}(k=0) = \sum_i F_{i,z} r_{i,z}$ is only valid for a system without P.B.C.

(ii) In the case of P.B.C Louwerse and Baerends have shown that an explicit dependence of the box size appears in the formulation of the stress tensor [64]

$$\sigma^e_{zz}(k=0) = \sum_i F_{i,z} r_{i,z} - L_z \frac{\partial E_P}{\partial L_z} \tag{2.28}$$

(iii) Fortunately for pair forces the problem is circumvented [64] and the usual formulation for the "2-body" stress tensor applies :

$$\sigma^e_{zz}(k=0) = \sum_i \sum_{j \neq i} F_{ji,z} \tilde{r}_{ji,z} \tag{2.29}$$

where $\tilde{r}_{ji,z} = \boldsymbol{r}_{ij} \cdot \boldsymbol{e}_z - L_z[(\boldsymbol{r}_{ij} \cdot \boldsymbol{e}_z / L_z]$ the z component of $\boldsymbol{r}_{ij}$ is compliant with the minimum image convention.

(iv) However for manybody force field can be a real challenge to find a pair decomposition that satisfies equation 2.29.

For the bidisperse Voronoi liquid it can be shown that a pair decomposition satisfying equation 2.29 is given by:

$$\boldsymbol{F}_{ji} = \boldsymbol{r}_{ij} \frac{\gamma}{2 r_{ij}} \int_{S_{ij}} dS(r^2 - R_i^2 + R^2) \tag{2.30}$$

where $\boldsymbol{F}_{ji}$ is the force that particle j exerts on particle i. It is interesting to mention that this is not the only pair decomposition compliant with equation 2.29. There should be other possible formulations and for instance, we could use the general procedure developed by Admal and Tadmor that enables to find a decomposition in pair forces which always satisfied 2.29 [65].

Regarding equation 2.30 as $\boldsymbol{r}_{ij} = \boldsymbol{r}_j - \boldsymbol{r}_i$ we immediately see that the force $\boldsymbol{F}_{ji}$ points toward the j particle meaning that i is attracted by j. Consequently neighboring particles in the Voronoi liquids are attracting each other which is coherent with the picture of fluid always under tension.

Knowing the expression of $\boldsymbol{F}_{ji}$ we computed the microscopic stress tensor defined via equation 2.29 and therefore we have access to the excess pressure. Excess pressure P_e as a function of temperature T is presented in Figure 2.11 where we notice the good agreement between the two methods mentioned above.

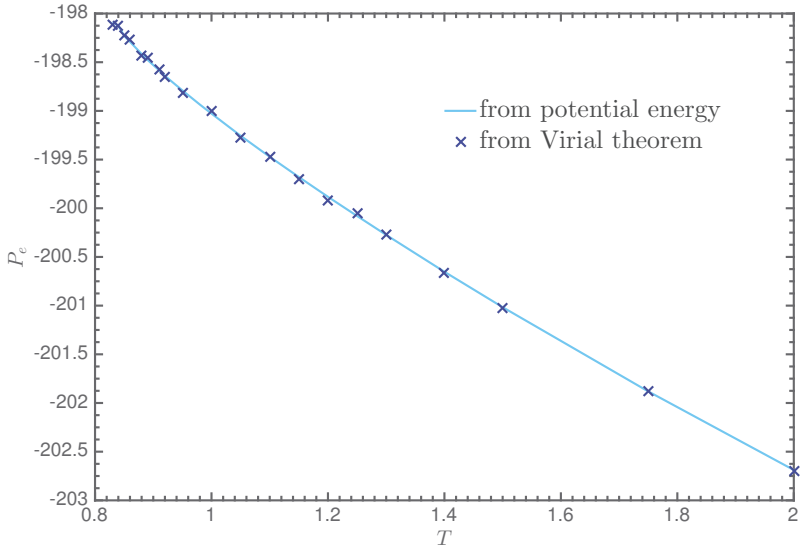

FIGURE 2.11: Excess pressure P_e as a function of temperature. The solid blue line corresponds to the computation directly made via equation 2.12 and dark blue crosses corresponds to the computation from the Virial theorem.

On the range of temperature represented, the total pressure P remains negative. Therefore we know that

$$\left.\frac{\partial P}{\partial T}\right|_V = -\left.\frac{\partial P}{\partial V}\right|_T \left.\frac{\partial V}{\partial T}\right|_P = \chi_T^{-1}\alpha \tag{2.31}$$

where χ_T is the thermal compressibility and α the volumetric coefficient of thermal expansion. As we have shown that the system is always stable, $\chi_T > 0$ and consequently we deduce that $\alpha < 0$. This means that, at constant pressure, under heating the system would contract.

In this chapter, we have observed that the bidisperse Voronoi liquid is able to avoid crystallization even at the slower cooling rates.
We were able to define and compute the main thermodynamic observables such as the excess free energy or the excess entropy. This latter will play an important role in Chapter 5 where we will focus on the potential energy landscape of the system. By looking at minima of the bidisperse Voronoi liquid (inherent structures) we will be able to compute the vibrational entropy S_{vib}. As a result, both knowledge of $S_{liq} = S_{id} + S_e$

(where S_{id} is the ideal gas contribution) and S_{vib} will enable to have access to the configurational entropy S_c which is a measure of the number of the different minima accessible by the system [8].
Finally we have observed the peculiarity that the bidisperse Voronoi liquid is a stable fluid always under tension.

In what follow, we will mainly focus on microscopic quantities and probe their sensitivity upon cooling. First we investigate the behavior of structural quantities in Chapter 3 and Chapter 4 is devoted to the analysis of dynamical observables.

Chapter 3

Structural observables

Contents

Finding the structure is a key step in the characterization of materials. Experimentally, structures of supercooled liquids or amorphous materials are generally investigated by mean of X-rays or neutron scattering. These methods allow to determine the static structure factor $S(k)$ and thereafter to find the pair correlation function $g(r)$, the static structure factor counterpart in real space [24, 66].

It is well established experimentally [67, 68] and numerically [29, 30] that structural changes upon cooling are weak for glass formers. One cannot distinguish on a qualitative level the liquid phase above the glass transition temperature T_G from the amorphous solid below T_G [8]. Liquids and amorphous solids do not show long range order contrary to crystalline structures but they rather exhibit a short range order. Therefore the macroscopic physical properties of these systems depend mostly on the short range order as they are mostly determined by the density and the strength of the forces between nearest neighbors [69].

Therefore if one wants to get more insight into the understanding of physical properties of the bidisperse Voronoi liquid, it is essential to characterize its structure. To this purpose we mainly focus in this chapter on pair correlation functions and structure factors that are accessible numerically.

3.1 Pair correlation function

For an isotropic liquid, the pair correlation function $g(r)$ measures the probability that two distinct particles are separated by distance r. The pair correlation function as defined in equation 1.21 considers that all particles in the mixture are identical. While working with a bidisperse mixture, it is interesting to introduce partial pair correlation function $g_{ab}(r)$ which would take into account the nature of species in the liquid. Partial pair correlation function $g_{ab}(r)$ where the particles are of type a or b such as $\{a, b\} \in \{A, B\}$, is defined as follow [69] :

$$
\begin{aligned}
g_{aa}(r) &= \frac{V}{N_a^2} \sum_{i=1}^{N_a} \sum_{j \neq i}^{N_a} \langle \delta(\boldsymbol{r} + \boldsymbol{r}_i - \boldsymbol{r}_j) \rangle \qquad (i,j) \in a \\
g_{ab}(r) &= \frac{V}{N_a N_b} \sum_{i=1}^{N_a} \sum_{j=1}^{N_b} \langle \delta(\boldsymbol{r} + \boldsymbol{r}_i - \boldsymbol{r}_j) \rangle \quad \text{with } i \in a, j \in b \text{ and } \forall a \neq b
\end{aligned}
\tag{3.1}
$$

The link between the total pair correlation function $g(r)$ and the three different partial pair correlation functions is provided via the following equation:

$$
g(r) = \alpha_A^2 g_{AA}(r) + (1 - \alpha_A)^2 g_{BB}(r) + 2\alpha_A(1 - \alpha_A) g_{AB}(r) \tag{3.2}
$$

where $\alpha_A = N_A/N$. This last relation can be understood by considering the expression 3.3 of the total pair correlation function $g(\boldsymbol{r})$ and by considering the different possibilities for i and j.

$$
g(\boldsymbol{r}) = \frac{V}{N^2} \sum_{i \neq j} \langle \delta(\boldsymbol{r} + \boldsymbol{r}_i - \boldsymbol{r}_j) \rangle \tag{3.3}
$$

1. We focus only on A particles, thus $i = A$ and $j = A$.
2. Only B particles are considered, $i = B$ and $j = B$.
3. Both particles A and B are considered. In this case $i = A$ and $j = B$ for instance, but as i and j are interchangeable, one can also write $i = B$ and $i = A$.

These observations imply that equation 3.3 can be rewritten as:

$$
g(r) = \frac{V}{N^2} \left[\frac{N_A^2}{V} \langle \delta(\boldsymbol{r} + \boldsymbol{r}_i^A - \boldsymbol{r}_j^A) \rangle + \frac{N_B^2}{V} \langle \delta(\boldsymbol{r} + \boldsymbol{r}_i^B - \boldsymbol{r}_j^B) \rangle + 2\frac{N_A N_B}{V} \langle \delta(\boldsymbol{r} + \boldsymbol{r}_i^A - \boldsymbol{r}_j^B) \rangle \right] \tag{3.4}
$$

From this last equation we immediately find the expression of equation 3.2.

Knowing equation 3.1, it is thus possible to compute numerically $g_{ab}(r)$ and to investigate its properties. The following paragraph is devoted to the impact of temperature on this observable.

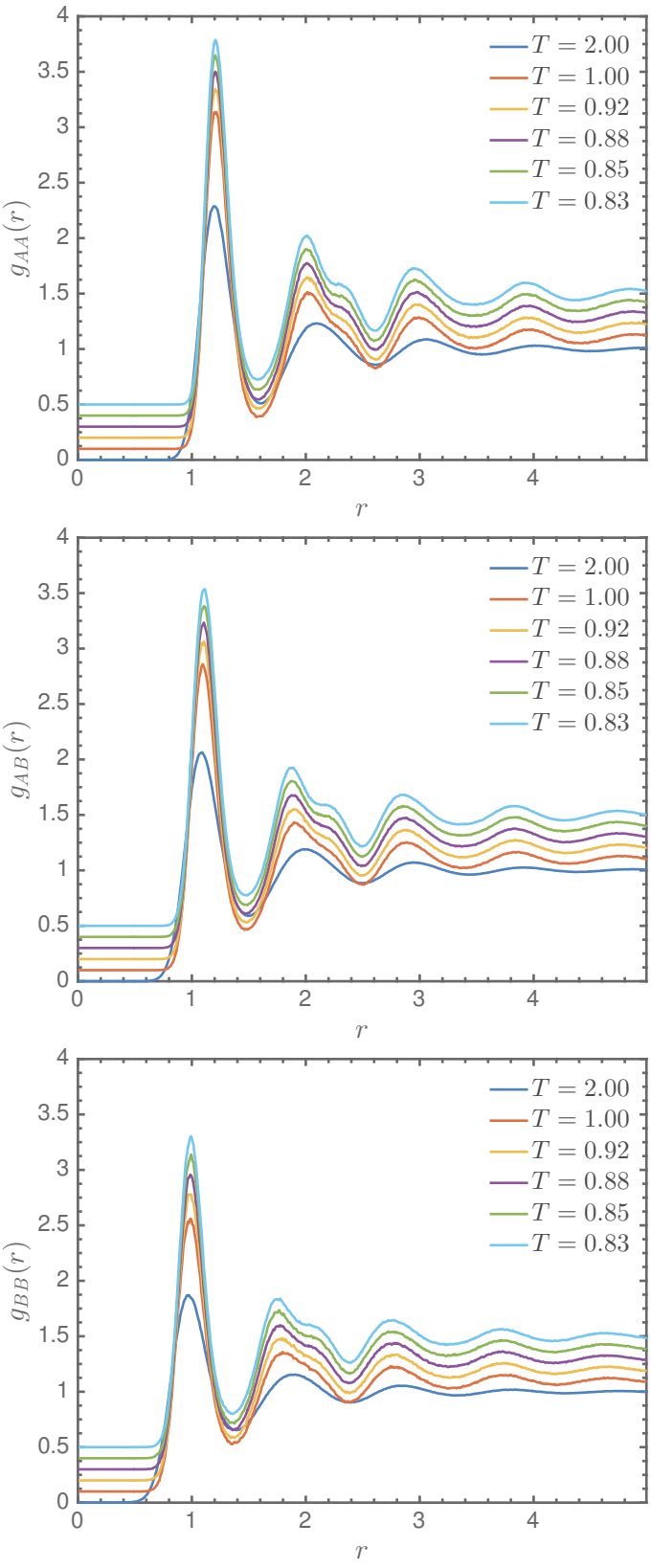

FIGURE 3.1: Partial pair correlation function $g_{ab}(r)$ evaluated for several temperature $T \in [0.83, 2.00]$ and for $N = 1000$. From top to bottom g_{AA}, g_{AB} and g_{BB}. Each curve has been shifted of 0.1 upward for clarity.

3.1.1 Evolution with temperature

The partial pair correlation functions have been computed for temperatures $T \in [0.83; 2.00]$ and $N = 1000$. They are represented in Figure 3.1 where, for T decreasing, each $g_{\alpha b}(r)$ has been shifted upward for sake of clarity.

We notice first that whatever the partial pair correlation function when the temperature is lowered, $g_{ab}(r)$ gets more and more structured as the decrease of temperature leads to the decrease of fluctuations around average values. However the system remains liquid as $g_{ab}(r) \to 1$ when $r \to \infty$. One might argue that for the lowest T, $g_{\alpha,b}(r)$ exhibits some order at $L/2$ but this order is weak and the effect of correlations would be negligible. It is interesting to notice that the partial pair correlation function computed for a larger system size of $N = 8000$ at $T = 0.85$ shows that total decorrelation is observed for $r \sim 6$ (see Figure 3.8).

Then we see in Figure 3.1 that for $T \leq 1.00$ the second peak of $g_{a,b}(r)$ starts to split. This phenomenon is related to the fact that, when the temperature is decreased locally, favored structures emerge and affect the local order upon cooling. First shell of neighbors organized into different preferred types of polyhedra and it was shown for metallic glasses that the splitting comes from the different possible connections between these preferred structures [70]. In order to characterize the local underlying structure for at least the first shell of neighbors we investigate the cosine distribution $P(R_c, \cos(\theta))$ which informs on the angular distribution of neighbors around a tagged particle.

3.1.2 Cosine distribution

The cosine distribution $P(R_c, \cos(\theta))$ informs on the angular distribution of the neighbors of a tagged particle located at the center of a sphere of radius R_c. It is computed as follows [71]. A particle i is located at the center of a sphere of radius R_c and two of its neighbors particles j and k are also inside the sphere. This means that distances from neighbors to the central particle are $r_{ij} = |\boldsymbol{r}_j - \boldsymbol{r}_i| \leq R_c$ and $r_{ik} \leq R_c$. In Figure 3.2 is represented the typical sketch of the situation in 2d. The angle θ which measures the angle formed by the triplet is defined as:

$$\cos(\theta) = \frac{\boldsymbol{r}_{ij} \cdot \boldsymbol{r}_{ik}}{r_{ij} r_{ik}} \tag{3.5}$$

From equation 3.5, one can defined the cosine distribution $P(R_c, \cos(\theta))$ which is normalized as:

$$\int_{-1}^{1} d(\cos(\theta)) P(R_c, \cos(\theta)) = 1 \tag{3.6}$$

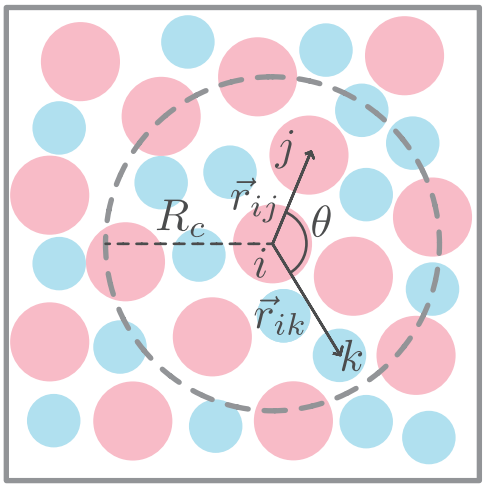

FIGURE 3.2: Illustration in 2d of the triplet of particles (i,j,k) included in the sphere of radius R_c. The angle θ is formed by bonds IJ and IK.

As the local order is prevailing at the first peak of the partial pair correlation function, the cutoff radius R_c is generally chosen to correspond to the position of the first minima of g_{ab} [71]. To investigate the structure of the neighborhood of A and B we respectively fix R_c to be equal to $R_{c,A} = 1.50$ and $R_{c,B} = 1.25$. We rename $P(R_c, \cos(\theta))$ as $P_{jik}(R_c, \cos(\theta))$ with $(i, j, k) \in \{A, B\}$. Here i is the central particle and j et k are the neighboring particles.

In Figure 3.3 is represented the cosine distribution at $T = 0.85$ when central particle is of A type (Top) and B type (Bottom). We first note the presence of three marked peaks whatever the nature of $P_{jik}(R_c, \cos(\theta))$. The values of the cosine taken at these three different maxima are converted into degrees and presented in Table 3.1.

$P_{jik}(\cos(\theta))$	θ_1 (1st peak)	θ_2 (2nd peak)	θ_3 (3rd peak)
P_{AAA}	57	108	154
P_{BAA}	55	103	152
P_{BAB}	50	98	149
P_{BBB}	57	115	169
P_{BBA}	61	118	169
P_{ABA}	65	120	169

TABLE 3.1: Values in degree of the angle θ taken for the different maxima observed from right to left in Figure 3.3.

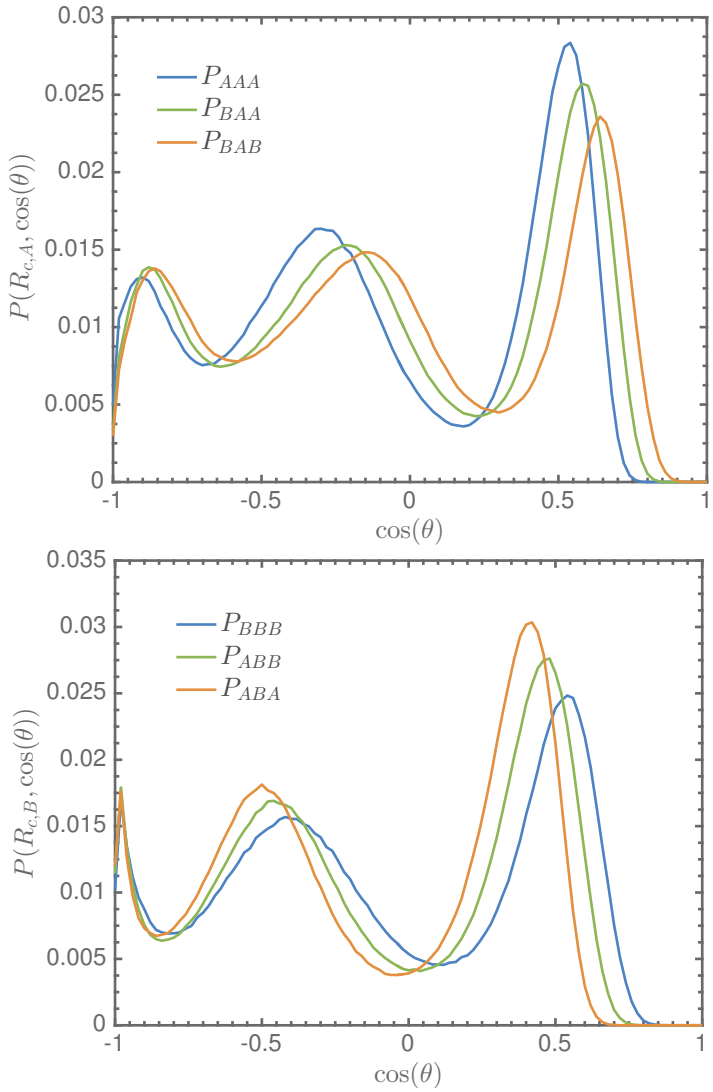

FIGURE 3.3: Representation of the cosine distribution $P_{jik}(R_c, \cos(\theta))$ when (Top) the central particle is of type A and $R_{c,A} = 1.5$ and when (Bottom) the central particle is of type B and $R_{c,B} = 1.25$. Both distributions have been computed at $T = 0.85$ for $N = 1000$.

Firstly we notice that in average, when a small particle is central, the 1st peak corresponds to an angle $\theta_1 \sim 60°$ which is very close to the typical angle $\varphi \sim 63°$ between particles in icosahedral configuration [39].

The left part in Figure 3.4 shows particles in an icosahedral environment and the right upper schema is a zoom over the upper part of the icosahedron. Each edge is of length a and the length of the central particles to each of the other particles is given by the circumradius $\approx 0.95a$. We look for the angle formed by the bond between top and central particles and the bond between the central particle and any particles belonging to the pentagon. The lower right illustration is the typical triangle formed by the particles of interest and we search for the value of φ which is given by $\varphi \approx 2\arcsin(1/(2\cdot 0.95) \approx 63°$. We can therefore also find the value of $\Gamma \approx 58.5°$ which is not so far from the values of θ_1 found when the central particle is a large one.

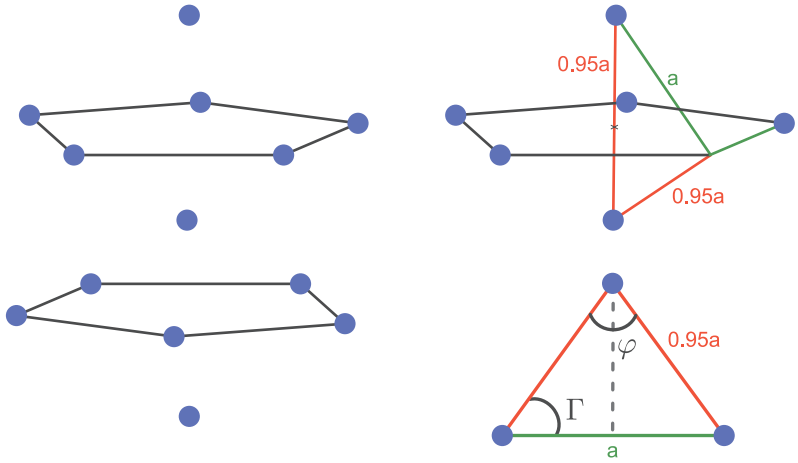

FIGURE 3.4: Left: Representation of particles in an icosahedral configuration. Right: Typical distances and angle in the icosahedron.

In both cases we observe that the second peak is in average located at $\theta_2 = 2\theta_1$. Other typical angles of the icosahedron are probed and it corresponds to cases illustrated in Figure 3.5 (Left). For the third peak there is a small difference as $\theta_3 \sim 3\theta_1$ (see Figure 3.5 (Right)) when the central particle is large whereas when the central particle is small this proportionality seems to break as we do not observe $\theta_3 \sim 180°$. As this would have suggested that three particles are aligned, it seems thus that the alignment of large particles is not favored. Therefore, the central particle of the icosahedron is likely to be a small one, and if we consider that the icosahedron has the conformation shown in Figure 3.4 (Left) thus the two particles, that do not belong to pentagons, should also be small particles to ensure the existence of angle $\sim 180°$.

When looking in deeper details to the relative position of the maxima of $P_{jAk}(R_c, \cos(\theta))$ (resp. $P_{jBk}(R_c, \cos(\theta))$) a small decrease (resp. increase) in the values of θ_1, θ_2 and θ_3 is observed when large (resp. small) particles are progressively replaced by small (resp. large) ones. This behavior can easily be explained and is illustrated in Figure 3.6 where we have arbitrary chosen to focus on configurations with a central small particle.

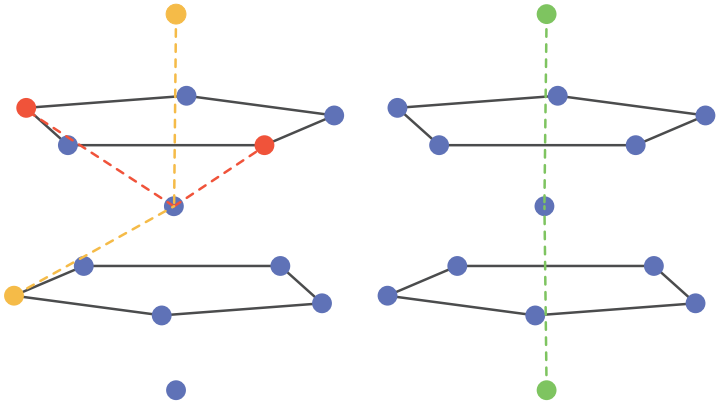

FIGURE 3.5: If $\theta_1 \approx 60$, Left: Representation of the possible ways to find angles $\sim 2\theta_1$. Particles colored in red or yellow are examples where the angle formed with the central particle $\sim 2\theta_1$. Right: Representation when $\sim 3\theta_1$, the green particles are representative of the typical angle.

The triplet under consideration is composed of the central particle i and two neighboring particles j and k. As shown in Figure 3.6 particles j and k are separated by distance d_{jk}. The distance d_{jk} is in average given by the position of the first peak r^*_{ab} of $g_{ab}(r)$. In Figure 3.8 are represented the three partial pair correlation functions for $T = 0.85$ and $N = 8000$. The detailed analysis of the position of r^*ab is postponed to next subsection. Nonetheless we observe that $r^*_{BB} < r^*_{AB} < r^*_{AA}$. Thus the distance between j and k is increasing when small particles are substituted for larger ones and as a result the angle θ_{jik} is also increasing. A similar argument (by considering a large particle at center of the triplet) would lead to a decrease of angle θ_{jik} . While the previous reasoning enables to explain the relative positions of the maxima of $P_{jik}(R_c, \cos(\theta))$ it is also interesting to notice that θ_3 remained unchanged when a small particle is at the center of the triplet.

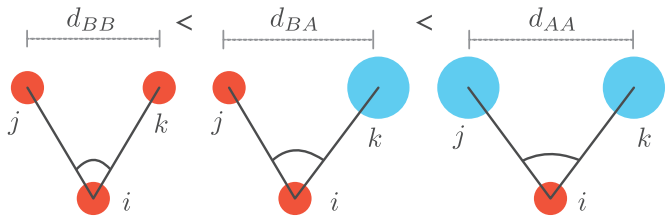

FIGURE 3.6: Representation of the three types of configurations that can be found when the central particle i is small.

In Figure 3.7 the evolution of $P_{AAA}(R_c, \cos(\theta))$ and $P_{BBB}(R_c, \cos(\theta))$ are represented upon cooling. For both distributions we observe for $T \leq 1.00$ that the emergence of marked peaks is related to the decrease of fluctuations around the average position also observed for partial pair correlation functions. In average particles tend to locate on preferred position relatively to a tagged central particle and this preferred position is characterized by the angular values given in Table 3.1.

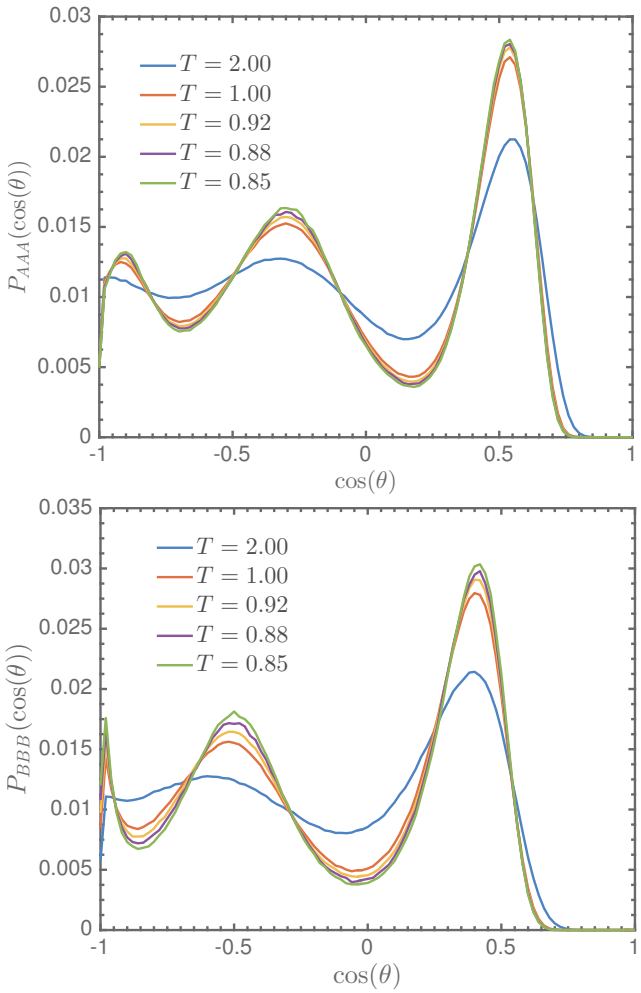

FIGURE 3.7: Evolution of $P_{AAA}(R_c, \cos(\theta))$ (Upper graph) and $P_{BBB}(R_c, \cos(\theta))$ (Lower graph) upon cooling.

The analyze of the neighborhood of a central particle brings informations on the local structures that emerge and reveal the presence of icosahedra where center might be occupied by small particles. In Chapter 6 when we will investigate the locally favored structures, we will observe that the bidisperse Voronoi liquid has a strong tendency to favor icosahedra-like structures. Moreover an analysis of the local structures by mean of Voronoi tessellation will reveal that small particles are at the center of icosahedra.

We have characterized geometrical properties of the first shell of neighbors. In the next paragraph we will focus on the extrema of the partial pair correlation functions and we will see that, in the limit of weak polydispersity, it is possible to define analytically the position of these extrema.

3.1.3 Relative position of the first peaks of $g_{ab}(r)$

3.1.3.1 Splitting of $g_{AA}(r)$ and $g_{BB}(r)$

The position r^* of the first peak of the pair correlation function informs on the average position of nearest neighbors. If we distinguish the different species by focusing on partial pair correlation functions, it is possible to determine r^*_{ab} and consequently the relative position of the first peaks for the two species. In Figure 3.8 are represented the three partial pair correlation functions.

At first sight, one could be surprised by the relative position of r^*_{AA} and r^*_{BB} as one could have imagined that first peaks associated to identical particle interactions would have superimposed. Because with Voronoi-Laguerre tessellation the position of the plane between two identical particles remains median. Therefore one may wonder why the first peaks of $g_{AA}(r)$ and $g_{BB}(r)$ split as observed in Figure 3.8.

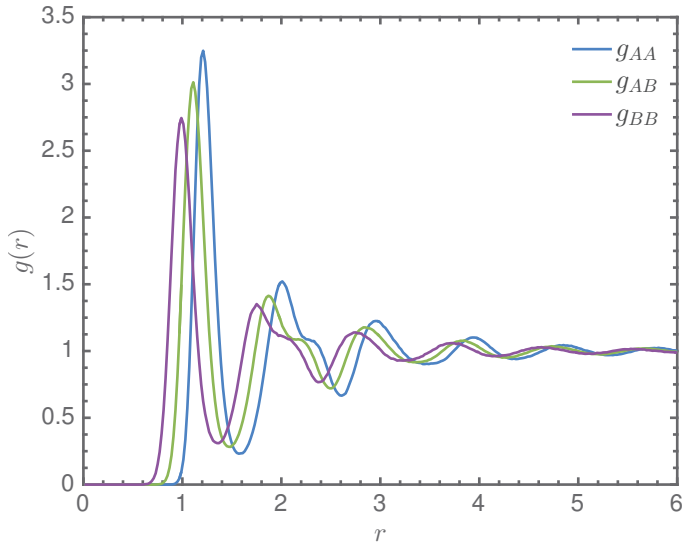

FIGURE 3.8: Representation of the relative position of the three partial pair correlation functions for $T = 0.85$ and $N = 8000$.

The explanation comes from the equilibration of internal pressure in the Voronoi cell and the splitting can easily be explained by a one dimensional reasoning as represented in Figure 3.9.

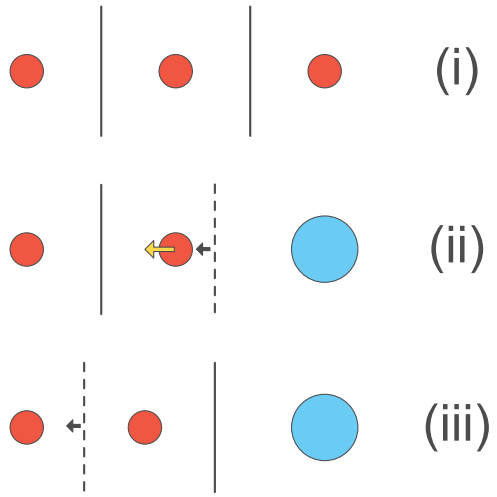

FIGURE 3.9: Explanation of the equilibration of pressure inside a Voronoi cell.

(i) Assuming that we start from a monodisperse configuration with only small particles, the plane between identical particles is median.

(ii) To generate a bidisperse configuration the radius of the right small particles is enlarged. Now as there is a size disparity between central and right particles, the Voronoi-Laguerre tessellation acts by shifting the plane between the particles to the left. As a consequence the Voronoi cell associated to the central particle is now smaller and the central particle does not coincide with its centroid anymore. A force is exerted on it and points toward the new position of the centroid of the central cell.

(iii) As a result the neutral position of the central particle shifts to the left, which induces a smaller average inter-particle distances between small particles. Therefore the plane between the two small particles is also shifted to the left to remain median.

A similar argument on big particles leads to the fact that big particles are farther apart in the bidisperse Voronoi liquid than in the monodisperse one. This simple argument in one dimension gives good indication to understand the relative position at first peak of g_{AA} and g_{BB}. In what follow we will show that in the limit of weak polydispersity, the relative position of first peaks can be computed.

3.1.3.2 Computation of first peak position for weak polydispersity

In Chapter 1 we explained that as $\eta \to 0$, $R_A \sim R_B$ and as a consequence we recover the monodisperse system. In what follow we propose to see how the polydispersity

affects the positions r^*_{ab} of the first peaks of the partial pair correlation functions. To this purpose we chose to work with values of η that avoid crystallization but are small enough to consider the system as weakly polydisperse.

When looking at the position of r^*_{ab} the position of the first maxima of $g_{ab}(r)$ in Figure 3.8, we observe that r^*_{AB} seems to be located at half the distance between r^*_{AA} and r^*_{BB}. More generally we are going to demonstrate that whatever the nature of the mixture:

$$r^*_{AB} = \frac{1}{2}(r^*_{AA} + r^*_{BB}) \tag{3.7}$$

When $\eta \to 0$, r^*_{ab} with $(a,b) \in \{A,B\}$ tends to the position r^*_0 of the first peak of the pair correlation function g_0 evaluated for the monodisperse liquid. As a consequence if we assume a small value of η we can write the position r^*_{ab} as $r^*_{ab} = r^*_0 + \delta r^*_{ab}$ where δr^*_{ab} is the deviation from the monodisperse case of the position of first peaks. The partial pair correlation functions can be expressed as $g_{ab}(r) = g_0(r) + \delta g_{ab}(r)$ where $\delta g_{ab}(r)$ also corresponds to the deviation from the monodisperse system.

We are interested in the values of δr^*_{ab} which measure for each interactions the distance to the monodisperse position r^*_0. At first peak, and this is also true for the other extrema, the first derivative of $g_{ab}(r)$ is zero and therefore we can write:

$$\begin{aligned} g'_{ab}(r^*_{ab}) = 0 &= g'_{ab}(r^*_0 + \delta r^*_{ab}) \\ &= g'_{ab}(r^*_0) + \delta r^*_{ab} g''_{ab}(r^*_0) \\ &= g'_0(r^*_0) + \delta g'_{ab}(r^*_0) + \delta r^*_{ab} g''_0(r^*_0) + \delta r^*_{ab} \delta g''_{ab}(r^*_0) \end{aligned} \tag{3.8}$$

By keeping terms of the lowest order and by noticing that by definition $g'_0(r^*_0) = 0$ and $g'_{ab}(r^*_{ab}) = 0$, equation 3.8 enables to find an expression for δr^*_{ab}, that is:

$$\delta r^*_{ab} = -\frac{\delta g'_{ab}(r^*_0)}{g''_0(r^*_0)} \tag{3.9}$$

We look now for an expression of $\delta g_{ab}(r) = g_{ab}(r) - g_0(r)$ as it would enable to express analytically the equation 3.9.

We start by evaluating $g_{ab}(r)$ which is defined as follow:

$$g_{ab}(r) = \frac{V}{N_\alpha N_\beta} \sum_{i=1}^{N_\alpha} \sum_{i=1}^{N_\beta} \frac{1}{Z_N} \int d\boldsymbol{r}_i \int d\boldsymbol{r}_j \delta(\boldsymbol{r} - \boldsymbol{r}_{ij}) \int d^{N-2}\boldsymbol{r}_k \exp(-\beta E_P(\boldsymbol{r}_1, \cdots, \boldsymbol{r}_N; \eta)) \tag{3.10}$$

with the partition function $Z_N = \int d^N \boldsymbol{r} \exp(-\beta E_P(\boldsymbol{r}_1, \cdots, \boldsymbol{r}_N; \eta))$. As η is considered as small, an expansion of the potential energy can be performed leading to :

$$E_P(\boldsymbol{r}_1, \cdots, \boldsymbol{r}_N; \eta) = E_P(\boldsymbol{r}_1, \cdots, \boldsymbol{r}_N) + \eta \frac{\partial E_P(\eta = 0)}{\partial \eta} \tag{3.11}$$

The partition function can also be expanded $Z_N = Z_0 \left(1 - \beta\eta \left\langle \frac{\partial E_P(\eta = 0)}{\partial \eta} \right\rangle_0\right)$ where the subscript "0" means that the average is performed on thermally equilibrated monodisperse configurations. Therefore by using the last two previous results in equation 3.10, $g_{ab}(r)$ becomes when $\eta \to 0$:

$$g_{ab}(r) = V\langle\delta(\boldsymbol{r} - \boldsymbol{r}_{ij})\rangle_0 + V\beta\eta \left\langle \delta(\boldsymbol{r} - \boldsymbol{r}_{ij}) \left(\left\langle \frac{\partial E_P}{\partial \eta} \right\rangle_0 - \frac{\partial E_P(\eta = 0)}{\partial \eta} \right) \right\rangle_0 \tag{3.12}$$

with the precision that particles i if of type a and particle j is of type b.

In Chapter 2, we have seen that for the potential energy only the component relative to the polydispersity 1.40 depends on η. As a consequence by rewriting equation 2.11 we find that $\frac{\partial E_P}{\partial \eta} = \gamma v^{2/3} \eta (V\alpha_A - V_A)$ and consequently $g_{ab}(r)$ becomes:

$$g_{ab}(r) = V\langle\delta(\boldsymbol{r} - \boldsymbol{r}_{ij})\rangle_0 + \gamma v^{2/3} V\beta\eta^2 \left\langle \delta(\boldsymbol{r} - \boldsymbol{r}_{ij}) \left(V_A - \langle V_A\rangle_0\right)\right\rangle_0 \quad \text{with } i \in a \text{ and j} \in \text{b} \tag{3.13}$$

Similarly we can express the pair correlation function for the monodisperse system and we have $g_0(r) = V \left\langle \delta(\boldsymbol{r} - \boldsymbol{r}_{ij})\right\rangle_0$. Combining with equation 3.13 $\delta g_{ab}(r)$ is of the form :

$$\delta g_{ab}(r) = \gamma v^{2/3} V\beta\eta^2 \left\langle \delta(\boldsymbol{r} - \boldsymbol{r}_{ij}) \left(V_A - \langle V_A\rangle_0\right)\right\rangle_0 \text{with } i \in a \text{ and j} \in \text{b} \tag{3.14}$$

At first sight the last formulation seems strange as it refers to type A particles in a monodisperse average. We propose to rewrite equation 3.14 by removing the explicit dependence on the particle type in the term relative to the average. There are 3 different cases.

• **1st case** $i \in A$, $j \in A$

The average term in equation 3.14 can be rewritten as:

$$\left\langle \delta(\boldsymbol{r} - \boldsymbol{r}_{ij}) \left(V_A - \langle V_A\rangle_0\right)\right\rangle_0 = 2 \left\langle \delta(\boldsymbol{r} - \boldsymbol{r}_{ij})[v_i - v]\right\rangle_0 + (N_A - 2) \left\langle \delta(\boldsymbol{r} - \boldsymbol{r}_{ij})[v_k - v]\right\rangle_0 \tag{3.15}$$

where $k \in A$.

We notice that $\langle \delta(\boldsymbol{r} - \boldsymbol{r}_{ij}) [V - \langle V \rangle_0] \rangle_0 = 0$ and $V = v_i + v_j + \sum_{k(\neq(i,j)} v_k$, where k represents now a particle without label A or B. This is possible as we perform the average on a thermally equilibrated monodisperse configuration. Therefore we deduce that the second average of the R.H.S is given by:

$$\langle \delta(\boldsymbol{r} - \boldsymbol{r}_{ij})[v_k - v] \rangle_0 = -\frac{2}{N-2} \langle \delta(\boldsymbol{r} - \boldsymbol{r}_{ij})[v_i - v] \rangle_0 \tag{3.16}$$

We can replace by equation 3.16 in equation 3.15 and by finally taking the thermodynamic limit, we find:

$$\langle \delta(\boldsymbol{r} - \boldsymbol{r}_{ij}) (V_A - \langle V_A \rangle_0) \rangle_0 = 2\alpha_B \langle \delta(\boldsymbol{r} - \boldsymbol{r}_{ij})[v_i - v] \rangle_0 \tag{3.17}$$

Thus we can express δg_{AA} as

$$\delta g_{AA}(r) = 2\alpha_B V \gamma v^{2/3} \beta \eta^2 \langle \delta(\boldsymbol{r} - \boldsymbol{r}_{ij})[v_i - v] \rangle_0 \tag{3.18}$$

• **2nd case** $i \in B$, $j \in B$

This approach is similar to the previous one. Equation 3.14 becomes in the case where both i and j are particles B:

$$\delta g_{BB}(r) = -\gamma v^{2/3} V \beta \eta^2 \langle \delta(\boldsymbol{r} - \boldsymbol{r}_{ij}) (V_B - \langle V_B \rangle_0) \rangle_0 \tag{3.19}$$

Using the same procedure as previously, the average in the R.H.S can be expressed as:

$$\langle \delta(\boldsymbol{r} - \boldsymbol{r}_{ij}) (V_B - \langle V_B \rangle_0) \rangle_0 = 2\alpha_A \langle \delta(\boldsymbol{r} - \boldsymbol{r}_{ij})[v_i - v] \rangle_0 \tag{3.20}$$

Consequently $g_{BB}(r)$ is given by:

$$\delta g_{BB}(r) = -2\alpha_A V \gamma v^{2/3} \beta \eta^2 \langle \delta(\boldsymbol{r} - \boldsymbol{r}_{ij})[v_i - v] \rangle_0 \tag{3.21}$$

• **3rd case** $i \in A$, $j \in B$

When $i \in A$, $j \in B$, equation 3.14 can be expressed as:

$$\delta g_{ab}(r) = \gamma v^{2/3} V \beta \eta^2 \langle \delta(\boldsymbol{r} - \boldsymbol{r}_{ij}) [\alpha_B (V_A - \langle V_A \rangle_0) - \alpha_A (V_B - \langle V_B \rangle_0)] \rangle_0 \tag{3.22}$$

The last equation 3.22 becomes:

$$\begin{aligned}&\langle\delta(\boldsymbol{r}-\boldsymbol{r}_{ij})\left[\alpha_B\left(V_A-\langle V_A\rangle_0\right)-\alpha_A\left(V_B-\langle V_B\rangle_0\right)\right]\rangle_0\\&=\langle\delta(\boldsymbol{r}-\boldsymbol{r}_{ij})[v_i-v](\alpha_B-\alpha_A)\rangle_0+2\left\langle\delta(\boldsymbol{r}-\boldsymbol{r}_{ij})[v_i-v]\left[\alpha_B\frac{N_A-1}{N-2}-\alpha_A\frac{N_B-1}{N-2}\right]\right\rangle_0\end{aligned} \tag{3.23}$$

We immediately see that the second term of the R.H.S vanishes in the thermodynamic limit as it is $\propto(\alpha_B\alpha_A-\alpha_A\alpha_B)$. Thus we obtain:

$$\delta g_{AB}(r)=(\alpha_B-\alpha_A)V\gamma v^{2/3}\beta\eta^2\left\langle\delta(\boldsymbol{r}-\boldsymbol{r}_{ij})[v_i-v]\right\rangle_0 \tag{3.24}$$

By using equation 3.9 and the fact that $g_0''(r_0^*)<0$ at the maximum, we have access to the expression of δr_{ab}^*:

$$\delta r_{AA}^*=\frac{2\gamma v^{2/3}\beta\eta^2 Q_g}{|g_0''(r_0^*)|}\alpha_B \tag{3.25}$$

where Q_g correspond to the following derivative:

$$Q_g=\frac{d}{dr}\left[\sum_{j/j\neq i}\left\langle\delta(\boldsymbol{r}-\boldsymbol{r}_{ij})[v_i-v]\right\rangle_0\right]_{r=r^*} \tag{3.26}$$

Similarly we can express δr_{BB}^* and δr_{AB}^*:

$$\delta r_{BB}^*=-\frac{2\gamma v^{2/3}\beta\eta^2 Q_g}{|g_0''(r_0^*)|}\alpha_A \tag{3.27}$$

$$\delta r_{AB}^*=\frac{2\gamma v^{2/3}\beta\eta^2 Q_g}{|g_0''(r_0^*)|}\frac{\alpha_B-\alpha_A}{2} \tag{3.28}$$

We define $\Delta_g=2\gamma v^{2/3}\beta\eta^2 Q_g/|2g_0''(r_0^*)|$ and we immediately see that:

- $\delta r_{AA}^*-\delta r_{AB}^*=\delta r_{AB}^*-\delta r_{BB}^*=\Delta_g$.
- Δ_g is independent of the nature of the composition, i.e independent of α_A. The two previous points are clearly visible in Table 3.2 where we have recorded the position of the two first peaks of g_{ab}. We see that $\Delta_g=0.1$ whatever the mixture.
- As we mentioned above, these results are not only valid for the first peaks but applied for all extrema as it is for instance shown in Figure 3.11 where we have zoomed on the two first maxima and minima of the three partial pair correlation functions. We observe furthermore that while increasing the number of large (resp. small) particles r_{AA}^* (resp. r_{BB}^*) is shifted toward the left (resp. the right) and is closer from $r_0^*\sim 1.1$.

- As $g_0'' < 0$ we have assumed for the moment that when looking at maxima $Q_g > 0$ as δr^*_{AA} (resp. δr^*_{BB}) should be shifted in the positive (resp. negative) direction with respect to the position r_0^* of the monodisperse system. On the opposite, we expect that $Q_g < 0$ for the minima as $g_0'' > 0$. To check this assumption we have computed $\langle \delta(\boldsymbol{r} - \boldsymbol{r}_{ij})\,(v_i - v)\rangle_0$ to see the variation of the function. It is represented in Figure 3.10 and we notice that indeed near maxima of $g_0(r)$ the function is increasing meaning that the derivative is positive whereas near mimima the derivative is negative.

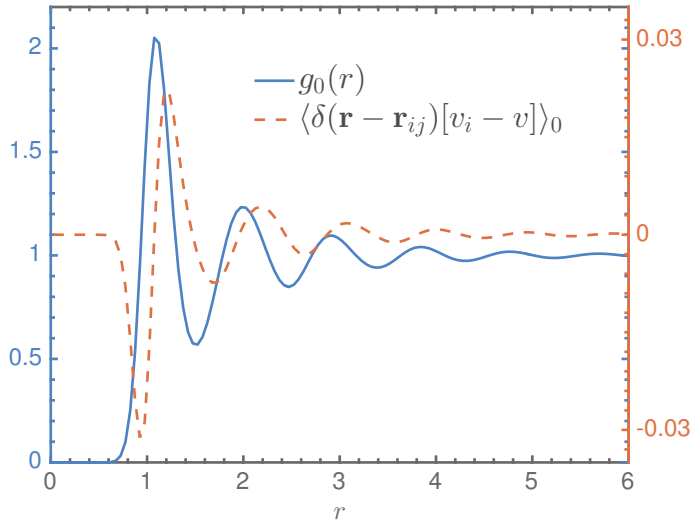

FIGURE 3.10: Representations of the monodisperse pair correlation function $g_0(k)$ in blue and $\langle \delta(\boldsymbol{r} - \boldsymbol{r}_{ij})\,(v_i - v)\rangle_0$ in dashed red line for $T = 2.00$ and $N = 8000$.

Mixture $A:B$	$r^*_{AA,1st}$	$r^*_{AB,1st}$	$r^*_{BB,1st}$	$r^*_{AA,2nd}$	$r^*_{AB,2nd}$	$r^*_{BB,2nd}$
20 : 80	1.275	1.175	1.075	2.125	2.025	1.925
30 : 70	1.225	1.125	1.025	2.125	2.025	1.925
40 : 60	1.205	1.105	0.995	2.105	2.005	1.905
50 : 50	1.175	1.075	0.975	2.075	1.975	1.875
60 : 40	1.145	1.045	0.945	2.065	1.965	1.865
70 : 30	1.125	1.025	0.925	2.025	1.925	1.825
80 : 20	1.125	1.025	0.925	2.025	1.925	1.825

TABLE 3.2: Values of the position of the first and second peaks of the partial pair correlation functions for different compositions $A:B$ of the mixture.

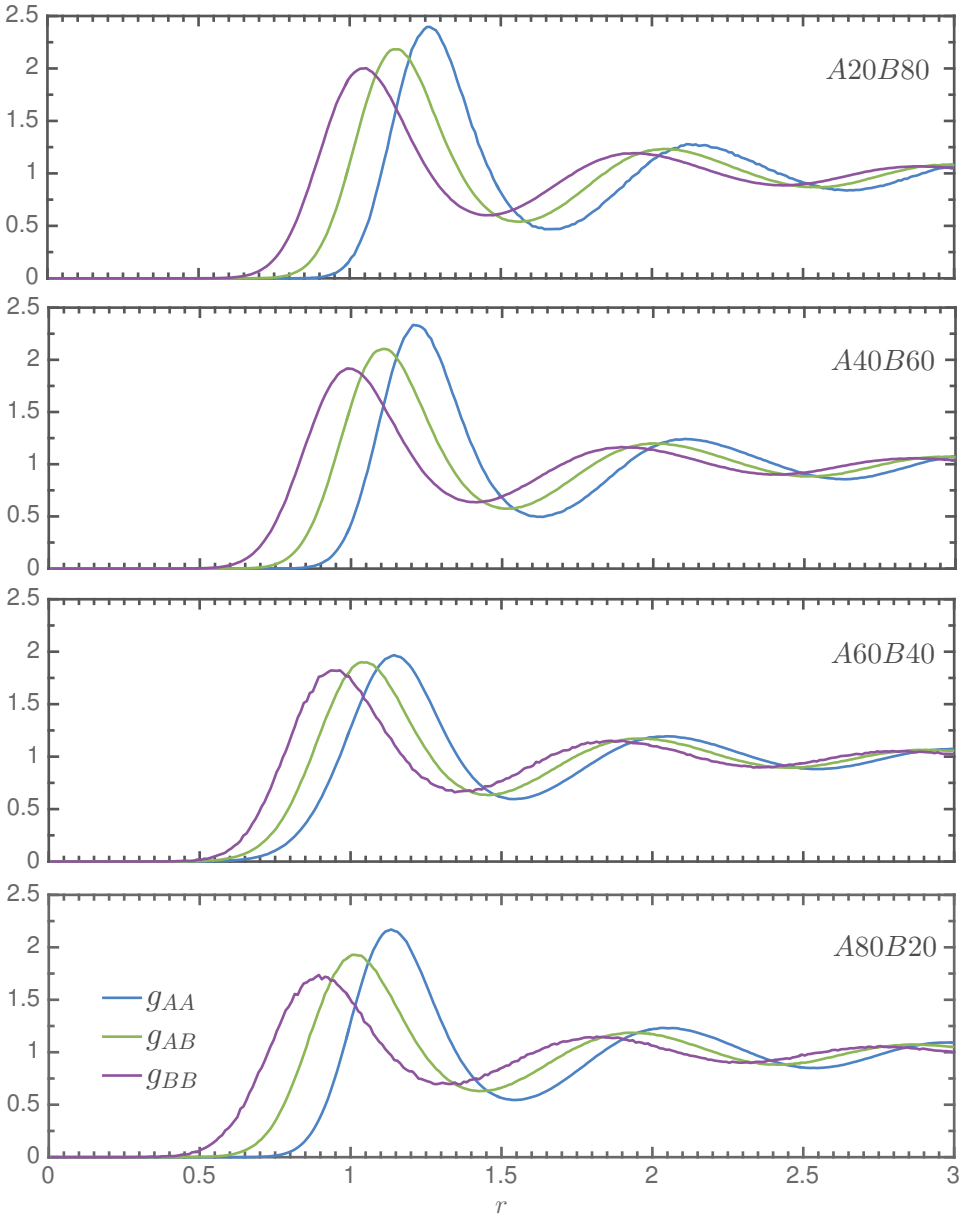

FIGURE 3.11: Representation of the relative positions of the two first peaks of the three partial pair correlation functions for $T = 2.00$, $N = 1000$ and for different compositions $A : B$ of the mixture.

We have characterized the properties of the pair correlation function, we propose in the following to investigate the properties of its Fourier transform, namely the structure factor.

3.2 Static structure factor

As for the monodisperse system, it is useful to compute the static structure factor $S(k)$ and the related partial structure factors $S_{ab}(k)$ defined by Ashcroft and Langreth [72] formalism by :

$$S_{ab}(k) = \frac{1}{\sqrt{N_\alpha N_\beta}} \langle \rho_\alpha(-\boldsymbol{k}) \rho_\beta(\boldsymbol{k}) \rangle \quad \text{where} \quad \rho_\beta(\boldsymbol{k}) = \sum_{j=1}^{N_\beta} \exp(-i\boldsymbol{k} \cdot \boldsymbol{r}_j) \tag{3.29}$$

The link between total static structure factor $S(k)$ and partial structure factors is provided by the following equation:

$$S(k) = \alpha_A S_{AA}(k) + (1 - \alpha_A) S_{BB}(k) + 2\sqrt{\alpha_A(1 - \alpha_A)} S_{AB}(k) \tag{3.30}$$

The partial structure factors $S_{ab}(k)$ can also be expressed as the Fourier transform of the partial pair correlation functions $g_{ab}(r)$:

$$S_{ab}(k) = \delta_{ab} + 4\pi \frac{N}{V} \sqrt{\alpha_A(1 - \alpha_A)} \int_0^\infty dr r^2 \frac{\sin(kr)}{kr} (g_{ab}(r) - 1) \tag{3.31}$$

where the large wavevector limit, i.e $k \to \infty$ of S_{ab} is given by

$$\lim_{k \to \infty} S_{ab}(k) = \delta_{ab} \tag{3.32}$$

3.2.1 Evolution with temperature

As for the partial pair correlation functions we observed in Figure 3.12 on the first hand, that when the temperature is lowered, due to the decrease of fluctuations, partial structure factors are more and more structured. On the other hand, there is also for each $S_{ab}(k)$ a marked shouldering of the second peak.

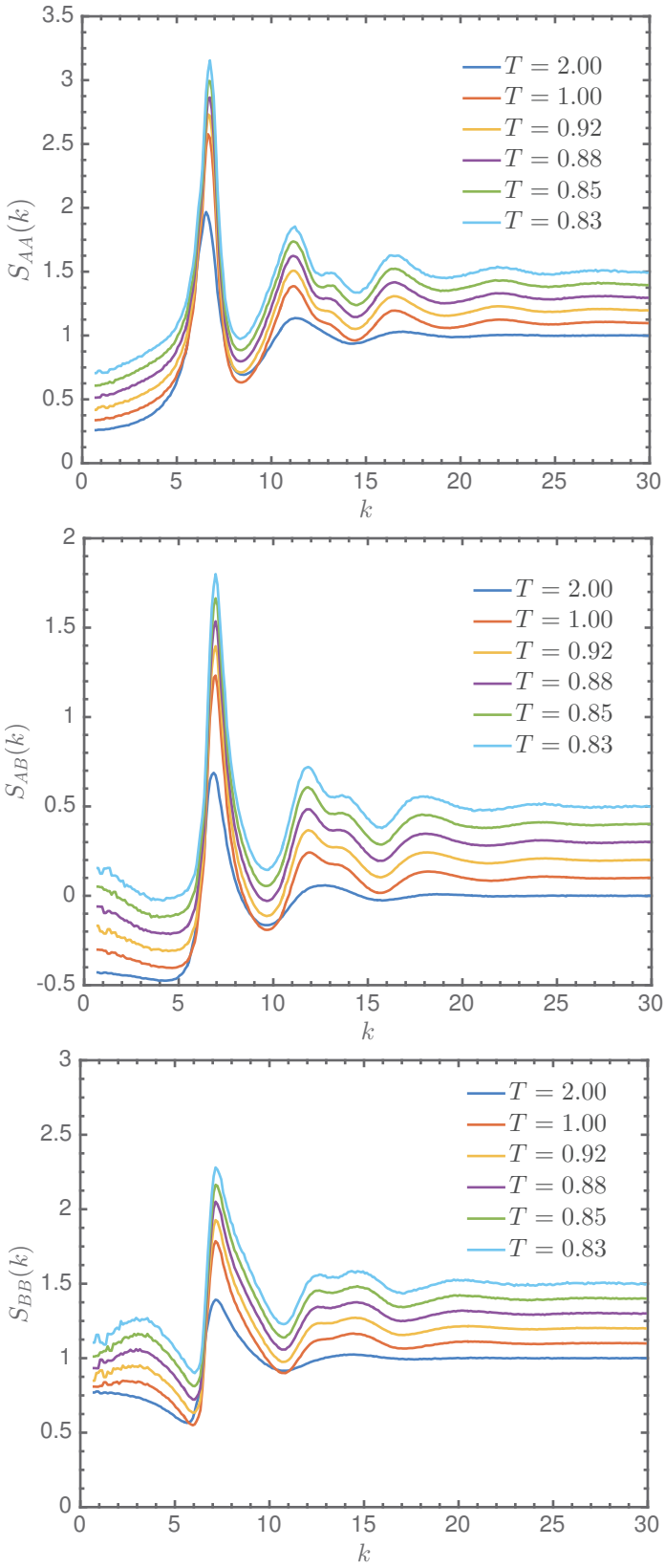

FIGURE 3.12: Partial pair structure factors $S_{ab}(r)$ evaluated for several temperatures $T \in [0.83, 2.00]$ and for $N = 1000$. From top to bottom S_{AA}, S_{AB} and S_{BB}. Each curve has been shifted of 0.1 upward for clarity.

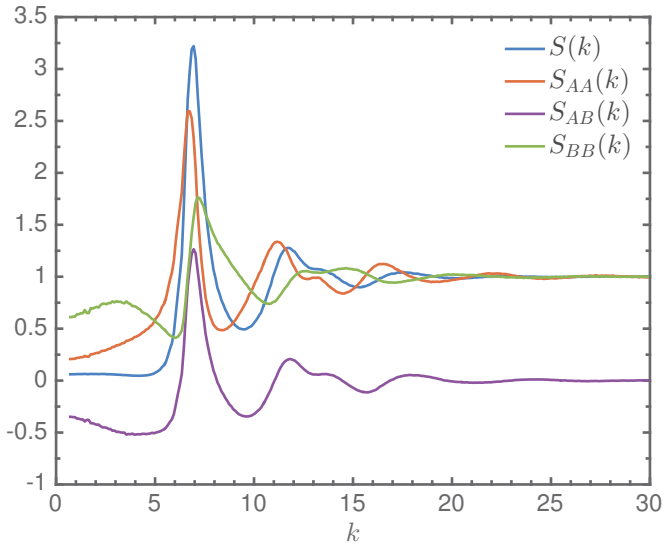

FIGURE 3.13: Representation of the total structure factors and of the different partial pair structure factor for $T = 0.85$ and $N = 1000$.

In Figure 3.13 is shown the three different partial structure factor and the total structure factor $S(k)$. We denote k^* and $k^*_{\alpha,\beta}$ the value of the wavevector corresponding respectively to the first peak of the total structure factor and of each of partial structure factors. Their are presented in Table 3.3 for different compositions of the binary mixture.

Mixture $A:B$	k^*	k^*_{AA}	k^*_{BB}	k^*_{AB}	$0.5(k^*_{AA}+k^*_{BB})$
50 : 50	6.85	6.75	7.15	6.95	6.95
60 : 40	6.85	6.75	7.15	6.95	6.95
70 : 30	6.85	6.85	7.25	7.05	7.05
80 : 20	6.95	6.85	7.25	7.05	7.05

TABLE 3.3: Values of the position of the first peak of structure factor.

Regarding the results in Table 3.3 it seems that, as for the partial pair correlation functions, the position of the first peak of S_{AB} is located at half the distance of S_{AA} and S_{BB}. In what follow we will show that it is indeed the case.

3.2.2 Relative position of the first peaks of $S_{ab}(k)$

As for the partial pair correlation functions we are interested in the position k^*_{ab} of the first peaks of the partial structure factors $S_{ab}(k)$ when the polydispersity is weak $\eta \to 0$. As we assume a small deviation from the monodisperse value, we can write

$k^*_{ab} = k^*_0 + \delta k^*_{ab}$ where k^*_0 is the position of the first peak in the monodisperse case and δk^*_{ab} is the functional deviation that we are looking for.

In the case of a weak polydispersity the partial structure factor given by equation 3.29 can be expressed as $S_{ab}(k) = S^0_{ab}(k) + \delta S_{ab}(k)$ where $S^0_{ab}(k)$ corresponds to structure factor of a monodisperse configuration where particles have been arbitrarily labelled as α or β and $\delta S_{ab}(k)$ is the deviation from the monodisperse case.

As for the partial pair correlation functions we assume an expansion at first order of $S'_{ab}(k^*_0 + \delta k^*_{ab})$ which leads to the following result:

$$\delta k^*_{ab} = -\frac{\delta S'_{ab}(k^*_0)}{S''^0_{ab}(k^*_0)} \tag{3.33}$$

Consequently we have to evaluate $\delta S_{ab}(k)$ to compare the different shifts δk^*_{ab}. The partial structure factors can be written as:

$$S_{ab}(k) = \frac{1}{\sqrt{N_\alpha N_\beta}} \frac{1}{Z_N} \int d^N \boldsymbol{r} \rho_\alpha(-k)\rho_\beta(k) \exp(-\beta E_P(\boldsymbol{r}_1, \cdots, \boldsymbol{r}_N; \eta)) \tag{3.34}$$

where the partition function is given by $Z_N = \int d^N \boldsymbol{r} \exp(-\beta E_P(\boldsymbol{r}_1, \cdots, \boldsymbol{r}_N; \eta))$.

Assuming small values of η we perform the same expansion for the potential energy as we did in the case of the partial pair correlation functions, this lead to the following result for $S_{ab}(k)$:

$$S_{ab}(k) = \frac{1}{\sqrt{N_\alpha N_\beta}} \langle \rho_\alpha(-k)\rho_\beta(k) \rangle_0 + \frac{\gamma v^{2/3} \beta \eta^2}{\sqrt{N_\alpha N_\beta}} \langle \rho_\alpha(-k)\rho_\beta(k) \left(V_A - \langle V_A \rangle_0\right) \rangle_0 \tag{3.35}$$

δS_{ab} is defined as $\delta S_{ab} = S_{ab}(k) - S^0_{ab}(k)$. With this definition we immediately see that by subtracting the first term of the R.H.S to the L.H.S we find δS_{ab} and consequently:

$$\delta S_{ab}(k) = \frac{\gamma v^{2/3} \beta \eta^2}{\sqrt{N_\alpha N_\beta}} \langle \rho_\alpha(-k)\rho_\beta(k) \left(V_A - \langle V_A \rangle_0\right) \rangle_0 \tag{3.36}$$

To find δk^*_{ab} defined by equation 3.33 we need to treat separately the different possible combinations of $(a, b) \in \{A, B\}$.

• **1st case** $\alpha = \beta = A$

We start by defining the partial structure factor S^0_{AA} for a monodisperse configuration. We recall that it corresponds to a configuration where N_A identical particles have been arbitrarily labelled as A. Consequently we have:

$$S^0_{AA}(k) = \frac{1}{N_A} \langle \rho_A(-k)\rho_A(k) \rangle_0 = \frac{1}{N_A} \left[N_A + N_A(N_A - 1) \langle e^{i\boldsymbol{k}\cdot\boldsymbol{r}_{ij}} \rangle_0 \right] \tag{3.37}$$

The average $\langle e^{i\boldsymbol{k}\cdot\boldsymbol{r}_{ij}}\rangle_0$ is related to the total structure factor of the monodisperse configuration by $\langle e^{i\boldsymbol{k}\cdot\boldsymbol{r}_{ij}}\rangle_0 = \dfrac{S(k)-1}{N-1}$ and we finally find that:

$$S^0_{AA}(k) = 1 + \alpha_A(S(k)-1) = \alpha_A S(k) + \alpha_B \tag{3.38}$$

This last equation enables to have access to the denominator of equation 3.33. To express the numerator we focus now on $\delta S_{AA}(k)$ and equation 3.36 can be written :

$$\begin{aligned}
\delta S_{AA}(k) &= \frac{\gamma v^{2/3}\beta\eta^2}{N_A}\langle \rho_A(-k)\rho_A(k)\,(V_A - \langle V_A\rangle_0)\rangle_0 \\
&= \gamma v^{2/3}\beta\eta^2(N_A-1)\langle e^{i\boldsymbol{k}\cdot\boldsymbol{r}_{ij}}\,(V_A - \langle V_A\rangle_0)\rangle_0 \quad \text{with } (i,j)\in A \\
&= \gamma v^{2/3}\beta\eta^2(N_A-1)\left[2\langle e^{i\boldsymbol{k}\cdot\boldsymbol{r}_{ij}}\,(v_i - \langle v_i\rangle_0)\rangle_0 + (N_A-2)\left\langle e^{i\boldsymbol{k}\cdot\boldsymbol{r}_{ij}}\,(v_k - \langle v_k\rangle_0)\right\rangle_0\right]
\end{aligned}$$

where $k \in A$. To find a more convenient expression for the average over v_k we use the fact that we are working at constant volume V meaning that $\langle \exp(\boldsymbol{k}\cdot\boldsymbol{r}_{ij})\,(V - \langle V\rangle_0)\rangle_0 = 0$ and as a result:

$$\langle e^{i\boldsymbol{k}\cdot\boldsymbol{r}_{ij}}\,(v_k - \langle v_k\rangle_0)\rangle_0 = -\frac{2}{N-2}\left\langle e^{i\boldsymbol{k}\cdot\boldsymbol{r}_{ij}}\,(v_i - \langle v_i\rangle_0)\right\rangle_0 \tag{3.39}$$

The last equation 3.39 reminds equation 3.16 derived in case of the partial pair correlation functions. The idea is similar. In equation 3.39, k is no more labeled A or B. This possible due to the fact that we perform the average on monodisperse configuration.

By using this last equation in the equation for $\delta S_{AA}(k)$ we finally find that:

$$\delta S_{AA}(k) = 2\gamma v^{2/3}\beta\eta^2\alpha_B\alpha_A N\left\langle e^{i\boldsymbol{k}\cdot\boldsymbol{r}_{ij}}\,(v_i - \langle v_i\rangle_0)\right\rangle_0 \tag{3.40}$$

Therefore equations 3.38 and 3.40 enable to express δk^*_{AA}

$$\delta k^*_{AA} = -\frac{\delta S'_{AA}(k^*_0)}{S^{0\prime\prime}_{AA}(k^*_0)} = -2\gamma v^{2/3}\beta\eta^2\frac{Q_S}{|S''(k^*_0)|}\alpha_B \tag{3.41}$$

Where $S^{''}(k^*_0) < 0$ and Q_S is the derivative of $N\left\langle e^{i\boldsymbol{k}\cdot\boldsymbol{r}_{ij}}\,(v_i - \langle v_i\rangle_0)\right\rangle_0$ and is given by:

$$Q_S = \frac{d}{dk}\left\langle \sum_j e^{i\boldsymbol{k}\cdot\boldsymbol{r}_{ij}}\,(v_i - \langle v_i\rangle_0)\right\rangle_0\Bigg|_{k=k^*_0} \tag{3.42}$$

We have thus find an expression for δk^*_{AA} in what follows we use the same procedure to find δk^*_{BB} and δk^*_{AB}.

• **2nd case** $\alpha = \beta = B$

As the previous case we can express the partial structure factor $S^0_{BB}(k)$ for a monodisperse configuration, it leads to

$$S^0_{BB}(k) = \alpha_B S(k) + \alpha_A \tag{3.43}$$

and $\delta S_{BB}(k)$ is given by:

$$\delta S_{BB}(k) = -2\gamma v^{2/3}\beta\eta^2\alpha_B\alpha_A N \left\langle e^{i\boldsymbol{k}\cdot\boldsymbol{r}_{ij}}\,(v_i - \langle v_i\rangle_0)\right\rangle_0 \tag{3.44}$$

Thus we find that:

$$\delta k^*_{BB} = -\frac{\delta S'_{BB}(k^*_0)}{S^{0\prime\prime}_{BB}(k^*_0)} = 2\gamma v^{2/3}\beta\eta^2\frac{Q_S}{|S''(k^*_0)|}\alpha_A \tag{3.45}$$

where Q_S is given by 3.42 and $S^{0\prime\prime}_{BB} < 0$.

• **3rd case** $\alpha = A$ **and** $\beta = B$

We use again the same procedure to express $S^0_{AB}(k)$

$$S^0_{AB}(k) = \sqrt{\alpha_A\alpha_B}(S(k) - 1) \tag{3.46}$$

and $\delta S_{AB}(k)$:

$$\delta S_{AB}(k) = \gamma v^{2/3}\beta\eta^2\sqrt{\alpha_A\alpha_B}\,(\alpha_B - \alpha_A)\,N\left\langle e^{i\boldsymbol{k}\cdot\boldsymbol{r}_{ij}}\,(v_i - \langle v_i\rangle_0)\right\rangle_0 \tag{3.47}$$

We find therefore that δk^*_{AB} is given by:

$$\delta k^*_{AB} = -\frac{\delta S'_{AB}(k^*_0)}{S^{0\prime\prime}_{AB}(k^*_0)} = 2\gamma v^{2/3}\beta\eta^2\frac{Q_S}{|S''(k^*_0)|}\left(\frac{\alpha_A - \alpha_B}{2}\right) \tag{3.48}$$

where Q_S is given by 3.42 and $S^{0\prime\prime}_{AB} < 0$.

Expressions of the different δk^*_{ab} have been derived and we remark that the first peak associated to the cross interaction $\delta k^*_{AB} = \frac{1}{2}(\delta k^*_{AA} + \delta k^*_{BB})$. This can be observed in Figure 3.15.

We define now $\Delta_S = 2\gamma v^{2/3}\beta\eta^2 Q_S/|2S''(k^*_0)|$ and we notice the following points:

- $\delta k^*_{BB} - \delta k^*_{AB} = \delta k^*_{AB} - \delta k^*_{AA} = \Delta_S$ and in Table 3.3 we notice that $\Delta_g = 0.20$ for the first peaks.
- As Δ_g for the partial pair correlation functions, we observe that Δ_S is independent of the composition $A : B$ of the mixture.
- These results do not concern only the first peak of the partial structure factors but are also valid for any extrema of $\delta S_{ab}(k)$.

- As $S''(k_0^*) < 0$ near maxima we have assumed that $Q_S < 0$ as δk_{AA}^* (resp. δk_{BB}^*) should be shifted negatively (resp. positively) with respect to the position k_0^* of the first peak of the monodisperse structure factor $S(k)$. We have computed $\left\langle \sum_j e^{i\boldsymbol{k}\cdot\boldsymbol{r}_{ij}} (v_i - \langle v_i \rangle_0) \right\rangle_0$ to study the variation of the function. We have represented it in Figure 3.14 where we observed that the function is decreasing near minima meaning that the derivative Q_S is negative. $S''(k_0^*) > 0$ for minima, and we find that as expected $Q_S > 0$ around minima.

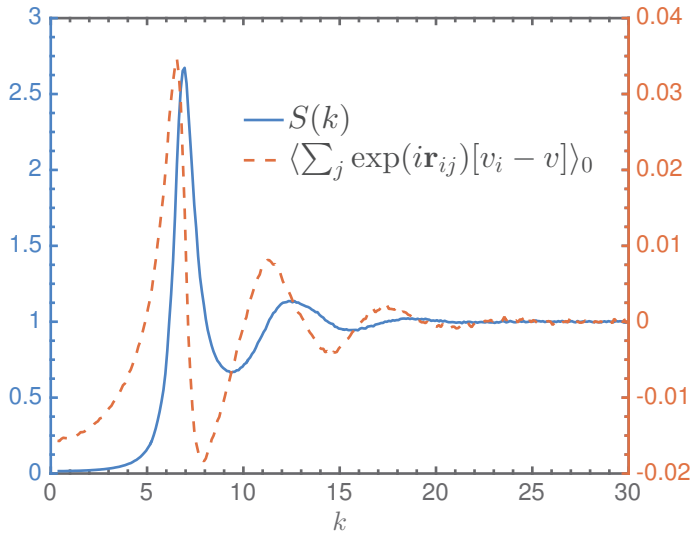

FIGURE 3.14: Representation of the monodisperse structure factor $S(k)$ in blue solid line and $\left\langle \sum_j e^{i\boldsymbol{k}\cdot\boldsymbol{r}_{ij}} (v_i - v) \right\rangle_0$ in dashed red line for $T = 2.00$ and $N = 8000$.

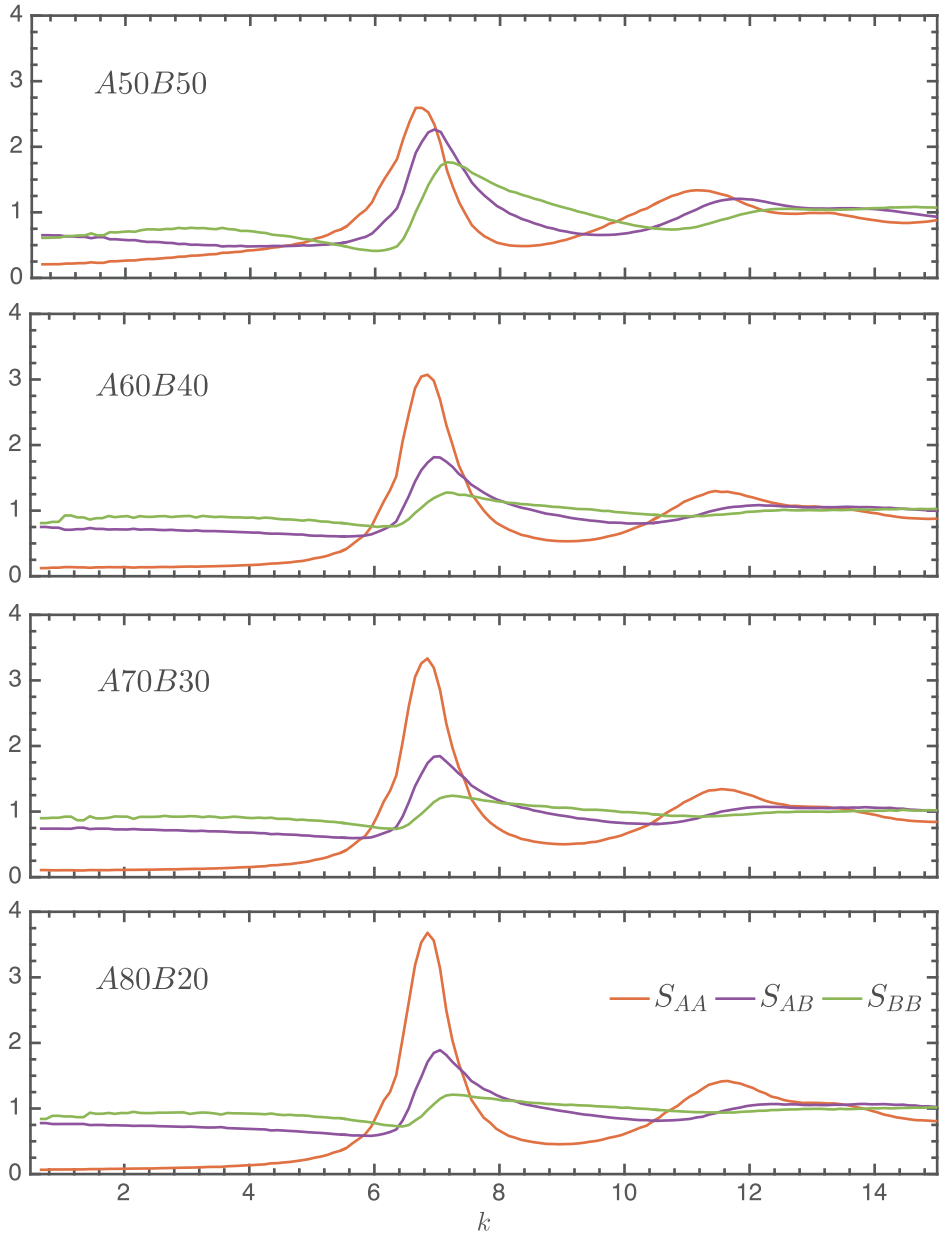

FIGURE 3.15: Representation of the relative positions of the first peaks of the three partial structure factors for $T = 0.85$, $N = 1000$ and for different compositions $A : B$ of the mixture. The curve of S_{AB} has been shifted on purpose to better compare the position of the different peaks.

Evolution with temperature of the partial pair correlation functions and of the partial structure factors have been described. Apart from the expected tendency to structure, these observables are not very sensitive upon cooling. We also observe that the polydisperse Voronoi liquid presents an apparent strong tendency to favor local structures as it

is suggested by the presence of a shouldering in $g_{ab}(r)$ and $S_{ab}(k)$. Moreover the cosine distribution have shown a tendency of the system to favor icosahedral order.

Relations for the position of the first peaks of partial correlation functions and partial structure factors have been derived, showing that position of the peaks associated to the cross interactions are always located at half the distance of identical interactions. For usual glass formers with additive interactions, such as the Wahnström binary mixture for instance [30], this characteristic positions of r^*_{ab} at low temperature is associated with the presence of additivity. For the bidisperse Voronoi liquid additivity cannot be defined. However when we will investigate locally favored structures (LFS) in Chapter 6, the analysis of LFS will reveal that the polydisperse Voronoi liquid forms icosahedra and shares similarities with additive glass formers.

Chapter 4

Dynamical observables

Contents

The main issue in the physics of supercooled liquids is to understand the origin of the important slowing down of the dynamics while approaching the glass transition temperature whereas there is no obvious structural changes. Dynamical arrest is well visible when probing molecular motion as for instance the typical relaxation time reaching $10 - 10^3$s which is 14 orders of magnitude larger than the typical picosecond relaxation observed above the melting point [9, 73]. Moreover viscosity, which measures the resistance of liquid to flow, may increase by 12 orders of magnitude whereas slight changes in the local packing are experimentally observed [9].

Depending on the nature of the species, viscosity or relaxation time does not slow down the same way near the glass transition. For instance materials such as SiO_2 exhibit an Arrhenian behavior, i.e the relaxation time $\tau \sim \exp(-E_A/k_BT)$. For these systems, an activation energy E_A can be extracted. Therefore the typical relaxation time corresponds to the time required before a microscopic event occurs that allows to overcome the energy barrier. In the case of SiO_2 it corresponds to the energy required to break the bond $Si-O$ [10, 73]. Most of glass-formers deviate more or less strongly from the Arrhenian behavior when the temperature is coming closer to T_G, implying an increase of the energy barriers as the temperature is lowered. The molecular origin of this "super-Arrhenian" behavior remains an open issue of the physics of supercooled liquids. [74].

From the statistical mechanics point of view, viscosity is a transport coefficient and is linked via the Green-Kubo relation to the shear correlation function. Viscosity is an example among others, and for instance we can also mention the diffusion coefficient which is linked to the velocity autocorrelation [40]. Consequently as transport coefficients seem to be very sensitive to the neighborhood of the glass transition, it appears reasonable to investigate the properties of their related correlation functions as they must convey information about what occurs near glass transition.

In this chapter, we first briefly describe the typical two-step relaxation processes that arise upon cooling. To this purpose, intermediate scattering functions and mean-square displacement of the bidisperse Voronoi liquid are computed. Therefore we extract respectively the relaxation time and the diffusion coefficient. Their evolution with temperature is then discussed in the framework of different approaches such as fragility or mode-coupling theory. Moreover a systematic comparison with usual glass-formers such as Kob-Andersen and Wahnström models is proposed.

4.1 Two-step relaxation processes

Assuming a structure-sensitive random observable $A(t)$, as for instance the density fluctuations, the correlation function $\phi_A = \langle A^\star(t)A(0)\rangle$ (where $A^\star(t)$ is the complex conjugate of $A(t)$) [74] measures the decay of correlations with time. [8]. Typical decays at high and low temperature are shown in Figure 4.1.

- At high temperature in the short-time ballistic regime, a tagged particle moves by being weakly sensible to interactions with its surrounding neighbors. Then the particle experiences collisions with their surrounding environment and after a certain number of collisions the tagged particle has forgotten about all the initial information. Therefore at large-time scale the associated stochastic process is

Markovian meaning that the relaxation is exponential $\phi_A(t) = \phi_0 \exp(-t/\tau)$ where τ is the characteristic relaxation time of the system.

- When the temperature is lowered while remaining greater than the glass transition temperature T_G, the correlation function is more complex. Following the ballistic regime $C(t)$ decays and exhibits a crossover to a plateau associated with the presence of an intermediate regime. This intermediate regime is reminiscent of the behavior found for crystals where the correlation function does not decay in the long-time limit as the motion of particles consists only on vibrations around their equilibrium position [69]. For supercooled liquids, a vibrational motion is also observed for intemediate time-scale. As a matter of fact particles remain trapped in the cage composed by their surrounding neighbors and consequently large displacements are hindered. Thus a certain time is required to enable particles to escape the cage [8]. Finally in the long-time relaxation also named α-relaxation the correlation function does not decay exponentially but the final relaxation is well described by the Kohlrausch-Williams-Watt (KWW) function given by $\phi(t) = \phi_0 \exp(-(t/\tau)^\beta)$ where $\beta < 1.00$ is called the stretched exponent [69].

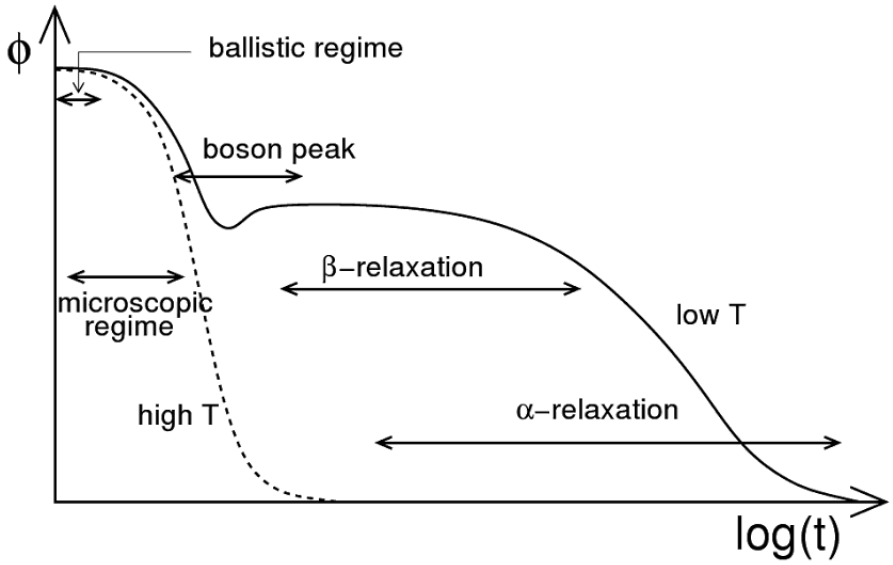

FIGURE 4.1: Illustration of the decay of a correlation function $\phi(t)$ at high temperature (dashed line) and at low temperature (solid line). Figure taken from [69].

4.1.1 Intermediate scattering function

As mentioned early a relevant structure-sensitive observable A is the fluctuations of density defined as follows:

$$\delta\rho(\boldsymbol{k},t) = \sum_{i=1}^{N} \exp(i\boldsymbol{k}\cdot\boldsymbol{r}_j(t)) \tag{4.1}$$

The associated correlation function is the total intermediate scattering function $F(k,t)$ given by the following relationship [40]:

$$F(k,t) = \frac{1}{N}\langle\delta\rho(-\boldsymbol{k},0)\delta\rho(\boldsymbol{k},t)\rangle = \frac{1}{N}\sum_{j=1}^{N}\sum_{k=1}^{N}\langle\exp(i\boldsymbol{k}\cdot(\boldsymbol{r}_j(t)-\boldsymbol{r}_k(0)))\rangle \tag{4.2}$$

$F(k,t)$ is also known as the coherent intermediate scattering function. It correlates the position of a tagged particle i at time $t=0$ to the position of another tagged particle j at time t [75]. It can be decomposed into self and distinct parts where we denote F_s the self part also known as the incoherent intermediate scattering function and defined as:

$$F_s(k,t) = \frac{1}{N}\sum_{j=1}^{N}\langle\exp(i\boldsymbol{k}\cdot(\boldsymbol{r}_j(t)-\boldsymbol{r}_j(0)))\rangle \tag{4.3}$$

It can be useful to study the incoherent intermediate scattering only for one specific type of particles, in either case we define:

$$F_s^a(k,t) = \frac{1}{N_a}\langle\delta\rho_a(-\boldsymbol{k},0)\delta\rho_a(\boldsymbol{k},t)\rangle = \frac{1}{N_a}\sum_{j=1}^{N_a}\langle\exp(i\boldsymbol{k}\cdot(\boldsymbol{r}_j(t)-\boldsymbol{r}_j(0)))\rangle \tag{4.4}$$

Given a specific wavevector $\boldsymbol{k}$, the incoherent intermediate scattering function measures the correlation between the position of a tagged particle at time $t=0$ and its position at time t.

Incoherent and coherent intermediate scattering function complement one another in the description of the liquid. Whereas the incoherent scattering function describes the dynamics of individual particles, the coherent scattering function informs on collective behaviors of particles [75].

The incoherent intermediate scattering function can be computed for any values of the wavevector k. However in Chapter 3 we have seen that the static correlations of density measured by the partial structure factors $S_{ab}(k)$ are maximal when $k \sim k^*_{ab}$ (where k^*_{ab} is the position of the first peak of $S_{ab}(k)$). As a consequence it corresponds to the region where the spatial fluctuations of density are maximal. It is thus interesting to see how these fluctuations are going to evolve with time.

In Figure 4.2 are represented for both species A and B the incoherent intermediate scattering functions computed for $k = k^*_{aa}$. We notice that they are both compliant with the two-step relaxationscheme when lowering the temperature such as the coherent intermediate scattering function which is also presented in Figure 4.2. For temperatures $T > 1.00$ the system exhibits the classical exponential decay and when the temperature is lowered below $T = 1.00$, we notice the emergence of a plateau whose size is increasing while T is decreased. As expected we observe the drop associated to the boson peak before the plateau but other oscillations appear on the plateau which are relatively pronounced for the incoherent intermediate scattering functions.

As the temperature is lowered, the separation of time scales is more and more pronounced. The structural relaxation time associated to the α-relaxation can be extracted from the long-time limit of the incoherent intermediate scattering function. We define arbitrarily the structural relaxation time τ_α as the value of the time t when $F^a_s(k^*_{aa}, t = \tau^a_\alpha) = 0.1$. This relaxation time corresponds to the individual relaxation of particles.
It is important to stress that one could also have chosen to define the relaxation time from the coherent intermediate scattering function $F(k, t)$. The information conveyed is a little bit different as it would correspond to a collective relaxation time which informs on the time particles need to rearrange cooperatively. In both cases the behavior of τ_α vs. T is qualitatively the same as it is shown in Figure 4.3 (Lower graph), however the value of τ_α are a bit larger in the collective case than in the individual.

In Figure 4.3 (Upper graph) we have represented the evolution of τ^A_α and τ^B_α as functions of the temperature T. We notice first that small particles relax a bit faster than the larger ones. We have deliberately chosen a semilogy representation to emphasize the Arrhenian behavior of the system for temperature $T \leq 1.10$ and the departure from this regime for temperature below $T \sim 1.10$.

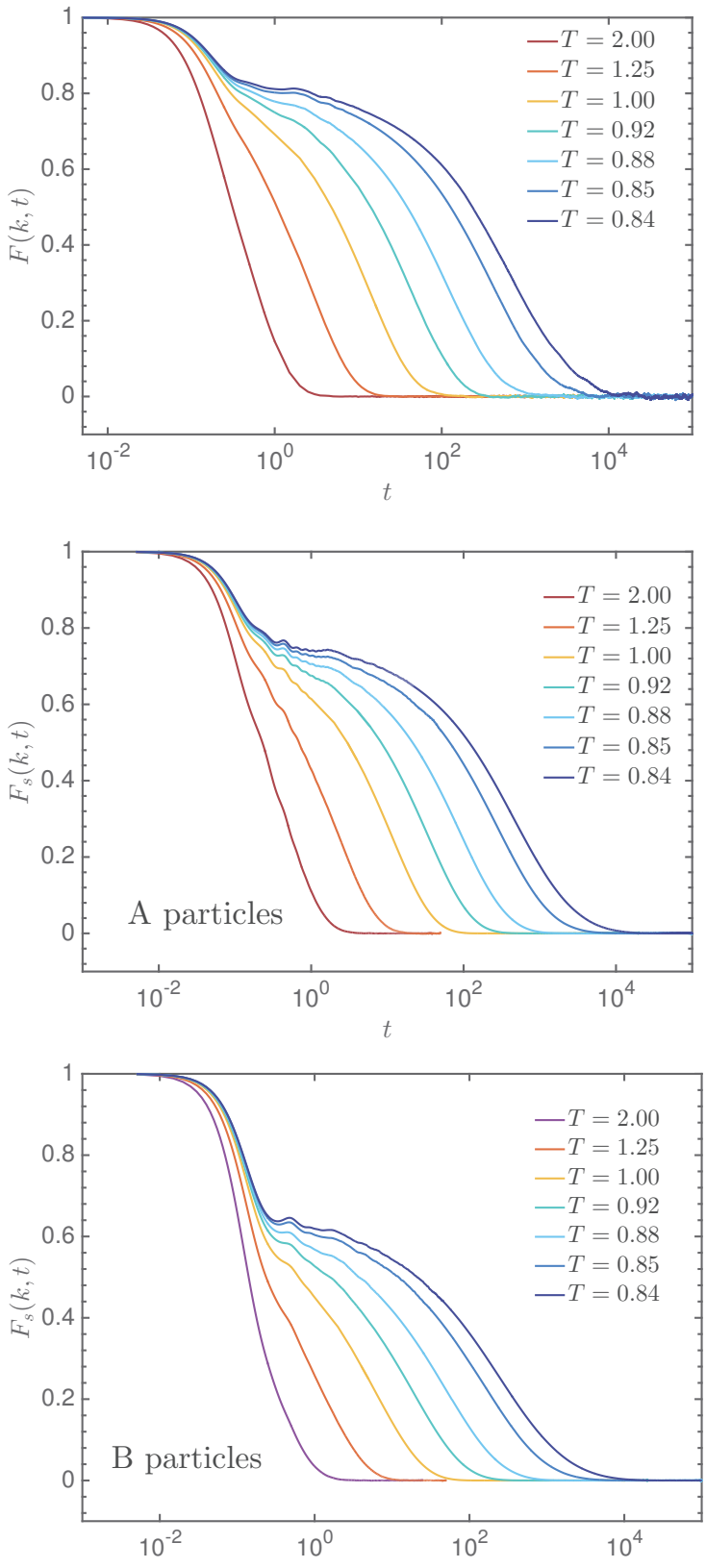

FIGURE 4.2: From top to bottom are respectively represented the coherent intermediate scattering functions, the intermediate scattering functions for A particles and the intermediate scattering function for B particles. They are all computed for different temperatures at $k = k^*$ or $k = k^*_{aa}$.

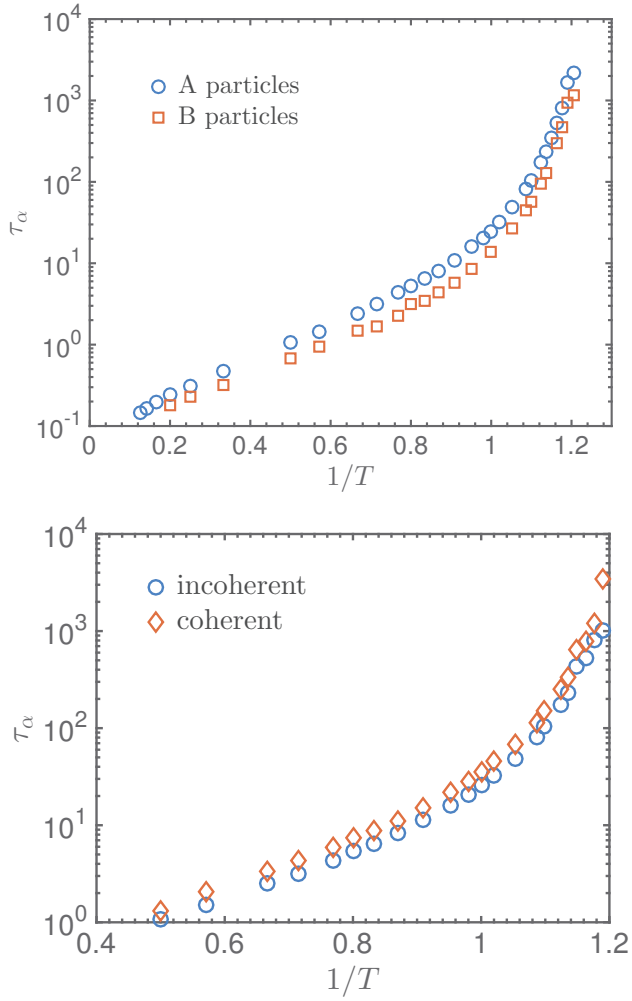

FIGURE 4.3: Upper graph: Comparison of the relaxation times of large and small particles for τ_α computed from the incoherent intermediate scattering function. Lower graph: Comparison of the relaxation computed from the incoherent and coherent intermediate scattering function.

4.1.2 Mean-square displacement

As already mentioned in Chapter 1, the mean-square displacement (MSD) measures the correlation between the position of a tagged particle i at time $t = 0$ and its position at time t and is related to velocity autocorrelation of the tagged particle via the following equation [39]:

$$\delta r^2(t) = \langle [\boldsymbol{r}_i^2(t) - \boldsymbol{r}_i^2(0)] \rangle = 2 \int_0^t d\tau (t - \tau) \langle \boldsymbol{v}_i(0) \cdot \boldsymbol{v}_i(\tau) \rangle \tag{4.5}$$

In the case of a binary mixture the MSD is more precisely computed by focusing on just one of the species.

The MSD also captures the two-step relaxation footprint of supercooling as we observe in Figure 4.4 that the short-time ballistic regime and the long-time diffusive regime are separated by a plateau. In the case of the MSD the increase of the size of the plateau when the temperature is lowered is directly related to the time needed by the tagged particle to escape its first shell of neighbors.

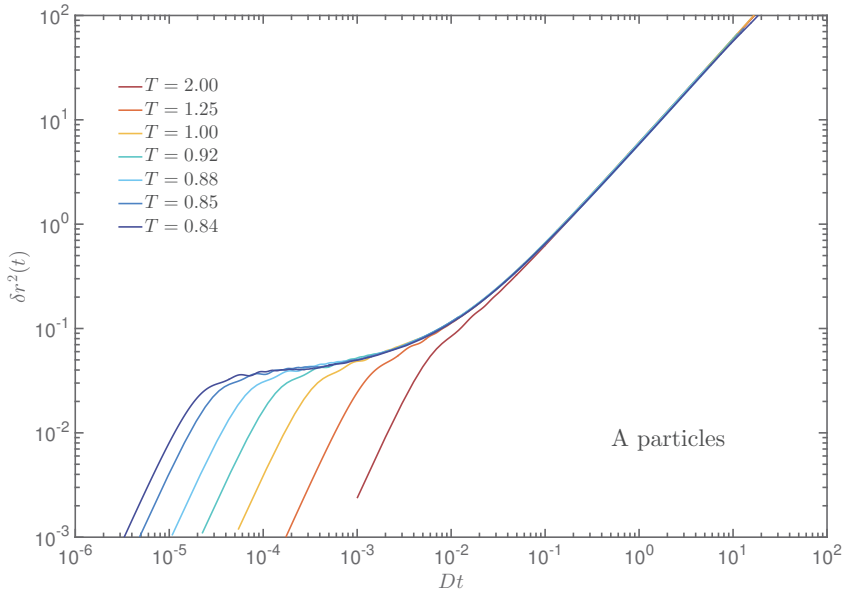

FIGURE 4.4: Representation of the MSD of A particles for several temperatures.

In the long-time limit the MSD describes a purely diffusive behavior and as a result the diffusion can be computed knowing that $\delta r^2(t) \sim 6Dt$. The results are presented in Figure 4.5 where the diffusion D_A and D_B of A and B species respectively are plotted as a function of temperature.

As for the structural relaxation time we have chosen a semilogy representation to stress the Arrhenian behavior at high temperature and the departure from this regime at lower temperature. We also notice the higher diffusivity of small particles compared to larger ones as it is generally observed in binary mixtures [76].

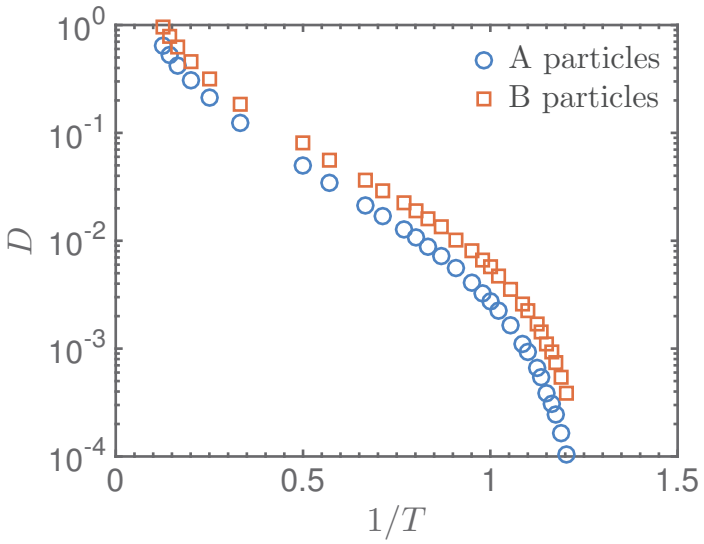

FIGURE 4.5: Diffusion coefficient computed at different temperatures for A and B particles.

Structural relaxation time τ_α and diffusion coefficient D have been computed and they both show a super-Arrhenian behavior below a certain temperature T^* called the crossover temperature. In the rest of the chapter, we attempt to analyze the temperature evolution of those two quantities in the framework of different approaches. A systematic comparison with Lennard-Jones glass-formers is also proposed.

4.2 Fragility

While comparing the behavior of the viscosity or the relaxation time as a function of temperature for different glass-formers obtained under the same experimental conditions, one may represent the evolution of these transport quantities as a function of $1/T$. However some insights into the relative behavior of the different materials can be gained by comparing the variation of η or τ_α with respect to the same corresponding-states variables, as the T_G scaled temperature in the case of an isosbaric cooling experiment for instance [12].

Such a rescaling of the temperature by introducing the glass transition temperature was firstly proposed by Oldekop in 1957 for comparing the evolution of the viscosity of different oxide and fluoride glass-formers [12, 77]. In 1972, Laughlin and Uhlmann reintroduced the T_G scaled temperature and compared different classes of species ranging from oxide to organic glass-formers. As Oldekop, they noticed that different systems belonging to the same class of materials have qualitatively the same evolution on the

$\log(\eta)$ vs. $1/T$ plot [78]. Furthermore they also observed without giving any explanation, that different classes of systems have different curvatures in the $\log(\eta)$ vs. $1/T$ plot.

In the 80s, Angell pushed further the work of Laughlin and Uhlmann by including other species to the $\log(\eta)$ vs. T plot, as for instance polymeric materials. Moreover Angell proposed and interpretation of the pattern observed. To this purpose he classified the behavior of the materials regarding their fragility index m [79] which is a measure of the slope of η when $T = T_G$:

$$m = \left.\frac{d\log(\eta)}{d(T/T_G)}\right|_{T=T_G} \tag{4.6}$$

A material with a low value of m is considered as *strong* whereas materials with a large m value is named *fragile*. These two terms *strong* and *fragile* were initially chosen by Angell to differentiate respectively species that have the ability to preserve a short and medium range order above and below T_G from species where the local order is submitted to substantial changes upon cooling [2, 13]. For instance materials like SiO_2, which are classified as strong liquids, preserve a tetrahedral structure upon cooling. On the opposite fragile liquids usually do not present directional bonds and correspond to materials with ionic or aromatic character [13]. However one has to be careful as this link between fragility and underlying structures of liquids is purely qualitative and some species do not conform to these observations as for instance methylcyclohexane which presents an intermediate behavior in the $\log(\eta)$ vs. T_G/T plot also known as Angell plot (see Figure 4.6). Nowadays the term *fragility* has a bit lost its original meaning and refers more to the way transport quantities such as viscosity or diffusion coefficient are evolving with temperature [73].

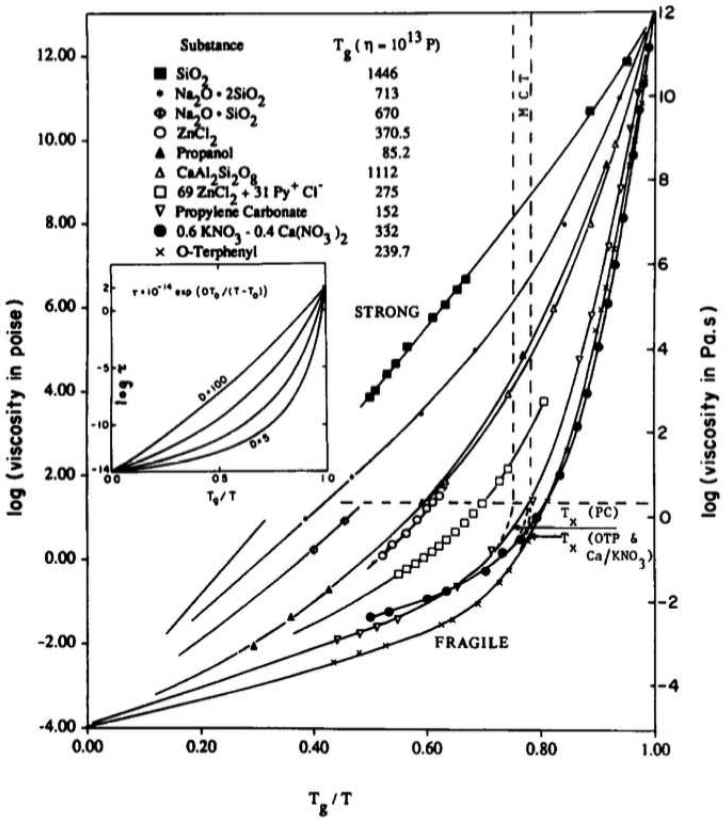

FIGURE 4.6: Angell-plot of the viscosity of several species as a function of T_G/T. (Reprinted with permission from [2], copyright of Elsevier, 1988.)

All the patterns observed in the Angell plot 4.6 are likely to be well-reproduced considering the variation of only one parameter D in the modified version of the Vogel-Fulcher-Tamman (VFT) equation [13]:

$$\eta = \eta_0 \exp[DT_0/(T - T_0)] \tag{4.7}$$

D is called the fragility parameter and is proportional to m [79]. Equation 4.7 implies a divergence of the transport quantity under interest, for $T = T_0$, supporting the idea of a phase change at $T = T_0$ [80]. The possible nature of this phase change and its link with thermodynamics will be discussed in Chapter 5 when we will deal with configurational entropy and the Kauzmann paradox. Regarding the fragility, generally speaking we can say that if T_0 is close from $T = 0$ the system investigated is more likely to have a strong behavior whereas if $T_0 \leq T_G$ the system is fragile [8].

As explained by Kivelson *et al.* [80] the VFT equation 4.7 can be used to fit the transport quantities at low and high temperatures. However it results in performing two distinct fits. On the one hand in the high temperature regime, a fit has to be performed above the crossover temperature T^*, which separates the Arrhenian from the super-Arrhenian

regime. On the other hand a second fit has to be done for $T < T^*$ in order to characterize the super-Arrhenian regime.
It is important to stress that using the VFT equation for fitting the whole range of temperatures would lead to inaccurate results. Moreover for high-temperature there is no peculiar interest to use the VFT instead of the usual Arrhenian law with all the more reason that the divergence of the transport quantity would have no physical meaning in the high temperature regime.

Recently in a systematic study of the isobaric fragility of various Lennard-Jones glass formers, Coslovich and Pastore [21] proposed to use an equation that enables to pass continuously from the Arrhenian to the super-Arrhenian regime:

$$\tau(T) = \begin{cases} \tau_\infty \exp\left[\dfrac{E_\infty}{T}\right] & T > T^* \\ \\ \tau'_\infty \exp\left[\dfrac{1}{K(T/T_0 - 1)}\right] & T < T^* \end{cases} \tag{4.8}$$

where for continuity one must have:

$$\tau'_\infty = \tau_\infty \exp\left[\frac{E_\infty}{T^*} - \frac{1}{K(T^*/T_0 - 1)}\right] \tag{4.9}$$

In equation 4.8 the expression used for $T < T^*$ corresponds to the VFT equation 4.7 where $D = 1/K$.

Contrary to Coslovich and Pastore, we also use the same set of equations to fit the diffusion coefficient.

$$D(T) = \begin{cases} D_\infty \exp\left[-\dfrac{E_\infty}{T}\right] & T > T^* \\ \\ D'_\infty \exp\left[-\dfrac{1}{K(T/T_0 - 1)}\right] & T < T^* \end{cases} \tag{4.10}$$

where

$$D'_\infty = D_\infty \exp\left[-\frac{E_\infty}{T^*} + \frac{1}{K(T^*/T_0 - 1)}\right] \tag{4.11}$$

These continuous descriptions of both relaxation time and diffusion coefficient involve the determination in each case of 5 parameters. We look for the values of these parameters not only for the bidisperse Voronoi liquids but also for 3 Lennard-Jones glass formers as our main motivation is to compare our system with well-known models of glass formers.

4.2.1 Influence of the mixture composition

For the Kob-Andersen mixture, it has been shown [81] that the composition of the mixture has a direct impact on fragility. As a matter of fact, the more the composition tends to be equimolar, the more fragile the mixture.

We test whether this observation is also valid in the case of the bidisperse Voronoi liquid. To this purpose in addition of the equimolar mixture, we have simulated three other mixtures where the percentage of large A particles has been systematically increased from 50% to 80%. We use equations 4.8 and 4.10 to fit the data.

As mentioned above, it is useful to compare the evolution of relaxation times with respect to the same corresponding states. In experiments the corresponding state is chosen when $T = T_G$. Numerically we could think of defining a temperature of reference denoted T_r which would correspond to a numerical glass transition. This idea was first suggested by Bordat *et al.* [82] and then used by Coslovich and Pastore [21]. In both works T_r is arbitrarily defined as the temperature at which $\tau_\alpha = 4 \cdot 10^4$ and its determination would require an extrapolation of the relaxation time to $\tau_\alpha = 4 \cdot 10^4$.

Results for the structural relaxation times are shown in Figure 4.7 and for the diffusion coefficient in Figure 4.8. The parameter extracted from the fit for the relaxation time and diffusion coefficient are presented respectively in Table 4.1 and Table 4.2. It is important to stress that, even if in practice the crossover temperature T^* is a fitting parameter, we have fixed its value in the case of the diffusion coefficient and this constraint does not alter the quality of the fit as it can be observed in Figure 4.8.

	τ_∞	E_∞	T^*	K	T_0	T_r
50 : 50	0.076	4.924	1.25	0.610	0.691	0.794
60 : 40	0.077	4.892	1.20	0.474	0.612	0.726
70 : 30	0.077	4.882	1.15	0.259	0.498	0.659
80 : 20	0.074	4.885	1.10	0.195	0.443	0.629

TABLE 4.1: Parameters obtained when fitting the structural relaxation time with equation 4.8. T_r is found when the relaxation time $\tau_\alpha(T = T_r) = 4 \cdot 10^{-4}$.

	D_∞	E_∞	K	T_0
50 : 50	0.984	5.291	0.692	0.6634
60 : 40	0.969	5.223	0.500	0.580
70 : 30	0.944	5.168	0.324	0.487
80 : 20	0.942	5.159	0.320	0.472

TABLE 4.2: Parameters obtained when fitting the diffusion coefficient with equation 4.10. For this fit the value of T^* corresponds to one determined when fitting τ_α.

We can make the following observations:

- As for the Kob-Andersen mixture, in the case of the bidisperse Voronoi liquid, an increase of the number of large particles will lead to a less marked fragility. This is suggested by the decrease of the parameter K when N_A is increased for both relaxation time and diffusion coefficient.
- The fragility parameter K is a bit stronger in the case of the diffusion coefficient than for the structural relaxation time.
- When looking at the evolution of T_0 we notice, that $T_0 < T_r$ but close from T_r, which is qualitatively in agreement with the fact that the bidisperse Voronoi has a fragile behavior. The gap between T_0 and T_r increases when K decreases supporting the idea that for strong mixture the value of T_0 is shifted toward $T = 0$ [8].
- The higher temperature regime where the Arrhenian regime occurs is only weakly sensitive to the composition of the mixture. Indeed, for both relaxation time and diffusion coefficient, τ_∞ and D_∞ are almost constant whatever the nature of the mixture. Moreover it is also the case for the activation energy E_∞ which is in average $E_\infty \sim 4.89$ for the relaxation time and $E_\infty \sim 5.21$ for the diffusion coefficient.

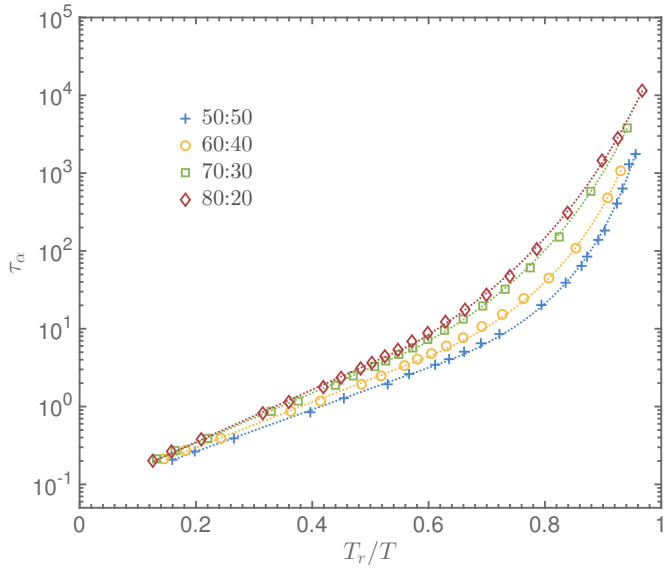

FIGURE 4.7: Angell-plot of the evolution of the relaxation time τ_α as a function of T_r/T for several compositions of the binary mixture.

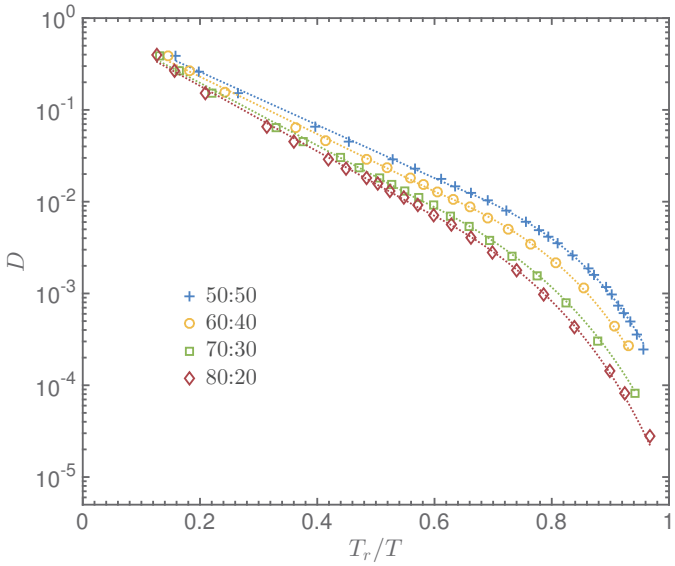

FIGURE 4.8: Angell-plot of the evolution of the diffusion coefficient D as a function of T_r/T for several compositions of the binary mixture.

The fragility of the bidisperse Voronoi liquid is now well-characterized. It could thus be useful to compare our model to other glass-formers to see to what extent it shares similarities in the behavior of the transport quantities upon cooling. To this purpose we consider the work of Coslovich and Pastore [21] as a starting point. They have investigated the isobaric fragility of different models of Lennard-Jones (LJ) glass formers

but some attention has also been paid to isochoric fragility for the Kob-Andersen mixture and the Wahnström model.

We decided to also investigate these two previous systems and an additional one, an additive mixture of Lennard-Jones particles that is described below. We firstly characterize the fragility of these models and see to what extent our results are consistent with the ones found by Coslovich and Pastore. Then a great attention is given to the comparison of the bidisperse Voronoi liquid with this LJ glass formers. A specific attention is given to define proper states of references for comparing efficiently these different models.

4.2.2 Comparing models: Lennard-Jones glass formers

To investigate the isochoric fragility we performed NVT simulations, using the Nosé-Hoover thermostat, on 3 different LJ glass-formers which are all binary mixtures $(A:B)$ composed of $N = 1000$ particles and interacting via the LJ potential:

$$U_{ab}(r) = 4\epsilon_{ab}\left[\left(\frac{\sigma_{ab}}{r}\right)^{12} - \left(\frac{\sigma_{ab}}{r}\right)^{6}\right] \quad \text{with } (a,b) \in \{A,B\} \tag{4.12}$$

To ensure the continuity of the energy, the potential is shifted to zero at its cutoff $r_c = 2.5$. We run the simulation using a timestep $\delta t = 0.001$ and the total time of the equilibrated trajectories correspond to at least $10\tau_\alpha$.
The glass-formers under interest are the following:

1. The classical Kob-Andersen (KA) mixture [76]. It is a non-additive mixture where the concentration of large particles $N_A/N = 0.8$.
2. The Wahnström model (WAHN) introduced by Wahnström [30] is an additive mixture where the mass ratio $m_2/m_1 = 0.5$ and the concentration of large particles is $N_A/N = 0.5$.
3. An additive mixture of a LJ particles (AMLJ-0.80) with a diameter $\sigma_{BB} = 0.8$ and $N_A/N = 0.5$.

Those peculiar models were chosen to span a wide range of isobaric fragility. Considering the work of Coslovich and Pastore, we can sort these systems by ascending fragility parameters, that is KA $<$ WAHN $<$ AMLJ-0.80. Despite the fact that the isochoric fragility has been experimentally [83] and numerically [21] reported weaker than the isobaric one, we can expect that the general tendency would be preserved.

All the parameters used to define these models are presented in Table 4.3.

	KA	WAHN	AMLJ-0.80
ρ	1.2	1.3	1.2
ε_{AA}	1.0	1.0	1.0
ε_{AB}	1.5	1.0	1.0
ε_{BB}	0.5	1.0	1.0
σ_{AA}	1.0	1.0	1.0
σ_{AB}	0.8	0.916	0.9
σ_{BB}	0.88	0.837	0.8
m_A	1.0	1.0	1.0
m_B	1.0	0.5	1.0
N_A/N	0.80	0.5	0.5

TABLE 4.3: Parameters of the Lennard-Jones potential of 3 glass-formers. Density, masses of particles and concentration number are also presented.

As for the bidisperse Voronoi liquid, the value of τ_α is chosen such that $F_s(k^*, t = \tau_\alpha) = 0.1$ and the diffusion coefficient is extracted from the long-time limit of MSD. We have used equations 4.8 and 4.10 to fit respectively the relaxation time and the diffusion coefficient of the 3 LJ systems.

Results for τ_α are presented in Table 4.4 and the fitting curves are represented in dashed lines in Figure 4.9.

	τ_∞	E_∞	T^*	K	T_0	T_r
KA	0.184	3.183	1.00	0.268	0.325	0.436
WAHN	0.140	3.201	1.00	0.400	0.428	0.524
AMLJ-0.80	0.260	1.636	0.60	0.626	0.280	0.322

TABLE 4.4: Fitting parameters extracted from equation 4.8 of the relaxation time for the three LJ systems. The reference temperature T_r has been chosen when $\tau_\alpha(T = T_r) = 4 \cdot 10^{-4}$.

The values of the fitting parameters are slightly different from the ones found by Coslovich and Pastore [21]. This could be due to the fact that the crossover temperature estimated by our fitting procedure is a bit lower than the one found in [21]. However values are qualitatively in good agreement. As expected the fragility of the KA mixture is weaker than the one of WAHN and AMLJ-0.80. AMLJ-0.80 has the more marked fragility as it is suggested by the value of K or the localisation of the graph of AMLJ-0.80 in the Angell-plot 4.9.

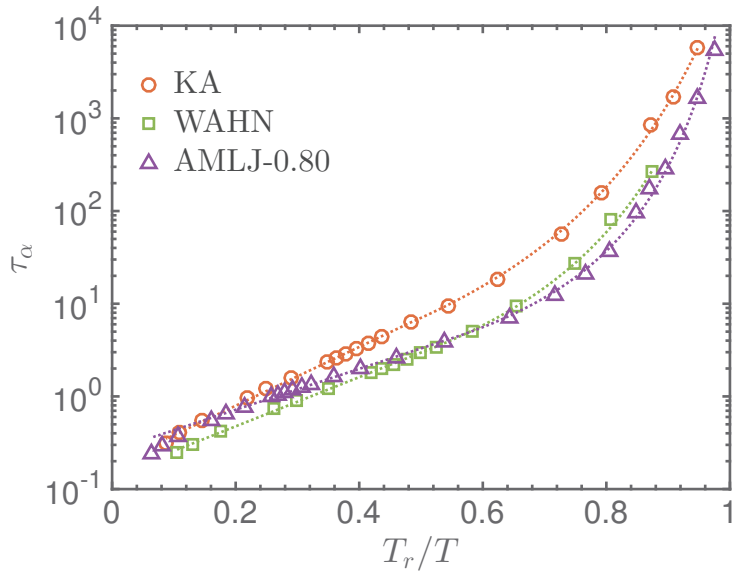

FIGURE 4.9: Angell-plot of the evolution of the relaxation time τ_α as a function of T_r/T.

While fitting the diffusion coefficient we found again values of K that are slightly lower than the one found in [21]. However as for the relaxation time, the fitting parameters for D are in good agreement with the ones found for the relaxation times. In the Angell-plot 4.10 and in Table 4.5 we observe that AMLJ-0.80 remains the more fragile mixture whereas KA is the strongest of the 3 LJ glass formers. We also note that the fragility index K is bigger than the one found for τ_α which was also observed in [21].

	D_∞	E_∞	T^*	K	T_0
KA	0.255	3.140	0.90	0.3852	0.3381
WAHN	0.319	3.227	0.90	0.534	0.429
AMLJ-0.80	0.179	1.644	0.50	0.617	0.247

TABLE 4.5: Fitting parameters extracted from equation 4.10 of the diffusion coefficient for the three LJ systems.

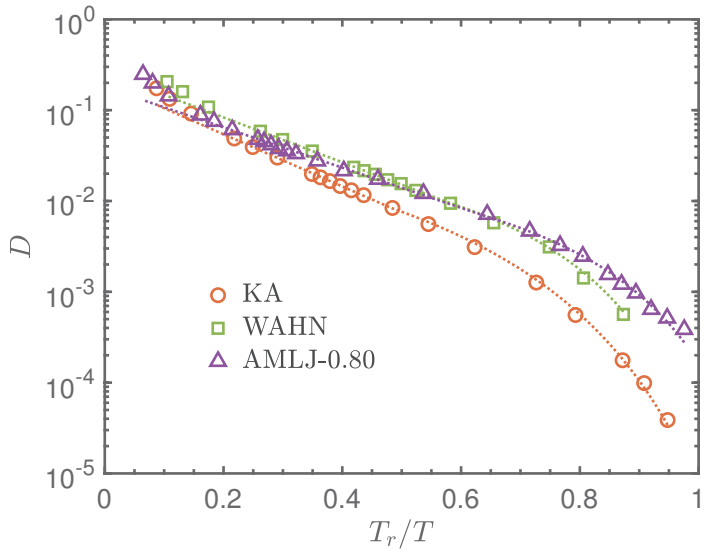

FIGURE 4.10: Angell-plot of the evolution of the diffusion coefficient D as a function of T_r/T.

We have characterized with the help of equations 4.8 and 4.10 the fragility of 3 Lennard-Jones glass formers. It is now possible to compare these systems with the bidisperse Voronoi liquid.

4.2.3 Comparing models : the problem of units

Previously we compared the fragility of the Voronoi liquid while changing the composition of the mixture. As all these systems were expressed in the same units the comparison of the fragility was straightforward and we didn't need to pay attention to a rescaling of the relaxation time or diffusion coefficient. In the same way, we didn't rescale these transport quantities when we looked at the fragility of the Lennard-Jones glass formers as all these different systems were expressed in the terms of LJ units.

Now, if we want to compare the bidisperse Voronoi liquid with these different glass-formers, we have to render the different physical observables dimensionless. To this end, we need characteristic time and length scales which would share a common physical basis, because the scales given by the "natural" units of the models (σ_{AA} and $\tau_{AA} = \sqrt{m_{AA}\sigma_{AA}^2/\epsilon_{AA}}$ for the LJ-inspired models, $v^{1/3}$ and $(\gamma v)^{-1/2}$ for the Voronoi models) are not physically fully justified, and would not allow a fair comparison (see 4.2.4.1).

The more straightforward approach here to rescale the temperature is to use again the extrapolated temperature T_r. For making the relaxation time dimensionless, we can use the typical time extracted from the Arrhenian fit. In this way we can see how the

different systems behave regarding their fragility between two points of references, one taken in the high temperature limit when $\tau_\alpha/\tau_\infty = 1.0$ and the other one in the low temperature limit when $T_r/T = 1.0$.

In Figure 4.11 represents the scaled relaxation time as a function of T_r/T. We observe that:

- The KA system appears to be the stronger of the four models whereas AMLJ-0.80 is visibly the more fragile glass formers.
- For temperatures where data are available for the Wahnström model, WAHN and the bidisperse Voronoi liquid seem to have a similar behavior. However this observation is based on extrapolation for $T \to T_r$ and it is not obvious that this trend would be confirmed when $T \to T_r$ which corresponds to the range of temperature where the fragility is defined.
- We notice that when $T \to T_r$ the fragility of the bidisperse Voronoi liquid is closer to the one of AMLJ-0.80 than from KA, meaning that our model might be considered relatively fragile.

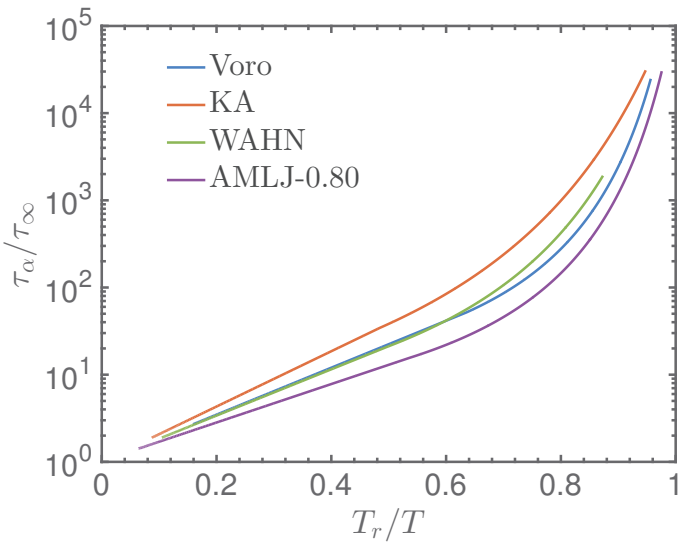

FIGURE 4.11: Angell-plot of the evolution of the scaled relaxation time as a function of T_r/T for the bidisperse Voronoi liquid and the 3 LJ glass-formers.

To confirm the previous observations we look now at the diffusion coefficient D that we have rescaled by D_∞. The evolution of D/D_∞ as a function of T_r/T is shown in Figure 4.12.

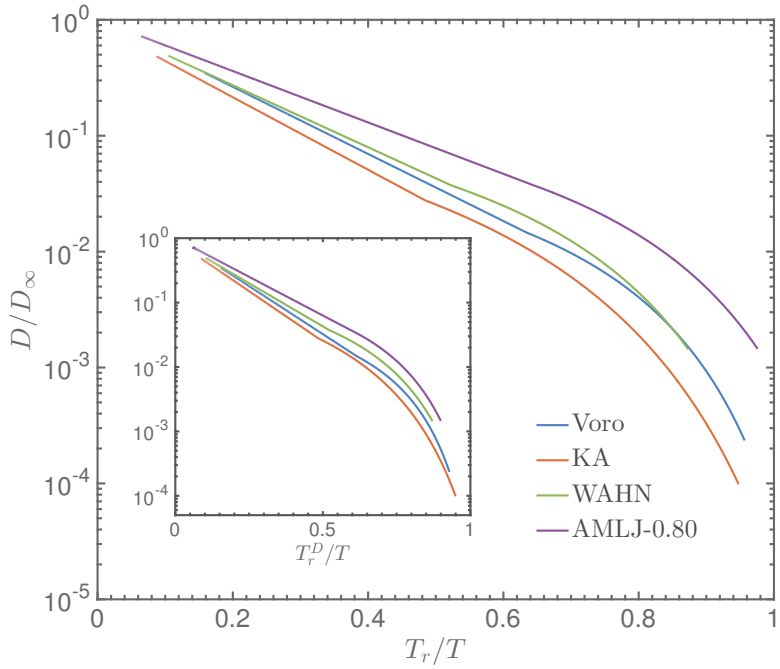

FIGURE 4.12: Angell-plot of the scaled relaxation diffusion coefficient as a function of T_r/T for the bidisperse Voronoi liquid and the 3 LJ glass-formers. Inset: same representation but the reference temperatures are the ones computed from the diffusion coefficient. Values are shown in Table 4.6.

Contrary to the relaxation time, it is less obvious that for $T = T_r$ all the curves would collapse on the same point. This is not a surprise, as it is well-known for supercooled liquids that there is not only one intrinsic time scale which would be given by the structural relaxation time τ_α computed at $k = k^*$. Therefore other observable may relax on shorter time-scale and this may be the case for the diffusion coefficient. A better choice for T_r would be for instance, the one defined arbitrarily when $D(T = T_r^D) = 10^{-5}$ where the values of $D(T_r)$ would be extrapolated from equation 4.10.

	Voro	KA	WAHN	AMLJ-0.80
T_r^D	0.771	0.445	0.521	0.294

TABLE 4.6: Reference temperature T_r^D extracted from the diffusion coefficient when $D(T = T_r) = 10^{-5}$.

When comparing Figure 4.12 and Figure 4.11 we observe that:

- The Kob-Andersen mixture is still the stronger glass formers whereas AMLJ-0.80 is the more fragile one. The Wahnström system has a fragility intermediate between those last two systems.

- Regarding the diffusion coefficient, when $T \to T_r$ the fragility of the bidisperse Voronoi liquid seems to be closer from KA. This is the opposite behavior of the one found for the relaxation time.

The last point suggests that there is a difference of behavior depending on the scale observed. When we are probing the microscopic scales, that is when we are looking at the relaxation time, the bidisperse Voronoi liquid has a fragility similar to the one of AMLJ-0.80, a LJ glass formers known to be relatively fragile. On the other hand when we are investigating hydrodynamic limit by looking at the diffusion coefficient, we notice that our system becomes less fragile and is comparable to the KA model.

This difference of behavior for the two transport quantities points to the weakness of a description in terms of fragility and reminds that Angell-plots are firstly a tool to sort systems and see how they behave qualitatively with respect to each other.
However the idea of representing transport quantities with respect to corresponding states, as for instance the glass transition temperature, is crucial to ensure efficient comparison among different classes of systems. In the case of the comparison of the Voronoi liquid with the LJ glass-formers, the breakdown of the Angell-plot representation suggests that the corresponding states chosen were probably not adequate.

One immediate objection to the classical Angell representation is that we compare systems with respect to a unique corresponding state that carries information of what happens at low temperature. Moreover, the corresponding state is chosen arbitrary, with an "anthropic" criterion $\tau/\tau_\infty \sim 10^4$ which cannot be satisfactorily. In computer simulation studies, we can benefit from the fact that many different observables are easily computed, and try to use for each temperature probed microscopic length and time scales which would be well adapted to each temperature probed. In any case an nondimensionalization of the axis $1/T$ and τ_α *must* be provided, otherwise the purpose of comparing different models cannot be undertaken.

In what follow we look for such quantities and we focus particularly on finding microscopic time and energy scales that would have a common definition to all the different systems of glass-formers.

4.2.4 Other nondimenzionalization of microscopic time and energy scales

Another simple possible dimensionless representation consists on rescaling relaxation time by τ_∞ and rescaling the temperature by E_∞/k_B where E_∞ corresponds to the height of the energy barriers in the Arrhenian regime. This implies first that all the different curves should collapse onto a master curve in the Arrhenian regime and then,

the departure from this master curve would mark the entrance in the super-Arrhenian regime. This is indeed what is observed in Figure 4.13.

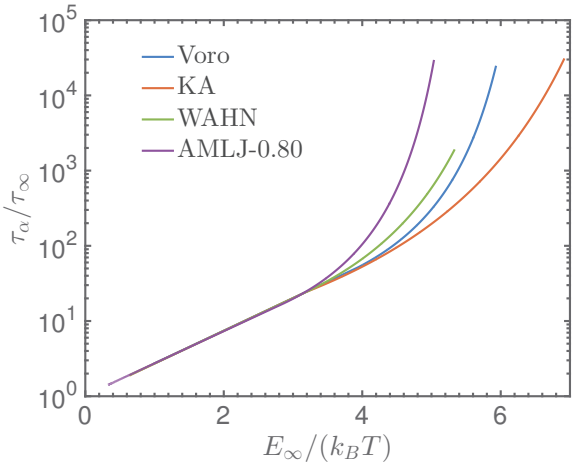

FIGURE 4.13: Evolution of the scaled relaxation time $\tau_/\tau_\infty$ as a function of the scaled temperature $E_\infty/(k_BT)$.

At first sight, one could say that the stronger the departure from the master curve, the more fragile the glass former. If this appears to be true for the LJ systems, it is not the case for the bidisperse Voronoi liquid and the order found in Figure 4.11 is apparently not conserved in this representation. This raises question about the relevance of the Angell plot, which seems not sufficient to capture all the phenomenology that occurs upon cooling. One could also a argue that rescaling T by E_∞ could make no sense at lower temperature as the structure of the liquids may have substantially changed in comparison to high temperature states.

In any cases, it could be safer to do a step backward and to try to make dimensionless quantities from 1) the fastest characteristic time of the system: the inverse of the Einstein frequency, and 2) a characteristic energy that would be shared by all the glass formers.

4.2.4.1 The Einstein-frequency a common microscopic time scale

In the short times limit when $t \to 0$, the velocity autocorrelation of a tagged particle can be expanded at the second order in t in the following way [39]:

$$\langle \boldsymbol{v}_i(t)\boldsymbol{v}_i(0)\rangle = \langle \boldsymbol{v}_i^2(0)\rangle - \langle \dot{\boldsymbol{v}}_i^2(0)\rangle(t^2/2) + O(t^4) \tag{4.13}$$

where $\langle \boldsymbol{v}_i^2(0)\rangle = 3k_BT/m$ corresponds to the square of the thermal velocity and $\langle \dot{\boldsymbol{v}}_i^2(0)\rangle = (3k_BT/m)\Omega_0^2$ with Ω_0 is the Einstein frequency. Ω_0^{-1} corresponds to the typical time at

which particles quit the ballistic regime and experience "collisions" with their neighbors [39]. Consequently it is the microscopic time for which a tagged particle starts to feel the presence of its surrounding environment. This microscopic time is accessible for all glass-formers and more important the physical meaning is preserved whatever the mixture under interest. Therefore it appears as a good candidate for rescaling the time.

Ω_0^{-1} can easily be computed from the knowledge of the forces:

$$\Omega_0^{-1} = \sqrt{\frac{3k_BT}{\langle \boldsymbol{F}_i^2(0)\rangle/m_i}} \tag{4.14}$$

Ω_0^{-1} has been computed for the Voronoi liquid and for the LJ glass-formers. Results are shown in Figure 4.14 where Ω_0^{-1} is rescaled on purpose by the characteristic time units τ_{voro} and τ_{LJ} defined above.

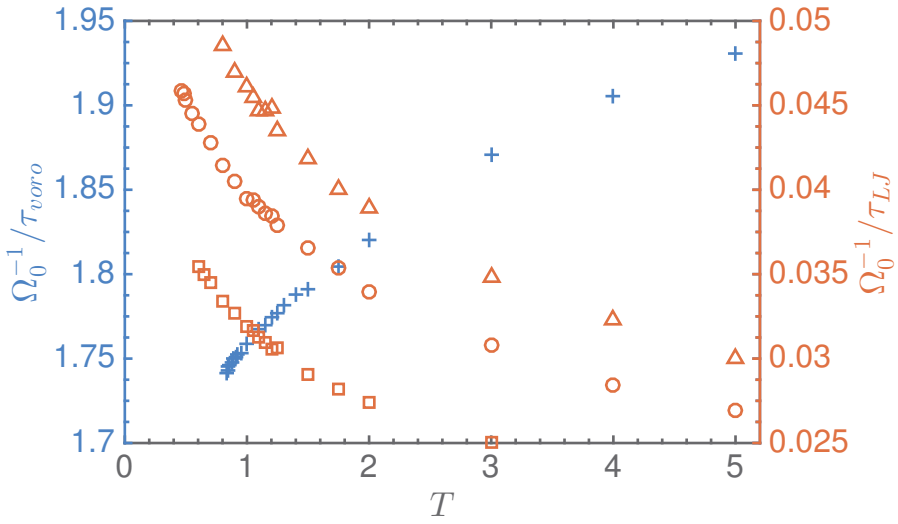

FIGURE 4.14: Evolution of the inverse of the Einstein frequency rescaled by the intrinsic time units as a function of temperature for the bidisperse Voronoi liquid (blue +) and for LJ systems (orange) KA (○), WAHN (□), AMLJ-0.80(△) .

Figure 4.14 is a typical illustration of the difference of the intrinsic time units calculated above as we see that $\Omega^{-1}/\tau_{voro} \sim 30\Omega^{-1}/\tau_{LJ}$. We immediately see that, as the proper intrinsic timescale is Ω_0^{-1}, the choice of τ_{LJ} and τ_{voro} to nondimentionalize the temporal observables would introduce a spurious large discrepancy factor.

Another representation of Ω_0^{-1} without rescaling is shown in Figure 4.15. We observe that in this case the values of Ω_0^{-1} expressed in the system units are of the same order.

This is strongly supporting the choice of the inverse of the Einstein frequency as a microscopic time of reference that would be common to all the glass-formers.

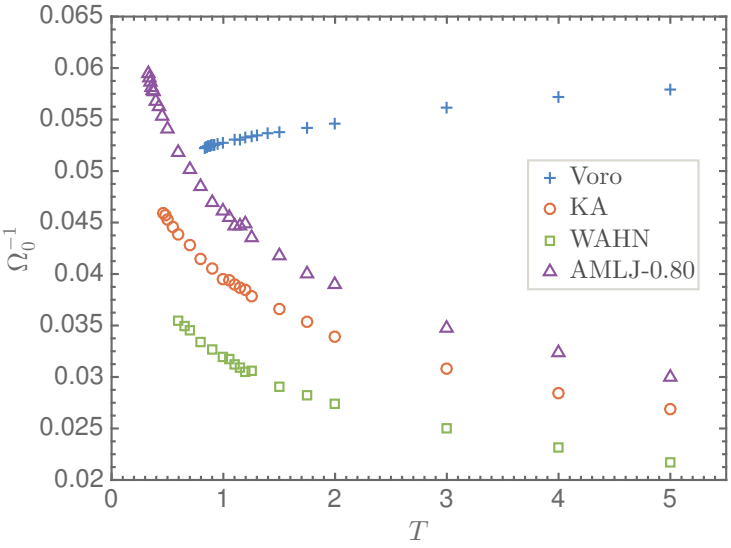

FIGURE 4.15: Evolution of the inverse of the Einstein frequency as a function of temperature for the bidisperse Voronoi liquid and for the 3 LJ glass formers. Notice that the choice of $\gamma = 1000$ put the typical values of Ω_0^{-1} close to that of LJ systems.

When looking into the qualitative behavior of Ω_0^{-1} we notice that it is increasing with temperature for the bidisperse Voronoi liquid whereas we observe the strict opposite for the LJ models. This is related to the interplay between kinetic contribution and the different nature of potentials, i.e soft-core vs. hard-core potentials.

To better understand how these potentials act, one can imagine the case where the nearest neighbors of a tagged particle are frozen. As a result, the tagged particle can only oscillate in its cage and it experiences a local effective potential whose form is represented in Figure 4.16. Apart from the immediate neighborhood of the minimum, both hard-core and soft-core potentials show anharmonicity. In the case of an hard-core potential (left), the potential is steeper than quadratic whereas the soft-core potential (right) is milder than the quadratic one.
As a result, for the hard-core potential, the period of the oscillations is decreasing when the temperature is increased, whereas for soft-core potential period is increasing with temperature.

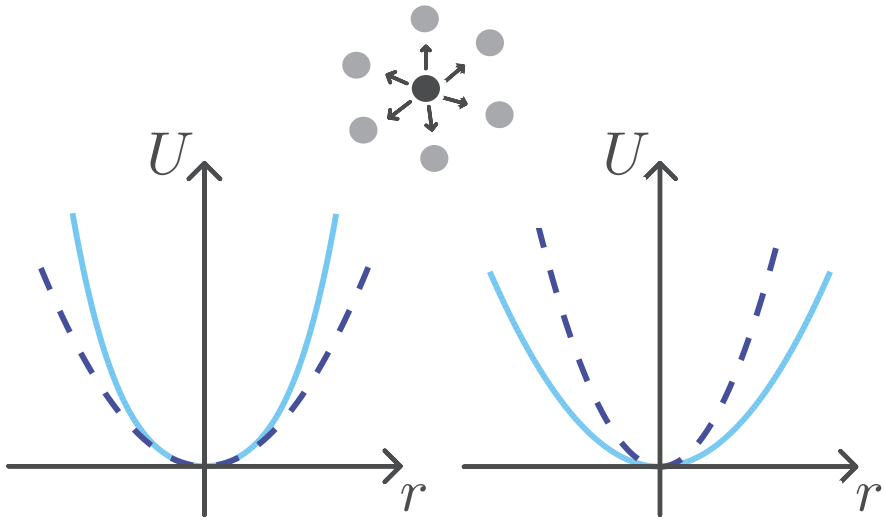

FIGURE 4.16: Sketch of the difference in the effective potential felt by a particle whose neighborhood has been frozen (upper schema). At left the effective potential is hard-core (solid line) whereas at right it is a soft-core potential (solid line). In both cases, the dashed line represents the harmonic approximation.

The inverse of the Einstein frequency can reasonably play the role of the microscopic time scale that we were looking for. Now it remains to define the microscopic energy length scale. Three plausible candidates have been identified: the typical microscopic work, the fluctuations of the potential energy and the high-frequency shear modulus. The choice of these quantities, their efficiency as energy length scale and the associated results are discussed in more details in what follows.

4.2.4.2 Microscopic energy length scale: Typical microscopic work

One of the easiest energy scale E_μ possible is related to the work exerted on a tagged particle to observe a displacement on a characteristic length ℓ, that is $E_\mu \sim \sqrt{\langle F^2(0)\rangle}\ell_c$ where $\boldsymbol{F}$ is the force exerted on a particle. There is no obvious choice of ℓ and one could use for instance chose σ_{AA} in the case of LJ systems. However as mentioned above a meaningful characteristic distance would be the one associated with the mean inter-particle distance $\ell = v^{1/3}$ which approximately corresponds to the distance a particle may travel before experiencing a "collision" with one of the neighbors.

As a consequence the characteristic energy scale E_μ could be written as:

$$E_\mu = \sqrt{\langle F^2(0)\rangle} v^{1/3} \tag{4.15}$$

In Figure 4.17 we have represented the evolution of $\sqrt{\langle F^2(0)\rangle}v^{1/3}$ as a function of the temperature for the Voronoi system and for the 3 other LJ glass formers. We observe that the energy required to displace a particles on the average inter-particle distance is decreasing when the temperature is lowered.

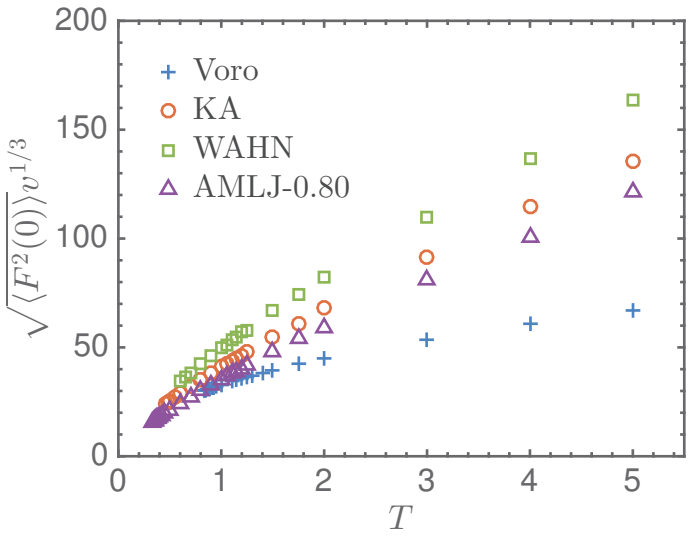

FIGURE 4.17: Evolution of the typical energy $E_\mu = \sqrt{\langle F^2(0)\rangle}v^{1/3}$ with temperature for the Voronoi liquid and the 3 LJ glass formers.

The evolution of the typical work while increasing the temperature is easily explained by the shape of the potentials shown in Figure 4.16. As a matter of fact, at low temperature, the particles vibrate around their equilibrium position and consequently explore a part of the potential $U(r)$ which is nearly flat or slightly curved. As a result the force which is the derivative of $U(r)$ is relatively weak. As the temperature is increased, the force increases as particles are able to explore part of $U(r)$ where the local slope of $U(r)$ is relatively important. Obviously this slope is more pronounced for hardcore potentials explaining why the increase of $\sqrt{\langle F^2(0)\rangle}v^{1/3}$ is larger for LJ glass-formers than for the bidisperse Voronoi liquid.

We thus propose to rescale the temperature by using E_μ/k_B. In Figure 4.18 is represented the scaled relaxation time as a function of the scaled temperature. We observe that:

- There is a clear distinction between the bidisperse Voronoi liquid and the LJ systems.
- However the curve of the Wahnström is somehow different as its high temperature regime does not collapse on the corresponding regime of KA and AMLJ-0.80.
- The marked increase of $\Omega_0\tau_\alpha$ for given values of $E_\mu/(k_BT)$ is enhanced by the decrease of E_μ with decreasing T. However for the LJ systems, it is reduced by

the simultaneous decrease of Ω_0^{-1}. The effect is the opposite for the bidisperse Voronoi liquid.

In conclusion we notice that Figure 4.18 shows that there is no universality among different classes of glass formers at the neighborhood of glass transition. Moreover we see that the sole microscopic parameters Ω_0^{-1} and E_μ are not sufficient to convey the whole phenomenology of what happens upon cooling. However, from a physical point of view, the representation in Figure 4.18 is a more reasonable comparison of widely different systems that those previously shown (Angell plot or (τ_∞, E_∞) scaling).

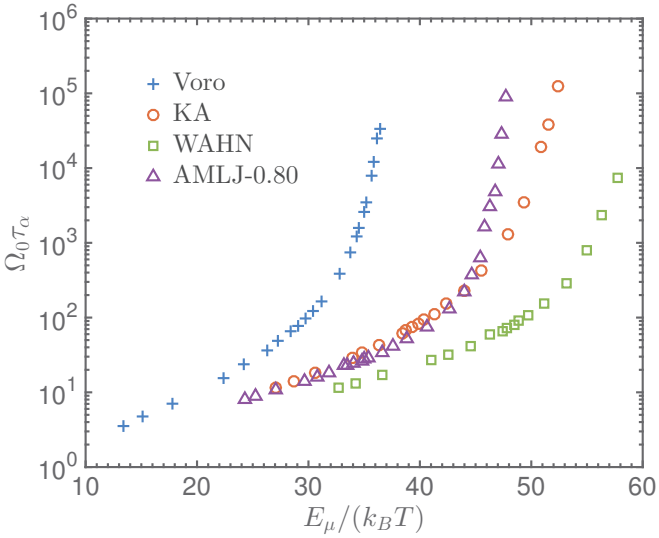

FIGURE 4.18: Representation of the relaxation time rescaled by the Einstein frequency as function of the inverse of the temperature rescaled by E_μ/k_B.

4.2.4.3 Microscopic energy length scale: Fluctuations of the potential energy

Another way to propose an energy scale is via the heat capacity at constant volume C_v^e as we know it is related to the average of the square of the fluctuations of the potential energy $\langle \delta E_P^2 \rangle$ through equation 2.22 in the canonical ensemble, thus we can write the fluctuation of the potential energy as $\sqrt{\langle \delta E_P^2 \rangle} = T\sqrt{k_B C_v^e}$. They provide a natural energy scale that we might use to define a microscopic energy scale.

In Figure 4.19 is shown the heat capacity at constant volume per particle as a function of the scaled temperature T/T^* (where T^* is the crossover temperature determined for the relaxation time τ_α) for the different systems under interest.

The increase of C_v^e is more pronounced for the bidisperse Voronoi liquid than for the LJ glass formers. Nevertheless AMLJ-0.80 shows also an important increase of C_v^e for

temperature just below T^*. In Chapter 2 the increase of the specific heat has been related to the rapid decrease upon cooling of $\langle e_{IS} \rangle$ the average energy of the inherent structures for temperatures below the crossover temperature T^*. It appears thus that the decrease of $\langle e_{IS} \rangle$ is more important for the Voronoi liquid and AMLJ-0.80 than for KA and WAHN. This will be confirmed during the exploration of the potential energy landscape presented in Chapter 5.

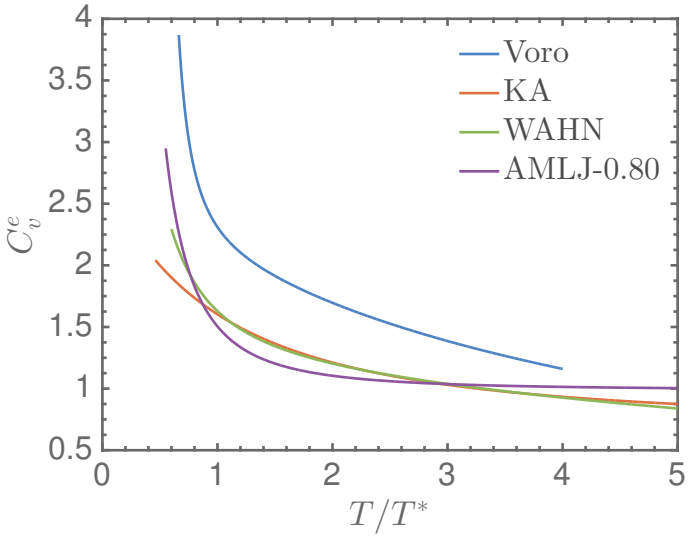

FIGURE 4.19: Representation of the heat capacity at constant volume as a function of the scaled temperature for the bidisperse Voronoi liquid and the LJ glass-formers.

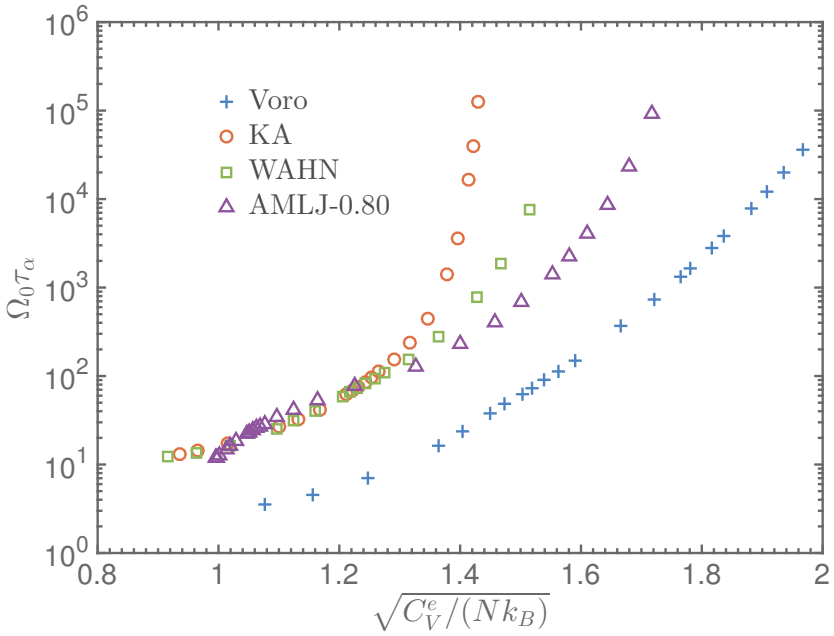

FIGURE 4.20: Scaled relaxation time as a function of the scaled temperature $\sqrt{C_V^e/(Nk_B)}$.

As $T\sqrt{k_B C_v^e}$ is a reasonable energy scale, we investigate the behavior of $\Omega_0\tau_\alpha$ as a function of $\sqrt{\langle \delta E_P^2 \rangle}/(k_B T)$ which is can also be rewritten as $\sqrt{C_v^e/(Nk_B)}$ where we have introduced the number of particles for questions of intensivity. Results presented in Figure 4.20 suggest that there is a clear separation between the different classes of system. Moreover we observe that among the LJ glass-formers, the high temperature behavior (equivalent to the low $\sqrt{C_v^e/(Nk_B)}$ behavior) appears similar for the different systems.

We notice also the presence of an exponential regime for the four glass-formers. This regime is for instance well-visible, in Figure 4.20, for the bidisperse Voronoi liquid for $\sqrt{C_v^e/(Nk_B)} \in [1.40, 1.70]$. This implies that $\Omega_0\tau_\alpha \sim \exp(A\sqrt{C_v^e/(Nk_B)})$. Therefore we propose to investigate this regime by testing the following fitting function:

$$\ln(\Omega_0\tau_\alpha) = A\sqrt{C_v^e/(Nk_B)} - B \equiv \frac{A}{T}\left[\sqrt{\langle \delta E_P^2 \rangle} - \frac{B}{A}T\right] \tag{4.16}$$

where A and B are fitting parameters. A can be interpreted as the average numbers of particles concerned by the fluctuation of energy $\sqrt{\langle \delta E_P^2 \rangle}$. The introduction of the parameter B can be seen as a renormalization of Ω_0^{-1} if $B < 0$ and $|B| \ll 1$. In the other cases, we must consider the entropic contribution B/A.

In Figure 4.21 is shown the results of this fit for the bidisperse Voronoi liquid and the Wahnström model.

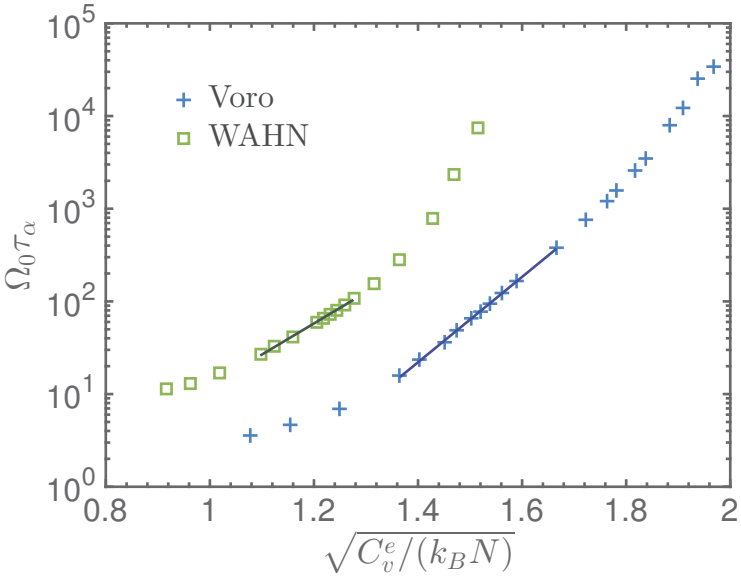

FIGURE 4.21: Scaled relaxation time as a function of the scaled temperature $\sqrt{C_V^e/(Nk_B)}$. The solid lines correspond to the exponential fit.

For sake of clarity we do not show the results for KA and AMLJ-0.80. Values of the fitting parameters A and B are presented in Table 4.7.

Systems	Voro	KA	WAHN	AMLJ-0.80
Fit interval $\sqrt{C_v^e/(Nk_B)}$	$[1.40, 1.70]$	$[1.10, 1.28]$	$[1.10, 1.26]$	$[1.06, 1.23]$
Fit interval T	$[1.00, 2.00]$	$[0.90, 1.50]$	$[1.00, 2.00]$	$[0.60, 1.50]$
A	10.5	10.8	7.7	6.5
B	11.5	8.9	5.2	3.6
B/A	1.10	1.21	1.48	1.81

TABLE 4.7: Fitting parameters found by using equation 4.16 for the fit of $\ln(\Omega_0\tau_\alpha)$ as a function of $\sqrt{C_v^e/(Nk_B)}$. The fit intervals are given in term of $\sqrt{C_v^e/(Nk_B)}$ and with the corresponding T-interval.

- For both Voro and KA we observe that the typical energy fluctuation involves ≈ 11 particles. This number drops to ≈ 8 for WAHN and ≈ 7 for AMLJ-0.80.
- We notice that parameter B cannot be considered here as a rescaling of Ω_0^{-1} as it would lead to times $\ll \Omega_0^{-1}$. This would have no physical meaning as Ω_0^{-1} corresponds the smallest accessible time scale of systems.
- Therefore we consider the ratio B/A which corresponds to a positive entropic contribution ≈ 1 or 2 for the different glass-formers.

Taking into account the previous observations, we could imagine the following scenario regarding the crossing of energy barrier. The initial configuration corresponds to a local minimum of the free energy landscape. Fluctuations of the potential energy would locally affect ≈ 10 particles. In the range of temperatures considered, this local supply in energy would enable those particles to rearrange locally and thus to have access to other new configurations of higher energy. As a result entropy is thus increased.

This scenario remains hypothetical but it could be tested by looking at the correlation between the fluctuations of the potential energy and the local rearrangements that occur in the liquid.

4.2.4.4 Microscopic energy length scale: Instantaneous shear modulus

The instantaneous shear modulus G_∞ corresponds to the shear modulus measured at $t = 0$ when the liquid does not have time to flow [84]. G_∞ is defined from the non-diagonal elements of the stress-tensor as [85]:

$$G_\infty = \frac{\langle \sigma_{xy}(0)^2 \rangle}{V k_B T} \tag{4.17}$$

As this quantity is measured on very short-time scale, it is a good candidate to define a microscopic energy scale as $G_\infty v$.

The idea of rescaling the temperature with respect to G_∞ was already suggested twenty years ago by Dyre when he introduced the shoving model [86], an elastic model used to describe the activated flow events that could occur for highly viscous liquids. The main idea of this model is that the appearance of flow events is related to the creation of an extra volume. To create this volume, particles shove aside the surrounding liquid to increase the available volume [86]. The work associated to this process corresponds to the activation energy [84]. As the flow event occurs on fast time scale, the surrounding liquid behaves like a solid and solid-state elasticity could be used to calculate the shoving work which is related to the shear modulus [84].
As a consequence of these observations Dyre proposed to express this T-dependent activation energy as a function of G_∞ [84]:

$$E(T) = V_C G_\infty(T) \tag{4.18}$$

where V_C is referred as the characteristic volume and it is assumed to be temperature independent [86].

In Figure 4.22 we have represented the dimensionless quantity $G_\infty/(\rho T)$ as a function of T/T^*. Rescaling T by the crossover temperature is motivated by the fact that the energy barriers below T^* are known to be temperature-dependent. As in the shoving model the energy barriers $\propto G_\infty(T)$, it is interesting to see how this quantity evolves above and below T^*.

We observe that all the systems exhibit the same decreasing behavior with temperature however values of G_∞ are weaker for the bidisperse Voronoi liquid than for the LJ glass-formers. We notice moreover a collapse onto the same master curve for the three LJ systems.

Shoving model has already been verified by experimental measurements as for instance on metallic glasses and molecular liquids [86–88]. Therefore we test numerically the shoving model for the bidisperse Voronoi liquid and the LJ glass-formers. In Figure 4.23 is represented the scaled relaxation time as a function of $G_\infty v/T$.

We note that once again there is a clear disparity between the Voronoi liquid and the LJ systems. We recall that the shoving model predicts that the relaxation time is given by $\tau_\alpha \sim \exp(G_\infty(T)/k_B T)$ as consequence a linear behavior is expected for all the systems in the semi-log representation in Figure 4.23.

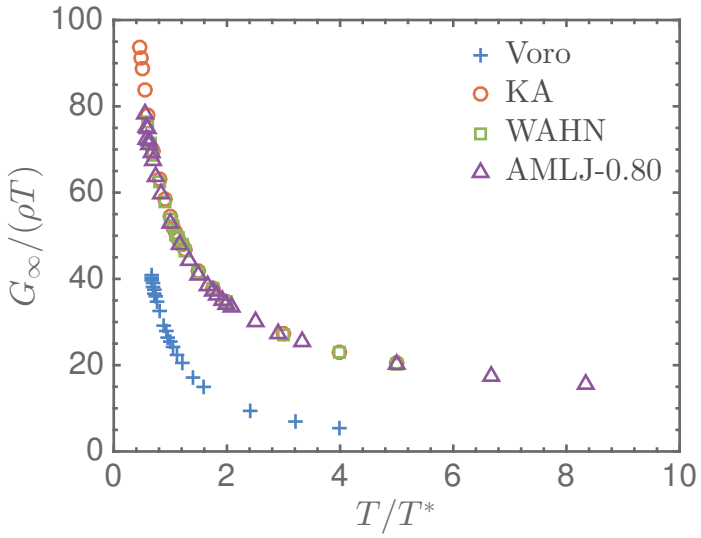

FIGURE 4.22: Evolution of the scaled instantaneous shear modulus as a function of the scaled temperature.

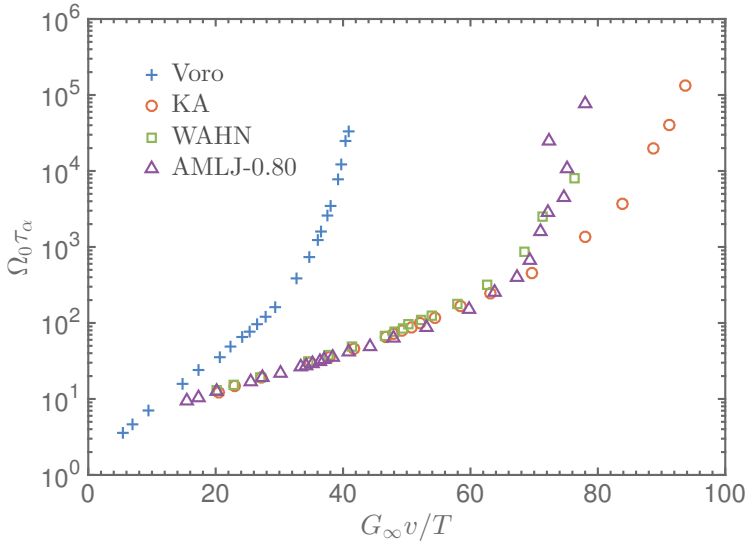

FIGURE 4.23: Evolution of the scaled relaxation time as a function of $G_\infty v/T$.

We observe that whatever the nature of the glass-former the predictions of the shoving model are valid from high temperature to intermediate temperature a bit below the crossover temperature. Moreover for the LJ systems there is a good collapse between the three systems on the same range of temperature where the shoving model applies.

The breakdown of the shoving model comes from the fact that we didn't use the appropriate definition of the instantaneous shear stress. Recently Puosi and Leporini [89] have shown that the right value of $G_\infty(T)$ to use corresponds to the plateau value $G_{\infty,p}(T)$

of $(Vk_BT)^{-1}\langle\sigma_{xy}(t)\sigma_{xy}(0)\rangle$. They found that rescaling the temperature by the plateau value $G_{\infty,p}(T)$ enables a good description, in terms of the shoving model, of the structural relaxation time of a melt composed of fully flexible linear chains of soft spheres. This observation is in agreement with experiments for which the shortest times accessible correspond to plateau values [88]. As a consequence further investigations could be done by computing $(Vk_BT)^{-1}\langle\sigma_{xy}(t)\sigma_{xy}(0)\rangle$ and then rescaling the temperature by the plateau value $G_{\infty,p}(T)$.

We attempted to rescale the transport quantity and the temperature in order to compare the different glass-formers on the one hand. On the other hand the idea was to find a set of parameters (time, temperature) that would make arise a common framework for all the systems. However we notice that for each of the representation that we used points towards the different natures that exist between the bidisperse Voronoi liquid and models built from the LJ potential. In this sense we face the fundamental open question related to glass-transition problem, *is there a fundamental mechanism responsible for the dynamical arrest that would be common to all the glassforming liquids ?*

In what follow we pursue our description and comparison of the Voronoi liquid by having a look to the Stokes Einstein relation which is known to be a sensitive marker of dynamical heterogeneties.

4.3 Stokes-Einstein relation

As mentioned before, both structural relaxation time and diffusion coefficient depart from the Arrhenian temperature below T^*. Regarding the results on fragility we already know that the deviation of both quantities is likely to differ one from each other. A way to quantify this difference is to use the Stokes-Einstein relation which links the diffusion coefficient D to the viscosity η through the following relation:

$$D = \frac{k_BT}{6\pi R\eta} \tag{4.19}$$

where R is the radius of the particle [40]. Physically this relation implies that two different measurements of the relaxation time R^2/D and $\eta R^3/T$ lead to the same timescale up to constant $1/6\pi R$ [73].

The Stokes-Einstein relation requires at first sight the knowledge of the viscosity η that we didn't compute. However we have access to the structural relaxation time which is linked to the viscosity via $\eta = G_\infty\tau_\alpha$ where G_∞ is the instantaneous shear modulus defined above. The evolution of G_∞ as a function of temperature has been computed in the previous section, see Figure 4.22. In comparison to the relaxation time which

increases of 3-4 orders of magnitude upon cooling, G_∞ observes a very slow variation in such a way that it can be considered constant and thus $\eta \sim \tau_\alpha$. Therefore a good way to check the validity of the Stokes-Einstein relation is to compute the ratio $D\tau_\alpha/T$ and to see to what extent it remains constant over the whole range of temperature investigated.

In Figure 4.24 we have represented the Stokes-Einstein relation rescaled by $G_\infty v^{1/3}$ as a function of T/T^*

- At high temperature for $T > T^*$ the presence of a plateau suggests that the Stokes-Einstein relation is valid and therefore $D\tau_\alpha/T \sim C^{te}$.
- When the temperature is decreased below T^* we observe the departure from the plateau meaning that the Stokes-Einstein breaks down.
- When looking at the deviation we notice that the more fragile the mixture, the more important the breakdown. Indeed it is particularly true for AMLJ-0.80 which has the highest values of the Stokes-Einstein ratio, 10 times more important than the other glass-formers.
- In comparison with the Kob-Andersen mixture and the Wahnström model, the bidisperse Voronoi shows also a marked deviation from its plateau value.

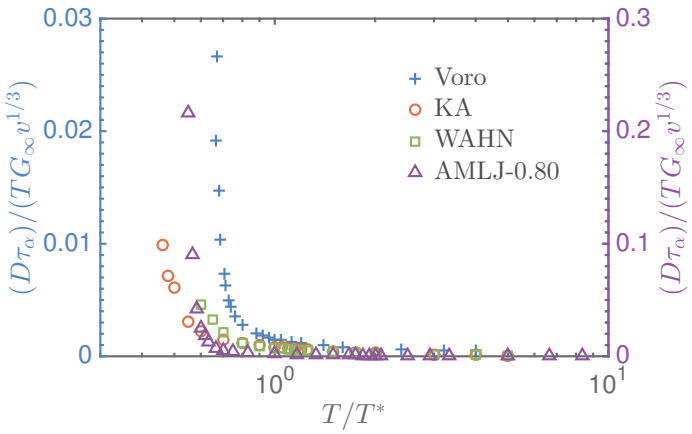

FIGURE 4.24: Semi-log representation of the scaled Stokes-Einstein relation as a function of the scaled temperature T/T^*. Note that the values at high temperature are very small 10^{-4}.

The breakdown of the Stokes Einstein relation is associated with the presence of dynamical heterogeneities [8]. Liquid and glassy systems present disordered structures and even if they are composed of identical particles, two tagged particles may experience two different local environments [20]. At high temperature, these differences are negligible and a tagged particle taken at random is representative of the other one. However upon cooling a tagged particle chosen at random may have a behavior completely different

from another one [20]. This is for instance the case when investigating the mobility of particles. It has been shown, experimentally for molecular liquids [10, 90], colloids and granular medial [91, 92] and also numerically [93, 94], that domains where particles are relatively mobile coexist with domains where particles only vibrate around their equilibrium position.

A typical sketch that would represent the different environments in a supercooled liquid is presented in Figure 4.25. Fast, intermediate and slow domains coexist and when one compute the usual microscopic quantities, more importance can given to a particular type of domain. It is for instance the case of the diffusion coefficient which is dominated by the diffusion that occurs in the fast domains whereas the relaxation time is associated to the relaxation of the slowest domains [8, 20]. Therefore the breakdown of the Stokes Einstein occurs as different environments are probed [8].

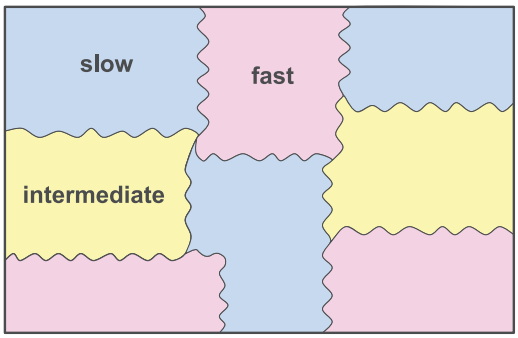

FIGURE 4.25: Sketch of the different domains in the liquid.

4.4 Individual and collective relaxations

Up to now, we only focussed on the relaxation time extracted from the density correlators computed for wavevector k^* corresponding to the maximum of the structure factor.
It is also interesting to investigate collective and individual relaxation times evaluated for other wavevectors. To do so we compute respectively the coherent and incoherent intermediate scattering function for several $k \in [2\pi/L; 14.0]$. The relaxation times τ are still defined as the value of the time when $F(k, t = \tau)/S(k) = 0.1$ (or $F_s(k, t = \tau) = 0.1$).

In Figures 4.26 and 4.28 we have represented for several temperatures respectively the individual and the collective relaxations rescaled by the structural relaxation time τ_α as a function of the wavevector rescaled by k^*.

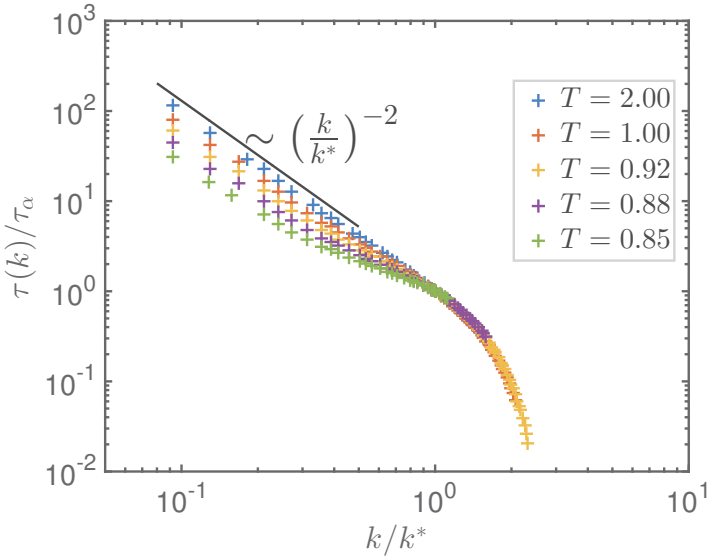

FIGURE 4.26: Scaled individual relaxation time as a function of the scaled wavevector computed for different temperatures. The black line represents a relaxation $\sim k^2$.

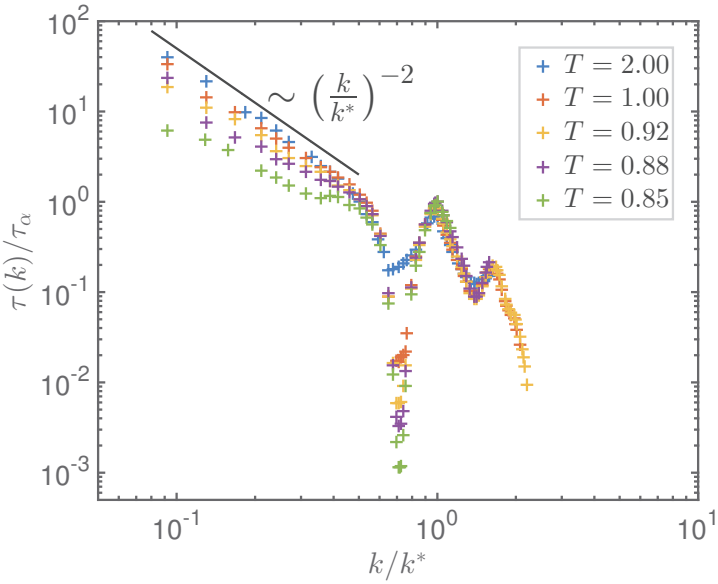

FIGURE 4.27: Scaled collective relaxation time as a function of the scaled wavevector computed for different temperatures. The black line represents a relaxation $\sim k^2$.

- For both individual and collective relaxations, we observe that for $k \geq k^*$ all the relaxation times rescaled by the structural relaxation time fall onto the same master curve. This suggests that the whole phenomenology that occurs at large wavevectors is governed by parameters τ_α and k^*.

  For $k \leq k^*$, we note the presence of an apparent power-law regime for which the power increases with the temperature.

- Whereas the individual relaxation decreases in a monotonic way as k is increased, the collective relaxation exhibits extrema and among them a very deep minima for wavevector $k \sim 4.90$. When looking in Figure 4.28 at the coherent structure factor $F(k = 4.90, t)$ computed for $k = 4.90$ we notice the presence of very fast decay followed by numerous oscillations reminiscent of the relaxation of the hydrodynamic sound modes at low k.

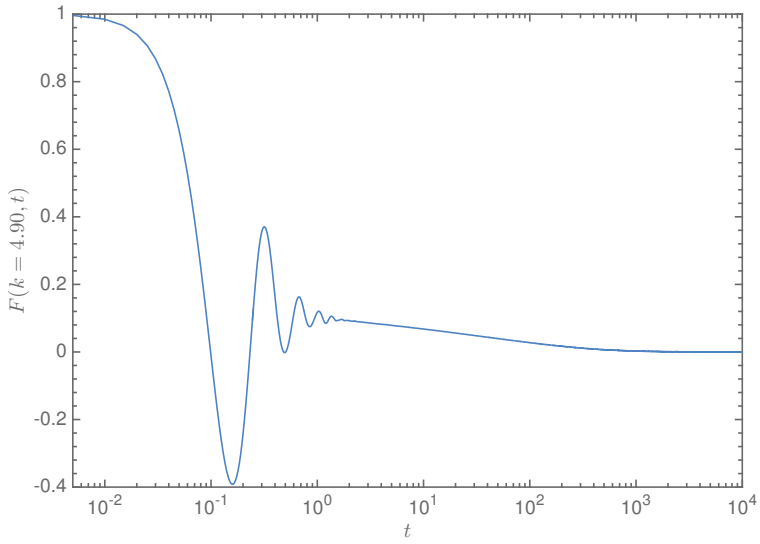

FIGURE 4.28: coherent intermediate scattering function computed at $k = 4.90$ for $T = 0.85$.

By comparing our results with the ones obtained for a polydisperse system of quasi-hard spheres studied by Weysser *et al.* [3] we notice a strong similarity between the individual relaxation of two systems as it is visible in Figures 4.29 and 4.30. The collective relaxation is relatively similar, apart from the huge decrease in the mesoscopic range. This suggests that for $k \sim 4.90$ the collective relaxation does not couple to the structural relaxation. A possible explanation of this phenomenon would be that the associated length $2\pi/4.90$ be exclusively associated to a transition state. This way, the relaxational dynamics of that wavelength would not couple to the slow dynamics induced by structural relaxation.

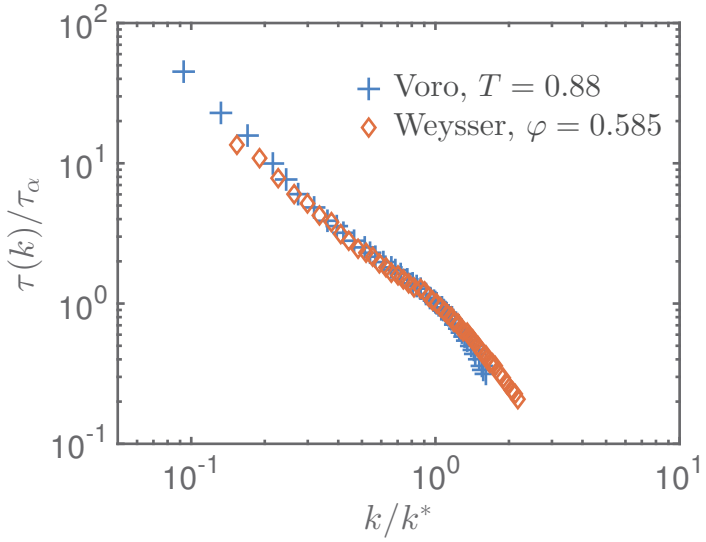

FIGURE 4.29: Comparison of the individual relaxation times obtained for the bidisperse Voronoi liquid at $T = 0.88$ and the polydisperse system of quasi-hard spheres of Weysser *et al.* [3] at $\varphi = 0.585$.

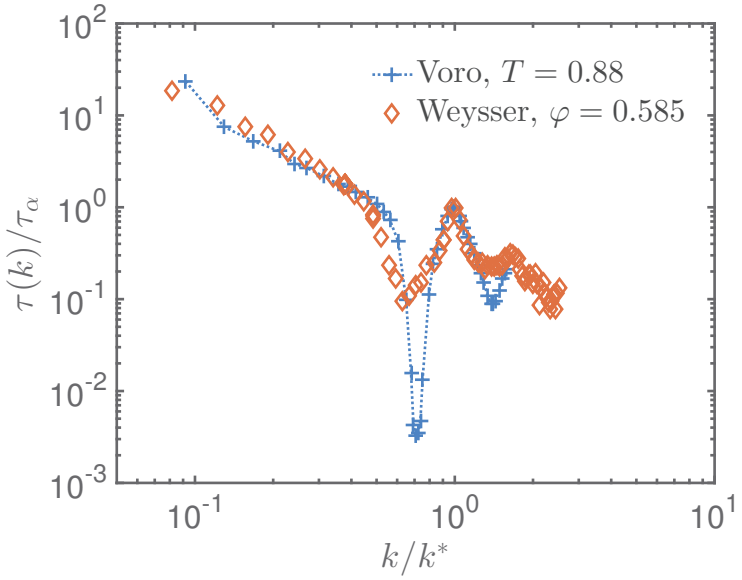

FIGURE 4.30: Comparison of the collective relaxation times obtained for the bidisperse Voronoi liquid at $T = 0.88$ and the polydisperse system of quasi-hard spheres of Weysser *et al.* [3] at $\varphi = 0.585$.

4.5 Ideal Mode Coupling Analysis

Previously the slowing down of the dynamics was described by mean of phenomenological theories. Evolution of the structural relaxation time has been characterized by mean of simple physical approaches which mainly focused on the presence of temperature-dependent energy barriers. These qualitative approaches are leading to equations that can be used to describe experimental or numerical data [69].

The quest for a theory that would enable to make comparison with experimental results and predict (possible new) non trivial phenomena is still nowadays a challenge as for the moment a theory that would describe the whole phenomenology of the glass-transition is still missing [69]. However there is one theory, the Mode-Coupling Theory (MCT) that enables quantitative calculations and which provides predictions that can be tested.

The MCT takes into account two main observations:

1. the weak temperature dependence of the structural properties
2. at low temperature the separation of time-scales, i.e α-relaxation is much more larger than the microscopic one

As a result a description in term of slow varying variables is possible. By identifying the slow variable of the structural relaxation, the Mori-Zwanzig projection operator formalism [95, 96] can be applied and an exact equation for the motion of $F(q,t)$ can be found [97]:

$$\frac{d^2F(q,t)}{dt^2} + \frac{q^2k_BT}{mS(q)}F(q,t) + \frac{m}{Nk_BT}\int_0^t d\tau M(q,\tau)\frac{dF(q,t-\tau)}{dt} \tag{4.20}$$

where $M(q,t)$, the memory kernel, is related to the fluctuating force acting on the density field [73, 97].

In the present form equation 4.20 is impossible to solve [97]. Nevertheless in order to close the equation some approximations can be done by noticing that the fluctuating force contains products of the density fluctuations: In other words $M(q,t)$ contains slow modes and it is possible to project the fluctuating force onto the slowest mode. After projections the memory kernel contains four-point density terms but it is possible to factorize them into products of two-point density functions $F(q,t)$ [73, 97].

The previous approximations enable to derive the MCT self-consistent equations [97]:

$$\frac{d^2F(q,t)}{dt^2} + \frac{q^2k_BT}{mS(q)}F(q,t) + \int_0^t d\tau M(q,t-\tau)\frac{dF(q,t)}{dt} \tag{4.21}$$

with the memory kernel expressed as

$$M(q,t) = \frac{\rho k_B T}{16\pi^3 m} \int d\boldsymbol{k} |\tilde{V}_{\boldsymbol{q}-\boldsymbol{k},\boldsymbol{k}}|^2 F(k,t) F(|\boldsymbol{k}-\boldsymbol{q}|,t) \tag{4.22}$$

where

$$\tilde{V}_{\boldsymbol{q}-\boldsymbol{k},\boldsymbol{k}} = \{(\hat{\boldsymbol{q}}\cdot\boldsymbol{k})c(k) + \hat{\boldsymbol{q}}(\boldsymbol{q}-\boldsymbol{k})c(|\boldsymbol{q}-\boldsymbol{k}|)\} \quad \text{with} \quad c(q) = (1 - 1/S(q))/\rho \tag{4.23}$$

Equation 4.21 is thus an approximate equation of motion for $F(q,t)$ at wavevector q. The expression 4.22 of the memory kernel shows that the mode q is coupled to the product of mode k by mode $|\boldsymbol{q}-\boldsymbol{k}|$ [98]. The coupling coefficients $c(q)$ are fully determined by the static structure factor of the glass former [98].

It is important to stress that the previous equations have been derived for a single component liquid. Generalization to binary mixture has been proposed by Barrat and Latz [99] and a general discussion can be found in the review written by Das[100].

Solutions of equations 4.21 have been discussed by Leutheusser [101] and Bengtzelius *et. al.* [102] and in what follow we propose to test for the bidisperse Voronoi liquid the predictions of the MCT.

4.5.1 Theoretical predictions of MCT

In its ideal form MCT predicts for the correlator of density fluctuations $\phi_q(t)$ [1] a transition from an ergodic to a non-ergodic phase at a critical temperature T_c, called the mode-coupling temperature [97]:

$$\lim_{t\to\infty} \phi_q(t) = \begin{cases} 0 & \text{for } T > T_c \\ f_q(T) & \text{for } T \leq T_c \end{cases} \tag{4.24}$$

This transition means that for temperature above T_c, the intermediate structure factor $\phi_q(t)$ may relax. In the long-time limit a tagged particle would transit through different cages of neighbors and would forgot about its initial position. This loss of memory is characteristic of the liquid phase. Below T_c the scenario is different, there is no complete decay of the density fluctuations [98]. A particle remains trapped in its surrounding environment and vibrates around its initial position. Consequently the particle does not lost completely the memory of its initial state and $f_q(T)$ also called the non-ergodicity parameter is a measure of the number of density fluctuations that becomes frozen at T_c [73, 98].

1. Only for this section we denote the coherent intermediate scattering function $\phi_q(t)$ (and no more $F(q,t)/S(q)$) as we decided to adopt the same notations as in [98].

The presence of the critical temperature T_c enables to introduce the "separation parameter σ" which measures the relative distance to T_c:

$$\sigma = C\frac{T_c - T}{T_c} \tag{4.25}$$

where C is a constant that depends on the system under interest [98]. The separation parameter plays the role of a small parameter used to compute the asymptotic expansions around T_c.

The MCT predicts that $\phi_q(t)$ relaxes in two steps when $T \to T_c^+$. The first step corresponds to the relaxation toward the plateau value given by $f_q^c = f_q(T_c)$ whereas in a second time, which corresponds to the α-relaxation, $\phi_q(t)$ departs from the plateau and decays to zero. The intermediate time regime including the plateau corresponds to the β-relaxation [69, 98]. In what follows we describe the prediction of the MCT for the β and α regimes.

4.5.1.1 Predictions for the β regime

This time scale corresponding to the location of the plateau is given by [69]

$$t_\sigma = \frac{t_0}{|\sigma|^{1/2a}} \tag{4.26}$$

where t_0 is a microscopic time-scale and a is an exponent whose calculation will be discussed below.

A interesting prediction of the MCT in the β-regime is the so-called *factorization theorem* which states that the correlator $\phi_q(t)$ can be expanded for $t \sim t_\sigma$ up to the first order [69, 98]:

$$\phi_q(t) = f_q^c + h_q\sqrt{|\sigma|}g(\hat{t}) \qquad \text{where } \hat{t} = t/t_\sigma \tag{4.27}$$

h_q is the critical amplitude. By defining $G(t) = \sqrt{|\sigma|}g(\hat{t})$ the previous equation may be rewritten as

$$\phi_q(t) = f_q^c + h_q G(t) \tag{4.28}$$

where we immediately see that the time-dependence of $\phi_q(t)$ is given by the sole function $G(t)$, also referred as the β correlator which is independent of q. As a consequence we remark that $\phi_q(t) - f_q^c$ corresponds to the product of a time-independent function h_q and a time-dependent function $G(t)$ [69].

4.5.1.2 Predictions for the α regime

For the α-relaxation the relevant time-scale is given by the following relationship:

$$t'_\sigma = \frac{t_0}{|\sigma|^\gamma} \tag{4.29}$$

where γ is an exponent related to the a exponent through the equation:

$$\gamma = \frac{1}{2a} + \frac{1}{2b} \tag{4.30}$$

Here b is the called the *von Schweidler* exponent. a and b are related one to each other by the exponent parameter λ:

$$\lambda = \frac{\Gamma(1-a)^2}{\Gamma(1-2a)} = \frac{\Gamma(1+b)^2}{\Gamma(1+2b)} \tag{4.31}$$

It has been shown that these exponents do not depend on T and can only take values in a certain range that are given by the equilibrium properties of the glass formers at T_c. Thus we expect from a system compliant with MCT that $\gamma > 1.765$, $0 < a < 0.3953$ and $1/2 \leq \lambda \leq 1$ [98].

An important prediction of the ideal MCT is that the α process must satisfy the time-temperature superposition principle (TTSP) when $T \to T_c^+$ which means that assuming a rescaling of the time t by the structural relaxation time t'_σ, correlators $\phi_q(t,T)$ taken at different temperatures T should collapse onto the same master curve $\tilde{\phi}_q$. This is expressed by the following analytical relation:

$$\phi_q(t,T) = \tilde{\phi}_q(t/t'_\sigma(T)) \qquad (t \geq t_\sigma) \tag{4.32}$$

This equation has two direct consequences: $\tilde{\phi}_q$ is independent of the temperature and there is only one time-scale t'_σ associated with the α process.

In the late β process and the early α regime the behavior of the correlator $\phi_q(t)$ is well-reproduced by the von Schweidler equation:

$$\phi_q(t) = f_q^c - \tilde{h}_q(t/t'_\sigma)^b + \tilde{h}_q\tilde{B}_q(t/t'_\sigma)^{2b} \qquad (t_\sigma \leq t) \tag{4.33}$$

where $\tilde{h}_q = h_q B$ and $\tilde{B}_q = BB_q$, h_q is the critical amplitude mentioned above, B is a constant and B_q is a q-dependent constant. Note here that we use an expression of the von Schweidler law with a second order corrective term [98].

4.5.1.3 Finding T_c

The MCT predicts that the structural relaxation time $\tau_\alpha(T)$ and the diffusion coefficient $D(T)$ follow a power law while approaching sufficiently close to T_c:

$$\tau_\alpha(T) = C_\tau(T - T_c)^\gamma \qquad \text{and} \qquad D(T) = C_D(T - T_c)^{-\gamma} \tag{4.34}$$

where C_τ and C_D are constants.

Consequently if one could have access to the exponent γ, the mode-coupling temperature T_c could be determined. The aim of the following work is thus to find γ by using the predictions of the MCT mentioned above and in particular extracting the value the exponent b from the von Schweidler equation 4.33. By knowing its value, equations 4.31 and 4.30 enable the determination of γ. However a special care should be taken if one would obtain a reasonable and coherent value of b.

The following procedure is applied to determine all the exponents and T_c:

1. In order to know in which range of temperature the ideal MCT is valid, the TTSP will be checked for temperatures $T \in [0.84, 0.88]$.
2. After defining the time interval of the β process, the factorization theorem will be tested. This step serves as a control to see if this prediction of MCT applies.
3. We use the von Schweidler equation 4.33 to determine the exponent b.
4. Finally a, γ and T_c can be found.

We performed the MCT analysis on the coherent intermediate scattering function and to test the reliability of our analysis we check then the validity of the results on the incoherent intermediate scattering function separately for the A and B particles .

4.5.2 Time-temperature superposition principle

As mentioned above the ideal MCT predicts that in the α regime, the TTSP should apply when $T \to T_c^+$. Thus a first test to check whether or not the ideal MCT applies for the bidisperse Voronoi liquid is to see if there exists an interval of temperatures into which the TTSP is satisfied.

We have thus computed the coherent intermediate scattering function $\phi_q(t)$ at first peak of the total structure factor $S(q)$. Three main points should be verified in order to confirm that the TTSP applies [75]:

- There should be an overlap of all $\phi_q(t, T)$ in the α regime when T is sufficiently close to T_c.

- Assume $T_1 < T_2$, $\phi_q(t, T_1)$ should not intersect with $\phi_q(t, T_2)$ or with any $\phi_q(t, T)$ computed for higher temperatures.
- The higher the temperature the earlier the departure of $\phi_q(t, T)$ from the master curve is observed.

In Figure 4.31 $\phi_q(t)$ is represented as a function of t/τ_α. We observe that in the range of temperatures selected, $T \in [0.84, 0.88]$, the different curves of $\phi_q(t)$ seem to collapse on a master curve. However one may wonder if $T = 0.88$ is satisfying the TTSP as it apparently does not collapse perfectly on the master curve. As a consequence of these observations the interval of temperatures in which the ideal MCT is valid is $T \in [0.84; 0.86]$.

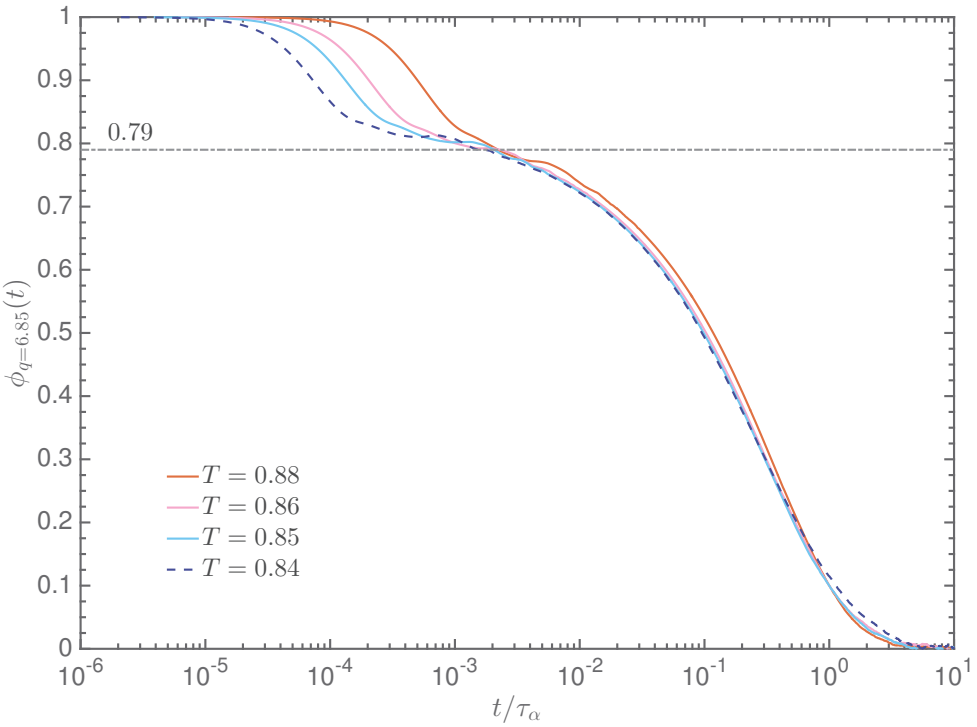

FIGURE 4.31: Test of TTSP for temperatures $T \in [0.84, 0.88]$. The dash-dot grey line corresponds to an estimation of the lower bound of the non-ergodicity parameter f_q^c.

4.5.3 Factorization theorem

Now that we have determined the temperature interval into which the MCT should be valid, we test another of its prediction, that is the factorization theorem. If we assume two times belonging to the β regime, t_1 and t_2, such as $t_1 < t_2$, the factorization theorem

states that:

$$R_q(t) = \frac{\phi_(t) - \phi_q(t_2)}{\phi_(t_1) - \phi_q(t_2)} = \frac{G(t) - G(t_2)}{G(t_1) - G(t_2)} \tag{4.35}$$

where we have used relation 4.27 as an expression for $\phi_q(t)$. We immediately see that the R.H.S of the equation is q independent. This observation implies that if the factorization theorem applies, different ratios R_q computed for different values of q should collapse onto the same master curve.

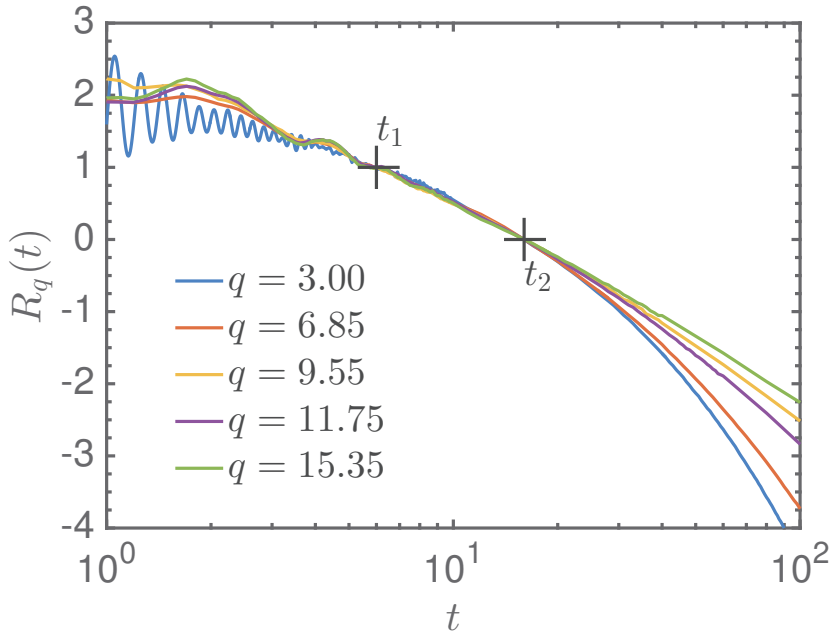

FIGURE 4.32: Test of the factorization theorem. $R_q(t_1 = 6.0) = 1.0$ and $R_q(t_2 = 16.0) = 0$ by definition.

At $T = 0.84$, we have computed $R_q(t)$ for different wavevectors q which, apart from $q = 4.00$, have been chosen in such way that they correspond to extrema of $S(k)$. The time t_1 and t_2 have been chosen in order to cover a large part of the β regime while avoiding the huge oscillations at the beginning of the plateau.

In Figure 4.32 we have represented $R_q(t)$ and we notice that the different curves collapse onto a master curve for a specific time interval $t \in [t_1 = 6.0, t_2 = 16.0]$. Moreover the ordering of the different curves when entering the plateau is preserved when they leave it. However whereas the collapse seems to remain valid for a short range of time $t > t_2$, we clearly see that for $t < t_1$ the factorization theorem does not hold anymore due to the presence of strong oscillations, in particular for $q = 3.00$.

4.5.4 von Schweidler fit

The main step in this analysis is to fit our data using the von Schweidler equation 4.33 in order to determined the exponent b and the other fitting parameters. To have the best precision, this fit must cover the late β process and the α process. The choice of the fit interval is thus primordial and will depend on the specie under interest. We have decided to fit the data of the lowest temperature that satisfies the TTSP, that is $T = 0.84$. This choice is motivated by the fact that the lower the temperature the longer the relaxation and consequently the time interval would be larger than for other temperature leading to better results [75]. In what follow we detail the procedure and we then explain the different procedures we use to verify that the results obtained from the fit are in agreement with ideal MCT.

4.5.4.1 Fit procedure

As mentioned above, the quality of the fit will strongly depend on the choice of the time interval. Our aim is to cover a large part of the late β relaxation and to take into account the α process. We thus need to define a left time-interval associated with the β process and a right-time interval associated with the α for which the fit would give good results.

For this purpose as a first step we started by fixing the right border in the late α process at $t = 1500$, then we change progressively the value of the left border from $t_{\beta 1} = 6.0$ to $t_{\beta 2} = 12.0$. The choice of $t_{\beta 1}$ is based on the fact that we want to avoid the oscillation regime that occurs at the beginning of the plateau. $t_{\beta 2} = 12.0$ is a limiting value. It corresponds more or less to the end of the plateau and we also noticed numerically that a choice of $t_{\beta 2} > 12.0$ would degrade the quality of the fit. Thus the time interval into which the left border may vary is $t_{left} \in [6.0, 12.0]$.

In a second step, we fix the value of left border to be equal to $t_{\beta 1} = 6.0$ and we vary the value of time in the late α regime from $t_{\alpha 1} = 1500$ to $t_{\alpha 2} = 2500$. For $t < t_{\alpha 1}$ the fit does not work well. This might be due to the fact that for $t < t_{\alpha 1}$ a relatively large part of the α process is neglected. For $t > t_{\alpha 2}$ the fit becomes deficient, we maybe cover a time interval which is too large to be suitable for a description with the von Schweidler equation.

To check the reliability of the time-interval for the α regime, we change at the same time the value of the left border to $t_{\beta 2}$. We found that this change affects very weakly the fitting parameters and as a result the right border may vary into a time interval $t_{right} \in [1500, 2500]$.

The time intervals for the left and right border for the fit with the von Schweidler equation are illustrated in Figure 4.33. One could assume that the best total time interval would have been $[t_{left} = 6, t_{right} = 2500]$ as it covers the largest part of $\phi_q(t)$. We would have certainly obtained a coherent result but it would have been difficult to appreciate the accuracy. So as we want to obtain the most representative values of the fitting parameters, we decide to increase the statistics by performing the calculation as follow:

1. We start by taking $t_{left} = 0.6$ and $t_{right} = 600$. We perform the von Schweidler fit and collect the fitting parameters. A representation of the von Schweidler fit is proposed in Figure 4.34.
2. We repeat the step 1 by increasing $t_{right} := t_{right}+200$ until it reaches $t_{right} = 2500$.
3. We increase the value of $t_{left} := t_{left} + 1$ and we repeat steps 1-2.
4. Steps 1-3 are repeated until $t_{left} = 12.0$ is reached . Average and standards deviation are computed for each of the fitting parameters. This values can be found in Table 4.8.

	f_q^c	t'_σ	b	B_q	h_q
average	0.8371	1404.1	0.5235	0.35512	1.0094
standard deviation	0.0016668	7.3768	0.0016061	0.00053202	0.0043676

TABLE 4.8: Table of the average and the standard deviation of the fitting parameters obtained from the fits performed on the coherent intermediate scattering function. The fit was done using the von Schweidler equation 4.33.

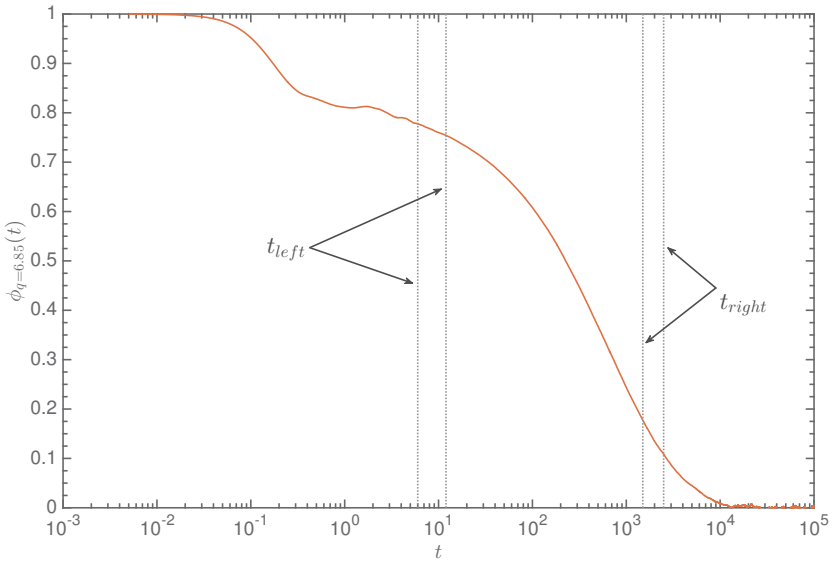

FIGURE 4.33: Coherent intermediate scattering function computed for $q = 6.85$ at $T = 0.84$. The dot grey lines correspond to the borders used to define the fit interval.

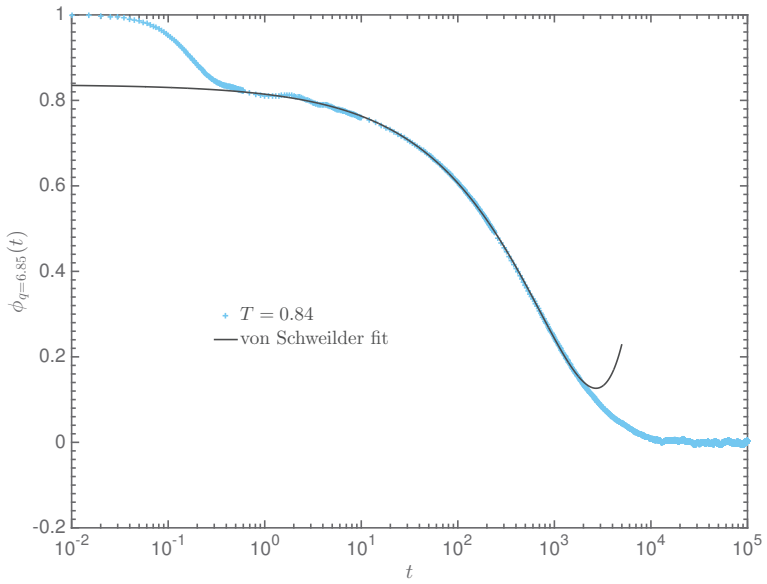

FIGURE 4.34: Coherent intermediate scattering function computed for $q = 6.85$ at $T = 0.84$ (blue +). The black solid line corresponds to the von Schweidler fit where the fitting parameters are the average values defined in Table 4.8.

4.5.4.2 Other q values

This step consists on checking the reliability of the values of the fitting parameters found in the previous series of fits. The aim is to fit $\phi_q(t)$ for other values of the wavevector q by reducing the number of fitting parameters. For this purpose we will consider that the values of both exponent b and relaxation time t'_σ are the ones found previously. It is possible to define the crossover-time t_{co} as the time for which $\phi_{q=q^*}(t_{co}) = f_q^c$ [98]. Knowing this time we can thus determine f_q^c for the other values of q. As a consequence in the following only B_q and h_q will be varying parameters.

This time, t_{co} corresponds logically to the left border of the time interval for the fit. The right border is adjusted for each values of q in such a way that $t_{right} < \tau_\alpha$, the relaxation time found when $\phi_q(t = \tau_\alpha) = 0.1$.

The results are presented in Figure 4.35. We notice that for high-q values, there is a quite good agreement between the constrained fits and the data points which suggests that the fixed values of b, t'_σ and f_s^c are consistent. For $q = 9.55$, the von Schweidler appears less good than for higher q-values. This is related to the fact that there are relatively marked oscillations at the beginning of the plateau and the crossover-time, which defines the left border of the fit interval, is located right in the middle of one of these oscillations leading to a biased fit. For this wavevector results are significantly

improved by shifting the left border to a larger time as it is suggested by the dashed black line in Figure 4.35.

However the result of the constrained fit is very bad for the lowest q represented. It is not very surprising as marked damped oscillations are visible on the plateau. We have already observed this phenomenon when looking at the important decrease of collective relaxation in the mesoscopic regime. We proceed the same way as for $q = 9.55$ to see to what extent the fit is improved when we shift the left border to $t_{left} = 10$. Contrary to $q = 9.55$ the late β regime and the beginning of the α process are not well described by the fit.

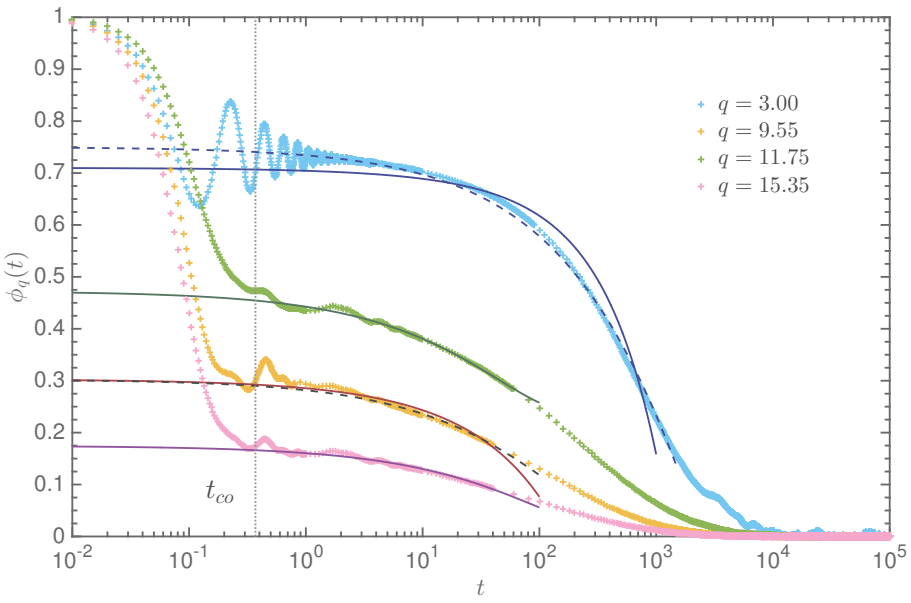

FIGURE 4.35: Test of the von Schweidler fit on $\phi_q(t)$ for several wavevectors q. The data points are represented by crosses (+). The dot grey line marks the value of the crossover time $t_{co} = 0.37$. The solid lines represent the von Schweidler fits where the left border of the time interval is given by the crossover time. The dashed black line is the von Schweidler fit for $q = 9.35$ but this time the left border has been shifted to larger time $t_{left} = 1.5$. The blue dashed line is von Schweidler fit for $q = 3.00$ where the left border has been shifted to $t_{left} = 10$. The right border is by $t_{right} = 100$ apart from $q = 3.00$ where $t_{right} = 1500$.

This first test of the fitting results are quite convincing apart from the results obtained for the smallest q value. We proceed now to another verification by fitting the incoherent scattering function $F_s(q,t)$ that we denote $\phi_q^s(t)$ for the purpose of the following analysis.

4.5.4.3 Incoherent intermediate scattering function

The procedure is similar to the previous one: b and t'_σ are taken equal to their average value shown in Table 4.8, f_q^{sc}, the parameter of non-ergodicity of $\phi_q^s(t)$ is given by the crossover-time t_{co} defined in the same way as before. Thus only B_q^s and h_q^s are varying parameters.

We test the von Schweidler fit for the incoherent intermediate scattering function of A and B particles and results are respectively shown in Figures 4.36 and 4.37. As for the coherent intermediate scattering functions, the values of q are chosen to be extrema of $S_{aa}(k)$.

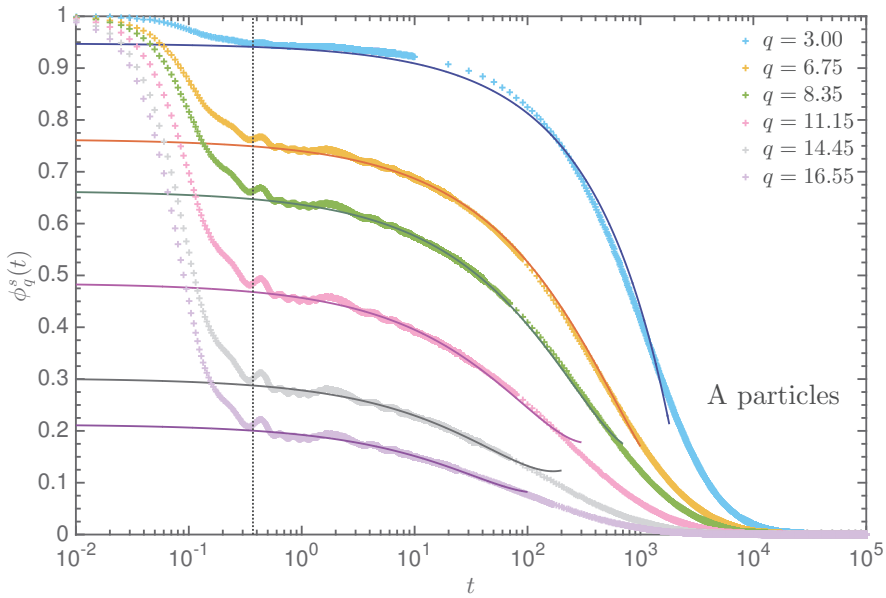

FIGURE 4.36: Test of the von Schweidler fit on $\phi_q^s(t)$ of the particles A for several wavevectors q. The data points are represented by crosses (+). The dot grey line marks the value of the crossover time $t_{co} = 0.37$. The solid lines represent the von Schweidler fit where the left border of the time interval is given by the crossover time. The right border changes for each q value and is given by $t_{right} = [1800, 1000, 700, 300, 200, 100]$ (from top to bottom).

- For the A particles, the von Schweidler fit appears to be in good agreement with the data for values of $q \geq 6.75$.
- For the B particles, the fit seems to underestimate a bit the value of the plateau but the early α process appears well fitted.
- For $q = 3.00$ we notice that in both cases the fits poorly describe $\phi_q^s(t)$. We recover the same issue that we had for the coherent intermediate scattering function.

The last point is not really suprising as the memory kernel involved in the MCT-equations of the incoherent intermediate scattering function is not quadratic in $F_s(q,t)$, but is in fact a bi-linear function of $F_s(q,t)$ and $F(q,t)$ [69]. This implies that to some extent the relaxation dynamics of a single tagged particle depends on the one of the whole ensemble of particles. This might explain why we recover the same issues for $q < q^*$. Behaviors are qualitatively the same for $\phi(q,t)$ and $\phi_q^s(t)$.

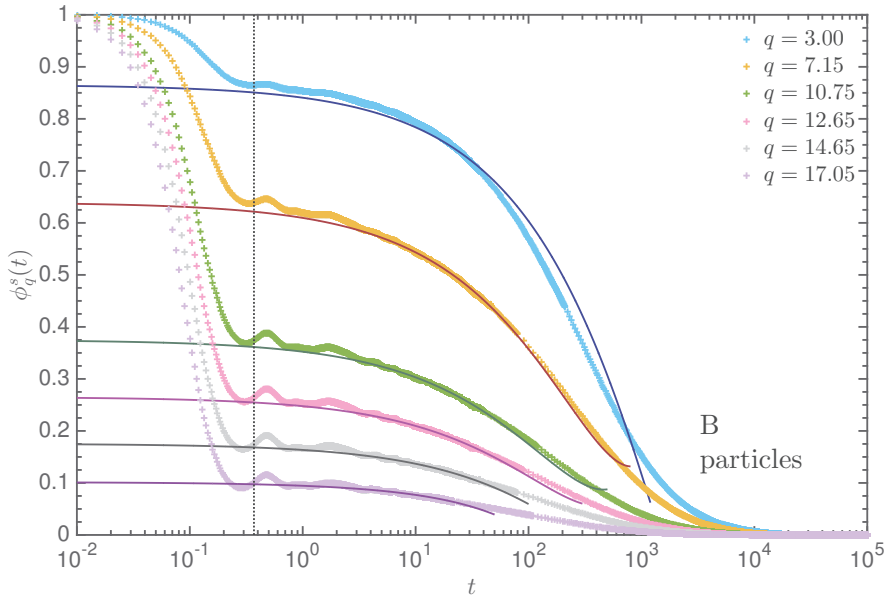

FIGURE 4.37: Test of the von Schweidler fit on $\phi_q^s(t)$ of the particles B for several wavevectors q. The data points are represented by crosses (+). The dashed grey line marks the value of the crossover time $t_{co} = 0.37$. The solid lines represent the von Schweidler fit where the left border of the time interval is given by the crossover time. The right border changes for each q values and is given by $t_{right} = [1200, 800, 500, 300, 200, 50]$ (from top to bottom).

To understand what occurs at low q, we proceeded to other investigations by testing first the constrained fit on $\phi_q^s(t)$ for other mesoscopic wavevectors. The main advantage of working with $\phi_q^s(t)$ is the lack of damped oscillations on the plateau. That allows for a better fitting process. However as for $q = 3.00$, it leads to very bad collapse between the fit and the data points. So we then decided to remove some constraints and to proceed to a fit by leaving the b exponent as a free parameter. Surprisingly we notice that the exponent b is more important in the mesoscopic regime than for high q values and that the lower q the higher b. It is indeed what we observe in Table 4.9 where we have collected the b exponent for several q. These observations suggest that for wavevectors in the mesoscopic range there is an apparent violation of the MCT predictions for the coherent and the incoherent intermediate scattering function.

q	1.00	2.00	3.00	4.00	4.50	5.00	5.50
b	0.904	0.814	0.722	0.651	0.637	0.616	0.590

TABLE 4.9: Evolution of the von Schweidler exponent b in the mesoscopic q range. b was computed from $\phi_q^s(t)$.

Apart from phenomena that occur in the mesoscopic regime we have observed that predictions of the MCT are well-verified. Therefore we assume that the ideal MCT applies and that we can compute the mode-coupling temperature T_c. The procedure is detailed below.

4.5.5 Determining T_c

From the fitting procedure, we have access to the average value of the exponent b, consequently we can compute λ which has been defined in equation 4.31. Once λ is determined, it is straightforward to find the exponent a. Finally we have all the required ingredients to determine the exponent γ defined in equation 4.30. The value of the exponents can be found in Table 4.10.

b	λ	a	γ	T_c
0.5235	0.7711	0.2943	2.6541	0.7989

TABLE 4.10: Table of the final results of the MCT exponents and mode-coupling temperature T_c.

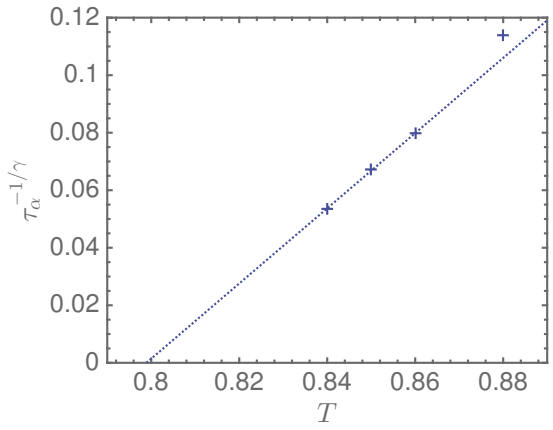

FIGURE 4.38: Representation of $\tau_\alpha^{-1/\gamma}$ as a function of the temperature. The linear fit gives the value of T_c when it intercepts the T-axis.

Once γ is found, we can use the equation 4.29 that gives the expression of t'_σ as a function of the separation parameter σ. As we explained, σ measures the distance from T_c thus it can be rewritten as $\sigma \sim T - T_c$ and consequently the expression for t'_σ is now given by [75]:

$$(t'_\sigma)^{-1/\gamma} = a(T - T_c) \tag{4.36}$$

By assuming that $\tau_\alpha \sim \tau'_\sigma$ we can easily have access to T_c with a linear fit as it can be seen in Figure 4.38. The value of T_c is found when linear fit intersects the T axis. We find that $T_c = 0.7989$.

T_c is a characteristic temperature of the glass transition. By considering equation 4.29 we see that T_c corresponds to the temperature at which the relaxation time would diverge revealing the transition from the ergodic to the non-ergodic behavior. Experimentally this is not observed and the relaxation time increases when cooling systems towards the glass transition temperature [98]. This divergence is thus an artefact of the theory which suggests that some other relaxation mechanisms should be taken into account and extension of the ideal MCT have been proposed [103].

Among the effects neglected in ideal MCT one may think about the hopping processes between minima that prevail at low temperature [104]. Therefore some useful informations on the slowing down of the dynamics are likely to be found in the underlying potential energy landscape whose study is the scope of next chapter.

Chapter 5

Potential Energy Landscape

Contents

In 1969, Goldstein [104] proposed an explanation of the huge increase of the viscosity based on the evolution of a system in its phase space. It corresponds to the space of all the configurational degrees of freedom [8]. Each configuration of the system is represented by a point in phase space and the dynamics of the system consists on motion of the point on the potential energy landscape (PEL) associated to the phase space [8].

Goldstein's ideas were the following [104] :

(i) At low temperature, as crystals, glassy systems are close to a minimum.

(ii) However, as the thermodynamic properties are sensitive to the cooling process, this implies that potential energy surface is not smooth but contains plenty of minima of various depth.

(iii) A system spends most of its time vibrating in amorphous minima but thanks to thermal energy it manages to overcome energy barriers and to visit other minima ensuring thus the ergodicity. As a consequence there is a clear separation of time scales: the thermal relaxation which corresponds to the vibration into a minimum

which is fast and the hopping between the several minima which require much more time to occur.

(iv) Overcome a potential energy barrier requires a local rearrangement of the system meaning that most of the particles would remain at the same position. Only a small number of particles are going to travel on a significative distance. More important these rearrangements are localized in limited regions of the space.

(v) This potential energy barriers description is not sufficient to describe the high-temperature behavior when thermal fluctuations are comparable to heights of the energy barriers.

This description suggests that upon cooling there is a crossover in the dynamics of a liquid from continuous fluid-type motion to an activated dynamics which consists on hopping over energy barriers [47]. As ideal MCT, which does not take activation into account, manages to describe the high-temperature phenomenology of supercooled liquids, it is generally assumed that the mode-coupling temperature T_c corresponds to the crossover temperature between the non-activated and the activated regime.

Goldstein gave a qualitative description of the dynamics near minima and we owe to Stillinger and Weber [105], the development of a formalism, still used today, that enables a thermodynamic description of the inherent structures (minima of E_P).

The aim of this chapter is to describe the PEL of the bidisperse Voronoi liquid. In a first section devoted to the study of inherent structures, we recall the formalism developed by Stillinger and Weber. It enables to derive an expression for the configurational entropy and therefore to test the Adam-Gibbs theory for our system.
In a second part we focus on saddles which are stationary points of the PEL with an arbitrary number of unstable directions. They play a significative role to understand the link between PEL and dynamics in real space when probing temperatures for which the hopping between minima could be neglected.

5.1 Inherent structures

In 1982, Stillinger and Weber published an article in which they introduced the concepts of what we call now *basins* and also presented the procedure that can be used to partition the PEL into disjoint basins [105].

Stillinger and Weber noticed that there exists a set of points in the configurational space that are connected to the local inherent structure (IS) via an energy minimization protocol, as for instance the steepest-descent [4, 105]. A typical sketch of the situation is represented in Figure 5.1 where we observe that each thermalized state, is uniquely

associated, via quenching, to an IS. It appears thus that the configurational space can be partitioned into the different contributions coming from the different basins. This last observation has enabled the derivation of a theoretical framework that we examine in the following paragraph.

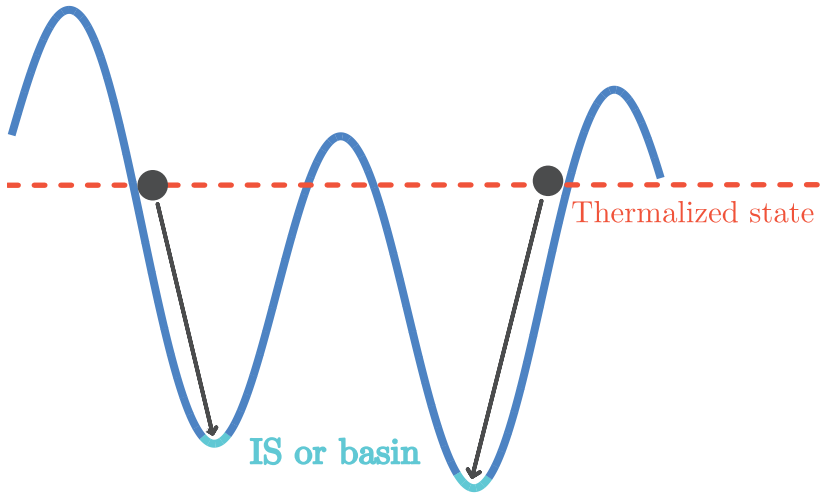

FIGURE 5.1: Sketch of the typical quenching of a thermalized configuration into its basin of attraction [4].

5.1.1 Theoretical framework

Let consider a binary mixture of $N = N_A + N_B$ particles contained into a volume V. The multidimensional vector $\boldsymbol{r}^N = (\boldsymbol{r}_1, \cdots, \boldsymbol{r}_N)$ contains the configurational coordinates of the N particles. As in [47] we denote $V(\boldsymbol{r}^N)$ the potential of this system. In these conditions, the partition function Z_N is given by:

$$Z_N = \frac{1}{N_A! N_B! \lambda^{3N}} \int_V d^N \boldsymbol{r} \exp(-\beta V(\boldsymbol{r}^N)) \tag{5.1}$$

where $\lambda = \sqrt{2\pi\beta\hbar^2/m}$ is the thermal de Broglie wavelength. Now if we assume that the configurational can be decomposes as the sum over all distinct basins, it is possible to rewrite the integral in the partition function as:

$$\int_V d\boldsymbol{r}^N \exp(-\beta V(\boldsymbol{r}^N)) = \sum_\alpha \exp(-\beta e_{IS}^\alpha) \int_{\mathcal{B}_\alpha} d\boldsymbol{r}^N \exp(-\beta \tilde{V}_\alpha(\boldsymbol{r}^N)) \tag{5.2}$$

where $\mathcal{B}_\alpha$ means that the integral is computed for the set of points of the αth basin [47]. The potential energy of the system has been decomposed into a sum of two elements $V(\boldsymbol{r}^N) = e_{IS} + \tilde{V}(\boldsymbol{r}^N)$, the potential energy of the inherent structure e_{IS} and $\tilde{V}$ is a non-negative quantity that measures, at a point $\boldsymbol{r}^N \in \mathcal{B}_\alpha$, the potential energy relative to the minimum [105, 106].

Minima can be classified according to their IS energy and as a consequence the sum over the basins can be split into a sum over all the possible values of e_{IS} and the sum over all basins α' at the same energy e_{IS} [106]. This implies the following expression for the partition function:

$$Z_N = \frac{1}{\lambda^{3N}} \sum_{e_{IS}} \exp(-\beta e_{IS}) \sum_{\alpha'} \int_{\mathcal{B}_{\alpha'}} d\boldsymbol{r}^N \exp(-\beta \tilde{V}_{\alpha'}(\boldsymbol{r}^N)) \tag{5.3}$$

We notice here that $N_A!N_B!$ vanishes as the sum over all distinct basins and the permutation of particles does not change the basin [47]. Henceforth, we consider only distinct IS with respect to trivial particle permutations.

As Stillinger and Weber, we define $\Omega(e_{IS})$ the IS density of states which counts the number of distinct basins of energy between e_{IS} and $e_{IS} + \delta e_{IS}$ [106]. It is then possible to define an average basin free energy $f(\beta, e_{IS})$ as:

$$-\beta f(\beta, e_{IS}) = \ln \left(\frac{1}{\lambda^{3N} \delta e_{IS} \Omega(e_{IS})} \sum_{\alpha'} \int_{\mathcal{B}_{\alpha'}} d\boldsymbol{r}^N \exp(-\beta \tilde{V}_{\alpha'}(\boldsymbol{r}^N)) \right) \tag{5.4}$$

We can therefore rewrite equation 5.3 as a function of the energy of the IS:

$$Z_N = \int de_{IS} \Omega(e_{IS}) \exp(-\beta e_{IS} - \beta f(\beta, e_{IS})) \tag{5.5}$$

The free energy F of the system is minimal when the integrand in equation 5.5 is maximal. Hence in the thermodynamic limit, a maximum-integrand evaluation enables to determine an expression for F:

$$F = e^*_{IS} - T S_c(e^*_{IS}) + f(\beta, e^*_{IS}) \tag{5.6}$$

where e^*_{IS} is the value that minimizes F. S_c is the configurational entropy which measures the number of distinct IS and is defined as:

$$S_c(e_{IS}) = k_B \ln(\Omega(e_{IS}) \delta e_{IS}) \tag{5.7}$$

Considering the basin free energy $f(\beta, e^*_{IS})$ in equation 5.6, it can be decomposed into its energetic term u_b and an entropic contribution s_b, which implies that the configurational entropy S_c corresponds to the difference between the liquid entropy S_{liq} and the basin entropy s_b, i.e the entropy of the system remaining in an IS with energy e^*_{IS} [106].

Low-temperature approximations regarding the form of $f(\beta, e^*_{IS})$ can be done [106].

- $\beta f(\beta, e^*_{IS}) \approx f(\beta)$: basins are likely to have the same shape in configuration space.

- $\beta f(\beta, e_{IS}^*) \approx g(\beta) + h(e_{IS})$: at different T, system visits basins that are always harmonic but have different densities of states. This is this factorization approximation that we consider thereafter.

For both forms, it is possible to factorize the partition function of equation 5.5 as $Z_N \approx Z^{IS} Z^b$. In the range of temperature where the factorization holds, the system can be decomposed into one subsystem corresponding to the IS which is weakly coupled to the vibrational degrees of freedom. The coupling between the two subsystems, essential for the process of equilibration, is possible via the weak T-dependence of the e_{IS} which is neglected in the factorization approximation. We look in deeper details to the result of the factorization approximation under the harmonic approximation which yields:$\beta f(\beta, e_{IS}^*) \approx g(\beta) + h(e_{IS})$.

Starting from equation 5.5, in the harmonic approximation, the Hessian of the potential energy is denoted $\underline{H}$. The term $\exp(-\beta f(\beta, e_{IS}^*))$ can be written as:

$$\begin{aligned}
\exp(-\beta f(\beta, e_{IS}^*)) &= \frac{1}{\lambda^{(3N-3)}} \int d^{(3N-3)}r \exp\left(-\frac{\beta}{2} \boldsymbol{r}^\intercal \underline{H} \boldsymbol{r}\right) \\
&= \frac{1}{\lambda^{3N}} \prod_{i=1}^{3N-3} \int dy_i \exp\left(-\frac{\beta}{2} m_i y_i^2 \omega_i^2\right) \\
&= \prod_{i=1}^{3N-3} \left(\frac{2\pi T}{m_i \omega_i^2 \lambda^2}\right)^{1/2}
\end{aligned} \tag{5.8}$$

where ω_i are the eigenfrequencies of the Hessian of the potential energy and m_i are the masses ($m_i = 1$). Thus by taking the logarithm of equation 5.8 we find:

$$-\beta f(\beta, e_{IS}^*) = \sum_{i=1}^{3N-3} \frac{1}{2} \ln\left(\frac{T^2}{\omega_i^2 \hbar^2}\right) \tag{5.9}$$

Therefore in the case of the bidisperse Voronoi liquid, equation 5.6 can be expressed as:

$$F = e_{IS}^* - T S_c(e_{IS}^*) - T \sum_{i=1}^{3N-3} \frac{1}{2} \ln\left(\frac{T^2}{\omega_i^2 \hbar^2}\right) \tag{5.10}$$

$$= e_{IS}^* - T \underbrace{\left[S_c(e_{IS}^*) - \sum_{i=1}^{3N-3} \ln\left(\frac{\omega_i \hbar}{\gamma v^{5/3}}\right)\right]}_{= \hat{S}_c(e_{IS}^*)} - T \sum_{i=1}^{3N-3} \ln\left(\frac{T}{\gamma v^{5/3}}\right) \tag{5.11}$$

where we define $\hat{S}_c(e_{IS})$ as the effective configurational entropy.

As mentioned by Sciortino *et. al* in [106], it is possible to look at a range of temperatures where the factorization holds by mean of numerical simulations. Assuming an equilibrated system at temperature T, we can define the probability density for finding

a configuration belonging to a basin with IS energy e_{IS}:

$$P(e_{IS}|T) = \frac{\Omega(e_{IS})\exp[-\beta e_{IS} - \beta f(\beta, e_{IS})]}{Z_N(T)} \tag{5.12}$$

By taking the logarithm of previous expression, we find:

$$\ln[P(e_{IS}|T)\delta e_{IS}] + \beta e_{IS} = k_B^{-1}\hat{S}_c(e_{IS}) - T\sum_{i=1}^{3N-3}\ln\left(\frac{T}{\gamma v^{5/3}}\right) - \ln[Z_N(T)] \tag{5.13}$$

If we consider the R.H.S of equation 5.13, we immediately see that if the factorization approximation holds, only the configurational entropy would depend on e_{IS}. Therefore Sciortino *et. al* highlighted that for different T, a shift of a temperature dependent quantity would lead to the collapse of the curves $\ln[P(e_{IS}|T)\delta e_{IS}] + \beta e_{IS}$ onto the same master curve which corresponds to the configurational entropy apart from an unknown constant.

The aim of this section is to determine the configurational entropy S_c and the effective one $\hat{S}_c$ and then to use it to test the Adam-Gibbs scenario that we will explain later. But prior to that we will briefly explain how IS are computed.

5.1.2 Computing IS and Gaussian landscape

As mentioned above any algorithm that minimizes the potential energy E_P is a good candidate to compute inherent structures. As there is a clear splitting of the PEL in terms of IS and related basin, the results should not differ from an algorithm to another one. In practice we selected the *Fast Inertial Relaxation Engine* algorithm (better known as FIRE) as it was shown that this algorithm is faster and has a better convergence than usual conjugate gradient or Newton methods [107].

We have computed the IS for the bidisperse Voronoi liquid and the LJ glass-formers. In Figure 5.2 we have represented the evolution of $(e_{IS} - e_{IS,\infty})/(k_B T^*)$ as a function of T^*/T. $e_{IS,\infty}$ is the average of the potential energy of the IS computed from high-temperature thermalized configurations. For all the systems we noticed that for $T > T^*$, the value of e_{IS} is almost constant, thus we have evaluated $e_{IS} - e_{IS,\infty}$ in order to measure the relative decrease of e_{IS} upon cooling. Results are presented in Figure 5.2.

We observe that the bidisperse Voronoi liquid has the more pronounced decrease of e_{IS} upon cooling. Regarding the LJ glass-formers, it seems that the more fragile the mixture, the more marked the decrease.

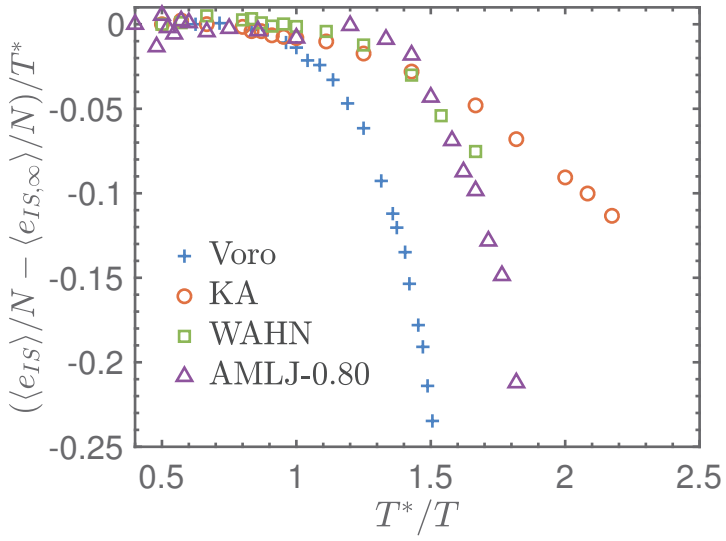

FIGURE 5.2: Evaluation of $(\langle e_{IS}\rangle/N - \langle e_{IS,\infty}\rangle/N)/T^*$ as a function of the scaled temperature T^*/T. Where we recall that T^* is the temperature at which the system enters into the super-Arrhenian regime. $T^* = 1.25$ for Voronoi, $T^* = 1.00$ for KA and WAHN and $T^* = 0.60$ for AMLJ-0.80.

We also notice the presence of a linear regime at low temperature which is more visible in Figure 5.3 where we have represented e_{IS} as a function of $1/T$. This observation is in agreement with the predictions of the random energy model (REM) [108, 109]. For the REM the number of distinct basins of energy between e_{IS} and $e_{IS} + de_{IS}$, which is given by $\Omega(e_{IS})de_{IS}$, can be described by a Gaussian distribution [60]:

$$\Omega(e_{IS})de_{IS} = e^{\alpha N}\frac{\exp[-(e_{IS} - E_0)^2)/(2\sigma^2)]}{\sqrt{2\pi\sigma^2}}de_{IS} \tag{5.14}$$

where the $e^{\alpha N}$ accounts for the total number of basins, E_0 is an energy scale and σ^2 measures the width of the distribution. By using the REM (or Gaussian harmonic approximation), one assumes that each IS can be decomposed into independent subsystems which have their own values of e_{IS}. Therefore, in the thermodynamic limit, the central limit theorem applies and the IS energy follows the gaussian distribution 5.14.

The knowledge of $\Omega(e_{IS})$ enables to rewrite all the thermodynamic observables described above. It can be shown [60, 110] that the average value of the IS energy obeys the following relationship:

$$\langle e_{IS}(T)\rangle = E_{max} - \frac{\sigma^2}{k_B T} \tag{5.15}$$

where E_{max} depends on E_0 and σ^2. We immediately see that equation 5.15 implies a linear behavior of $\langle e_{IS}(T)\rangle$ when represented as a function of $1/T$. It has been shown

that theoretical predictions of the Gaussian harmonic approximation are only valid in a range of temperature where the two-step relaxation behavior is already well-developed [60]. Therefore it is not a surprise to see that the linear regime is only seen at low temperature in Figure 5.3. We performed a linear fit on the range of temperature where equation 5.15 holds. We found thus values of σ^2 that are shown in Table 5.1. Whereas the three LJ systems have approximately the same value of σ^2 we observe that this value is 10 times greater in the case of the bidisperse Voronoi liquid.

	Voro	KA	WAHN	AMLJ-0.80
σ^2/N	1.474	0.127	0.189	0.139

TABLE 5.1: Value of σ^2 found from a fit with equation 5.15

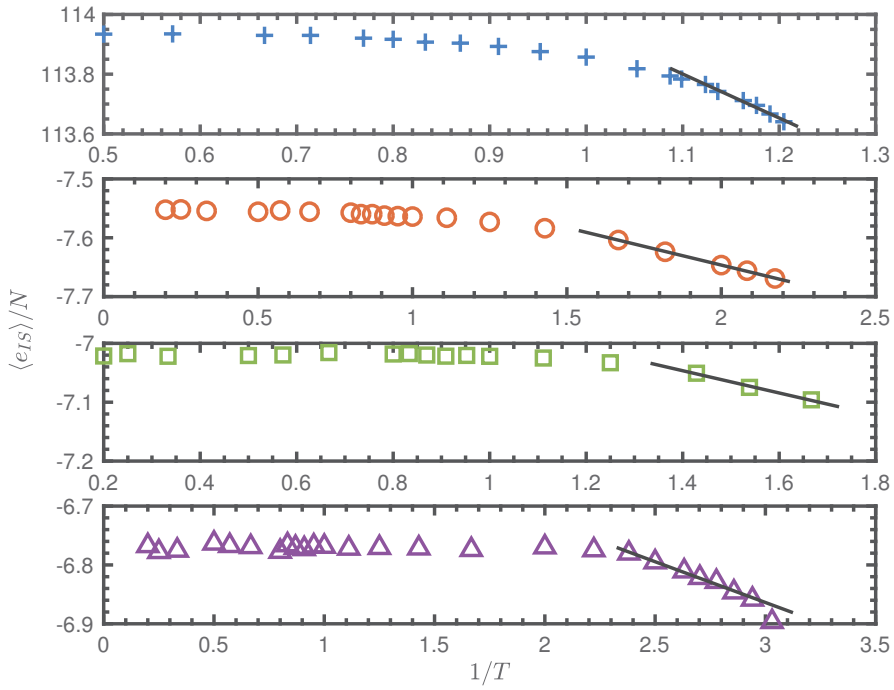

FIGURE 5.3: Evolution of $\langle e_{IS}\rangle/N$ as function of $1/T$ for the bidisperse Voronoi liquid (+), KA (○), WAHN (□) and AMLJ-0.80 (△). The dark straight line corresponds to a linear fit performed on lowest temperatures.

The relatively big large value of σ^2 could be correlated to the important values of C_v^e for the bidisperse Voronoi liquid. Indeed if we assume that $\langle E_P\rangle = \langle e_{IS}\rangle + 3NT/2$, we find that:

$$C_V^e = \frac{\partial\langle e_{IS}\rangle}{\partial T} + \frac{3N}{2} = \frac{\sigma^2}{T^2} + \frac{3N}{2} \tag{5.16}$$

From equation 5.16, we notice that the larger σ^2, the more important is C_V^e.

Previous numerical studies have shown that fragile glass-formers generally satisfy the predictions of the Gaussian harmonic approximation. Our observations are thus consistent with the fact that both the bidisperse Voronoi liquid and the LJ glass formers exhibit a certain degree of fragility.

The Gaussian harmonic approximation provides also an expression which can be numerically tested for the probability density $P(e_{IS}, T)$ defined in equation 5.12. We will see this in more details when computing the configurational entropy from the IS.

5.1.3 Configurational entropy

In what follow we compute the configuration entropy in two different ways. On the one hand, we use the fact that S_c is given by the difference between the liquid and the basin entropies. On the other hand, we will see that the low-T factorization approximation holds and consequently S_c may be expressed as a function of e_{IS}. We will test the consistency between the two approaches.

5.1.3.1 Temperature dependence

In Chapter 2 we computed the excess part of the entropy S_e from the knowledge of the excess part of the free energy F_e defined in equation 2.19. The total entropy of the liquid is $S_{liq} = S_{id} + S_e$ where S_{id} is the ideal part defined in the case of a binary mixture as [111]:

$$\frac{S_{id}(T,V,N)}{Nk_B} = -\frac{N_A}{N}\ln\left(\frac{N_A}{N}\right) - \frac{N_B}{N}\ln\left(\frac{N_B}{N}\right) + \frac{3}{2}\ln\left(\frac{mV^{2/3}}{\beta\hbar^2 2\pi}\right) - \ln(N) + \frac{5}{2} \quad (5.17)$$

It can be assumed that for the lowest T studied, the term $f(\beta, e_{IS})$ in equation 5.13 can be approximated by the harmonic free energy of a disordered solid whose eigenfrequencies are calculated from the IS at T [106]. Thus the basin entropy corresponds to the one of the disordered solid $S_{sol}(T,V)$ and is given by:

$$S_{sol}(T,V) = \sum_{j=1}^{3N-3}\left[1 - \ln(\beta\hbar\omega_j)\right] \quad (5.18)$$

where ω_j is the eigenfrequency of the jth normal mode.

Both liquid entropy $S_{liq}(T)$ and entropy of the disordered solid $S_{sol}(T)$ are represented in Figure 5.4 where we observe that as expected they both decrease upon cooling. From

the lowest accessible temperatures, we can extrapolate the values of $S_{liq}(T)$ and $S_{sol}(T)$ to lower temperatures. If the extrapolation are valid, we observe that at a certain temperature, the entropy of the liquid is equal to the entropy of the disordered solid. This temperature, that we denote T_K, is analogous to the Kauzmann temperature [112], which is defined as the temperature for which the liquid entropy equals the crystal entropy. Thus in our case, T_K corresponds to the Kauzmann temperature, only if the crystal vibrational entropy is a good approximation of the vibrational entropy of the basin [106].

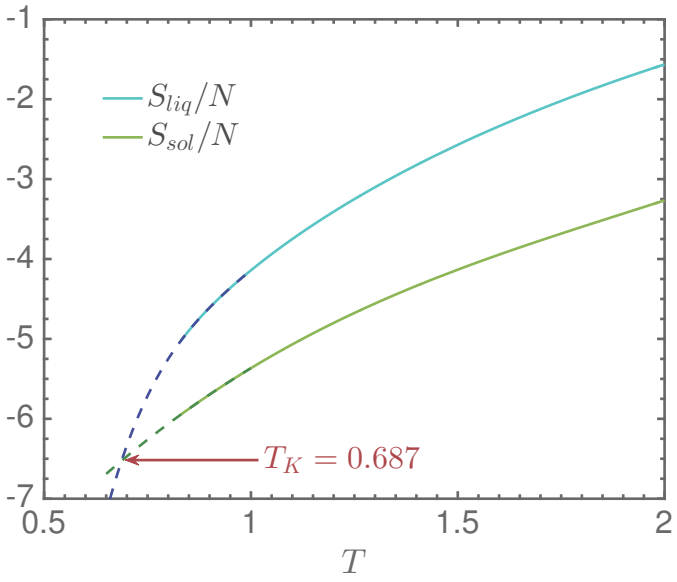

FIGURE 5.4: Evolution of the entropies per particle S_{liq} and S_{sol} as a function of the temperature.

The knowledge of $S_{liq}(T)$ and $S_{sol}(T)$ allows the determination of $S_c(T) = S_{liq}(T) - S_{sol}(T)$ which is represented in Figure 5.5. We observe that the configurational entropy decreases upon cooling and that if we extrapolate its value to the temperature T_K for which $S_c(T_K) = 0$, we find $T_K = 0.687$.

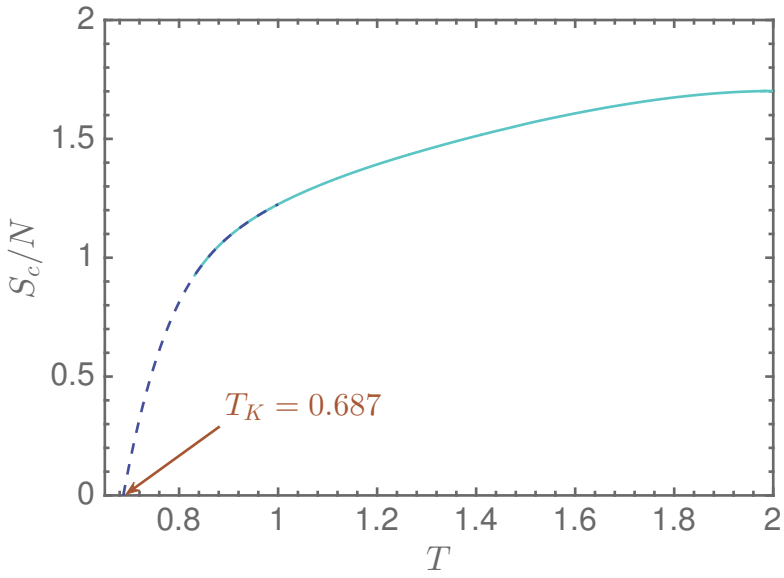

FIGURE 5.5: Configurational entropy S_c per particles as a function of temperature T.

We have computed S_{liq} and S_{sol} and deduced the value of S_c. However we need to test whether the harmonic approximation is valid to see to what extent the configurational entropy is reliable. Therefore we evaluate the energy of the anharmonicity by using the following relation [60]:

$$E_{anh}(T,V) = E_P(T,V) - \langle e_{IS}\rangle(T,V) - \frac{3}{2}Nk_BT \tag{5.19}$$

One possible way to describe anharmonicities is by assuming that E_{anh} is only a function of the temperature and can be described by polynomial whose lower order is T^2 [60]:

$$E_{anh}(T,V) = \sum_{i=2}^{i_{max}} c_i(V)T^i \tag{5.20}$$

where c_i is a coefficient that only depends on the volume V. The corresponding anharmonic entropy is given by:

$$S_{anh}(T,V) = \sum_{i=2}^{i_{max}} \frac{ic_i(V)}{i-1}T^{i-1} \tag{5.21}$$

In the upper part of Figure 5.6 the energy per particle of anharmonicity for the bidisperse Voronoi liquid is represented as a function of the temperature. As expected the anharmonicities become more important when the temperature is increased. In the range of temperature investigated, the values of E_{anh}/N are of the order of 10^{-1} and therefore

are only 10 times smaller than the vibrations $3/2k_BT$ what means that for the bidisperse Voronoi liquid, anharmonicities might play a role at some point.

Below T^*, we can describe E_{anh} by using the polynomial expressed in equation 5.20. However we notice that we need to start with a term in T^4 to obtain a good fit. Indeed, polynomials in T^2 and T^3 were not able to fit the data. We have thus described E_{anh} with a polynomial $c_6T^6+c_5T^5+c_4T^4$. We also observed that if we limit the investigation to $T < 1.00$, E_{anh} for the Voronoi liquid can be well described by only c_4T^4.

As it is surprising that the starting term of the polynomial is in T^4, we computed E_{anh} to see to what extent our observation is specific to the bidisperse Voronoi liquid. In the lower part of Figure 5.6, E_{anh} is shown for the three LJ glass formers. Whereas a polynomial $c_4T^4 + c_3T^3 + c_2T^2$ describes well the data for the Kob-Andersen model and the Wahnstöm mixture, a polynomial of the form $c_6T^6 + c_5T^5 + c_4T^4$ is required to fit properly the data of AMLJ-0.80. It appears thus that AMLJ-0.80 behaves similarly than the bidisperse Voronoi liquid. It is not straightforward to explain this phenomenon and for the moment an explanation is still lacking. Values of coefficients c_i can be found in Table 5.2.

	Voro	KA	WAHN	AMLJ-0.80
c_2	N.A	-0.4912	-1.028	N.A
c_3	N.A	1.122	2.271	N.A
c_4	-0.1362	-0.5858	-1.196	-1.706
c_5	0.6351	N.A	N.A	11.56
c_6	-0.3276	N.A	N.A	-13.38

TABLE 5.2: Table of the coefficients c_i involved in the polynomial expressions for anharmonicity. N.A stands for Non Applicable.

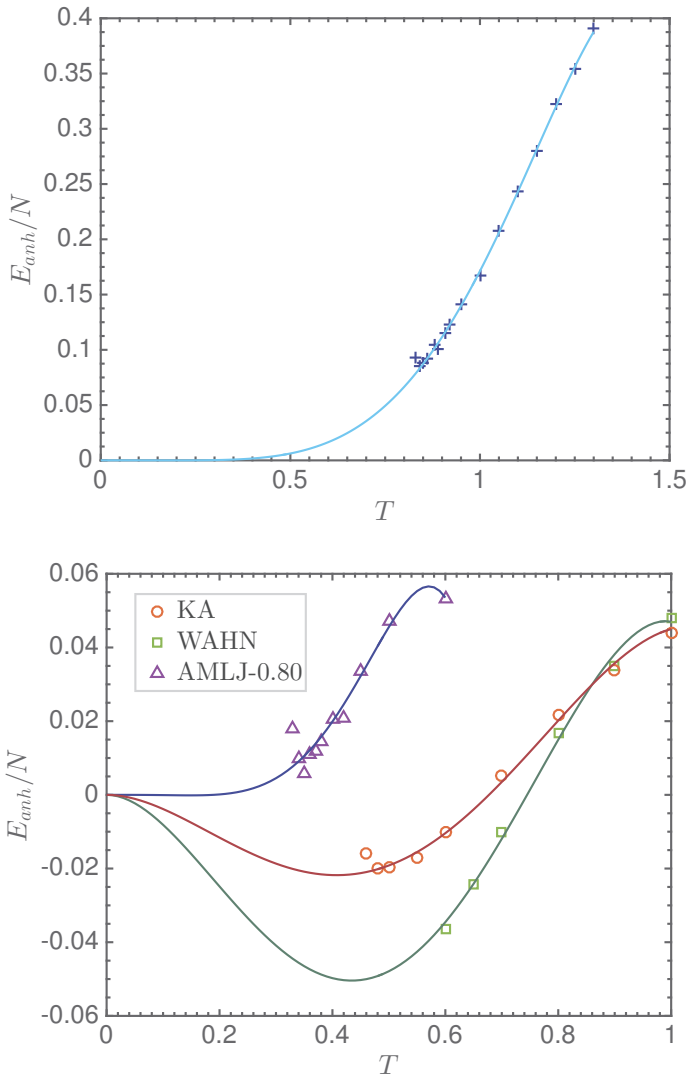

FIGURE 5.6: Energy per particle of the anharmonicity as a function of temperature for the bidisperse Voronoi liquid (upper graph) and for the 3 LJ glass formers (lower graph).

By means of equation 5.21 we were able to determine the anharmonic entropy per particle for the bidisperse Voronoi liquid and the result is presented in Figure 5.7. Anharmonic entropy per particle is increasing with temperature but its values remain 100 times weaker than the values of S_c, S_{liq} or S_{sol}.

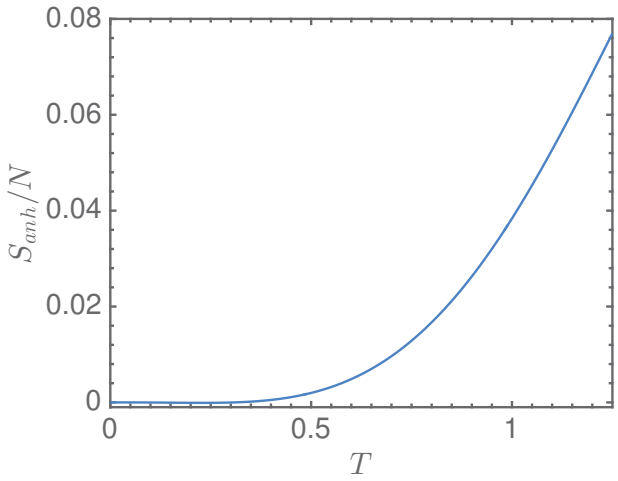

FIGURE 5.7: Anharmonic entropy as a function of temperature for the bidisperse Voronoi liquid.

5.1.3.2 Effective configurational entropy

We have determined the configurational entropy $S_c(T)$ in the harmonic approximation as $S_c = S_{liq} - S_{sol}$. We look now for the value of the effective configurational entropy $\hat{S}_c(e_{IS})$ which is linked to S_c via equation 5.11. The aim is to see first whether the factorization approximation holds, meaning that in equation 5.13 only the term $\hat{S}_c$ would depend on e_{IS}. Then assuming it is the case, we would have access to $\hat{S}_c$ up to a constant and therefore we could determine whether the harmonic approximation is valid.

The first step to test the factorization approximation is to compute the probability density $P(e_{IS}|T)$ defined in equation 5.12. As $P(e_{IS}|T)$ corresponds to probability to find from a thermalized configuration an IS with energy e_{IS} knowing the temperature T, it is easily accessible numerically. In Figure 5.8 is represented $P(e_{IS}|T)$ as a function of e_{IS}/N, we notice that the distribution of e_{IS} reflects what has already been observed in Figure 5.2:

- At high temperature, the distribution of e_{IS} is weakly influenced by temperature at which the IS are extracted. All distributions are centered around the same average value $\langle e_{IS} \rangle \approx 113.95$.
- As the temperature decreases, e_{IS} of lower energy could be extracted, the distributions of e_{IS} are influenced by temperature and a shift towards smaller values of e_{IS} is observed upon cooling.

It is possible to give an analytical expression of the probability $P(e_{IS}|T)$ if we assume that the Gaussian harmonic approximation (see equation 5.14) holds [113]:

$$P(e_{IS}|T) = \frac{1}{\sqrt{2\pi\sigma_P^2}} \exp\left[-\frac{(e_{IS} - \langle e_{IS}(T,V)\rangle)^2}{2\sigma_P^2}\right] \tag{5.22}$$

Here the width of the gaussian σ_P and the average value $\langle e_{IS}(T,V)\rangle$ are both functions of variables E_0 and σ defined in equation 5.14 [113]. We fitted the data of $P(e_{IS}|T)$ with equation 5.22 and we notice a good agreement between the data points and the fit as observed in Figure 5.8.

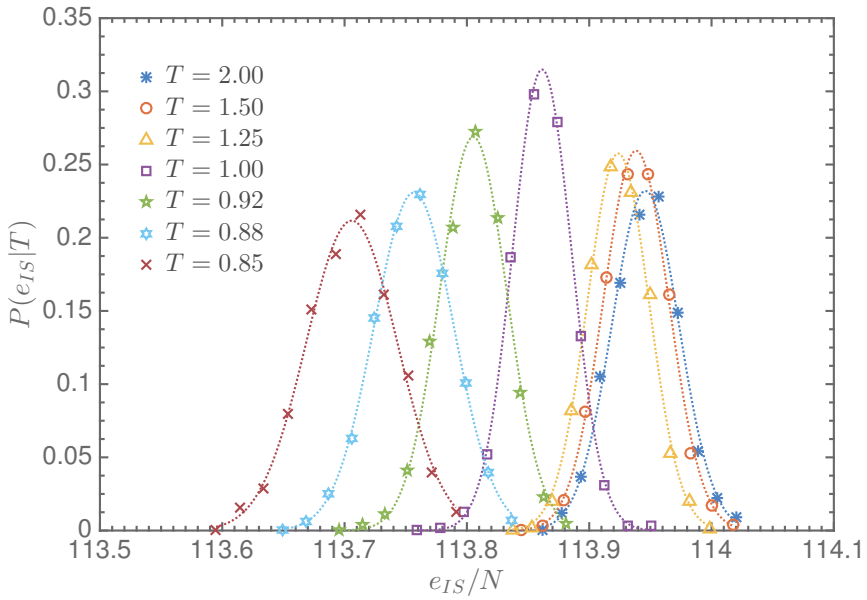

FIGURE 5.8: Representation of the probability $P(e_{IS}|T)$ of having an IS of energy e_{IS} at a given temperature T as a function of the energy of IS per particle. The dot lines corresponds to the gaussian fit using equation 5.22.

Now that we have characterized $P(e_{IS}|T)$, it is possible to test the predictions of the factorization approximation by evaluating the left part of equation 5.13. We compute thus $\ln(P(e_{IS}|T)) + e_{IS}/T$ which should only have a dependence in e_{IS} through $\hat{S}_c$, if the factorization approximation holds [106]. In Figure 5.9 we remark that for the different temperatures investigated IS consists on a system of levels characterized by an energy e_{IS} an a degeneracy $\Omega(e_{IS})$. Now we can test the validity of the factorization approximation. Thus it should be possible to superimpose the different curves in Figure 5.9 by shifting them by a T-dependent quantity. Apart from a constant, the resulting master curve for e_{IS} describes the effective configurational entropy $\hat{S}_c$. It is indeed what is observed in Figure 5.10 where we find that for all temperature $T < 1.20$, the graphs of $\ln(P(e_{IS}|T)) + e_{IS}/T$ shifted by T-dependent quantity collapse onto a master

curve. This master curve can be fitted by a polynomial of order 2 in the range where $e_{IS} \in [1.136 \cdot 10^5, 113.8 \cdot 10^5]$. To check if this master curve corresponds to the effective configurational entropy $\hat{S}_c$, we have to compare with the expression $\hat{S}_c$ that has been derived in the harmonic approximation, where $\hat{S}_c$ and S_c as they are linked by equation 5.11.

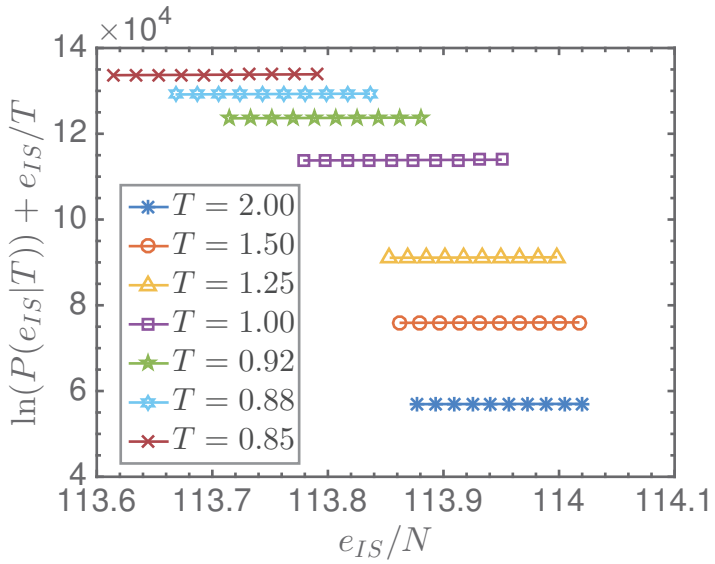

FIGURE 5.9: Test of the factorization approximation. Representation of $\ln(P(e_{IS}|T)) + e_{IS}/T$ as a function of of the energy of IS per particle.

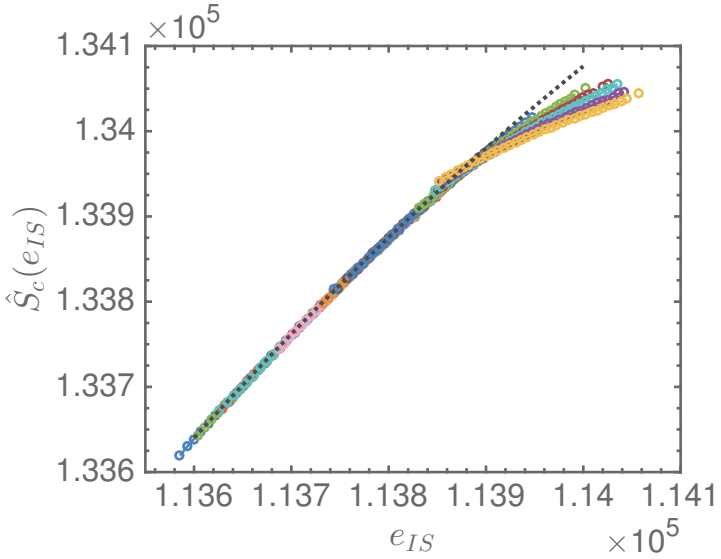

FIGURE 5.10: Effective configurational entropy as a function of the inherent structure energy (colored circles). Notice that the collapse is not working for $T \geq 1.20$. The black dotted line corresponds to a polynomial fit $(-4.30 \cdot 10^{-4} e_{IS}^2 + 98.9 e_{IS} - 5.6 \cdot 10^6)$ done on $e_{IS} \in [1.136 \cdot 10^5, 1.138 \cdot 10^5]$.

In practice, we determine $\hat{S}_c$ directly from S_{liq} as it avoids the determination of the eigenfrequencies of the Hessian of E_P. Thus if the factorization approximations works:

$$\hat{S}_c = S_{liq} - 3(N-1)\left[1 + \ln\left(\frac{T}{\gamma v^{5/3}}\right)\right] \tag{5.23}$$

In equation 5.23, $\hat{S}_c$ depends on T. To determine its e_{IS}-dependence, for $T \leq 1.00$, we fit $\langle e_{IS}\rangle(T)$ with a polynomial expression of order 4. This enable us to determine $\hat{S}_c(e_{IS})$ and therefore it can be compared to the polynomial of order 2 that represents the master curve in Figure 5.10. This comparison is shown in Figure 5.11 where we observed that there is a good agreement between the two methods for values of $e_{IS} \in [1.1365 \cdot 10^5, 1.1375 \cdot 10^5]$ which correspond to very low temperatures.

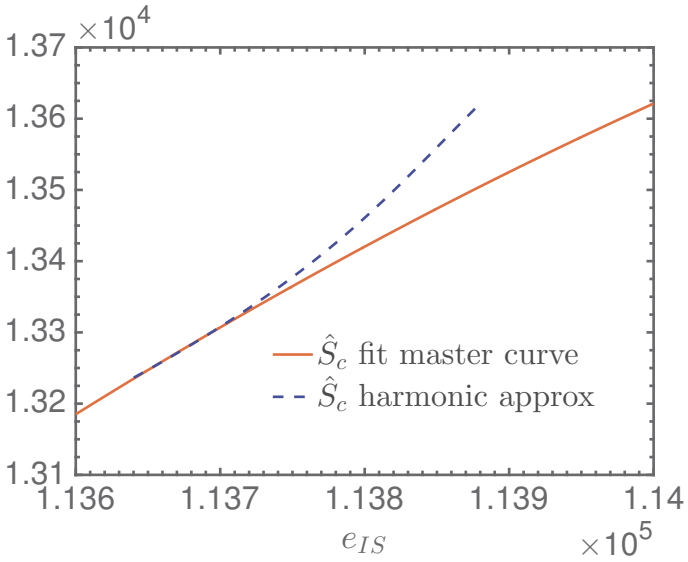

FIGURE 5.11: Comparison between $\hat{S}_c(e_{IS})$ obtained from the polynomial fit of order 2 performed in Figure 5.10 and $\hat{S}_c(e_{IS})$ obtained from equation 5.23.

This observation immediately raises the question of the validity of the harmonic approximation. We have seen previously that the anharmonic contribution are non-negligible and therefore we should take them into account. We have noticed that for $T \leq 1.00$, $E_{anh} \approx N c_4 T^4$ where c_4 is a constant. Thus with equation 5.21 we find that $S_{anh} \approx \frac{4}{3} c_4 T^4$ (where $c_4 = 0.17$). By taking into account anharmonicities, equation 5.23 is now given by:

$$\hat{S}_c = S_{liq} - 3(N-1)\left[1 + \ln\left(\frac{T}{\gamma v^{5/3}}\right)\right] - \frac{4}{3} c_4 T^3 \tag{5.24}$$

In Figure 5.12, we compare $\hat{S}_c$ from equation 5.24 with the polynomial of order 2 that represents the master curve in Figure 5.10. We notice first that adding the anharmonic contribution seems to improve a bit the results, especially for $e_{IS} \geq 1.1375 \cdot 10^5$. However

for $e_{IS} \geq 1.1370 \cdot 10^5$ the agreement between equation 5.24 and the fit in Figure 5.10 is less good than in the harmonic approximation.

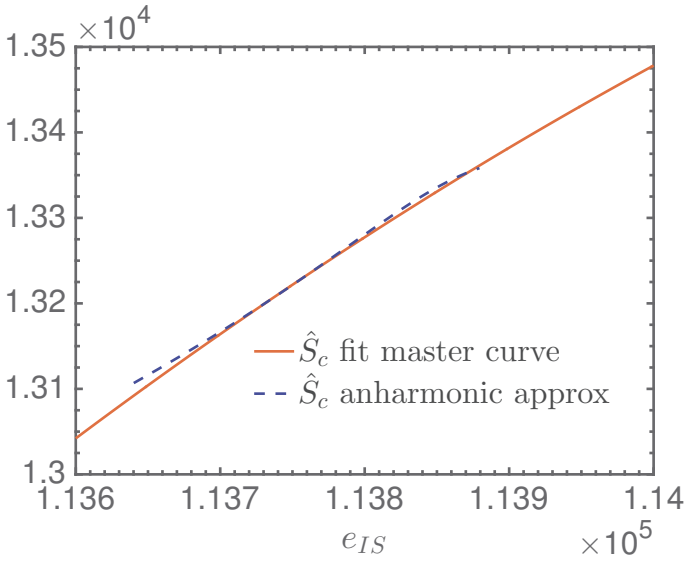

FIGURE 5.12: Comparison between $\hat{S}_c(e_{IS})$ obtained from the polynomial fit of order 2 performed in Figure 5.10 and $\hat{S}_c(e_{IS})$ obtained from equation 5.24.

These mixed results point toward the fact that formulation 5.20 of E_{anh} is likely to be not adapted to our model. We have already stressed that for the bidisperse Voronoi liquid $E_{anh} = c_4 T^4$ whereas $E_{anh} = c_2 T^2$ is expected.

In [60], Sciortino proposed another formulation for the energy relative to anharmonicity, which comes from the perturbative development at order 3 of the Hessian of E_P, where the T^2 dependence is assumed to be always valid but this time c_2 is more a constant but depends on e_{IS}:

$$E_{anh} = c_2(e_{IS})T^2. \tag{5.25}$$

As a consequence the corresponding anharmonic entropy is:

$$S_{anh} = -2c_2(e_{IS})T \tag{5.26}$$

We can therefore rewrite equation 5.24 as:

$$\hat{S}_c = S_{liq} - 3(N-1)\left[1 + \ln\left(\frac{T}{\gamma v^{5/3}}\right)\right] - 2c_2(e_{IS})T \tag{5.27}$$

Again we compare the results of equation 5.27 with the fit obtained from Figure 5.10 as shown in Figure 5.13. We notice that within this approximation of the anharmonicity,

the agreement between equation 5.27 and the polynomial fit of order 2 is worst pointed toward the fact that this description of anharmonicity does not apply for our system.

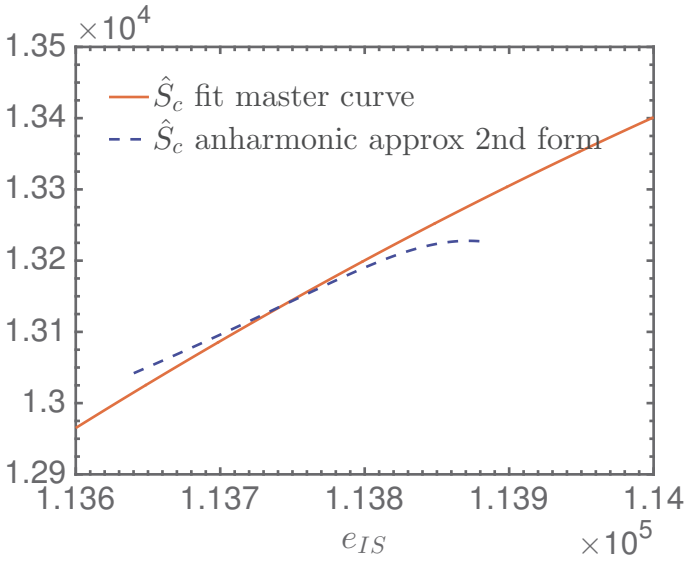

FIGURE 5.13: Comparison between $\hat{S}_c(e_{IS})$ obtained from the polynomial fit of order 2 performed in Figure 5.10 and $\hat{S}_c(e_{IS})$ obtained from equation 5.27.

5.1.4 Adam-Gibbs theory

The knowledge of the configurational entropy $S_c(T)$ allows to test the Adam-Gibbs theory which links the relaxation time through the configurational entropy via relation [14]:

$$\tau(T) = \tau_0 \exp\left[\frac{B}{TS_c(T)}\right] \tag{5.28}$$

where B is a constant. The activation energy in this model is thus $\Delta E \propto 1/S_c(T)$.

Relation 5.28 comes from the fact that Adam and Gibbs postulated that structural relaxation is due to rearrangement of regions of correlated particles that they called *cooperative rearranging region* (CRR). These rearrangements could be due to a local fluctuation of the enthalpy that promote collective motion. The Adam-Gibbs model assumes the following ideas [14]:

(i) The CRR is defined as the smallest region that can rearrange independently from their surrounding environment.

(ii) A typical CRR has a small number Ω of accessible states. The minimal number of accessible states to a CRR is $\Omega = 2$: the state before the transition and the state after the rearrangement.

(iii) The configurational entropy S_c is directly related to Ω and the number of particles involved in CRR.

(iv) The energy barrier ΔE is proportional to the number of particle involved in the CRR and as consequence the size of CRR increases when S_c decreases.

We also immediately see from equation 5.28 that whether the configurational entropy vanishes for $T_K > 0$ (T_K corresponds to the Kauzmann temperature), the structural relaxation time would diverge suggesting the presence of a phase transition. In 1958, prior to the theory of Adam and Gibbs, Gibbs and Di Marzio demonstrated that the vanishing S_c leads to a second order phase transition at T_K, also called *ideal glass transition*, and the resulting phase corresponds to a disordered solid to which is associated only one peculiar configuration [114, 115].

Equation 5.28 provides also an interesting explanation for the fragility. By assuming that configurational entropy is given by $S_c = S_{liq} - S_{sol}$, we easily see that the variation of configurational entropy $\Delta S_c(T)$ is proportional to ΔC_p the variation of heat capacity at constant pressure. Adam and Gibbs assumed that ΔC_p is T-independent. Therefore if one considers that the configurational entropy vanishes at the Kauzmann temperature T_K, it results that for T close to T_K, $S_c(T) \sim \Delta C_p(T - T_K)/T_K$ [8, 14, 69]. Thus equation 5.28 becomes:

$$\tau(T) = \tau_0 \exp\left[\frac{BT_K}{\Delta C_p T(T - T_K)}\right] \overset{T\to T_K}{\approx} \tau_0 \exp\left[\frac{B}{\Delta C_p (T - T_K)}\right] \tag{5.29}$$

We recognize that the last term in equation 5.29 corresponds to the VFT law and by comparing with equation 4.7, two observations can be made:

- The fragility is proportional to the variation of the heat capacity ΔC_p at glass transition [8].
- The temperature T_0 at which the VFT law diverges, corresponds to the Kauzmann temperature T_K. In Figure 5.5 we have shown that the temperature at which $S_c(T)$ vanishes for the bidisperse Voronoi liquid is given by $T_K = 0.687$. In Chapter 4 by mean of the VFT equation 4.8, we were able to extract T_0 which was equal to $T_0 = 0.691$ (see Table 4.1). Thus we notice that $T_K \approx T_0$.

We test the Adam-Gibbs theory for the bidisperse Voronoi liquid. In Figure 5.14 we have represented in a semi-log plot the structural relaxation time τ_α as function of $1/(TS_c)$. If the Adam-Gibbs theory holds, we should observe a linear relation between the two quantities and it is indeed the case for low temperatures ($T < 0.92$). This observation tends to suggest that at enough low temperature, the structural relaxation is partly driven by cooperative rearrangements.

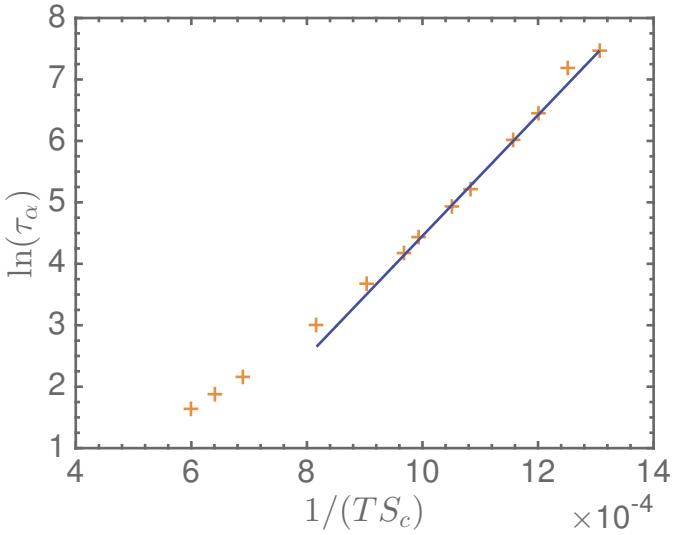

FIGURE 5.14: Evolution of the structural relaxation time τ_α (extracted from $F_s(k,t)$) as a function of the $1/(TS_c)$. The data points are symbolized by (+) and the solid line represents the exponential fit performed on the lowest temperatures.

Despite the success of the Adam-Gibbs theory, it failed to win unanimous support for several reasons:

- The predictions of Adam-Gibbs theory regarding the fact that $T_K/T_0 \sim 1$ is generally observed for fragile liquids [116] but it is not satisfied when liquids tends to have an intermediate behavior or are considered as strong [117].
- The ideal glass transition is controversial, firstly because this range of temperature cannot be reached experimentally and secondly one can wonder about the nature of the "new phase" reached at T_K [118]. Moreover whether a transition occurs, there should be a diverging length scale associated to it. However Adam and Gibbs didn't provide a clear definition of what should be this diverging length-scale.
- The Adam-Gibbs theory has been verified numerically for LJ glass formers as KA and WAHN systems [119, 120]. However this validity is also directly linked to the way configurational entropy is computed. Recently Berthier and Coslovich proposed a novel approach to determine the configurational entropy [121] where no evaluation of the liquid entropy neither the vibrational entropy is required. In particular they showed for the KA model and for a binary mixture of harmonic spheres that the Adam-Gibbs theory does not apply anymore for $T > T_c$.

With this relatively good verification of the Adam-Gibbs theory, we end our study devoted to the IS. We focus now on saddles which are other existing stationary points of the PEL. They can be relevant to get a better understanding of the dynamics when Goldstein's description breaks at sufficiently high temperature.

5.2 Saddles

Goldstein's description of the dynamical evolution of a supercooled liquids in terms of the motion of the state point in the PEL is valid at low temperature where there is a clear separation of time scales between the thermal relaxation into basins (intra-basin relaxation) and the relaxation related to the hoppings from basin to basin by overcoming energy barriers (inter-basins relaxation).

However when the temperature is increased, there exists a crossover temperature T_x for which these two time scales are of the same order, and therefore Goldstein's description breaks down. Angell [2] and then Sokolov [122] suggested that T_x corresponds to the mode-coupling temperature T_c as for temperature above T_x, experimental results satisfy MCT predictions, whereas for $T < T_x$ it is no more the case.

In 2001, Cavagna published a letter [123] in which he proposed a generalization for $T > T_x$ of Goldstein's landscape picture. His central idea is that for high temperatures the relevant stationary points of the PEL are no more the minima, but saddles. This can be understood by the fact that at high-temperature,

5.2.1 Theoretical considerations

Saddles are unstable equilibrium points ($\boldsymbol{\nabla} E_P = \mathbf{0}$), characterized by an arbitrary number K of negative eigenvalues of the Hessian of the potential energy [123]. If we assume working with N particles in a 3-dimensional space, then the index K can take any values between $K = 0$ and $K = 3N$. We can define:

- the index density of negative direction denoted k and defined as $k = K/3N$;
- the potential energy density $u = U/N$ where U is the average potential energy $\langle E_P \rangle$.

An observable useful to consider, is the average index density k of saddles located at potential energy density u, which is assumed to be a increasing function of u and this was indeed proven initially by Broderix *et al.* [124] and Angelani *et al.* [125] who published independent studies in which they observed that for LJ liquids $k(u)$ increases monotonously with u.

The notion of potential energy barrier can be introduced for saddles and is defined as the energy ΔU required to pass from a saddle of index K to an adjacent higher saddle of index $K + 1$. We immediately see that, in the case where $K = 0$, we recover the standard definition of an energy barrier between a minima and a simple saddle. If $k(u)$

is known, the average energy ΔU can be estimated [123]:

$$\Delta U \approx \frac{1}{3}\frac{du}{dk} \tag{5.30}$$

This last approximation means that potential barriers between saddles change as the slope of the function $k(u)$.

As Goldstein did with minima, Cavagna proposed a description of the diffusion in terms of motion of the state point among the neighborhood of saddles [123]. A relevant question is now how to define the neighborhood of a saddle point ? Stationary points are known to be zeros of function $W = |\boldsymbol{\nabla} U|^2$ [126, 127]. Therefore saddle points can be seen as solutions of $W = 0$ for which the density index $k > 0$. Similarly to the approach of Stillinger and Weber, a quench of W can therefore be performed and results depends on temperature:

- if $T < T_x$, U is small enough to ensure that on average $k = 0$, thus a quench is likely to lead to a minimum of U;
- if $T > T_x$, a quench leads to a saddle of U.

However it is important to stress that contrary to the approach Stillinger and Weber, the method described previously does not partition the whole phase space into basins and saddles as there exists local minima of W which are > 0 [123]. However in 2003, Wales and Doye proposed a theoretical and a computational scheme that allows to partition the PEL into basins whatever the stationary point [128]. These different approaches developed for computing saddles are discussed in the following subsection.

Cavagna identified two main mechanisms denoted A and B, that could lead to the motion of the state point among saddles:

(A) The first mechanism is driven by activation as it implies the crossing of an potential-energy barriers. The system close to a saddle of index K, takes an uphill stable direction to reach a saddle of index $K + 1$ and then take an downhill direction to end in a saddle with the same potential energy as the initial one. As in the case of inherent structures, overcoming an energy barrier implies structural rearrangement in the system involves a finite number of particles. The probability to have a transition is given by $P_A \sim \exp[-\Delta U/k_B T]$ where ΔU is the energy barrier estimated above.

(B) The second mechanism is driven by entropy. Saddles have generally nonzero K, the system can use one of the unstable downhill directions to reach a lower potential energy level with an excess of kinetic energy that could be used to take an uphill direction in order to reach finally a saddle with the same potential energy as the initial one. At very low temperature when only minima are visited this mechanism becomes inefficient by the system as there is no more negative direction.

Efficiency of both mechanisms decreases upon cooling and for a given T we can assume that the diffusion is run by the most efficient one. To have a better insight into the mechanism responsible for the slowing-down of the dynamics it is interesting to compare both mechanisms. To do so it is useful to start by looking at mechanism B and to determine the temperature T_B at which the mechanism would be frozen.

Therefore we introduce the threshold energy u_{th} defined as the energy below which minima prevails and consequently there is no more negative directions:

$$k(u_{th}) = 0 \tag{5.31}$$

From u_{th} we can find T_B. First we notice that u_{th} corresponds to the energy density of the threshold minima without taking into account the vibrational contributions [123]. Then assuming an harmonic approximation for the vibration, the total potential energy density of a system vibrating around an IS is given by:

$$u(T) = e_{IS} + \frac{3}{2}k_B T \tag{5.32}$$

Therefore if we consider the peculiar case where $e_{IS} = u_{th}$, the temperature T_B is defined as:

$$u_{th} = u(T_B) - \frac{3}{2}k_B T_B \tag{5.33}$$

Thus below T_B we are sure that mechanism B is totally inefficient. On the opposite mechanism A could always apply as it requires only thermal activation. However depending on the size of energy barriers at $\Delta U(u_{th})$, the slowing-down of the dynamic would not be impacted the same way. This observation allows for a classification of liquids in two distinct classes.

(I) $\Delta U(u_{th}) \ll k_B T_B$: potential energy barriers are small compared to thermal energy, as a result when mechanism B freezes, mechanism A is relatively efficient. The decrease of the temperature below T_B leads to a slowing down of mechanism A until reaching Goldstein's temperature T_x where $\Delta U \sim k_B T_x$. In the case where ΔU does not depend a lot on u, the energy barriers remain relatively constant and it is legitimately to say that the relaxation time follows an Arrhenian law. This description is thus in agreement with the definition of a strong liquid.

(II) $\Delta U(u_{th}) \gg k_B T_B$: potential energy barriers are large compared to thermal energy and consequently mechanism A is already slow when mechanism B becomes inefficient. We can assume that for $T > T_B$, mechanism B is more advantageous than mechanism A as the system do not need to overcome energy barriers. Thus when T_B is reached, the only way to diffuse is by activation and consequently $T_x = T_B$.

For this class of liquids, the relaxation time is expected to exhibit a sharp increase which is related to the slowing-down of mechanism B. This observation corresponds to the definition of fragile glass-formers.

We only deal with the two extreme cases but we can assume that cases where $\Delta U(u_{th}) \approx k_B T_B$ would lead to a description of relaxation time compatible with intermediate fragility. This qualitative reasoning on relaxation mechanisms related to saddles enable to have a better physical insight into what could lead to strong/fragile behaviors.

These theoretical considerations on saddles can be advantageously tested by means of numerical simulations. In the beginning of the 2000s, some studies focusing on saddle analysis were published [123–125, 129]. The principal interest was to find T_B as it is assumed to correspond to the mode coupling temperature T_c for fragile glass-formers. Evaluations of energy barriers for $T > T_x$ have been proposed [5, 130]. Some attempts were also made to correlate unstable directions and dynamical heterogeneities [131].

All these works face the difficulty to compute efficiently true saddle points. In the following we discuss two computational approaches commonly used to get saddle points in the case of supercooled liquids. We will use these two methods to perform a saddle analysis of the bidisperse Voronoi liquid.

5.2.2 Computing saddles: Saddles vs. Quasisaddles

5.2.2.1 Minimizing W : the problem of Quasisaddles

As suggested above a way to extract saddles is to minimize the function $W = |\boldsymbol{\nabla} U|^2$. This minimization was originally proposed by Weber and Stillinger [126] as saddles correspond minima of W. However Doyes and Wales have shown that minimizing W leads most of time to local minima of W and actually only a few numbers of absolute minima are actually found [5, 129, 132, 133]. These local minima of W correspond to inflection points of the potential energy U and therefore they are not stationary points of U and cannot be considered as true saddles [132].

Angelani *et al.* proposed to refer to these local minima as quasisaddles (QS) [132]. They make the assumption that if the Hessian has a small numbers zero eigenvalues [1], apart the one associated to translations, then QS point is very close from the true saddles and therefore it is possible to identify QS with saddles. Some evidences point toward the validity of their hypothesis as they showed numerically that for LJ glass-formers the index density of negative directions expressed as a function of the temperature is the same of QS

1. It was actually shown by Doyes and Wales [133] that the QS investigated by Angelani *et al.* in [132] have only one zero eigenvalue which is not associated with translations.

and true saddles. Therefore it appears that QS and saddles convey the same information that can be used to understand the slowing down of the dynamics in supercooled liquids [5, 134]. This observation leads to numerous study where the the minimization of $W = |\boldsymbol{\nabla} U|^2$ was the criterion selected to determine "saddles" [5, 124, 125, 131, 132].

Any minimization algorithm could be used to compute saddles but in practice, the L-BFGS algorithm (where L-BFGS stands for Limited-memory Broyden-Fletcher-Goldfarb-Shanno algorithm) is generally used [135].

5.2.2.2 Finding true saddles by mean of the Eigenvector-Following method

Doye and Wales pointed to the problem of finding non-stationary points while investigation the minimization of W [129]. To get rid of this problem, they propose an alternative minimization scheme based on the Eigenvector-Following (EF) method developed in 1981 by Cerjan and Miller to locate transition state [136]. The EF method is based on two central ideas

1. The potential energy surface can be approximate by a quadratic form for each point of the phase state.
2. A saddle of index K can be viewed as a maximum in K directions and like a minimum in the (3N-K) other directions. Thus to find the saddle, one must maximize the energy in K uphill directions and minimize it in the other downhill directions.

Doye and Wales proposed to embed the EF scheme into a Newton-Raphson method in order to converge to stationary-points of index K of the Hessian [128, 129] Technical descriptions of the Eigenvector-Following method can be found in [136] (for its original formulation) and in [137] (for details on EF embedded in Newton-Raphson).

The algorithm proposed by Wales and Doye contains 3 main steps: 1) a minimization using LBFGS 2) a transition step search using an Newton-Raphson-EF method and 3) a minimization of W using LBFGS [128].
Later in 2006, Grigera proposed an alternative to the scheme of Doye and Wales [138] where the Newton-Rapshon-EF method is directly used to converge to a saddle point from a thermalized state. This alternative scheme gave good results and appears easier to implement. Thus we selected this method to compute saddles in the bidisperse Voronoi liquid.

To work properly the EF method requires the computation of eigenvalues and eigenvectors of the Hessian at each iteration. The Newton-Raphson step $\Delta \boldsymbol{x}$ is evaluated in the

base that diagonalize the Hesssian [138]:

$$\Delta x_\mu = S_\mu \frac{2g_\mu}{|h_\mu|(1+\sqrt{4g_\mu^2/h_\mu^2})} \tag{5.34}$$

where h_μ are the eigenvalues of the Hessian and g_μ are the components of the gradient in the diagonal base. For the directions where $h_\mu = 0$, Δx_μ is set to zero.

$S_\mu = \pm 1$ defined the sign of the Newton-Raphson step. When $S_\mu = 1$, the energy increases along the uphill direction μ, whereas when $S_\mu = -1$, the energy decreases along the downhill direction μ. Thus by choosing $S_\mu = \mathrm{sgn}(h_\mu)$ the algorithm should converge to a saddle of index K. However the convergence may be not reached when dealing with high-temperature [128]. A solution to this problem is to perform a certain number N_{ns} of steps by leaving K "free" and then to fix K to its final value until reaching the stationary point. Wales and Doye have chosen $N_{ns} = 20$ [128] and so did Grigera in [138]. We started also by fixing $N_{ns} = 20$, however we encountered problems of convergence and in our case very small values of N_{ns} are required to observe a convergence. In practice, $N_{ns} = 1$, meaning that we fixed K directly from the theamalized configuration.

To remain in the region where a quadratic approximation of the potential energy is valid, a set of trust radii $\{\delta_\mu\}$ is considered. The step Δx_μ is rescaled in order to satisfy $\forall \mu, |\Delta x_\mu| \leq \delta_\mu$. Initially $\delta_\mu = 0.001$ and at each step these values are increased (or decreased) by a factor 1.2 if the quantity $r = (h_e - h_\mu)/h_\mu$ is less (or larger) than 1. h_e is an estimation of the eigenvalue at current step. Wales in [137] and Grigera in [138] have estimated that:

$$h_e = \frac{g_\mu(n) - g_\mu(n-1)}{\delta x_\mu(n-1)} \tag{5.35}$$

where n is the current step. However with this approximation of h_e, we were unable to make the algorithm converge for the bidisperse Voronoi liquid. We thus proposed an improvement in the estimation of h_e.

In order to estimate h_e, we evaluate the evolution of the gradient of the potential energy between two points of space phase which are very close. We denote $\{\boldsymbol{e}_j\}$ the set of eigenvectors of the Hessian.

In $\boldsymbol{X}$ the gradient of the potential energy $U(\boldsymbol{X})$ is expressed in the base that diagonalizes the Hessian $\underline{H}$ as $\boldsymbol{\nabla} U(\boldsymbol{X}) = \sum_j g_j \boldsymbol{e}_j$. Thus in the peculiar direction j the component of the gradient g_j is:

$$g_j = \frac{\boldsymbol{\nabla} U(\boldsymbol{X}) \cdot \boldsymbol{e}_j}{e_j^2} \tag{5.36}$$

Now we consider a small evolution of the point in phase space $\boldsymbol{X} + d\boldsymbol{X}$. At first order the jth component of the gradient is now given by:

$$g'_j = \frac{\boldsymbol{\nabla} U(\boldsymbol{X}) \cdot \boldsymbol{e}_j + \boldsymbol{\nabla} U(\boldsymbol{X}) \cdot \delta \boldsymbol{e}_j + \underline{H}(\boldsymbol{X}) d\boldsymbol{X} \cdot \boldsymbol{e}_j}{e_j^2} \tag{5.37}$$

We immediately see that the first term in the sum in numerator corresponds to the gradient evaluated in $\boldsymbol{X}$, therefore the difference between the jth component of gradient evaluated in two points is:

$$\delta g_j = g'_j - g_j = \frac{\boldsymbol{\nabla} U(\boldsymbol{X}) \cdot \delta \boldsymbol{e}_j + \underline{H}(\boldsymbol{X}) d\boldsymbol{X} \cdot \boldsymbol{e}_j}{e_j^2} \tag{5.38}$$

By using the relation $\underline{H}(\boldsymbol{X}) \boldsymbol{e}_j = h_j \boldsymbol{e}_j$, previous equation becomes:

$$\delta g_j = \frac{h_j \boldsymbol{e}_j \cdot d\boldsymbol{X} + \boldsymbol{\nabla} U(\boldsymbol{X}) \cdot \delta \boldsymbol{e}_j}{e_j^2} \tag{5.39}$$

Now we select the direction of $\boldsymbol{X}$ parallel to $\boldsymbol{e}_j$, we can write that $d\boldsymbol{X} \cdot \boldsymbol{e}_j = \Delta x_j$. It is finally possible to estimate the eigenvalue $h_e = h_j$:

$$h_j = \frac{\delta g_j}{\Delta x_j} - \frac{\boldsymbol{\nabla} U(\boldsymbol{X}) \cdot \delta \boldsymbol{e}_j}{\Delta x_j e_j^2} \tag{5.40}$$

In equation 5.40 we recognize that the first term of the R.H.S corresponds to the estimation 5.35 of the eigenvalue. Interestingly our result presents an additional term to the formulation proposed by Grigera *et al.* [138]. Thus we observe that in our case the estimation at first order of h_e implies a corrective term related to the force field in $\boldsymbol{X}$ which is absolutely required for the convergence of the algorithm.

Finally it is important to mention that $W = |\boldsymbol{\nabla} U|^2$ is monitored at each iteration and the convergence of the EF-Newton-Raphson procedure is assumed when $W \sim 10^{-16}$ which corresponds to limiting precision of the calculation.

We detailed the two processes that could be used to obtain QS and saddles. In the following, we compare the two methods to test the assumption that QS and saddles are conveying the same kind of information is true for a system with a potential that differs from the LJ one. Then by means of a saddle analysis we determine the mode coupling temperature T_c that we can compare to the value of T_c found by ideal MCT analysis. Finally we evaluate the energy barrier between saddles to see first to what extent we can interpret the increase of relaxation time for $T > T_c$ by means of motion of the system in a PEL dominated by saddles.

5.2.3 Numerical results

5.2.3.1 General observations on saddles and quasisaddles

Using both methods described above we compute QS and saddles for systems with $N = 125$, 512 and 729 particles. These choices are motivated by the facts that:

(i) For very small systems $N \leq 125$, the LBFGS algorithm is efficient. The final value of $W \sim 10^{-10}$ which corresponds to a zero value relatively to the numerical precision. Thus there are higher chances to reach true stationary points.

(ii) The EF method requires the computation of the Hessian (a $3N \times 3N$ matrix) at each iteration. Therefore we must favor small systems to perform calculation in a reasonable time and with a limited amount of memory.

(iii) We could have limited our analysis to $N = 125$, however we are interested by the N-dependence of the quantities measured.

For each system of N particles we perform the calculation for temperatures $T \in [0.86, 2.00]$ and for each saddle or quasisaddle computed, we collect the index density k and the energy density u.

In Figure 5.15 is represented the evolution of the density index k as a function of the potential energy density u for a system of $N = 125$ particles. In this case saddles have been computed by mean of the EF method.

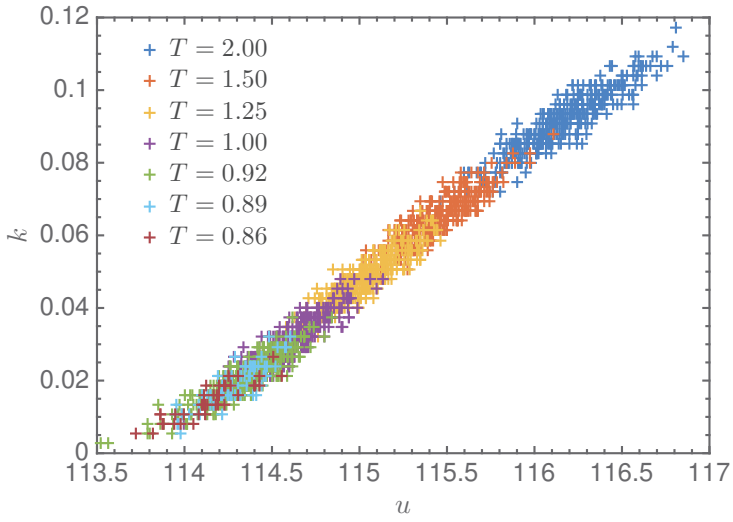

FIGURE 5.15: Representation for a system of $N = 125$ particles of the index density of negative direction k as function of the potential energy density u for "true" saddle points computed with the EF method at several temperature T.

The plot in Figure 5.15 is very similar to what has been observed for a Kob-Andersen mixture by Broderix *et al.* in [124]. Indeed we observe that k is an increasing function

of u. Moreover as suggested by Broderix and Cavagna [123, 124] the curve of $k(u)$ seems to be an underlying geometric feature of the PEL which can be seen as temperature-independent. As a matter of fact, sampling saddles as different temperatures enable to reveal different parts of $k(u)$ as different regions of the PEL are explored [124].

To support this conjecture, Broderix proposed to perform two kind of averages on the scatter plot 5.15. They were labeled as geometric and parametric averages [124]. The geometric average enables to exclude the temperature dependence by averaging all the values of k associated to the same energy density u whereas the parametric average implies averaging over k and u for each temperature.

These two kinds of averages are shown in Figures 5.16 (for true saddles) and 5.20 (for QS). In both cases we observe the good collapse between the two ways of averaging meaning that the sampling of saddles is correctly done and it allows for a fair exploration of the geometric curve $k(u)$ [124].

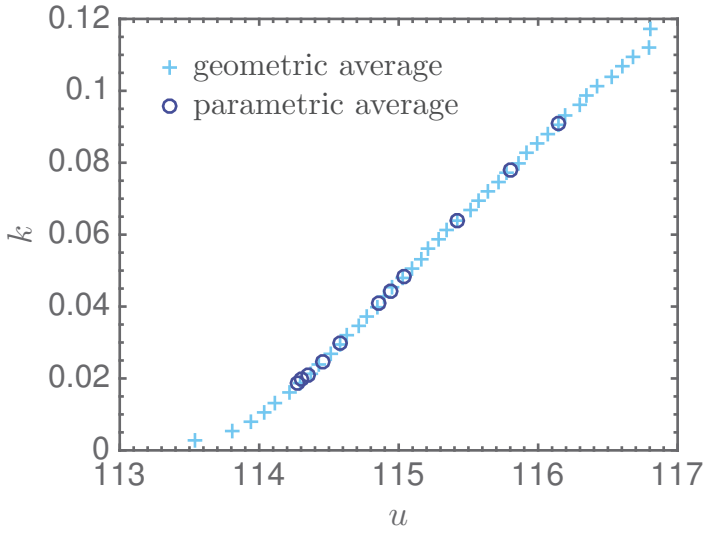

FIGURE 5.16: Comparison of the two possible ways of averaging the scatter plot 5.15. The parametric averages (○) has been done for temperatures $T \in [2.00, 1.75, 1.50, 1.25, 1.20, 1.15, 1.00, 0.95, 0.92, 0.91, 0.89]$ (from top to bottom).

We compare now the geometric averages of true saddles and QS for each system size. Results are represented in Figure 5.17. First we notice a relatively good agreement between the two methods used to compute the saddle points at the exception of $k \gtrapprox 0.07$ where the minimization of W seems to lead to QS with a density index higher than the corresponding index for true saddle points.

We also observe that apart from the smallest system, the EF method leads to a sampling of saddles points with large values of (k, u) and the region where $k \leq 0.02$ is not populated

for $N = 512$ and $N = 729$. This is more visible in the lower part of Figure 5.18 where we have represented the geometric average for the three system sizes. We notice the good collapse between the three systems meaning that the curve $k(u)$ is independent of the number of particles as expected by its definition. (This observation is also valid in the case of QS represented in the upper part in Figure 5.18).

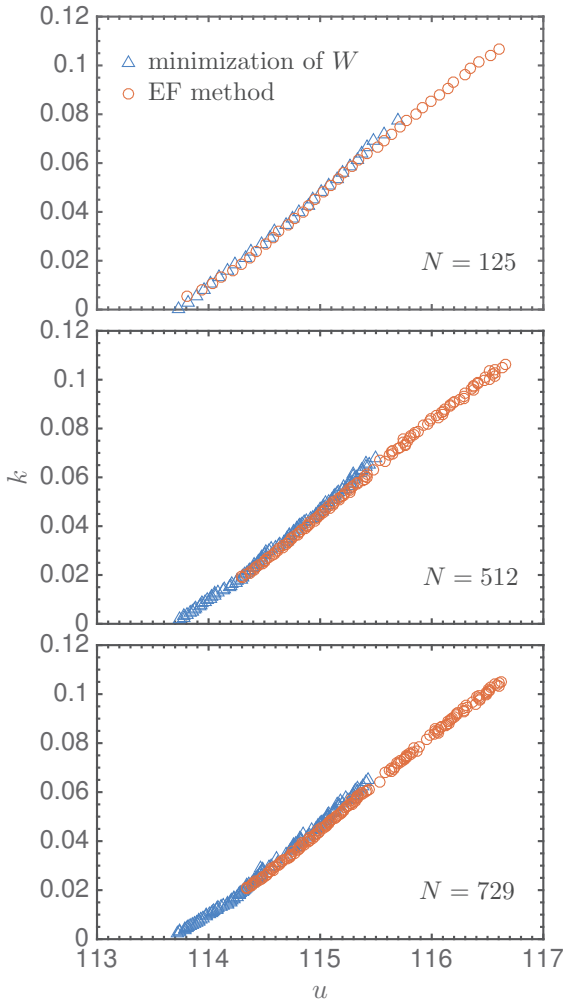

FIGURE 5.17: Representation for the 3 systems size of the geometric average of k as a function of the energy density u. The blue triangles correspond to results obtained by minimizing W (Quasisaddles) and the red circles are results of the EF method (Saddles).

This lack of information for $k < 0.02$ can be explained by the way we used the EF method. We recall that we fix the index of negative directions K at the beginning the Newton-Raphson procedure meaning that K is very close (or equal) to the number of negative directions that could be found with an instantaneous normal mode analysis (INM).

We noticed that if we leave K varying during a certain number of iterations before fixing

its value as it was suggested by Doye and Wales [128] or Grigera [138], K stabilized around a lower value than the initial one. However in most of cases the convergence is not reached and $W = |\boldsymbol{\nabla} U|^2$ gets stuck around 10^{-2}.

We tried another approach to populate the region $k < 0.02$. Assuming that sampling saddles from low temperatures corresponds to exploring the lower part of the curve $k(u)$ for $T \leq 1.00$, we fixed K to values that allow for $k \in]0; 0.2]$. Again the convergence was not observed.

These unsuccessful attempts reveal that the difficulties encountered to find true saddles when the number of particles is increased. Even by fixing K from the beginning the convergence is not ensured and for instance the success rate is $\approx 96\%$ for $N = 125$, it decreases to $\approx 70\%$ for $N = 512$ and it falls to $\approx 40\%$ for $N = 729$.

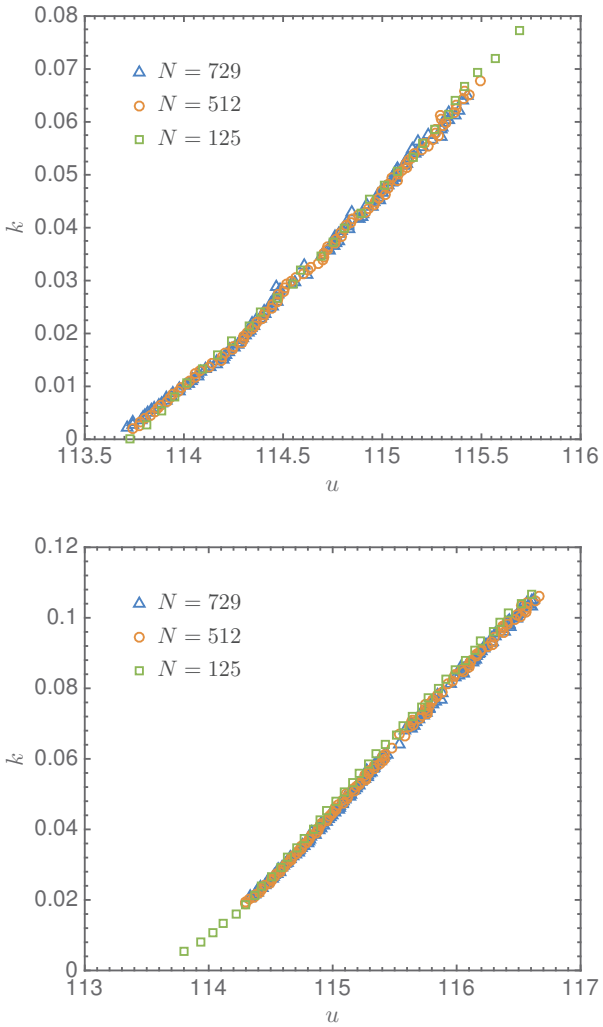

FIGURE 5.18: Representation of the geometric average of k as a function of the energy density u for the 3 systems size. The upper graph is for QS whereas the lower graph is for true saddles.

In Figure 5.17 we observe finally that for $N = 125$, k seems to be a linear function of u whereas for $N = 512$ or 729 there is an apparent change in the slope when $k \leq 0.2$. For the reasons mentioned just above, this change is only visible when considering QS. As explained by Cavagna [123] the derivative of $k(u)$ is directly related to the energy barriers which exist between adjacent saddles. Thus we can assume that this change of slope is the signature of differences that occur at the level of the energy barriers. More precisely the apparent change of slope is likely to be associated to the transition from the Arrhenian to the super-Arrhenian regime. As a matter of fact, by using the parametric average we can determine the range of temperature for which the change in the slope of $u(k)$ occurs.

In Figure 5.20, we have represented for $N = 729$ both parametric and geometric averages of QS. We observe that the slope of $u(k)$ changes for a temperature $1.00 < T < 1.10$ which is cooler (but close) than the crossover temperature $T^* = 1.25$ for which we have identified the transition from the Arrhenian to the super-Arrhenian behavior in Chapter 4.

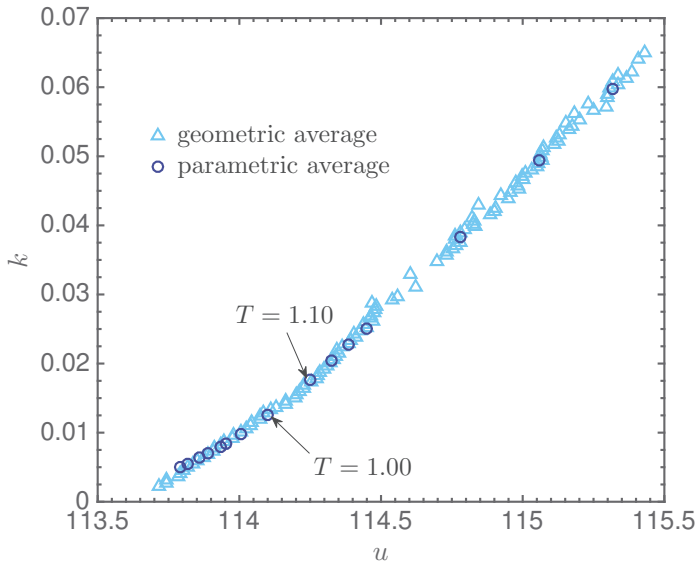

FIGURE 5.19: Representation of both geometric (△) and parametric (○) averages computed from QS for a system of $N = 729$ particles.

This observation suggests that the slowing down of the relaxation time and its departure from the Arrhenian behavior might be interpreted in terms of a change in the potential energy barriers between saddles. Of course, one must be careful by doing such an interpretation as the activation barriers related to the Arrhenian regime are *free* energy barriers. However if we assume that the entropic contribution could be neglected, the evolution of the potential energy barriers might give a reasonable insight into the

underlying phenomenon responsible of the change from Arrhenian to super-Arrhenian behavior. To check this assumption we compute for saddles and QS the energy barrier ΔU_b using equation 5.30 proposed by in Cavagna [123].

5.2.3.2 Energy barriers

For saddles and QS we determine the energy barrier for the three system sizes. To do so, we followed the procedure described by Coslovich and Pastore in [130]. We performed a linear regression on the point cloud (u, k) associated to each temperature as shown in Figure 5.20. The slope of the linear regression gives dk/du and thus thanks to equation 5.30 the energy barrier ΔU_b can be estimated.

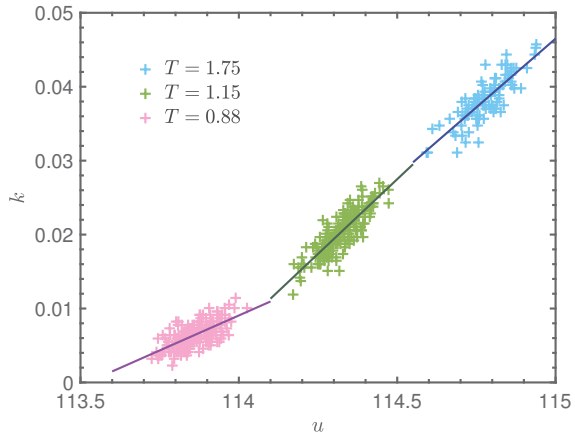

FIGURE 5.20: Representation of the linear regression performed on scatter data. For sake of clarity only 3 temperatures are represented.

In practice we computed also the slope du/dk by performing a linear regression on (k, u). In the case where the statistics would be sufficient, the slope dk/du would be equal to $(du/dk)^{-1}$. However in our case, we do not have enough statistics and we note some disparities between the two measurements. Therefore we made an average with both estimations and the energy barrier is now given by:

$$\Delta U_b = \frac{1}{6}\left[\frac{du}{dk} + \left(\frac{dk}{du}\right)^{-1}\right] \tag{5.41}$$

Results are shown in Figure 5.21 where we have represented the evolution of ΔU_b as a function of the scaled temperature $(T - T_c)/T_c$.

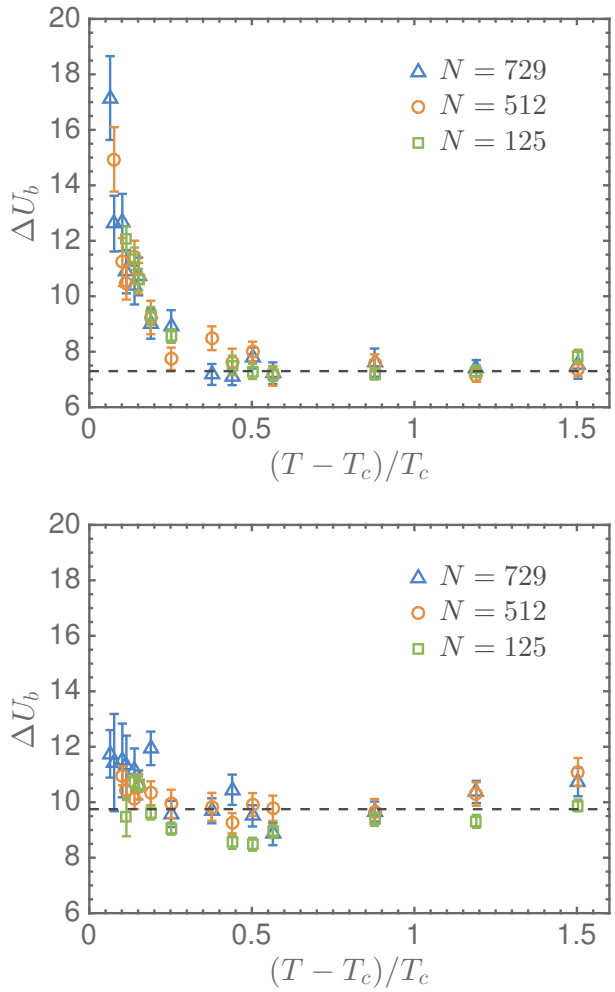

FIGURE 5.21: Estimation of the potential energy barriers ΔU_b as a function of the rescaled temperature $(T - T_c)/T_c$. Energy barriers are determined by using equation 5.41 for QS (upper graph) and for saddles (lower graph). The dashed black line corresponds in each case to the value of the constant energy E_h found for high-temperature regime: $E_h = 7.3$ for QS and $E_h = 9.8$ for saddles.

We observe that:

- For high temperature $T \geq 1.20$ ($(T - T_c)/T_c \geq 0.5$), the height of the energy barriers remains constant $\Delta U_b = E_h$. We notice however that the value of the energy barrier E_h is higher for saddles, indeed, $E_h = 9.8$ for saddles whereas $E_h = 7.3$ for QS. These values reflect the disparities observed in Figure 5.17 at high temperatures.
- For temperature $T < 1.20$ ($(T - T_c)/T_c < 0.5$), the height of the energy barriers increases while the system is cooled toward T_c. This observation is in agreement with the presence below T^* of temperature-dependent energy barriers whose height increases when the temperature is decreased. We notice however the limited increase of the energy barriers for the true saddle points. This is related to the fact

that even at low temperature we were not able to access the regime $k \leq 0.2$ where significant changes in the curve of $k(u)$ are expected.

Coslovich and Pastore perfomed a saddle analysis on LJ glass-formers [130] and observed the same phenomenology described above for ΔU_b. They also showed that the more fragile the mixture the higher ΔU_b [130]. To see whether this effect is also visible in our system we have computed the energy barrier ΔU_b for a mixture with 80% of large particles. Indeed, in Chapter 4 we have seen that by changing the mixture composition of the bidisperse Voronoi liquid and increasing the number of large particles, the fragility decreases. In Figure 5.22 is represented ΔU_b as a function of T/T^* for the 80 : 20 and the 50 : 50 mixtures. We observe that at high temperature ΔU_b has almost the same value whatever the mixture. However when the temperature is decreased below the crossover temperature T^*, we notice that the increase of ΔU_b is less pronounced for the 80 : 20 mixture.

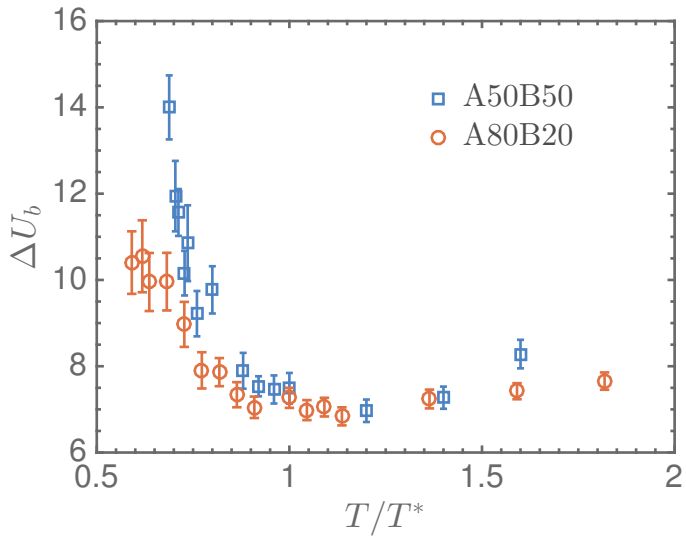

FIGURE 5.22: Evaluation of the energy barrier ΔU_b for systems of $N = 1000$ particles with different compositions.

For the moment we focused only on the evolution of the density index k as a function of density energy u to describe phenomena that occurs at the saddles level in the PEL. Angelani *et al.* proposed an alternative view of the problem by considering the elevation in potential energy with respect to the corresponding IS [125]. They investigated the quantity $u - e_{IS}$ as a function of k for several LJ simple liquids and glass-formers and found that they all collapse on the same master curve [5]. This suggests that these different systems share common features regarding the PEL.

In order to see if this observation is more general and concerns also liquids whose potential is different from the LJ potential, we computed the difference $u - e_{IS}$ for the

bidisperse Voronoi liquid. Results are shown in Figure 5.23 where we have represented $u - e_{IS}$ scaled by $k_B T_c$ as a function of k for the bidisperse Voronoi liquid and for four different LJ liquids [5]:

- The modified monatomic LJ (MLJ) at $\rho = 1.0$, the potential is given by $V_{MLJ}(r) = 4\epsilon[(\sigma/r)^{12} - (\sigma/r)^6] + \delta V$ where δV is a small many-body term used to inhibits crystallization, $\delta V = \alpha \sum_{\boldsymbol{q}} \theta(S(\boldsymbol{q}) - S_0)[S(\boldsymbol{q}) - S_0]^2$ with $\alpha = 0.8$ and $S_0 = 10$ and the sum is made over all q such as $q_{max} - \Delta < |\boldsymbol{q}| < q_{max} + \Delta$, $q_{max} = 7.2\rho^{1/3}$.
- The modified monoatomic soft spheres (MSS) at $\rho = 1.0$, the potential is given by $V_{MSS}(r) = 4\epsilon(\sigma/r)^{12} + \delta V$ where δV is defined just above.
- The Kob-Andersen (KA) mixture described in Chapter 4.
- A modified version of KA (KA2) where σ_{AA} and σ_{BB} are exchanged.

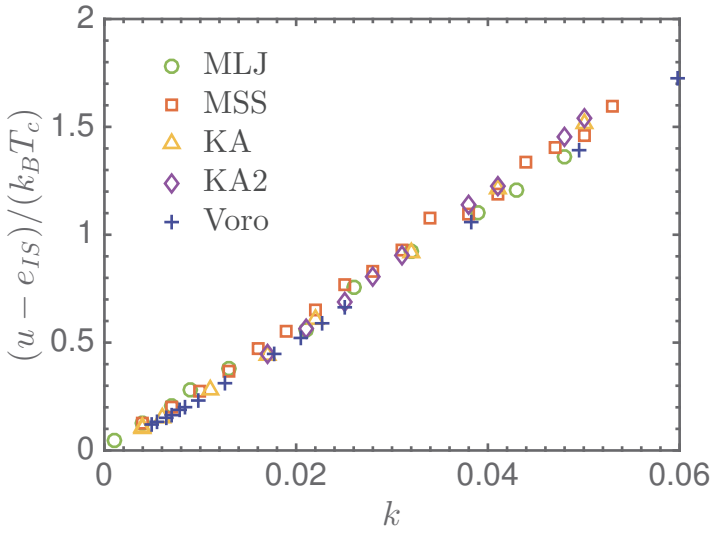

FIGURE 5.23: Representation of the elevation in potential energy rescaled by the energy at T_c as a function of the density index of negative direction. Data of LJ systems are taken from [5].

We observed that the bidisperse Voronoi liquid seems to collapse on the same master curve as the LJ systems, meaning that all these systems share universal common features.

Moreover Angelani *et al.* defined the elementary elevation ΔE, which corresponds to the energy to pass from a saddle of order n to a saddle of order $n + 1$ [5]:

$$\Delta E = \frac{1}{3} \frac{d(u - e_{IS})}{dk} \tag{5.42}$$

Apart from the presence of the IS energy, e_{IS}, this formulation is similar to the definition of ΔU (see equation 5.30) provided by Cavagna [123].

The value of ΔE is easily found by doing a linear fit on the data in Figure 5.23 before rescaling by $k_B T_c$. Angelani *et al.* recorded the values of ΔE for the 4 LJ systems and then computed $\Delta E^* = \Delta E / k_B T_c$. They found that for all models $\Delta E \approx 10 k_B T_c$. The collapse of the bidisperse Voronoi liquid on the master curve implies that, in our case, the relation $\Delta E \approx 10 k_B T_c$ is also valid.

As mentioned by Angelani *et al.*, it appears that the landscape of different systems share common features and that only one parameter ΔE describes the organization of saddles above the IS [5]. More important this phenomenon is not related to a specific class of potential, i.e LJ potential. Indeed, it was already shown that the Morse potential satisfied this observation[5]. Now we notice it is also the case for the bidisperse Voronoi liquid which is a many-body potential.

5.2.3.3 Evaluation of the mode-coupling temperature T_c

In his letter [123], Cavagna explained that the mode-coupling temperature T_c is often associated to the transition from a non-activated to an activated dynamics. Regarding the mechanisms he proposed to explain diffusion, in the case of fragile glass-formers T_c could be associated to the temperature T_B below which mechanism B becomes inefficient as there is no more negative directions at saddle points. Consequently, we can test numerically this assumption by considering equation 5.43 which links T_c to the threshold energy E_{th} below which there is no more negative direction.

$$E_{th} = \frac{\langle E_P(T_c) \rangle}{N} - \frac{3}{2} k_B T_c \tag{5.43}$$

E_{th} is obtained by fitting linearly the part of $k(u)$ below the crossover regime that we identified in Figure 5.20. As a consequence, we have to performed these fits on quasisaddles for which the regime of small values of $k(u)$ is accessible. Example of such a fit is shown in Figure 5.24 for a system of $N = 729$ particles and values of E_{th} for the other system sizes can be found in Table 5.3.

N	125	512	729	1000
E_{th}	113.7358	113.6619	113.6401	113.6438
T_c	0.8320	0.8088	0.8029	0.8038

TABLE 5.3: Table of the threshold energy E_{th} and mode-coupling temperature T_c computed from QS.

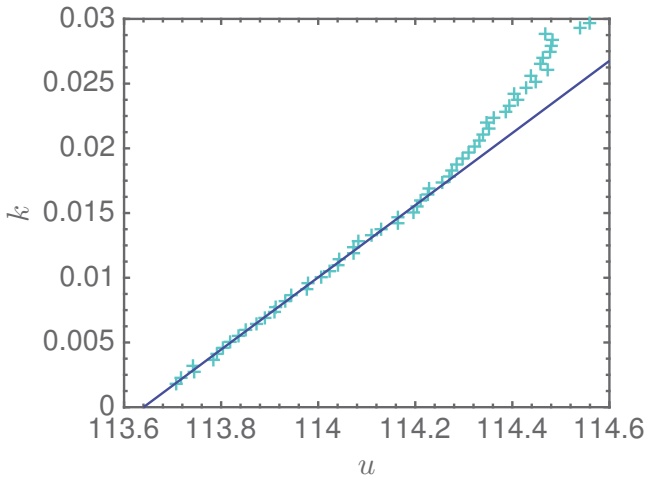

FIGURE 5.24: For N=729, representation of the geometric average (+). The linear solid line corresponds to the fit performed for $k \leq 0.015$.

As E_{th} corresponds to an energy without vibration, to determine T_c we remove the vibrational contribution to the average value of the potential energy $\langle E_P \rangle$ and by using equation 5.43 we can easily find T_c. In Figure 5.25 is shown $\langle E_P \rangle / N - 3/2 k_B T$ as function of T. Values of E_{th} for the different system sizes are also represented. The value of T_c corresponds to the temperature for which E_{th} intercepts the extrapolation of $\langle E_P \rangle / N - 3/2 k_B T$ for low temperature which are currently inaccessible by simulation. These values of T_c are shown in Table 5.3.

We notice that for the smallest system, the value found for T_c with a saddle analysis (performed on QS) is overestimated in comparison to the value of T_c^{MCT} found with ideal MCT analysis. However when the number of particles is increased, the values of $T_c \to T_c^{MCT}$ but remain slightly larger. This in agreement with what have been shown by Broderix *et al.* who determined from a saddle analysis the mode-coupling temperature for the Kob-Andersen model [124]. They found $T_c \approx 0.44$ which is a bit greater than $T_c^{MCT} = 0.435$ the value determined by ideal MCT [76].

This observation highlights that below $T_c \approx T_c^{MCT}$, Goldstein's scenario applies and the dynamics in the system is activated. When the temperature is increased, the dynamics becomes non-activated and this crossover is related to the presence of saddle points whose number of negative directions increase with temperature.

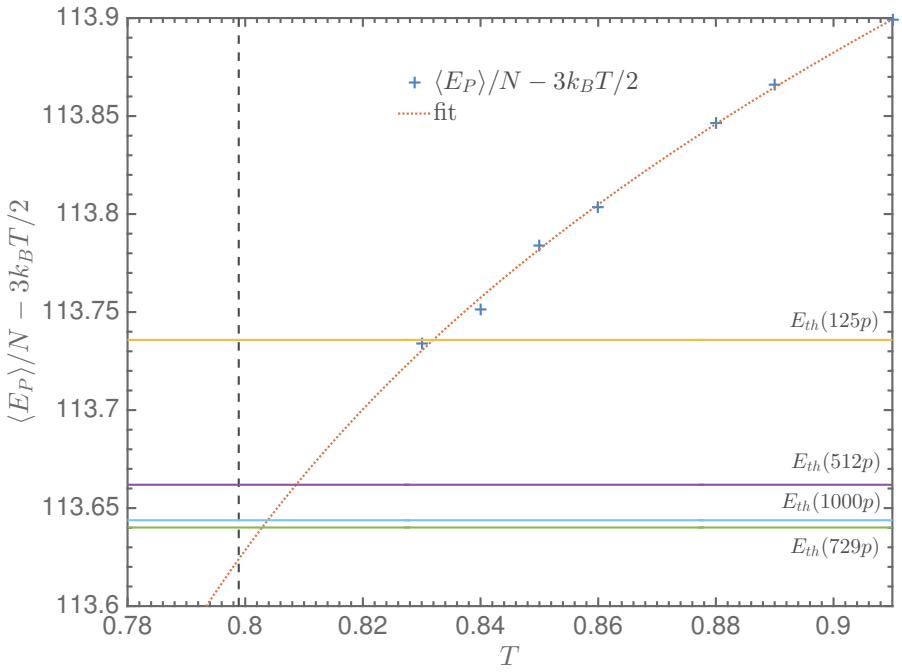

FIGURE 5.25: Potential energy per particle without vibration term as a function of temperature (+). The dot red line correspond to a fit performed on all data points of $\langle E_P\rangle/N - 3/2k_BT$ and we extrapolate the fit to values of T lower than the lowest isotherm. The horizontal solid lines are the values measured for E_{th} for the different system size. The vertical dashed line corresponds to the value of T_c found with the ideal MCT analysis.

The analysis in terms of saddles shows that, as suggested by Angelani *et al.* [132**?**], QS convey important information about dynamics that occur in real space. The remaining problem for saddles analysis is that, contrary to IS, there is no unique partitioning of the space and therefore using different methods to compute saddles would lead to different saddle points.

In the following chapter, we come back to the real space to investigate the relation between the slowing down of the dynamics and the presence of locally favored structures.

Chapter 6

Locally favored structures and crystallization

Contents

In Chapter 3, we have investigated the behavior of classical microscopic observables such as pair correlation function or its Fourier transform, the static structure factor. The relatively weak sensitivity of these observables upon cooling might lead to the wrong conclusion that structure plays a minor role in the dynamical arrest at glass transition. However one just has to remind that static structure factor is taken as input in MCT calculations to immediately realize that, even if the static density fluctuations are weakly varying when temperature decreases, these variations are sufficient to capture the slowing down of the dynamics.

Angell also referred to the differences in the structure of liquids when he proposed an explanation to the fragile/strong behavior [2, 13]. Indeed, strong liquids such as SiO_2 do not present important changes in their local order due to the strong directional bondings. On the opposite, the local environment of fragile liquids changes upon cooling.

The super-Arrhenian behavior is assumed to be related to the growth of domains composed of an underlying structure that minimizes locally the free energy, but which does not manage to tile the Euclidian space [24, 139] leading to the theoretical concept of geometrical frustration [140, 141].

The idea that some non-tiling local structures could minimize the local free energy dated back to the 50's when Frank showed that the ground state of 13 identical particles subjected to the Lennard-Jones potential, was the icosahedron [24, 142]. More recent studies identified the ground state of isolated clusters of different potentials and investigated how the spatial extension of these clusters could have a direct impact on the dynamics of glass formers. [22, 143].

The link between the presence of favored structures and slowing down of the dynamics have been observed in several studies. In 2002, Dzugutov *et al.* investigated a system of monoatomic particles where the potential was specially designed to favor icosahedral structures. He noticed that the dynamics of particles inside icosahedra was slower than the other ones [25]. In 2007 Coslovich and Pastore investigated the locally favored structures of numerous LJ binary mixtures by means of Voronoi tessellations and found that the icosahedron is the favored structure for the Wahnström model, whereas it is the bicapped square antiprism for the Kob-Andersen mixture. [21]. These results were thereafter confirmed by Malins *et al.* who investigated the locally favored structures using the Topological Cluster Classification (TCC) [22, 144].

The first section is devoted to the theory of geometric frustration which predicts a certain formulation of the free energy barriers in the super-Arrhenian regime. We will test to what extent this prediction applies for the bidisperse Voronoi liquid. Then in a second section, we will focus on finding the locally favored structures for the bidisperse Voronoi liquid. To that purpose, we will use the same method as Coslovich and Pastore [21]. The aim is to see if 1) a peculiar structure emerges upon cooling, 2) if it's the case, how the dynamics is impacted by its presence. In the final section we will present some results that tend to show that at low temperature a quasicrystal forms characterized by the presence of Frank-Kasper phases.

6.1 Geometric frustration

The theory of geometric frustration is based on three propositions that have already been well-verified for spherically symmetric particles but still remain postulates for molecular liquids, mixtures and polymers [141]. We summarize here the ideas that can be found [140, 141, 145].

(i) A liquid is characterized by a locally favored structure (LFS) that minimizes the local free energy of a small number of particles.

(ii) The LFS cannot tile the Euclidian space. The incompatibility between the local order and the global space filling is at the origin of *frustration*. The spatial extension of LFS generates superextensive strain as the space cannot be tiled with the LFS.

(iii) There exists a reference system in which the effect of the frustration can be turned off. For instance, it has been shown that in curved space a complete tilling of the space with icosahedra is possible [146]. In this reference system, there is a critical point reached when $T = T^*_{FL}$ for which a transition toward an ordered phase [145].

The theory supposes the existence of a critical point when there is no frustration. However this critical point would vanish as soon as a very small amount of frustration is introduced. Due to the presence of frustration, long-range order is forbidden. Therefore below T^*_{FL}, the temperature at which would occur the transition when no frustration is present, the liquid breaks up into different domains composed of LFS whose size and future growth is limited by frustration [20, 140].

In the frustration-limited domain picture, T^*_{FL} is the temperature at which the behavior of the liquid is impacted by the presence of domains. A scaling description of the slowing-down of the dynamics is proposed and it predicts a super-arrhenian behavior of the relaxation time below T^*_{FL}:

$$\tau = \tau_0 \exp\left[\frac{E_A(T)}{k_B T}\right] \tag{6.1}$$

where the free energy barrier $E_A(T)$ is given by:

$$E_A(T) = \begin{cases} E_\infty & T > T^*_{FL} \\ E_\infty + BT^*_{FL}\left(1 - \dfrac{T}{T^*_{FL}}\right)^\psi & T < T^*_{FL} \end{cases} \tag{6.2}$$

B is a parameter measuring the departure from the Arrhenian behavior, so in other words it measures the fragility of the system [140]. It can be shown that B increases as the frustration decreases [141].

The exponent ψ has a universal character as it has been shown experimentally that for a wide range of liquids, $\psi = 8/3$ [80] and then it was analytically demonstrated that the value of the exponent is 8/3 [140]. However for certain systems it can weakly deviate from 8/3 and it has been shown experimentally that it could vary between 7/3 to 3 [141].

To test the predictions of the frustration-limited theory we try to fit the data of relaxation time of the bidisperse Voronoi liquid by using equations 6.1 and 6.2. The result of the fits are represented in Figure 6.1.

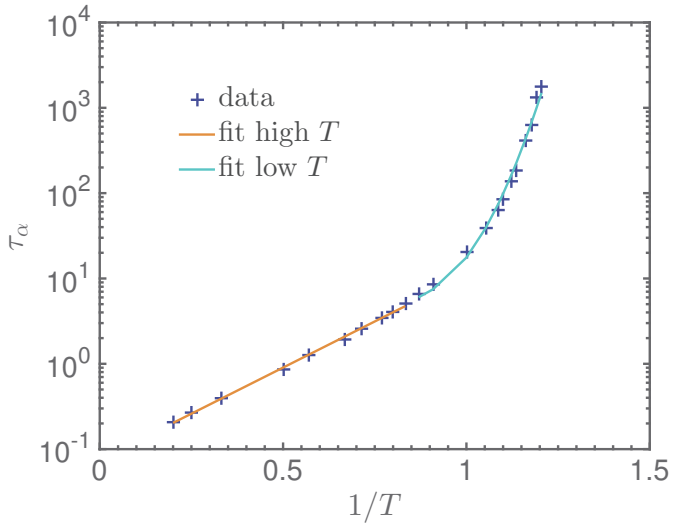

FIGURE 6.1: Fit of the relaxation time τ_α with equations 6.1 and 6.2. The pink solid line corresponds to the fit at high temperature when $T > T^*_{FL}$ whereas the blue solid line corresponds to the one at low temperature when $T < T^*_{FL}$.

We noticed first that equations 6.1 and 6.2 allow a quite good description of the data. We briefly discuss the results for the fitting parameters (B, T^*_{FL} and ψ):

- The temperature at which the crossover to the domains-dominated dynamics takes place is $T^*_{FL} = 1.15$ and is close from $T^* = 1.25$, the crossover temperature to the super-Arrhenian regime.
- In our case we found that the parameter $B \sim 128$. It is a relatively small values in comparison to what has been observed for experimental systems [147]. This means that our system has a relatively high degree of frustration.
- Finally in our case we found that $\psi = 8/3$ which is in agreement with most of results found in litterature [141, 145, 147].

All these observations suggest the presence of an underlying locally preferred structure that we need now to identify. In the next section we use a Voronoi analysis to determine the most frequent polyhedra present in the bidisperse Voronoi liquid.

6.2 Locally favored structures (LFS)

6.2.1 Computing LFS

In 2007, Coslovich and Pastore investigated the link between fragility and the emergence of locally favored structures for several LJ glass formers by means of Voronoi tessellations

[21]. We naturally chose to proceed in the same way as the Voronoi analysis is particularly straightforward for our model. However, contrary to Coslovich and Pastore, who proceeded to a classical Voronoi analysis, all the LFS analysis will be performed within the specific framework of Voronoi-Laguerre tessellation since the bidisperse Voronoi liquid is directly built from the geometrical properties of this tessellation.

In Chapter 1 we have seen that to each particle is associated a Voronoi polyhedron and that this polyhedron is composed of faces which are polygons. To identify the LFS, we compute the distribution of faces, i.e we look for each polyhedron to the number of faces associated to a specific polygon composed of k vertices. Thus in practice each polyhedron can be described by a succession of integers $(n_3, n_4, n_5, n_6, \cdots)$ where n_k is the number of faces composed of k vertices [21]. In other words, it corresponds to the number of times a specific polygon $(\triangle, \square, \pentagon, \hexagon, \cdots)$ appears in the Voronoi polyhedron. The smallest polygons that can be observed are triangles and so we start our classification with triangles. For each temperature $T \in [0.83; 2.00]$ we investigated the LFS of 1000 independent thermalized configurations and IS configurations. By independent we mean that configurations are space out by at least τ_α.

We started by investigating the LFS on all particles and as Coslovich and Pastore, we observed that the small B particles are more likely to be at the center of a well-defined geometry whereas no peculiar structure seems to be associated to large particles. Therefore in what follow we focused only on small particles and in Table 6.1 is presented the three most frequent structures at $T = 2.00$ and $T = 0.83$. We notice that:

- At high temperature, in thermalized configurations the fraction of LFS is relatively weak. The most frequent structure represents less than 5% of all the structures associated to B particles. However when looking at IS configurations, we observe that favored structures are already substantial, more than 16% of B particles are involved in a distorted icosahedron ($(0, 2, 8, 2)$ signature).
- At low temperature, icosahedron ($(0, 0, 12)$ signature) is the most frequent structure that appears in both thermalized and IS configurations. Distorted icosahedra represent still a non-negligible fraction of the LFS.

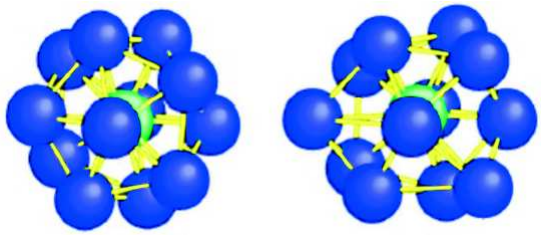

FIGURE 6.2: Left: icosahedron. Right: distorted icosahedron. (Reproduced with permissions from [6], copyright The American Association for the Advancement of Science 2013.)

$T = 2.00$				$T = 0.83$			
Thermalized config.		IS config.		Thermalized config.		IS config.	
Signature	%	Signature	%	Signature	%	Signature	%
$(0, 3, 6, 4)$	4.1	$(0, 2, 8, 2)$	16.4	$(0, 0, 12)$	17.7	$(0, 0, 12)$	26.4
$(0, 3, 6, 3)$	3.6	$(0, 3, 6, 4)$	12.5	$(0, 2, 8, 2)$	13.1	$(0, 2, 8, 2)$	16.2
$(0, 2, 8, 2)$	3.2	$(0, 0, 12)$	9.3	$(0, 3, 6, 4)$	7.7	$(0, 3, 6, 4)$	8.8
$(0, 0, 12)$	0.5	$(0, 3, 6, 3)$	8.2	$(0, 3, 6, 3)$	4.7	$(0, 3, 6, 3)$	5.6

TABLE 6.1: Table representing the three most frequent Voronoi polyhedra around small particles for $T = 2.00$ and $T = 0.83$. For both temperatures polyhedra have been identified for the thermalized and the IS configurations. The last line of the table shows structures that are not the most representative at T but they are mentioned for purpose of comparison.

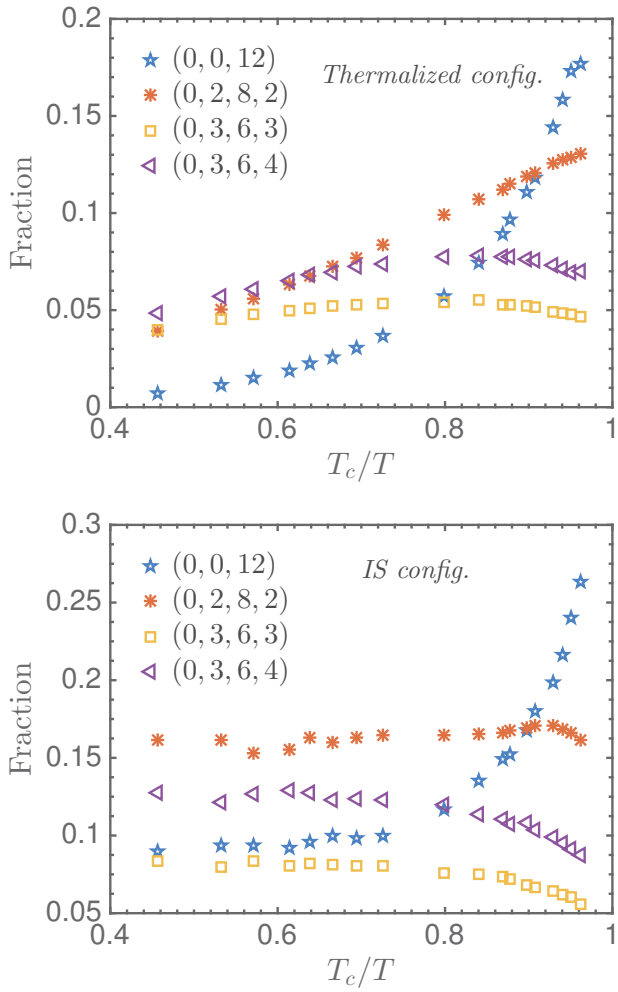

FIGURE 6.3: Evolution of the fraction of the LFS with temperature for thermalized configuration (upper graph) and IS (lower graph). $T_c = 0.7989$.

The evolution of the LFS over the whole range of temperatures is shown in Figure 6.3 where we observe that:

- When the temperature is decreased, there is a huge increase of the number of icosahedra for both thermalized and IS configurations.
- The number of distorted icosahedra in thermalized configurations is increasing slowly upon cooling whereas it remains barely constant in IS configurations.
- The LFS $(0, 3, 6, 4)$ and $(0, 3, 6, 3)$ slightly increase in thermalized configurations and decrease in IS configurations.

The increase of icosahedra is certainly the most striking result. We also notice in Figure 6.3 that this increase is much more pronounced when $T_c/T \gtrsim 0.7$ which corresponds to $T \lesssim 1.15$. Interestingly this temperature corresponds to the temperature T^*_{FL} below which the formation of domains of LFS is expected.

The temperature is also very closed from the crossover temperature $T^* = 1.25$. Therefore this suggests a possible correlation between the strong increase of icosahedra and the presence of a marked super-Arrhenian regime. Increase of icosahedra have already been observed for fragile glass formers such as binary alloys [148] or the Wahnström model [21, 22]. Knowing that, we computed the LFS of the Wahnström model and the AMLJ-0.80 mixture and we indeed found an increase of the number of icosahedra. In a second step, we compared results obtained for the bidisperse Voronoi liquid with those of LJ glass formers. In Figure 6.4 we have represented for thermalized and IS configurations, the evolution with temperature of the fraction of icosahedra as a function of the scaled temperature T_r/T.

We observe that the increase of the fraction of icosahedra is qualitatively the same for the three glass formers. All these systems have barely no icosahedra at height temperature when they are thermalized and only a small fraction of icosahedra exists in the IS configurations. As the temperature decreases, the fraction of icosahedra increases. Moreover, for both thermalized and IS configurations when the temperature $T < T^*$, the increase is much more pronounced which correlates with the entrance into the super-Arrhenian regime. When considering only the IS configurations, we notice that the bidisperse Voronoi liquid exhibits a steeper increase of the fraction of icosahedra than the two other LJ glass formers.

Moreover Coslovich and Pastore have determined, for the Wahnström model, that the other most frequent Voronoi polyhedron associated to small particles, is $(0, 2, 8, 2)$ [21]. Our analysis reveals that the same observations also hold for AMLJ-0.80. Therefore there must be some common underlying features between all these glass formers.

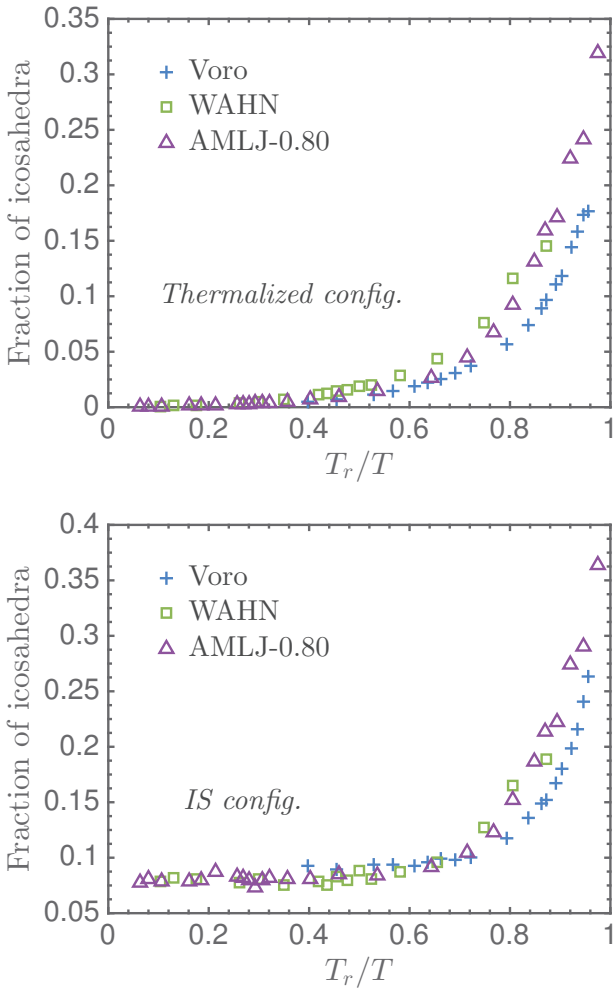

FIGURE 6.4: Evolution of the fraction of icosahedra as a function of T_r/T for the bidisperse Voronoi liquid and two LJ glass formers WAHN and AMLJ-0.80. The upper graph shows the evolution for thermalized configuration whereas the lower graph focuses on IS configurations.

It was suggested by Crowther *et al.* that, in case of LJ systems, the definition of σ_{AB} might be the common trait between systems sharing the same LFS [81]. When $\sigma_{AB} = 0.5(\sigma_{AA} + \sigma_{BB})$ one speaks about an additive mixture whereas $\sigma_{AB} \neq 0.5(\sigma_{AA} + \sigma_{BB})$ corresponds to a non-additive mixture. The assumption of Crowther *et al.* seems to be verified for the KA model (which is non-additive) as it shares the same LFS as non additive metallic glasses [81]. We also notice in this study that WAHN and AMLJ-0.80, which are both additive, share the same LFS.

Although the definition of σ_{AB} might give intuition about the possible LFS, it is not sufficient to predict the LFS. Indeed Coslovich and Pastore performed isobaric simulations on various additive mixture of LJ by changing only the value of σ_{BB}. They found that when σ_{BB} is decreased, the fraction of icosahedra is also decreasing and for $\sigma_{BB} < 0.7$, icosahedra are not found among the most frequent structure [21]. Thus it seems that

one needs to consider also the ratio σ_{BB}/σ_{AA}.
Moreover in the case of the bidisperse Voronoi liquid, we cannot speak about additive or non-additive interactions, as a term like σ_{AB} does not exist, only the definition of $\eta = \sqrt{R_A^2 - R_B^2}/v^{1/3}$ makes sense. However we have demonstrated in Chapter 3 that for the pair correlation function, the position of the first peak r^*_{AB} associated to A-B interaction is always equal to $0.5(r^*_{AA} + r^*_{BB})$, which is a characteristic of additive mixture at low temperature. Thus we could assume that the bidisperse Voronoi liquid possesses some characteristics of additive interactions and if we consider that the size ratio $R_B/R_A = 0.83$ is the same as for the Wahnström model, that might explain why our system shares similarities with WAHN and AMLJ-0.80 regarding the LFS.

In Figure 6.5 is represented the evolution of the fraction of icosahedra with temperature for different compositions $A : B$ of the bidisperse Voronoi liquid. We observe that the larger the number of A particles, the weaker is the increase of icosahedra upon cooling for both thermalized and IS configurations. We even notice that for the 80 : 20 mixture, the number of icosahedra remains constant for IS configurations. Moreover we observe for the IS configurations that the fraction of icosahedra at $T_r/T = 0.4$ is decreasing when the number of large particles A is increased. For each configuration we computed the average numbers n_A of large A particles and n_B of small B particles that composed the icosahedra. Results are shown in Table 6.2.

A50B50				A60B40				A70B30				A80B20			
$T = 2.00$		$T = 0.83$		$T = 2.00$		$T = 0.76$		$T = 2.00$		$T = 0.65$		$T = 2.00$		$T = 0.65$	
n_A	n_B	n_A	n_B	n_A	n_B	n_A	n_B	n_A	n_B	n_A	n_B	n_A	n_B	n_A	n_B
6	6	7	5	5	7	6	6	6	6	6	6	6	6	6	6

TABLE 6.2: Evolution with the composition of the average numbers n_A and n_B of A and B particles composing the icosahedra at $T = 2.00$ and $T = T_{min}$.

For mixtures 70 : 30 and 80 : 20 the average numbers of neighbors A and B is similar at high and low temperature as it was observe for additive mixtures and Wanström model in [21]. For 50 : 50 and 60 : 40 we observe slight variations and we notice that for the equimolar mixture, there are more large neighbors of type A at $T = 0.83$. For this low temperature, this change in the neighborhood, even if small, could be an indicator of the ease to generate Frank-Kasper network. This point will be more detailed in the last section of this chapter.

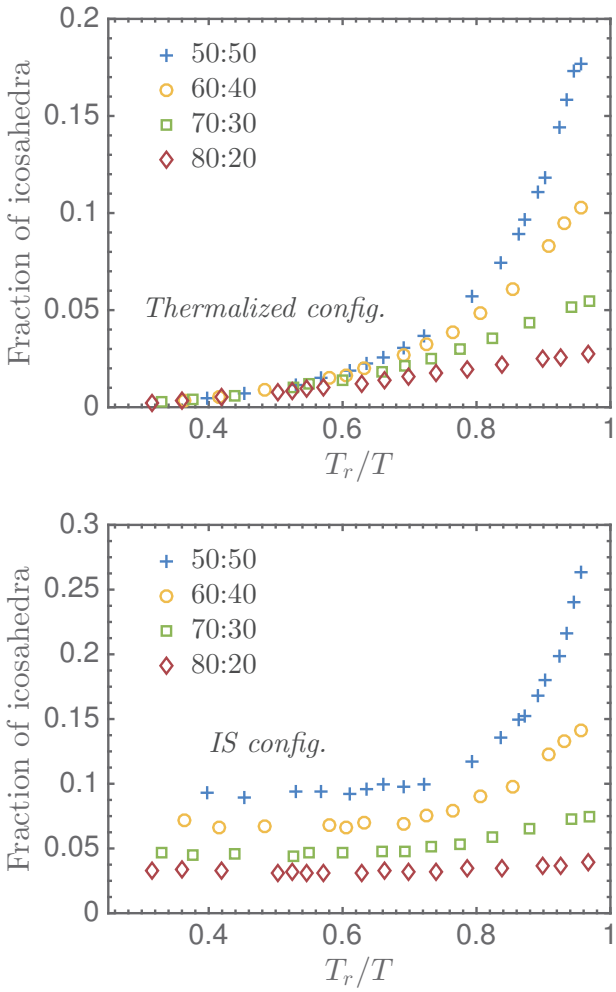

FIGURE 6.5: Evolution of the fraction of icosahedra as a function of T_r/T for different compositions of the bidisperse Voronoi liquid. The upper graph shows the evolution for thermalized configuration whereas the lower graph focuses on IS configurations.

We also identify the LFS for each composition for thermalized configuration as it is shown in Table 6.3. We notice that when the number of large particles is increased the icosahedron is no more the favorite structure and it is little by little replaced by other structures such as (0,2,8,1) or the distorted icosahedron, which seems to be the LFS common to all the mixture composition with a fraction always greater than 10%.

A60B40			
$T = 2.00$		$T = 0.76$	
Signature	%	Signature	%
(0,3,6,3)	3.8	(0,2,8,2)	14.2
(0,3,6,4)	3.6	(0,0,12)	12.5
(0,2,8,2)	3.2	(0,2,8,1)	9.1

A70B30			
$T = 2.00$		$T = 0.65$	
Signature	%	Signature	%
(0,3,6,3)	3.8	(0,2,8,2)	15.3
(0,2,8,2)	3.2	(0,2,8,1)	12.8
(0,3,6,4)	3.0	(0,0,12)	9.3

A80B20			
$T = 2.00$		$T = 0.65$	
Signature	%	Signature	%
(0,3,6,3)	3.6	(0,2,8,1)	13.7
(0,4,4,3)	3.5	(0,2,8,2)	12.2
(0,2,8,1)	3.1	(0,2,8,4) [1]	10.0

TABLE 6.3: Table of the most frequent LFS for different compositions of the bidisperse Voronoi liquid at $T = 2.00$ and $T = T_{min}$ the lowest simulated temperature for each composition. The LFS were determined for thermalized state.

This change of LFS with composition is likely to be related to the fragility of each mixtures. In Chapter 4 we have seen that when the number of large particles is increased, the bidisperse Voronoi liquid is less and less fragile. Thus we see that the more icosahedra, the more fragile the mixture. On the opposite when the mixture is strong other LFS seem to emerge. However their fraction does not exceed 14% of small particles meaning that domains of LFS should not be abundant, if any. Composition also influences the LFS of usual LJ glass formers and it is interesting to notice that Coslovich and Pastore also found for the AMLJ systems a reduction of the fraction of LFS when the parameter σ_{BB} is decreased or equivalently when systems become less fragile [21]. Moreover by using TCC, Crowther *et al.* have also observed modifications in the LFS of the Kob Andersen model when changing the composition and observed that the fraction

1. This LFS is found around large A particles. Its percentage was computed with respect to large particles.

of bicapped square antiprism increases when the number of small particles is increased [81].

Additionally Crowther *et al.* have shown that bicapped square antiprisms are associated with an important slowing down of the dynamics. Some similar observations occur when the LFS is composed of icosahedron [25]. These lead us to investigate the effect of icosahedra on the dynamics of the bidisperse Voronoi liquid, but prior to this we want to characterize the spatial extension of this icosahedral order.

6.2.2 Presence of domains

As suggested by the frustration-limited theory, below T^*_{LFS}, the preferred structures tend to spatially extend upon cooling and as a result the formation of clusters have been reported [21, 25, 143, 144]. To test whether this observation also applies for the bidisperse Voronoi liquid we looked for the presence of clusters of icosahedra for $T < T^*_{LFS}$.

To determine the existence of such clusters, we proceeded in the following way:

1. We determine the particles i located at the center of icosahedra. To do so we focus on particles whose Voronoi polyhedron is (0,0,12).
2. Then for each i, we identify the 12 neighbors j that form the icosahedron.
3. Before defining the algorithm for the clusters search, we need to define how two icosahedra i and j can be connected. We highlight the fact that we only consider the problem from a geometrical point of view and we do not search for clusters that minimize locally the potential energy as it was for instance done by Doyes *et. al* [143]. As a result 4 connections can be considered. An illustration of these four connections is provided in Figure 6.7.
   (a) The minimal connection that can link two icosahedra consists on one common nearest neighbor shared by i and j.
   (b) Two icosahedra can be linked through a common edge. This implies that i and j have 2 common nearest neighbors.
   (c) It is possible that two icosahedra share a common facet, in this case 3 common neighboring particles of i and j are involved in the process.
   (d) Finally j can be one of the nearest neighbors of i and in this case they both share 5 common neighbors.

   We consider that the minimal connection in our cluster-search procedure and therefore two icosahedra are considered as belonging to the same cluster if they share at least one common neighbor.

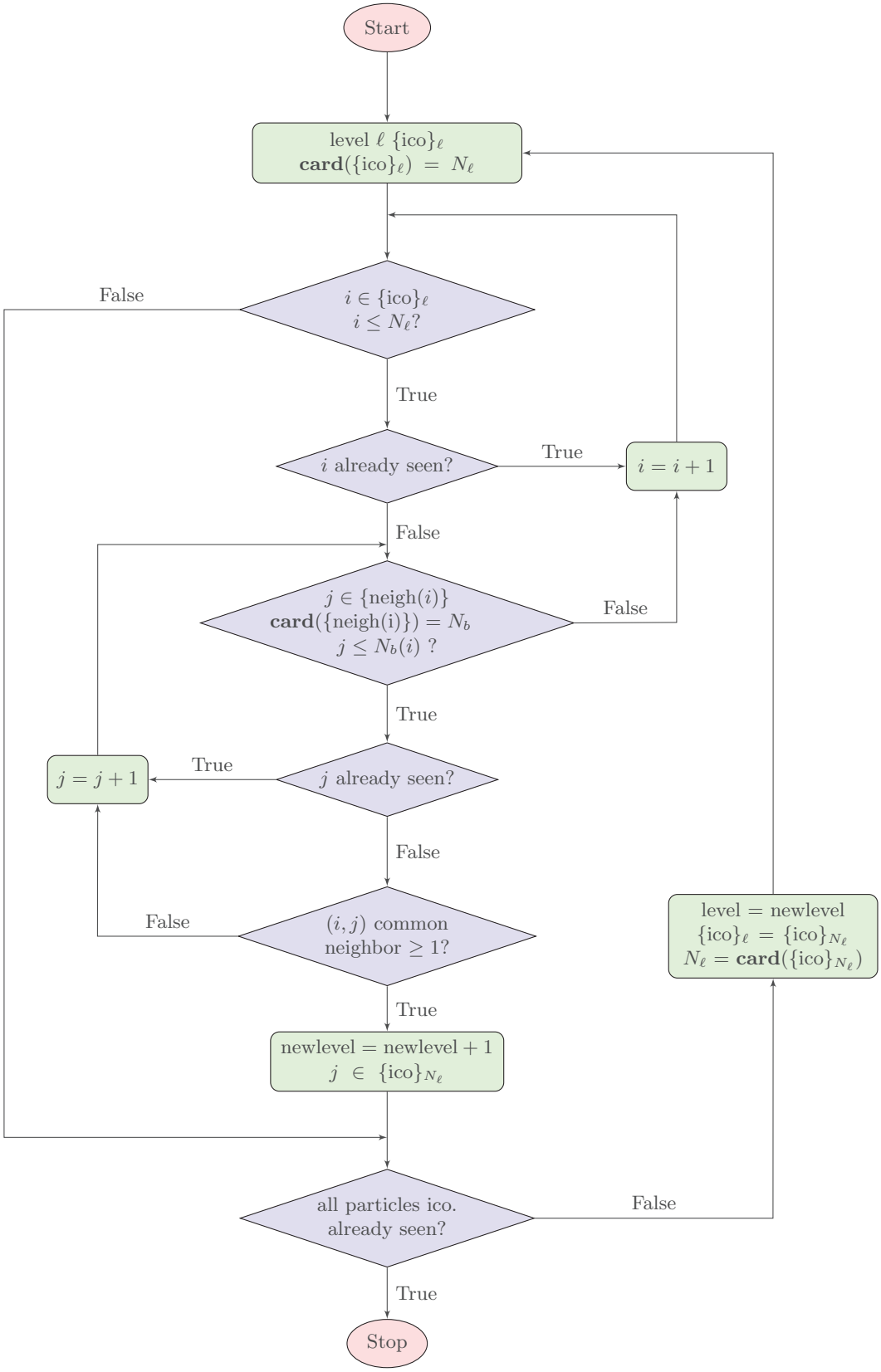

FIGURE 6.6: Algorithm for the clusters search. To find a cluster we consider a particle at the center of an icosahedron (level $\ell = 0$) and we identify the neighbors which are also at the center of icosahedra (level $\ell = 1$). Then for each of these specific neighbors, their own neighbors are also analyzed to determine those inside icosahedra. We repeat this procedure until the particle analyzed has no unseen icosahedra in its neighborhood (level=newlevel). To avoid the possibility of considering two times or more the same particles we label as "seen" each particle analyzed.

4. The algorithm designed for the cluster search is represented in the flowchart in Figure 6.6.

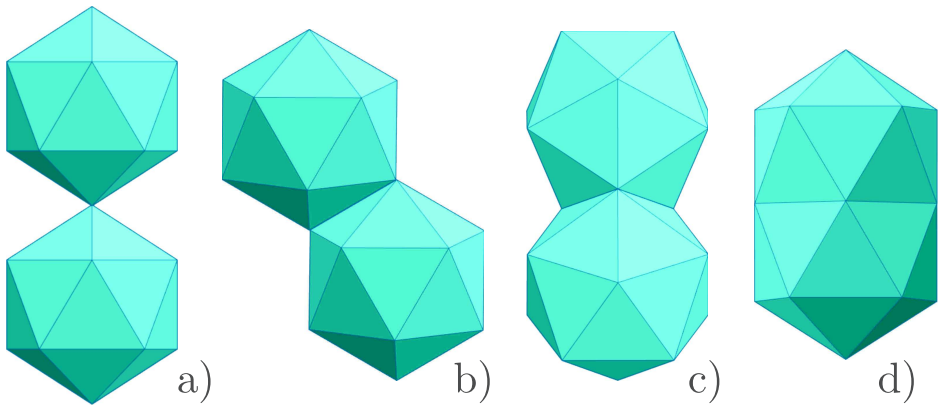

FIGURE 6.7: Representation of the different type of connections that can be found between two neighboring icosahedra: a) only one particle is common to the two icosahedra, b) in this case, an edge is shared and two neighboring particles are involved, c) the two neighboring icosahedra share a facet meaning that 3 neighbors are concerned and d) the two icosahedra interpenetrate. This implies that 5 neighbors are shared.

Now that we have a tool to identify clusters, we can measure the probability $P(n_i)$ of having clusters composed of n_i icosahedra. This probability is represented in Figure 6.9 (upper graph) for temperatures $T \in [0.83, 1.00]$. We observe that:

- For the highest temperature $P(n_i)$ is monotonously decreasing as n_i increased. However we underline the fact that clusters of more than 50 icosahedra can already be observed at $T = 1.00$.
- When the temperature is decreased, the behavior of $P(n_i)$ is no longer monotonous. A decrease is observed and then for $n_i > n_c$, a critical size, $P(n_i)$ is increasing and a maximum is reached. We notice that this phenomenon is enhanced upon cooling.
- For $T \leq 0.85$, the presence of large clusters is significative in the system as it is suggested by the growth of maximum of $P(n_i)$ for $n_i \sim 90$. In Figure 6.8 is shown a snapshot of a configuration where 96 icosahedra were counted and 90 of them have formed a cluster.

Figure 6.8 suggests the ability of icosahedra to arrange in the different directions of the space. One can assume that connections involving 1,2 or 3 neighbors should make easier changes in any direction of space, whereas 5 neighbors connections may favor the formation of linear clusters. In order to test this hypothesis, we have computed the probability $P(n_i)$ by considering the following rule: "two icosahedra belong to the same cluster if they share only N_{nn} nearest neighbors." We recall that, initially, we require that these icosahedra share at least one nearest neighbor ($N_{nn} \geq 1$). Results of such process for the lowest temperature $T = 0.83$ is shown in the lower part in Figure 6.9.

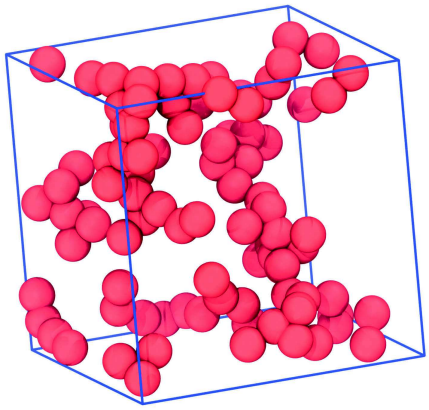

FIGURE 6.8: Snapshot of typical clusters of $n_i = 90$ icosahedra at $T = 0.83$. 96 icosahedra are represented in total.

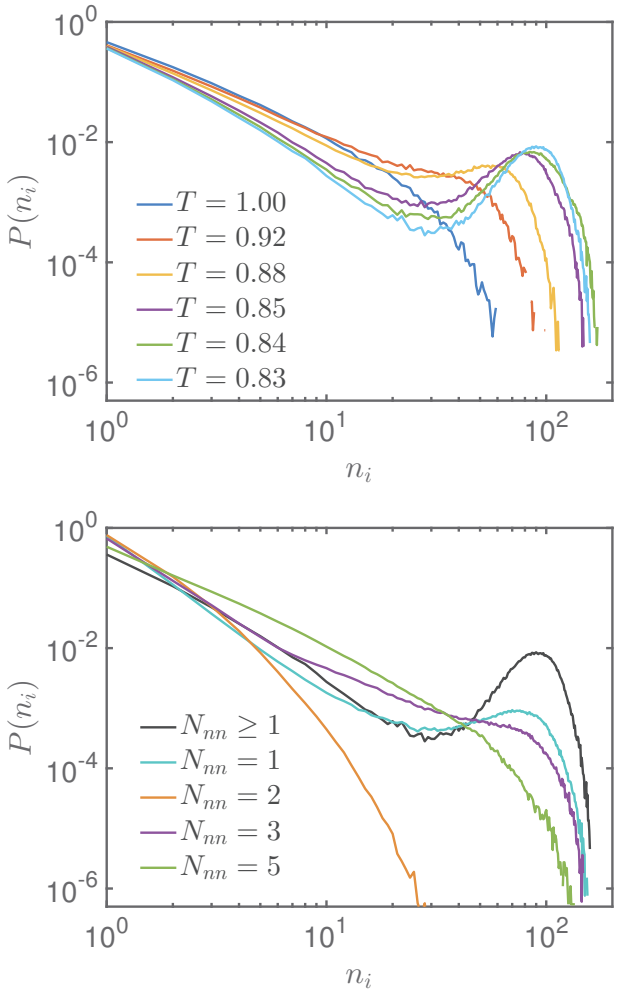

FIGURE 6.9: Upper graph: Probability $P(n_i)$ of having clusters composed of n_i icosahedra. Lower graph: Evolution of $P(n_i)$ in function of the number of common nearest neighbors N_{nn} between icosahedra at $T = 0.83$.

- As expected, the formation of large clusters is favored by the possibility of sharing one common neighbor. We notice also that sharing a face is also increasing $P(n_i)$ for relatively large n_i.
- Surprisingly sharing an edge, i.e $N_{nn} = 2$, does not enable to form large clusters. This might be due to steric effects between neighboring particles of both icosahedra.
- Finally we observe that when $N_{nn} = 5$, $P(n_i)$ continuously decreases but there is a non-zero probability to find a large cluster where the center of icosahedron $i+1$ is located in the closest neighborhood of icosahedron i.

The probability $P(n_i)$ have shown the existence of large clusters composed of icosahedra. One can wonder to what extent these clusters are representative. In other words, if one selects a particle arbitrarily, what is probability that this latter is located at the center of an icosahedron included in a cluster of size n_i ?

To answer this question we define the probability $Q(n_i)$ that for a configuration sampled from thermal equilibrium, a particle chosen at random is located at the center of an icosahedron which is included in a cluster of size n_i.
For a configuration with a relatively large number of particles, if N_c is the total number of clusters, $\langle N_c \rangle P(n_i)$ measures the number of clusters of size n_i, then $\langle N_c \rangle P(n_i) n_i$ counts the number of particles located at the center of icosahedra in a cluster of size n_i. Therefore the probability $Q(n_i)$ is given by $Q(n_i) = \langle N_c \rangle P(n_i) n_i / N_c \propto n_i P(n_i)$.

As a result we compute $n_i P(n_i)$ which conveys the relevant informations. It is shown in the lower graph in Figure 6.10. We observe that when the temperature is lowered, there are more chances that a particle chosen at random is located at the center of an icosahedron in a large cluster. This is suggested by the pronounced maximum exhibited by $n_i P(n_i)$. Therefore the bidisperse Voronoi liquid has a clear tendency to form large clusters of icosahedra upon cooling.

Figures 6.8, 6.9 and 6.10 suggest a possible percolation of icosahedra in the system at low temperatures where the size of the percolating cluster would be given by the value of n_i when $P(n_i)$ is maximal ($n_i \approx 95$). An immediate perspective to this work would be to determine the percolation threshold and to see how it evolves with temperature. Moreover Figure 6.8 raises the question of the fractal character of such clusters and one could try to characterize it.

As predicted by the frustration-limited theory, the formation of domains has been observed for the bidisperse Voronoi liquid, we are now interested in the impact of these domains on the dynamics.

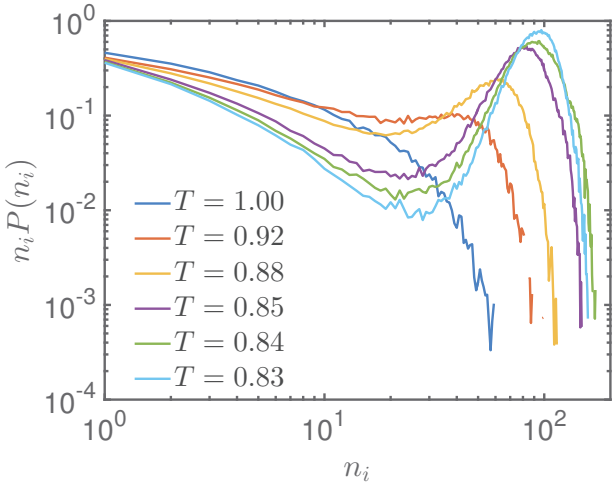

FIGURE 6.10: Evolution of $n_i P(n_i)$ with n_i for different temperatures. $n_i P(n_i)$ is proportional to the probability that a particle chosen at random is in cluster of size n_i for a configuration sampled from thermal equilibrium (see text for details).

6.2.3 Effect on the dynamics

The LFS are generally associated to slow domains as shown by Dzugutov *et al.* [25], Coslovich and Pastore [21] in the case of icosahedra, and then by Crowther *et al.* [81] for the bicapped square antprism. It is interesting to see to what extent clusters of icosahedra found above are likely to have an influence on the dynamics of the bidisperse Voronoi liquid.

Previously we focused only on the particles located at the center of icosahedra. We want now to differentiate all the N particles contained in the bidispserse Voronoi liquid and to do so we use the same scheme as in [21]. We define thus three sub-ensembles:

- the *ico*-ensemble which corresponds to the particles located at the center of icosahedra;
- the *neigh*-ensemble which deals with nearest neighboring particles belonging to the icosahedra but which are not located at the center. Particles are considered as neighbors if they share a face in the Voronoi tessellation.
- the *other*-ensemble which consists of particles that are neither at the center of an icosahedron nor in the LFS.

Therefore using equation 4.3, it is now possible to compute the intermediate scattering function for each of these sub-ensembles, i.e $F_s^{ico}(k,t)$, $F_s^{neigh}(k,t)$, $F_s^{other}(k,t)$ [21]. The relaxation times τ_{ico}, τ_{neigh} and τ_{other} can be extracted with the criterion $F_s^{sub}(k, t = \tau^{sub}) = 0.1$ where the subscript *sub* stands for "sub-ensemble".

The idea is then to compare the relaxation times of particles involved in LFS, meaning τ_{ico} and τ_{neigh}, to the relaxation time τ_{other} which concerns particles which do not belong to LFS. Results of ratios τ_{ico}/τ_{other} and $\tau_{neigh}/\tau_{other}$ are presented respectively in Figures 6.11 and 6.12. In Figure 6.13 we have represented the ratio $\tau_{other}/\tau_{\alpha}$ to see how τ_{other} behaves with respect to the structural relaxation time.

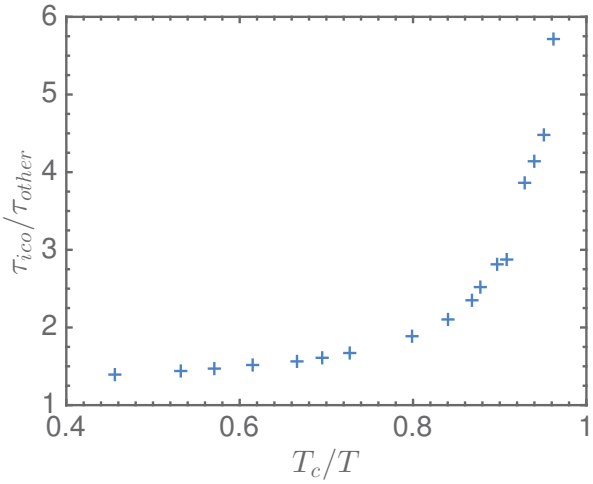

FIGURE 6.11: Evolution of the ratio τ_{ico}/τ_{other} as a function of the scaled temperature T_c/T. The ratio τ_{ico}/τ_{other} corresponds to the relaxation time of particles inside icosahedra with respect to particles that do not belong to icosahedra.

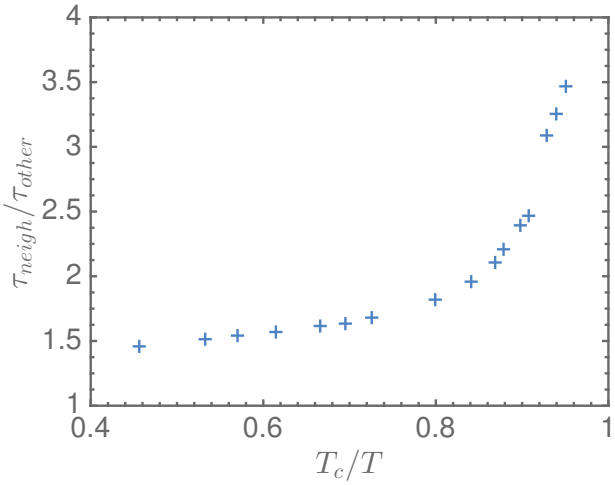

FIGURE 6.12: Evolution of the ratio $\tau_{neigh}/\tau_{other}$ as a function of the scaled temperature T_c/T. The ratio $\tau_{neigh}/\tau_{other}$ corresponds to the relaxation time of particles that composed icosahedra without being at the center with respect to particles that do not belong to icosahedra.

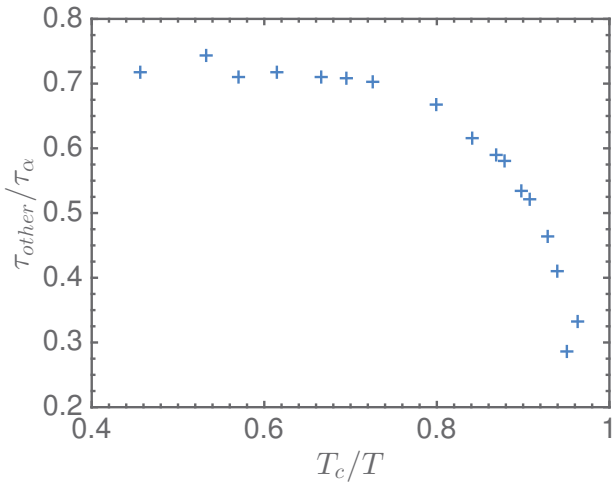

FIGURE 6.13: Evolution of the ratio τ_{other}/τ_α as a function of the scaled temperature T_c/T.

In both Figures 6.11 and 6.12 we observe that for $T_c/T \leq 0.72$ ($T \geq 1.10$), the ratios τ_{ico}/τ_{other} and $\tau_{neigh}/\tau_{other}$ are constant and ≈ 1.5, meaning that dynamics is already sensitive to LFS at high temperature. When $T_c/T > 0.72$, both ratios are increasing and the ratio τ_{ico}/τ_{other} becomes more important than $\tau_{neigh}/\tau_{other}$. Therefore we can conclude that 1) the relaxation of particles involved in LFS is indeed slower than other particles, 2) particles at the center of icosahedra relax even more slowly than their neighbors. In Figure 6.13 we observe that particles which do not belong to LFS formed by icosahedra relax faster with respect to the structural relaxation time. This implies that the structural relaxation τ_α is partly dominated by the relaxation of underlying LFS.

In Chapter 4, we explained that the breakdown of the Stokes-Einstein relation is related to the presence of dynamical heterogeneities. We can now explain the violation of SE relation by the presence of LFS which, as in Figure 4.25, tends to separate the liquid in regions where the relaxation of particles is more or less slowly.

The influence of LFS on the dynamics is more and more pronounced when the temperature is decreased. At sufficiently low temperatures, we have seen that the system exhibits a strong tendency to form large clusters of icosahedra. In what follows we will see that, for the lowest temperatures, the system tends to form a quasicrystal which seems to be associated with the formation of Frank-Kasper phases.

6.3 "Crystallization"

6.3.1 Decrease of the potential energy

When we investigated the low temperature $T \in [0.83, 0.84]$, we faced difficulties to obtain equilibrated trajectories of the supercooled liquid. For $T = 0.83$ and $T = 0.84$ we generated 10 trajectories of duration $t = 6 \cdot 10^5$. To appreciate the length of the trajectory, we recall that the relaxation time at these temperature is $\tau_\alpha \approx 2000$.
Among these trajectories only a few ones were representative of the supercooled state and most of them tend to observe a decrease of the potential energy which cannot be assimilated to simple fluctuations of E_P. In Figure 6.14 is represented the typical behavior of potential energy per particles E_P/N as a function of the time t when such phenomenon occurs. We selected two specific trajectories where both the decrease of E_P/N and its stabilization are visible.

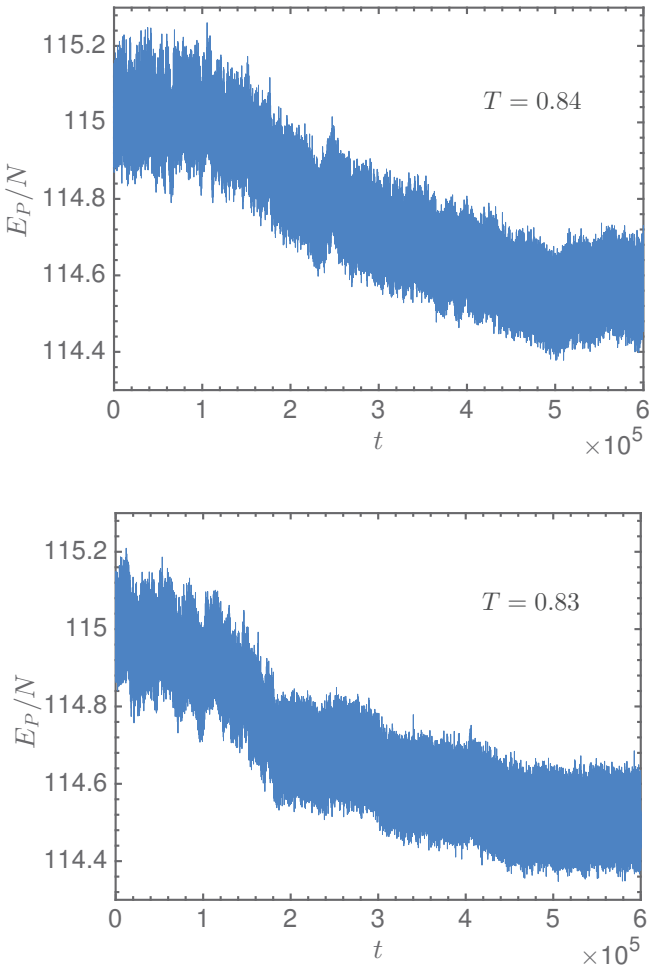

FIGURE 6.14: Representation of the decrease of the potential energy per particles during time observed for $T = 0.84$ (upper graph) and $T = 0.83$ (lower graph).

For both temperatures, we clearly see that the system passes from an high energy level to a lower one. The transition seems to be rather smooth, there is no brutal change in the value of E_P and it takes place on a period of time which is relatively long compared to the total length of the trajectory. After a time $t \geq 5 \cdot 10^6$ the system seems to stabilize around an average value of the potential energy. Same kind of phenomena have been observed by Pedersen *et al.* when they investigated the Wahnström model at low temperatures [149]. They have shown that for the Wahnström model, the decrease of the potential energy is associated with the formation of a quasicrystal, and Frank-Kasper phases (defined below) were also found.

Owing to the similarities that exist between the bidisperse Voronoi liquid and the Wahnström model, one can think that quasicrystals are also forming in the bidisperse Voronoi liquid and we therefore investigate the nature of this quasicrystal and the possible presence of such Frank-Kasper phases. We also highlight that for the rest of this section, for $T = 0.84$ and $T = 0.83$, we consider that equilibrated crystalline phase corresponds to portion of the total trajectory where the energy is stabilized, which occurs when $t \geq 5 \cdot 10^6$.

6.3.2 The structure factor : another proof of crystallization

The structure factor is a useful tool when looking for the characteristics of a crystal, as the position of peaks may inform on the underlying structure. We compute the partial structure factors $S_{ab}(k)$ for crystalline configurations at $T = 0.84$ and $T = 0.83$. The results are represented in Figure 6.15.

For each partial structure factor we observe that they are more structured that their supercooled counterparts shown in Chapter 3 in Figure 3.12. We note the presence of a succession of narrow peaks which are characteristic of a crystalline structure.

Surprisingly, the partial structure factors at $T = 0.84$ and $T = 0.83$ differ and peaks are narrower for $T = 0.84$. The splitting of the first peak of $S_{AA}(k)$ is well-marked at $T = 0.84$ whereas it is less visible at $T = 0.83$. On the contrary, the second peak of S_{AA} is more pronounced at $T = 0.83$ than $T = 0.84$. Moreover for $T = 0.84$, $S_{BB}(k)$ shows an important peak for $k \sim 3.75$ which is less pronounced for $T = 0.83$. The same kind of observations apply for $S_{AB}(k)$. These differences in the partial structure factors suggest the possibility that the crystalline structure may change upon cooling.

From the partial structure factor, it seems relatively complicated to extract the crystalline structure as we are not facing usual crystalline such as b.c.c or f.c.c. Another

possibility to determine the structure is to compute Voronoi polyhedra, and find if a preferred structure seems to emerge from the crystalline configurations.

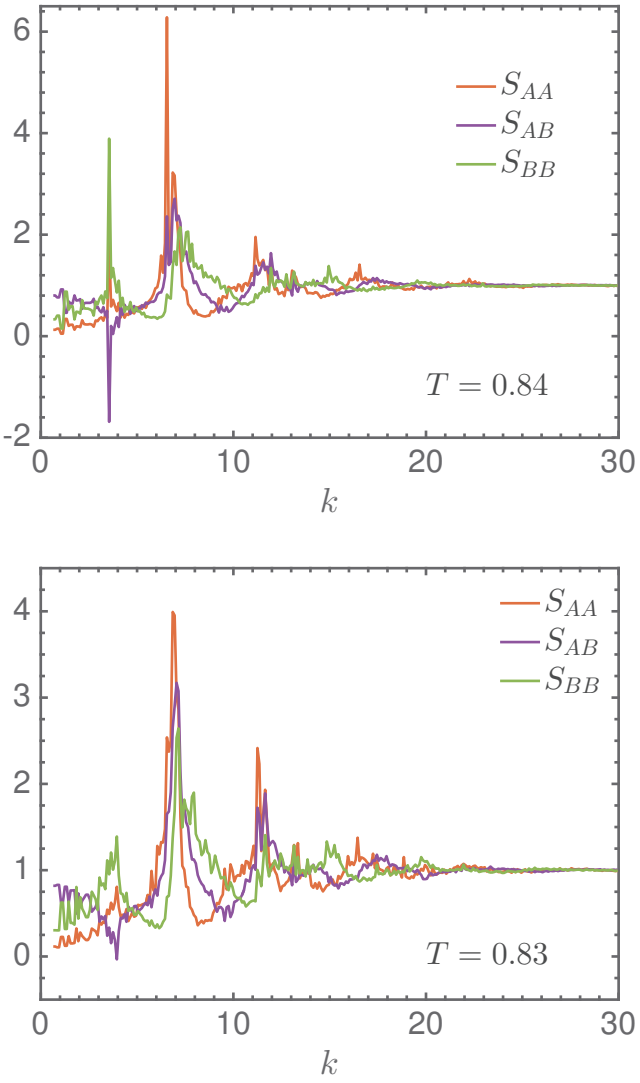

FIGURE 6.15: Partial structure factors obtained when the bidisperse Voronoi liquid is in the "crystalline" phase at $T = 0.84$ (upper graph) and $T = 0.83$ (lower graph).

6.3.3 A Frank-Kasper phase ?

Regarding the Wahnström binary mixture, Pedersen *et al.* [150] have notice that the LFS around small particles are the same in the liquid and the crystalline phase. However they observe a change in the LFS of large particles. Therefore for the bidisperse Voronoi liquid we investigate, in the crystalline phase, the LFS for small and large particles at $T = 0.84$ and $T = 0.83$. The results are shown in Table 6.4.

- The LFS of the small particles remain unchanged, the icosahedron and the distorted icosahedron are still the two preferred structures. However their fraction has spectacularly increased. More than the half of small particles are now involved in icosahedra and one can easily imagine that the clusters they form are much larger. In Figure 6.16 we have represented such a cluster composed of 260 particles at the center of icosahedra and we notice that the cluster has percolated.
- The neighborhood of large particles is different in the crystalline phase with respect to the liquid phase. We observe clearly the presence of preferred structures with fraction $> 10\%$. We therefore have qualitatively the same kind of results than the ones obtained by Pedersen *et al.* for the Wahnström binary mixture.

$T = 0.84$				$T = 0.83$			
Particles A		Particles B		Particles A		Particles B	
Signature	%	Signature	%	Signature	%	Signature	%
$(0, 0, 12, 4)$	17.8	$(0, 0, 12)$	54.8	$(0, 0, 12, 4)$	17.6	$(0, 0, 12)$	59.7
$(0, 1, 10, 4)$	10.6	$(0, 2, 8, 2)$	10.7	$(0, 0, 12, 3)$	15.0	$(0, 2, 8, 2)$	11.3

TABLE 6.4: Table representing the two most frequent Voronoi polyhedra around large A particles and small B particles for $T = 0.84$ and $T = 0.83$.

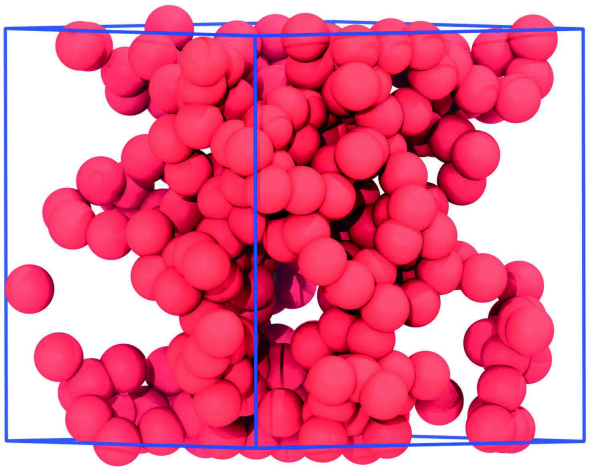

FIGURE 6.16: Snapshot of typical clusters that can be found when the system is in the "crystalline" phase at $T = 0.83$. The cluster is composed of $n_i = 260$ particles.

Pedersen *et al.* have identified this change in the neighborhood of particles to the presence of Frank-Kasper structures [149, 151]. Frank-Kasper structures, defined in 1958 by Frank and Kasper [23], are tetrahedrally close-packed periodic structures [7]. In these structures, the atoms occupy sites which are characterized by the value Z of the coordination number (or number of nearest neighbors).

Frank and Kasper showed that $Z = 12$, 14, 15 or 16 [23] and furthermore they investigated the Voronoi polyhedron associated to particles characterized by Z, and they demonstrated that faces of the polyhedra must be pentagons or hexagons. In other words faces have 5 or 6 vertices [23]. As a consequence, the particles with $Z = 12$ are icosahedra which have only faces with 5 vertices. For the other particles with higher values of Z, the number of faces with 6 vertices is given by $Z - 12$. The different types of polyhedra are represented in Figure 6.17.

Frank and Kasper considered in a second step, the global structures formed by the connection between the different polyhedra. They named *minor* the sites where $Z = 12$ and *major* the sites where $Z \geq 14$. An atom in a minor site has no neighbor with which it has 6 neighbors in common. On the contrary an atom A in a major site has $Z - 12$ B neighbors with which it shares 6 common neighbors. Frank and Kasper defined as *major ligand* the line between A and B. There are 3 possible topologies for connected the major ligands as it is represented in Figure 6.17 (black lines). Therefore it is possible to consider an extended structure composed of all the connected networks of major ligands that is called the *major skeleton* of the structure.

One important point is that the network of major ligands is infinite as there is no case where $Z = 13$ (or equivalently there is no polyhedron with only one face with 6 vertices). Frank and Kasper rejected the possibility that a network of major ligands close on itself and they therefore concluded that layering of the major skeleton must occurs [23].

The previous description of the Frank-Kasper phase informs us that if such structures are present in the bidisperse Voronoi liquid, then one must observe a huge number of icosahedra and a smaller fraction of structures such as $Z = 14$, 15 or 16 [151]. This implies the presence of the following Voronoi polyhedra (0,0,12,2), (0,0,12,3) or (0,0,12,4) [152].

When comparing the signatures of this polyhedra with the ones found in Table 6.4, we immediately see that the polyhedron (0,0,12,4) is the favored structure around A particles for $T = 0.84$, and (0,0,12,3) or (0,0,12,4) are both the LFS of A at $T = 0.83$. Therefore, there are strong evidences in favor of the existence of Frank-Kasper structures in the crystalline phase of the bidisperse Voronoi liquid. It is also interesting to notice that as polyhedra (0,0,12,3) are only present at $T = 0.83$, Frank-Kasper structures are likely to be different at $T = 0.83$ and $T = 0.84$. This is in agreement with the observations done for the partial structure factors.

At this stage of the work, the crystalline structures have not been identified and further investigations are required to identify the underlying Frank-Kasper phases.

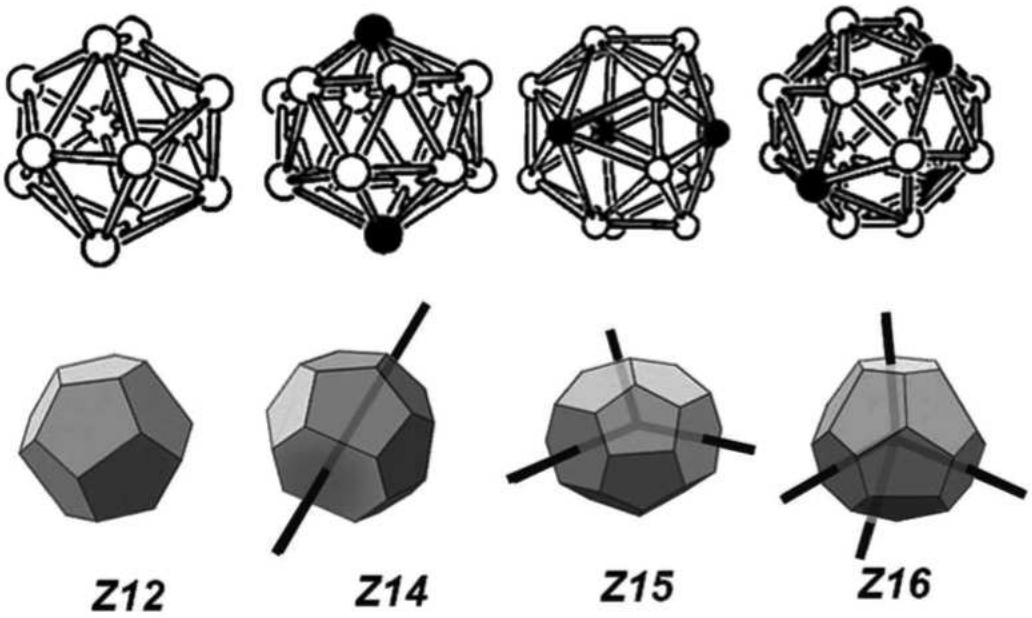

FIGURE 6.17: Upper graph: Representation of the four coordination polyhedra of Frank-Kasper. The white spheres are the minor sites whereas the black spheres correspond to the major sites. Lower graph: The associated Voronoi polyhedra. The black lines that start from the center of the Voronoi polyhedra and go through hexagonal faces show how major ligands can be connected and form for these local structures the major skeleton. (Reproduced with permissions from [7], copyright Springer 2017.)

Conclusion & Perspectives

During this thesis, we introduced a brand-new class of liquids, the Voronoi liquids, where the interaction among particles are directly related to the geometrical properties of Voronoi tessellations. Therefore the interactions are intrinsically manybody. In its simplest form, the monodisperse Voronoi liquid is unable to avoid crystallization. Therefore, as our aim was to probe the neighborhood of glass transition, we proposed a bidisperse extension where the geometrical properties are now those of the Voronoi-Laguerre tessellations. We investigated theoretically and through molecular dynamics simulations the properties of the bidisperse Voronoi liquid for which we mainly focused on an equimolar binary mixture. During cooling experiments, we observed that the bidisperse Voronoi liquid was able to avoid crystallization and therefore we used it to probe the neighborhood of glass transition. To see to what extent the properties of the bidisperse Voronoi liquid are unusual, we compared our results with the ones found for three usual Lennard-Jones glass formers: the Kob-Andersen model, the Wahnström mixture and an additive mixture of Lennard-Jones particles where $\sigma_{BB} = 0.80$.

We firstly focused on the behavior of thermodynamic observables upon cooling. Contrary to thermodynamic potentials which were not really sensitive to the cooling, the excess heat capacity at constant volume C_v^e, shows a marked increase when the temperature is decreased below the temperature T^*, which marks the crossover from the Arrhenian to the super-Arrhenian regime. Considering the underlying PEL, we attributed the behavior of C_v^e to the huge decrease of the average value of the IS energy for $T < T^*$. Then the computation of the excess pressure revealed that this quantity is strongly negative. Moreover it was possible to determine a pair decomposition of the manybody force field for which we observed that two neighboring particles attract each other. This means that the bidisperse Voronoi liquid is always under tension but the nature of the forces prevents cavitation to occur, leading thus to a stable fluid always under tension.

We investigated then the microscopic structural observables such as the pair correlation function and the structure factor. We found for both observables that the bidisperse Voronoi liquid is compliant with usual phenomenology of glass transition, i.e structural

observables are weakly sensitive to cooling. Moreover, we were able to derive analytically the position of the first peak of partial pair correlation function and structure factor. An analysis of the angle distribution revealed a tendency to form icosahedra that was confirmed during the study of the locally favored structures. Indeed, we found that upon cooling, an increasing fraction of small particles is located at the center of icosahedra which spatially extend into large clusters that seem to percolate at very low temperature. The characterization of this percolation has not been done yet and represents a future work that would give a better understanding of the behavior of these clusters. Moreover we notice that the presence of clusters of icosahedra impacts directly the dynamics as the relaxation time inside LFS is slower than the relaxation time of particles which are not involved in LFS. This clearly shows the heterogeneous nature of the dynamics at low temperatures which was also revealed by the breakdown of the Stokes-Einstein relation.

A particular interest was given to analyze of dynamical observables. We noticed that upon cooling, both relaxation and coefficient diffusion strongly deviate from the Arrhenian regime. We quantified this deviation by measuring the fragility for relaxation time and diffusion coefficient and then by comparing the fragility of the bidisperse Voronoi liquid with the ones of the LJ glass formers. We found that the fragility of the Voronoi liquid is changing in function of the scale observed. As a matter of fact, when investigating microscopic scales, thus when the structural relaxation time is considered, the system has a marked fragility. However, when probing the hydrodynamic limit, thus when looking at the diffusion coefficient, the fragility appears less marked. This difference was not observed for LJ glass formers. This led us to propose an alternative to Angell-plot and to search for intrinsic microscopic time and energy scales that would be common to different systems.
We proposed to define the microscopic intrinsic time-scale as the inverse of the Einstein's frequency Ω_0^{-1}, as this latter is the fastest physical time in liquids. The definition of a proper energy scale E_μ was much more tricky and we proposed three possible candidates: the microscopic work, the fluctuations of the potential energy and the infinite-frequency shear modulus. The representations in terms of $\tau_\alpha\Omega_0$ as a function of $E_\mu/(k_BT)$ brought, on the first hand, physical informations on the increase of the relaxation time. On the other hand they emphasized the difference between classes of system as clear separations between the bidisperse Voronoi liquid and the LJ glass formers were observed. A remaining major challenge would be to find the right couple $(\Omega_0^{-1}\ ,\ E_\mu)$ that would enable to reproduce the T-dependence of the energy barriers in such a way that the relaxation time could be written $\tau_\alpha = \Omega_0^{-1}\exp(E_\mu/(k_BT))$. Then the Holy Grail would be to find a representation that would take into account the diversity of microscopic interactions and offer a universal interpretation of the behavior of relaxation time.
Furthermore our investigations of the collective relaxation time on different length-scales

revealed that, in the mesoscopic range for $k \approx 4.90$, the relaxation does not couple to the structural relaxation time τ_α. To the best of our knowledge, this behavior is specific to the bidisperse Voronoi liquid and we did the hypothesis that this length scale is associated to the presence of a transition state, that we still have to identify.
We also investigated the dynamics by testing the predictions of the ideal MCT. We found that for wavevectors $k \geq k^*$, the ideal MCT managed to describe the relaxation time relatively well, whereas in the mesoscopic range, we noticed that the value of the von Schweidler exponent does not remain constant, which suggests a breakdown of the theory. Understanding the origin of this violation would be of great interest to capture the specific phenomenology of the mesoscopic range.

To get more insight into the physical origin of the glass transition, we investigated the PEL of the bidisperse Voronoi liquid and of the 3 LJ glass formers. The study of the underlying inherent structures revealed that their distribution is well-described by the Gaussian approximation. However the width σ^2 of the distribution is 10 times greater for the Voronoi liquid than for the LJ systems. We correlated this observation to the huge increase C_v^e at the neighborhood of the glass transition.
Moreover a particular interest was given to the determination of the configurational entropy S_c. In the harmonic approximation, we can distinguish between the usual configurational entropy defined as $S_c = S_{liq} - S_{sol}$, and the effective configurational entropy $\hat{S}_c$ which is linked to S_c via the spectrum of the Hessian of the potential energy. Harmonic approximation implies that $\hat{S}_c$ should be given by $\ln(P(e_{IS}|T)) + e_{IS}/T$ for $T < T^*$. By comparing the results of $\ln(P(e_{IS}|T)) + e_{IS}/T$ with an analytical expression of $\hat{S}_c$ we find an agreement only at very low temperature. However an estimation of the anharmonic contribution to the potential energy showed that there are non-negligible even for $T \lesssim T^*$. We therefore took them into account into the analytical expression $\hat{S}_c$. We observed that in the limit of weak anharmonicity, the results were even worst than without taking them into account. However when we considered stronger anharmonicities, the agreement between $\hat{S}_c$ and $\ln(P(e_{IS}|T)) + e_{IS}/T$ appeared better. We therefore concluded that anharmonicity played a significant role in the bidisperse Voronoi liquid even for low temperature. Their precise origin have still to be determined as it will allow a better understanding of the thermodynamics of inherent structures.
From the knowledge of the configurational entropy S_c, we tested the theory of Adam-Gibbs for the relaxation time and at very low temperature, we found a good agreement between the theory and our numerical results.
Furthermore we pursued our analysis of the PEL by focussing on saddle points for which we underlined the difficulty to determine them numerically, especially when large systems are considered. We compared two different numerical methods: the minimization of $\boldsymbol{\nabla} E_p^2$ and the Eigenvector-Following (EF) method. Whereas the minimization of $\boldsymbol{\nabla} E_p^2$

allows only for the determination of quasisaddles, the EF method enables to find true saddle points. The investigation of the index of negative directions k as a function of the energy density of the saddle u revealed the presence of an underlying geometric feature of the PEL. Exploration of k vs. u with the different methods shows that the crossover from Arrhenian to super-Arrhenian regime is captured in the quasisaddles behavior. Considering the limit where $k \to 0$, we were able to determine the threshold energy below which there is no more negative directions and thus to give an estimation of the mode coupling temperature T_c. We found that by increasing the system size, the value of T_c determined by this method tends to the value found with ideal MCT analysis. Unfortunately the EV method allowed only an exploration high k-high u regime (associated with the Arrhenian regime) and we didn't succeed to explore the low k- low u regime to validate the results found for quasisaddles. However understanding why quasisaddles, which are not proper stationary points, seem to convey correctly information about the dynamics in the real space, remains an open question.

Finally we observed that, at very low temperature, the equimolar bidisperse Voronoi liquid crystallizes. The precise crystalline structure has not been identified yet but we found strong evidences in favor of the formation of Frank-Kasper phases.

During this work, we didn't pay to much attention to the dynamical heterogeneities despite strong evidences of their presence in the bidisperse Voronoi liquid. In the past two decades, they deserved much attentions as it has been shown that the four-point susceptibility $\chi_4(t)$ informs on the spatial extension of these heterogeneities [20]. Moreover in the hydrodynamic limit, the dynamical correlation length $\xi_4(t)$ can be extracted from the four-point structure factor $S_4(\boldsymbol{q}, \boldsymbol{k}, t)$ which exhibits a power-law behavior [153]. It could be interesting to compute these quantities for the bidisperse Voronoi liquid to obtain precise informations about the dynamical heterogeneities. However this will be technically difficult. For the monodisperse Voronoi liquid, it has been shown that the hydrodynamics regime developed only for very small values of k [27] much more smaller than for the usual LJ systems. The same behavior is also likely to be present for the bidisperse model and therefore having access to $\xi_4(t)$ would require to work, at constant density, with systems with more than $N = 2 \cdot 10^6$ resulting on very long simulation time.

Due to the difficulties encountered to express the stress tensor, we didn't have time to look at the behavior of the shear-stress in the system. It would be interesting to see how the bidisperse Voronoi liquid behaves under shear as we assumed in [27], that it is relatively easy to shear the system. Monitoring the evolution of the shear relaxation upon cooling could bring further information about what happens close to glass transition. Moreover as proposed in [154] for the Wahnström model, it could be interesting to see

how the LFS evolves under shear. One could also imagine working in the amorphous phase too.

Bibliography

[1] H. Imai, M. Iri, and K. Murota. Voronoi diagram in the laguerre geometry and its applications. *SIAM J. COMPUT*, 14, 1985.

[2] C.A Angell. Perspectives on the glass transition. *J. Phys. Chem. Solids*, 49(8), 1988.

[3] F. Weysser, A. M. Puertas, M. Fuchs, and Th. Voigtmann. Structural relaxation of polydisperse hard spheres: Comparison of the mode-coupling theory to a langevin dynamics simulation. *Physical Review E*, 82(011504), 2010.

[4] D.M. Heyes. *Chemical Modelling Applications and Theory*, volume 2, chapter Simulation of the Liquid State. The Royal Society of Chemistry, 2002.

[5] L. Angelani, G. Ruocco, M. Samponi, and F. Sciortino. General features of the energy landscape in lennard-jones-like model liquids. *J. Chem. Phys.*, 119(4), 2003.

[6] A. Hirata, L. J. Kang, T. Fujita, B. Klumov, K. Matsue, M. Kotani, A. R. Yavari, and M. W. Chen. Geometric frustration of icosahedron in metallic glasses. *Science*, 431, 2013.

[7] J-F Sadoc and R. Mosseri. Quasiperiodic frank–kasper phases derived from the square– triangle dodecagonal tiling. *Struct. Chem.*, 28:63–73, 2017.

[8] Andrea Cavagna. Supercooled liquids for pedestrians. *Physical Reports*, (476):51–124, 2009.

[9] M.D. Ediger, C.A Angell, and S.R Nagel. Supercooled liquids and glasses. *J. Phys. Chem.*, 100:13200–13212, 1996.

[10] M.D. Ediger. Spatially heterogeneous dynamics in supercooled liquids. *Annu. Rev. Phys. Chem.*, 51:99–128, 2000.

[11] L. Leuzzi and T. M. Nieuwenhuizen. *Thermodynamics of the Glassy State*. Series in Condensed Matter Physics. Taylor and Francis, 2008.

[12] K.L. Ngai. *Relaxation and Diffusion in Complex Systems*. Partially Ordered Systems. Springer, 2011.

[13] C.A Angell. Relaxation in liquids, polymers and plastic crystals - strong/fragile parrterns and problems. *Journal of Non-Crystalline Solids*, 131-133:13–31, 1991.

[14] G. Adam and J. H. Gibbs. On the temperature dependence of cooperative relaxation properties in glass forming liquids. *J. Chem. Phys.*, 43(139), 1965.

[15] C. Dasgupta, A. V. Indrani, S. Ramaswamy, and M. K. Phani. Is there a growing correlation length near the glass transition? *Europhysics Letters*, 15(3):307–312, 1991.

[16] P. Z. Hanakata, J. F. Douglas, and F. W. Starr. Interfacial mobility scale determines the scale of collective motion and relaxation rate in polymer films. *Nature Communications*, 5, 2014.

[17] B. A. Pazmino Betancourt, J. F. Douglas, and F. W. Starr. String model for the dynamics of glass-forming liquids. *J. Chem. Phys.*, 140, 2014.

[18] S. Karmakar, C. Dasgupta, and S. Sastry. Growing length and time scales in glass-forming liquids. *PNAS*, 106(10), 2009.

[19] L. Berthier, G. Biroli, J-P Bouchaud, L. Cipelletti, D. El Masri, D. L'Hôte, F. Ladieu, and M. Pierno. Direct experimental evidence of a growing length scale accompanying the glass transition. *Science*, 310, 2005.

[20] L. Berthier, G. Biroli, J-P Bouchaud, L. Cipelletti, and W. Van Saarloos. *Dynamical Heterogeneities in Glasses, Collloids and Granular Media*. Oxford Science Publications, 2011.

[21] D. Coslovich and G. Pastore. Understanding fragility in supercooled lennard-jones mixtures. i. locally preferred structures. *J. Chem. Phys.*, 127(124504), 2007.

[22] A. Malins, J. Eggers, C. P. Royall, S.R Williams, and H. Tanaka. Identification of long-lived clusters and their link to slow dynamics in a model glass former. *J. Chem. Phys.*, 138(12A535), 2013.

[23] F. C. Frank and J. S. Kasper. Complex alloy structures regarded as sphere packings. i. definitions and basic principles. *Acta Cryst.*, 11(184), 1958.

[24] C. P. Royall and S.R Williams. The role of local structure in dynamical arrest. *Physics Reports*, 560:1–75, 2015.

[25] M. Dzugutov, S. I Simdyankin, and F. H. M. Zetterling. Decoupling of diffusion from structural relaxation and spatial heterogeneity in a supercooled simple liquid. *Physical Review Letters*, 89(19), 2002.

[26] C.Ruscher, J.Baschnagel, and J.Farago. The voronoi liquid. *Eur. Phys. J. E*, 112(66003), 2015.

[27] C. Ruscher, A. N. Semenov, J. Baschnagel, and J. Farago. Anomalous sound attenuation in voronoi liquid. *J. Chem. Phys.*, 146, 2017.

[28] W. Kob and H. C. Andersen. Testing made-coupling theory for a supercooled binary lennard-jones mixture: The van hove correlation function. *Physical Review E*, 51(5), 1995.

[29] W. Kob and H. C. Andersen. Testing mode-coupling theory for a supercooled binary lennard-jones mixture. ii. intermediate scattering function and dynamic susceptibility. *Physical Review E*, 52(4), 1995.

[30] Göran Wahnström. Molecular-dynamics study of a supercooled two-component lennard- jones system. *Physical Review A*, 44(6), 1991.

[31] Jean Farago, Alexander N. Semenov, Stefan Frey, and Joerg Baschnagel. New conserved structural fields for supercooled liquids new conserved structural fields for supercooled liquids. *Eur. Phys. J. E*, 37, 2014.

[32] F. Aurenhammer and H. Edelsbrunner. An optimal algorithm for constructing the weighted voronoi diagram in the plane. *Pattern Recognition*, 17(2):251 – 257, 1984.

[33] H. G. E. Hentschel, Valery Ilyin, Nataliya Makedonska, Itamar Procaccia, and Nurith Schupper. Statistical mechanics of the glass transition as revealed by a voronoi tesselation. *Physical Review E*, 75(050404(R)), 2007.

[34] Chaoming Song, Ping Wang, Yuliang Jin, and Hernán A. Makse. Jamming i: A volume function for jammed matter. *Physica A: Statistical Mechanics and its Applications*, 389(21):4497 – 4509, 2010.

[35] Chris H. Rycroft. Voro++: A three-dimensional voronoi cell library in c++. *Chaos*, 19(041111), 2008.

[36] Thomas B. Schrøder, Ulf R. Pedersen, Nicholas P. Bailey, Søren Toxvaerd, and Jeppe C. Dyre. Hidden scale invariance in molecular van der waals liquids: A simulation study. *Physical Review E*, 80(041502), 2009.

[37] Nicholas P. Bailey, Lasse Bohling, Arno A. Veldhorst, and Thomas B. Schroder. Statistical mechanics of roskilde liquids : Configurational adiabats specific heat contours, and density dependence of the scaling exponent. *The Journal of Chemical Physics*, 139, 2013.

[38] Emmanuel Meeron and Arnold J. F. Siegert. Statistical mechanics of hard particle systems. *The Journal of Chemical Physics*, 48(3139), 1968.

[39] Balucani Umberto and Marco Zoppi. *Dynamics of the Liquid State*. Oxford: Clarendon Press, 1994.

[40] Jean-Pierre Hansen and Ian R. McDonald. *Theory of Simple Liquids, 4th Edition*. Academic Press, 2013.

[41] Chase E. Zachary, Frank H. Stillinger, and Salvatore Torquato. Gaussian core model phase diagram and pair correlations in high euclidean dimensions. *The Journal of Chemical Physics*, 128(224505), 2008.

[42] Gabriele C. Sosso, Ji Chen, Stephen J. Cox, Martin Fitzner, Philipp Pedevilla, Andrea Zen, and Angelos Michaelides. Crystal nucleation in liquids: Open questions and future challenges in molecular dynamics simulations. *Chemical Reviews*, 116:7078–71160, 2016.

[43] Swetlana Jungblut and Christoph Dellago. Crystallization on prestructured seeds. *Physical Review E*, 012305, 2013.

[44] G. Foffi, W. Götze, F. Sciortino, P. Tartaglia, and Th. Voigtmann. Mixing effects for the structure relaxation in binary hard-sphere liquids. *Physical Review Letters*, 91(085701), 2003.

[45] L. Verlet. Computer "experiments" on classical fluids. i. thermodynamical properties of lennard-jones molecules. *Physical Review*, 159(98), 1967.

[46] S. J. Plimpton. Fast parallel algorithms for short-range molecular dynamics. *J Comp Phys*, 117, 1995.

[47] S. P. Das. *Statistical Physics of Liquids at Freezing and Beyond*. Cambdrige University Press, 2011.

[48] H.J. Fecht. Thermodynamic properties of amorphous solids - glass formation and glass transition (overview). *Materials Transactions, JIM*, 36(7):777–793, 1995.

[49] Y. Zhang, A. Navrotsky, J. A. Tangeman, and J. K. R. Weber. Thermochemistry of glasses along the 2ndalo3–3sio2 join. *J.Phys.:Condens. Matter*, 15, 2003.

[50] L. B. Skinner, A. C. Barnes, and W. Crichton. Novel behaviour and structure of new glasses of the type ba–al–o and ba–al–ti–o produced by aerodynamic levitation and laser heating. *J.Phys.:Condens. Matter*, 18, 2006.

[51] K. S. Ranasinghe, C. S. Ray, D. E. Day, J. R. Rogers, R. W. Hyers, and T. Rathz. Containerless processing of a lithium disilicate glass. *J Mater Sci*, 42:4291–4297, 2007.

[52] C. A. Angell and W. Sichina. Thermodynamics of the glass transition: empirical aspects. *Annals of the New York Academy of Sciences*, 279, 1976.

[53] C. A. Angell. Thermodynamic aspects of the glass transition in liquids and plastic crystals. *Pure and Appl. Chem.*, 63(10):1387–1392, 1991.

[54] J. R. Fox and H. C. Andersen. Molecular dynamics simulations of a supercooled monatomic liquid and glass. *J. Phys. Chem.*, 88:4019–4027, 1984.

[55] K. Vollmayr, W. Kob, and Kurt Binder. How do the properties of a glass depend on the cooling rate? a computer simulation study of a lennardjones system. *J. Chem. Phys.*, 105(4714), 1996.

[56] J. Buchholz, W. Paul, F. Varnik, and K. Binder. Cooling rate dependence of the glass transition temperature of polymer melts: Molecular dynamics study. *J. Chem. Phys.*, 117(15), 2002.

[57] C. A. Kreck and R. L. Mancera. Characterization of the glass transition of water predicted by molecular dynamics simulations using nonpolarizable intermolecular potentials. *J. Phys. Chem. B*, 118:1867–1880, 2014.

[58] C. A. Angell, R.C. Stell, and W. Sichina. Viscosity-temperature function for sorbitol from combined viscosity and differential scanning calorimetry studies. *J. Phys. Chem.*, 86(9):1540–1542, 1982.

[59] J. M. Hutchinson. Determination of the glass transition temperature - methods correlation and structural heterogeneity. *J Therm Anal Calorim*, 98:579–589, 2009.

[60] F. Sciortino. Potential energy landscape description of supercooled liquids and glasses. *J. Stat. Mech.*, 2005.

[61] F. H. Stillinger. *Energy Landscapes, Inherent Structures, and Condesend Matter Phenomena*. Princeton University Press, 2015.

[62] P. G. Debenedetti and F. H. Stillinger. Supercooled liquids and the glass transition. *Nature*, 410(8), 2001.

[63] E. Herbert, S. Balibar, and F. Caupin. Cavitation pressure in water. *Physical Review E*, 74(041603), 2006.

[64] M. J. Louwerse and E. J. Baerends. Calculation of pressure in case of periodic boundary conditions. *Chemical Physics Letters*, 421:138–141, 2006.

[65] N. C. Admal and E. B. Tadmor. A unified interpretation of stress in molecular systems. *J. Elast.*, 100:63–143, 2010.

[66] J. S. Higgings and H. C. Benoît. *Polymers and Neutron Scattering*. Oxford Science Publications, 1994.

[67] A. Menelle, R. Bellisent, and A. M. Flank. A neutron scattering study of supercooled liquid tellurium. *Europhysics Letters*, 4(6):705–708, 1987.

[68] R. L. Leheny, N. Menon, and S. R. Nagel. Structural studies of an organic liquid through the glass transition. *J. Chem. Phys.*, 105(7783), 1996.

[69] Kurt Binder and Walter Kob. *Glassy Materials And Disordered Solids*. World Scientific, 2011.

[70] J. Ding, E. Ma, M. Asta, and R. O. Ritchie. Second-nearest-neighbor correlations from connection of atomic packing motifs in metallic glasses and liquids. *Scientific Reports*, 5, 2015.

[71] U. Balucani and R. Vallauri. Evolution of bond-angle distribtuion from liquid to glassy states. *Chemical Physics Letters*, 166(1), 1990.

[72] N. W. Ashcroft and D. C. Langreth. Structure of binary liquid mixtures. i. *Physical Review*, 1967.

[73] L. Berthier and G. Biroli. Theoretical perspective on the glass transition and amorphous materials. *Reviews of Modern Physics*, 83, 2011.

[74] J. Baschnagel, I. Kriuchevskyi, J. Helfferich, C. Ruscher, H. Meyer, O. Benzerara, J. Farago, and J. P. Wittmer. *Polymer Glasses*, chapter Glass transition and relaxation behavior of supercooled melts: An introduction to modeling approaches by molecular dynamics simulations and to comparison with mode-coupling theory. CRC Press, 2017.

[75] Stephan Frey. *Propriétés viscoélastiques des fondus de polymères vitrifiables*. PhD thesis, Université de Strasbourg, 2012.

[76] W. Kob and H. C. Andersen. Scaling behavior in the beta-relaxation regime of a supercooled lennard-jones mixture. *Physical Review Letters*, 73(10), 1994.

[77] Von W. Oldekop. *Glasstechnische BErichte*, 30(8), 1957.

[78] W. T. Laughlin and D. R. Uhlmann. Viscous flow in simple organic liquids. *J. Phys. Chem.*, 76(2317), 1972.

[79] R Böhmer and C.A Angell. Correlations of the nonexponentiality and state dependence of mechanical with bond connectivity in ge-as-se supercooled liquids. *Physical Review B*, 45(17), 1992.

[80] D. Kivelson, G. Tarjus, X. Zhao, and S.A Kivelson. Fitting viscosity: Distinguishing the temperature dependences predicted by various models of supercooled liquids. *Physical Review E*, 53(1), 1996.

[81] P. Crowther, F. Turci, and C. P. Royall. The nature of geometric frustration in the kob-andersen mixture. *J. Chem. Phys.*, 143(044503), 2015.

[82] P. Bordat, F. Affouard, M. Descamps, and K.L Ngai. Does the interaction potential determine both the fragility of a liquid and the vibrational properties of its glassy state? *Physical Review Letters*, 93(10), 2004.

[83] D. Huang, D. M. Colucci, and G. B. McKenna. Dynamic fragility in polymers: A comparison in isobaric and isochoric conditions. *J. Chem. Phys.*, 116(3925), 2002.

[84] J. C. Dyre, T. Christensen, and N. B. Olsen. Elastic models for the non-arrhenius viscosity of glass-fromings liquids. 2005.

[85] R. Zwanzig and R. D. Mountain. Highfrequency elastic moduli of simple fluids. *The Journal of Chemical Physics*, 43(4464), 1965.

[86] J. C. Dyre, N. B. Olsen, and T. Christensen. Local elastic expansion model for viscous-flow activation energies of glass-forming molecular liquids. *Physical Review B*, 53(5), 1996.

[87] B.Xu and G. B. McKenna. Evaluation of the dyre shoving model using dynamic data near the glass temperature. *J. Chem. Phys.*, 134(124902), 2011.

[88] J. C. Dyre and W. H. Wang. The instantaneous shear modulus in the shoving model. *J. Chem. Phys.*, 136(224108), 2012.

[89] F. Puosi and D. Leporini. Correlation of the instantaneous and the intermediate-time elasticity with the structural relaxation in glassforming systems. *J. Chem. Phys.*, 136(041104), 2012.

[90] H. Sillescu. Heterogeneity at the glass transition: a review. *J. Non-Cryst. Solids*, 243(81), 1999.

[91] E. R. Weeks, J. C. Crocker, A. C. Levitt, A. Schofield, and D. A. Weitz. Three-dimensional direct imaging of structural relaxation near the colloidal glass transition. *Science*, 287(627), 2000.

[92] O. Dauchot, G. Marty, and G. Biroli. Dynamical heterogeneity close to the jamming transition in a sheared granular material. *Physical Review Letters*, 95(265701), 2005.

[93] A. Widmer-Cooper and P. Harrowell. On the study of collective dynamics in supercooled liquids through the statistics of the isoconfigurational ensemble. *J. Chem. Phys.*, 126(154503), 2007.

[94] R. Candelier, A. Widmer-Cooper, J. K. Kummerfeld, O. Dauchot, G. Biroli, P. Harrowell, and D. R. Reichman. Spatiotemporal hierarchy of relaxation events, dynamical heterogeneities, and structural reorganization in a supercooled liquid. *Physical Review Letters*, 105(135702), 2010.

[95] Hazime Mori. Transport, collective motion and brownian motion. *Progress of Theoretical Physics*, 33(3), 1965.

[96] Robert Zwanzig. Memory effects in irreversible thermodynamics. *Physical Review*, 124(4), 1961.

[97] D. R. Reichman and P. Charbonneau. Mode-coupling theory. *J. Stat. Mech.*, 2005.

[98] J.Baschnagel and F.Varnik. Computer simulations of supercooled polymer melts in the bulk and in confined geometry. *Journal of Physics*, 17, 2005.

[99] J-L. Barrat and A. Latz. Mode-coupling theory for the glass transition in a simple binary mixture. *J.Phys.:Condens. Matter*, 2:4289–4295, 1990.

[100] S. P. Das. Mode-coupling theory and the glass transition in supercooled liquids. *Reviews of Modern Physics*, 76, 2004.

[101] E. Leutheusser. Dynamical model of the liquid-glass transition. *Physical Review A*, 29(2765), 1984.

[102] U. Bengtzelius, W. Götze, and A. Sjolander. Dynamics of supercooled liquids and the glass transition. *Journal of Physics C: Solid State Physics*, 17(33), 1984.

[103] M Fuchs, W. Götze, S Hildebrand, and A Lam. A theory for the beta-relaxation process near the liquid-to-glass crossover. *J.Phys.:Condens. Matter*, 4:7709–7744, 1992.

[104] M. Goldstein. Viscous liquids and the glass transition: A potential energy barrier picture. *The Journal of Chemical Physics*, 51(9), 1969.

[105] F. H. Stillinger and T. A. Weber. Hidden structure in liquids. *Physical Review A*, 25(2), 1982.

[106] F. Sciortino, W. Kob, and P. Tartaglia. Thermodynamics of supercooled liquids in the inherent-structure formalism: a case study. *J.Phys.:Condens. Matter*, 12:6525–6534, 2000.

[107] E. Bitzek, P. Koskinen, F. Gähler, M. Moseler, and P. Gumbsch. Structural relaxation made simple. *Physical Review Letters*, 97(170201), 2006.

[108] B. Derrida. Random-energy model: An exactly solvable model of disordered systems. *Physical Review B*, 24(5), 1981.

[109] T. Keyes. Entropy, dynamics, and instantaneous normal modes in a random energy mode. *Physical Review E*, 62(6), 2000.

[110] Andreas Heuer and Stephan Büchner. Why is the density of inherent structures of a lennard-jones-type system gaussian? *J.Phys.:Condens. Matter*, 12:6535–6541, 2000.

[111] Z. Shi, P. G. Debenedetti, F. H. Stillinger, and P. Ginart. Structure, dynamics, and thermodynamics of a family of potentials with tunable softness. *The Journal of Chemical Physics*, 135(084513), 2011.

[112] W. Kauzmann. The nature of the glassy state and the behavior of liquids at low temperatures. *Chemical Reviews*, 43(2):219–256, 1948.

[113] Ivan Saika-Voivod and Francesco Sciortin. Distributions of inherent structure energies during aging. *Physical Review E*, 70(041202), 2004.

[114] J. H. Gibbs and E. A. DiMarzio. Nature of the glass transition and the glassy state. *J. Chem. Phys.*, 28(373), 1958.

[115] F. H. Stillinger. Supercooled liquids, glass transitions, and the kauzmann paradox. *J. Chem. Phys.*, 88(12), 1988.

[116] C. A. Angell. Entropy and fragility in supercooling liquids. *J. Res. Natl. Inst. Stand. Technol.*, 102(171), 1997.

[117] H. Tanaka. Relation between thermodynamics and kinetics of glass-forming liquids. *Physical Review Letters*, 90(5), 2003.

[118] J. C. Dyre, T. Hechsher, and K. Niss. A brief critique of the adam-gibbs entropy model. *Journal of Non-Crystalline Solids*, 355:624–627, 2009.

[119] S. Sengupta, S. Karmakar, C. Dasgupta, and Srikanth Sastry. Adam-gibbs relation for glass-forming liquids in two, three, and four dimensions. *Physical Review Letters*, 109(095705), 2012.

[120] S. Mossa, E. La Nave, H. E. Stanley, C. Donati, F. Sciortino, and P. Tartaglia. Dynamics and configurational entropy in the lewis-wahnström model for supercooled orthoterphenyl. *Physical Review E*, 65(041205), 2002.

[121] L. Berthier and D. Coslovich. Novel approach to numerical measurements of the configurational entropy in supercooled liquids. *PNAS*, 111(32), 2014.

[122] A.P.Sokolov. The glass transition: general scenario and crossover temperature. *Journal of Non-Crystalline Solids*, 235-237:190–195, 1998.

[123] A. Cavagna. Fragile vs. strong liquids: a saddles-rules scenario. *Europhysics Letters*, 53(4):490–496, 2001.

[124] K. Broderix, K.K Bhattacharya, A. Cavagna, A. Zippelius, and I. Giardina. Energy landscape of lennard-jones liquid: Statistics of stationary points. *Physical Review Letters*, 85(25), 2000.

[125] L. Angelani, R. Di Leornardo, G. Ruocco, A. Scalla, and F. Sciortino. Saddles in the energy landscape probed by supercooled liquids. *Physical Review Letters*, 85(25), 2000.

[126] T. A. Weber and F. H. Stillinger. Local order and structural transitions in amorphous metal-metalloid alloys. *Physical Review B*, 31(4), 1985.

[127] J. W. McIver and A. Komornicki. Structure of transition states in organic reactions. general theory and an application to the cyclobutene-butadiene isomerization using a semiempirical molecular orbital method. *Journal of the American Chemical Society*, 94(8), 1972.

[128] D. J. Wales and J. P. K. Doye. Stationary points and dynamics in high-dimensional systems. *J. Chem. Phys.*, 119(12409), 2003.

[129] J. P. K. Doye and D. J. Wales. Saddle points and dynamics of lennard-jones cluster, solids dans supercooled liquids. *J. Chem. Phys.*, 116(9), 2002.

[130] D. Coslovich and G. Pastore. Understanding fragility in supercooled lennard-jones mixtures. ii. potential energy surface. *J. Chem. Phys.*, 127(124505), 2007.

[131] D. Coslovich and G. Pastore. Are there localized saddles behind the heterogeneous dynamics of supercooled liquids? *Europhysics Letters*, 75(5):784–790, 2006.

[132] L. Angelani, R. Di Leornardo, G. Ruocco, A. Scalla, and F. Sciortino. Quasisaddles as relevant points of the potential energy surface in the dynamics of supercooled liquids. *J. Chem. Phys.*, 116(23), 2002.

[133] J. P. K. Doye and D. J. Wales. Comment on "quasisaddles as relevant points of the potential energy surface in the dynamics of supercooled liquids". *J. Chem. Phys.*, 118(11), 2003.

[134] L. Angelani, R. Di Leornardo, G. Ruocco, A. Scalla, and F. Sciortino. Reply to "comment on "quasisaddles as relevant points of the potential energy surface in the dynamics of supercooled liquids"". *J. Chem. Phys.*, 118(11), 2003.

[135] D. C. Liu and J. Nocedal. On the limited memory bfgs method for large scale optimization. *Mathematical Programming*, 45:503–528, 1989.

[136] C. J. Cerjan and W. H. Miller. On finding transition states. *J. Chem. Phys.*, 75(2800), 1981.

[137] D. J. Wales. *Energy Landscapes*, chapter Exploring the landscape. Cambdrige University Press, 2003.

[138] T. S. Grigera. Geometrical properties of the potential energy of the soft-sphere binary mixture. *J. Chem. Phys.*, 124(064502), 2006.

[139] H. Shintani and H. Tanaka. Frustration on the way to crystallization in glass. *Nature Physics*, 2, 2006.

[140] G. Tarjus, D. Kivelson, and P. Viot. The viscous slowing down of supercooled liquids as a temperature-controlled super-arrhenius activated process: a description in terms of frustration-limited domains. *J.Phys.:Condens. Matter*, 12, 2000.

[141] G. Tarjus, S.A Kivelson, Z. Nussinov, and P. Viot. The frustration-based approach of supercooled liquids and the glass transition: a review and critical assessement. *J.Phys.:Condens. Matter*, 17, 2005.

[142] F. C. Frank. Supercooling of liquids. *Proc. R. Soc. Lond.A.*, 215(1120):43–46, 1952.

[143] J. P. K. Doye, D. J. Wales, F. H. M. Zetterling, and M. Dzugutov. The favored cluster structures of model glass formers. *J. Chem. Phys.*, 118(6), 2003.

[144] A. Malins, J. Eggers, H. Tanaka, and C. P. Royall. Lifetimes and lengthscales of structural motifs in a model glassformer. *Faraday Discuss.*, 167(405), 2013.

[145] P. Viot, G. Tarjus, and D. Kivelson. A heterogeneous picture of alpha relaxation for fragile supercooled liquids. *J. Chem. Phys.*, 112(23), 2000.

[146] D. R. Nelson. *Defects and Geometry in Condensed Matter Physics*. Cambdrige University Press, 2002.

[147] S.A Kivelson, X. Zhao, D. Kivelson, T. M. Fischer, and C. M. Knobler. Frustration-limited clusters in liquids. *J. Chem. Phys.*, 101(3), 1994.

[148] M. Shimono and H. Onodera. Icosahedral symmetry, fragility and stability of supercooled liquid state of metallic glasses. *Rev. Metall.*, 109(1):41–46, 2012.

[149] U. R. Pedersen, N. P. Bailey, J. C. Dyre, and T. B. Schrøder. Crystallization of the wahnström binary lennard-jones liquid. *arXiv:0706.0813.*, 2013.

[150] U. R. Pedersen. *Long-time simulations of viscous liquids from strong correlations to crystallization*. PhD thesis, Danish National Research Foundation Centre "Glass and Time", IMFUFA, Department of Science, Systems and Models, Roskilde University, Denmark, 2009.

[151] U. R. Pedersen, T. B. Schrøder, J. C. Dyre, and P. Harrowell. Geometry of slow structural fluctuations in a supercooled binary alloy. *Physical Review Letters*, 104(105701), 2010.

[152] L. H. Bennett and R. E. Watson. Local atomic environments of hard magnets, metallic glasses and icosahedral phases. *Journal of Alloys and Compunds*, 197:271–280, 1993.

[153] E. Flenner and G. Szamel. Large and long-range dynamic correlations in supercooled fluids revealed via four-point correlation functions. *J. Phys. Chem. B*, 119(25), 2015.

[154] R. Pinney, T. B. Liverppol, and C. P. Royall. Structure in sheared supercooled liquids: Dynamical rearrangements of an effective system of icosahedra. *J. Chem. Phys.*, 145(234501), 2016.

Céline RUSCHER

Direction de la Recherche
Université de Strasbourg

The Voronoi Liquid:
a new model to probe the glass transition

Résumé

Comprendre l'origine microscopique du ralentissement de la dynamique au voisinage de la transition vitreuse reste l'un des problèmes fondamentaux de la physique de la matière condensée. Au cours de ce travail, nous introduisons un nouveau modèle de liquide, appelé liquide de Voronoï, et dont les interactions sont directement reliées aux propriétés géométriques des tessellations de Voronoï. Pour cette classe de liquides, les interactions sont à plusieurs corps et agissent de telle sorte que le système est toujours sous tension tout en restant stable.

Le but de ce travail est d'étudier un mélange binaire du liquide de Voronoï et de voir de quelles façons ces interactions exotiques affectent le scénario habituel de la transition vitreuse.

Tout au long de ce travail, nous caractérisons le liquide de Voronoï bidisperse théoriquement et par le biais des simulations numériques. Nous proposons également des comparaisons avec des liquides de Lennard-Jones surfondus bien décrit dans la littérature.

Mots clés : *transition vitreuse, tessellations de Voronoï, simulation de dynamique moléculaire, ralentissement de la dynamique, fragilité, théorie du couplage de modes, paysage d'énergie potentiel, structure localement favorisée*

Summary

Understanding the origin of the important slowing down of the dynamics near glass transition is still one of the remaining fundamental problems of condensed matter physics. During this work we introduced a brand-new model of liquids named Voronoi liquid, whose interactions are directly related to the geometrical properties of Voronoi tessellations. For these class of liquids interactions are intrinsically manybody and act in such a way that the liquid is always under tension but remains stable.

The aim of this work is to use a binary mixture of the Voronoi liquid to see to what extend these exotic interactions may affect the classical scenario of glass transition.

Throughout this work we characterize theoretically and by mean of numerical simulation the bidisperse Voronoi liquid. Comparisons with well-known Lennard-Jones glass formers are systematically performed.

Keywords: *glass transition, Voronoi tessellations, molecular dynamic simulations, dynamical arrest, fragility, mode coupling theory, potential energy landscape, locally favoured structures*